

# Analyzing Rotational Spectra of Complex Organic Molecules



Inaugural-Dissertation zur Erlangung des Doktorgrades  
der Mathematisch-Naturwissenschaftlichen Fakultät  
der Universität zu Köln

vorgelegt von

Luis Bonah  
aus Neuwied

angenommen im Jahr 2025

Berichterstatter:  
(Gutachter)

Prof. Dr. Stephan Schlemmer  
Prof. Dr. Zbigniew Kisiel  
Prof. Dr. Laurent Margulès

Tag der mündlichen Prüfung:

11.03.2025

# Kurzzusammenfassung

Diese Arbeit analysiert die Rotationsspektren der vier komplexen organischen Moleküle Aceton- $^{13}\text{C}_1$  ( $^{13}\text{CH}_3\text{C}(\text{O})\text{CH}_3$ ), Ethylphosphaethin ( $\text{C}_2\text{H}_5\text{CP}$ ), Cyclopentadien (*c*- $\text{C}_5\text{H}_6$ ), und Glycidaldehyd ( $(\text{C}_2\text{H}_3\text{O})\text{CHO}$ ). Breitbandmessungen zwischen 37 GHz und 1.1 THz wurden an drei verschiedenen Absorptionsspektrometern in Köln aufgenommen. Sowohl einfach  $^{13}\text{C}$  substituierte Isotopologe als auch vibrationsangeregte Zustände konnten auf Grund der hohen Sensitivität der Spektrometer identifiziert werden. Mit der Ausnahme von Aceton wurden alle einfach  $^{13}\text{C}$  substituierten Isotopologe analysiert sowie acht Vibrationszustände von Cyclopentadien und 17 Vibrationszustände von Glycidaldehyde. Fünf Interaktionssysteme wurden zwischen den Vibrationszuständen identifiziert und in den Modellen explizit behandelt, was es ermöglichte die Spektren mit experimenteller Genauigkeit zu beschreiben.

Die spektroskopische Analyse profitierte dabei von verschiedenen Methoden und Werkzeugen, von denen einige im Rahmen dieser Arbeit entwickelt wurden. Quantenchemische Rechnungen auf dem CCSD(T) Niveau wurden zusammen mit Ergebnissen vorheriger Analysen für initiale Werte der Rotationskonstanten genutzt. Abweichungen vom experimentellen Spektrum konnten leicht in Loomis-Wood Plots in der neu entwickelten LLWP Software verfolgt werden. Eine aktualisierte Version der Doppelresonanz-Doppelmodulation Messmethode erlaubte das Spektrum nach Linien zu filtern, die ein gemeinsames Energieniveau aufweisen. Damit konnten insbesondere Übergänge, die schwach in der Intensität, von stärkeren Übergängen überlagert, und/oder schlecht vorhergesagt waren, identifiziert werden. Durch die Kombination dieser Methoden war der Analyseprozess effizient und zuverlässig.

Die resultierenden Frequenzvorhersagen ermöglichen radioastronomische Suchen der Moleküle über einen weiten Frequenz- und Quantenzahlenbereich. Vibrationszustände dienen dabei als ausgezeichnete astronomische Temperaturmesser und die Isotopologe als Sonden für die astronomische  $^{12}\text{C}/^{13}\text{C}$ -Häufigkeit. Zusätzlich wurden anhand der Isotopologenergebnisse die (eingeschränkten) semi-experimentellen Gleichgewichtsstrukturen von Ethylphosphaethin und Cyclopentadien bestimmt.

Die hohe Anzahl an Zuständen, die mit experimenteller Genauigkeit analysiert wurden, verdeutlicht die Effizienz und Güte des Analyseprozesses und der eingesetzten Werkzeuge. Es ist zu erwarten, dass davon auch zukünftige spektroskopische Untersuchungen profitieren werden.

# Abstract

This thesis presents the rotational analyses of the complex organic molecules acetone- $^{13}\text{C}_1$  ( $^{13}\text{CH}_3\text{C}(\text{O})\text{CH}_3$ ), ethyl phosphoethyne ( $\text{CH}_3\text{CH}_2\text{CP}$ ), cyclopentadiene ( $c\text{-C}_5\text{H}_6$ ), and glycidaldehyde ( $(\text{C}_2\text{H}_3\text{O})\text{CHO}$ ). Three absorption spectrometers in Cologne were used to record high-resolution broadband spectra between 37 GHz and 1.1 THz resulting in a total coverage of 2.2 THz for the four species. Due to the high sensitivity of the experimental setups, singly substituted  $^{13}\text{C}$  isotopologues and vibrationally excited states up to  $873\text{ cm}^{-1}$  could be identified. The singly substituted  $^{13}\text{C}$  isotopologues were analyzed for all species but acetone- $^{13}\text{C}_1$  in addition to eight vibrationally excited states of cyclopentadiene and 17 vibrationally excited states of glycidaldehyde. Five interaction systems, resulting from Fermi and Coriolis interactions between vibrationally excited states, were identified and described to within experimental accuracy with combined fits.

A diverse set of tools was used for the spectroscopic analyses and in part also developed in the course of this thesis. Quantum chemical calculations at the CCSD(T) level together with previous analyses provided initial parameter values for the models which were efficiently extended with Loomis-Wood plots in the newly developed LLWP software. Additionally, an updated version of the recently developed double-modulation double-resonance technique was used to filter spectra for lines sharing an energy level. This greatly simplified the identification of lines in very dense spectra, especially if the lines of interest were weak, blended, and/or poorly predicted. The combination of these tools tremendously increased the speed and reliability of the analysis process.

The resulting frequency predictions allow for radio astronomical searches over a wide range of frequencies and quantum numbers. Rotational lines from vibrationally excited states are useful as astronomical temperature probes while the isotopologue predictions are useful for tracing the astronomical  $^{12}\text{C}/^{13}\text{C}$  ratio. In addition, the isotopologue data were used to derive (constrained) semi-experimental equilibrium  $r_e^{\text{SE}}$  geometries for ethyl phosphoethyne, and cyclopentadiene.

The high number of assigned transitions and states analyzed to within experimental uncertainty highlights the quality and efficiency of the analysis process and the tools used. Future analyses of other molecular species are expected to benefit from these advancements, especially in terms of efficiency and reliability.

# List of Publications

All publications of the author of this thesis are listed below. The five publications that are incorporated in this thesis are highlighted in bold text.

- C. P. Endres, M.-A. Martin-Drumel, O. Zingsheim, L. Bonah, O. Pirali, T. Zhang, A. Sánchez-Monge, T. Möller, N. Wehres, P. Schilke, M. C. McCarthy, S. Schlemmer, P. Caselli, S. Thorwirth, SOLEIL and ALMA views on prototypical organic nitriles:  $C_2H_5CN$ , *J. Mol. Spectrosc.* 375 (2021) 111392. doi:10.1016/j.jms.2020.111392.
- O. Zingsheim, L. Bonah, F. Lewen, S. Thorwirth, H. S. P. Müller, S. Schlemmer, Millimeter-millimeter-wave double-modulation double-resonance spectroscopy, *J. Mol. Spectrosc.* 381 (2021) 111519. doi:10.1016/j.jms.2021.111519.
- S. Herbers, O. Zingsheim, H. V. L. Nguyen, L. Bonah, B. Heyne, N. Wehres, S. Schlemmer, Internal rotation arena: Program performances on the low barrier problem of 4-methylacetophenone, *J. Chem. Phys.* 155 (2021) 224302. doi:10.1063/5.0070298.
- O. Zingsheim, H. S. P. Müller, L. Bonah, F. Lewen, S. Thorwirth, S. Schlemmer, (Sub-)millimeter-wave spectroscopy of *gauche*-propanal, *J. Mol. Spectrosc.* 384 (2022) 111565. doi:10.1016/j.jms.2021.111565.
- O. Zingsheim, J. Maßen, H. S. P. Müller, B. Heyne, M. Fatima, L. Bonah, A. Belloche, F. Lewen, S. Schlemmer, Rotational spectroscopy of *n*-propanol: *Aa* and *Ag* conformers, *Astron. Astrophys.* 662 (2022) A111. doi:10.1051/0004-6361/202243571.
- **L. Bonah, O. Zingsheim, H. S. P. Müller, J.-C. Guillemin, F. Lewen, S. Schlemmer, LLWP—A new Loomis-Wood software at the example of Acetone- $^{13}C_1$ , *J. Mol. Spectrosc.* 388 (2022) 111674. doi:10.1016/j.jms.2022.111674.**
- P. B. Changala, N. L. Chen, H. L. Le, B. Gans, K. Steenbakkers, T. Salomon, L. Bonah, I. Schroetter, A. Canin, M.-A. Martin-Drumel, U. Jacovella, E. Dartois, S. Boyé-Péronne, C. Alcaraz, O. Asvany, S. Brünken, S. Thorwirth, S. Schlemmer, J. R. Goicoechea, G. Rouillé, A. Sidhu, R. Chown, D. Van De Putte, B. Trahin, F. Alarcón, O. Berné, E. Habart, E. Peeters, Astronomical  $CH_3^+$  rovibrational assignments: A combined theoretical and experimental study validating observational findings in the d203-506 UV-irradiated protoplanetary disk, *Astron. Astrophys.* 680 (2023) A19. doi:10.1051/0004-6361/202347765.
- S. Thorwirth, K. Steenbakkers, T. Danowski, P. C. Schmid, L. Bonah, O. Asvany, S. Brünken, S. Schlemmer, Gas-Phase Infrared Action Spectroscopy of  $CH_2Cl^+$  and  $CH_3ClH^+$ : Likely Protagonists in Chlorine Astrochemistry, *Molecules* 29 (2024) 665. doi:10.3390/molecules29030665.

- 
- W. G. D. P. Silva, L. Bonah, P. C. Schmid, S. Schlemmer, O. Asvany, Hyperfine-resolved rotational spectroscopy of  $\text{HCNH}^+$ , *J. Chem. Phys.* 160 (2024) 071101. doi:10.1063/5.0185365.
  - L. Bonah, S. Schlemmer, J.-C. Guillemin, M. E. Harding, S. Thorwirth, On the Spectroscopy of Phosphaalkynes: Millimeter- and Submillimeter-Wave Study of  $\text{C}_2\text{H}_5\text{CP}$ , *J. Phys. Chem. A* 128 (2024) 4859–4866. doi:10.1021/acs.jpca.4c02566.
  - L. Bonah, B. Helmstaedter, J.-C. Guillemin, S. Schlemmer, S. Thorwirth, Extending the rotational spectrum of cyclopentadiene towards higher frequencies and vibrational states, *J. Mol. Spectrosc.* 408 (2025) 111967. doi:10.1016/j.jms.2024.111967.
  - L. Bonah, J.-C. Guillemin, A. Belloche, S. Thorwirth, H. S. P. Müller, S. Schlemmer, Leveraging MMW-MMW Double Resonance Spectroscopy to Understand the Pure Rotational Spectrum of Glycidaldehyde and 17 of its Vibrationally Excited States, *ACS Earth Space Chem.* in press (2025). doi:10.1021/acsearthspacechem.4c00360.
  - L. Bonah, S. Schlemmer, S. Thorwirth, Spectroscopy of Vibrationally Excited Complex Organic Molecules for Radio Astronomy, *in prep.*

# Contents

<b>1</b>	<b>Introduction</b>	<b>1</b>
<b>2</b>	<b>Theory</b>	<b>6</b>
2.1	Spectrum . . . . .	6
2.2	The Rotational Hamiltonian . . . . .	7
2.2.1	Linear Molecules . . . . .	9
2.2.2	Symmetric Molecules . . . . .	11
2.2.3	Asymmetric Molecules . . . . .	12
2.3	Lineshape, Population and Intensity . . . . .	17
2.3.1	Lineshape . . . . .	17
2.3.2	Population and Degeneracy . . . . .	18
2.3.3	Transition Dipole Moment and Einstein Coefficient . . . . .	19
2.3.4	Intensity . . . . .	20
2.4	Internal Rotation and ERHAM . . . . .	21
2.4.1	Internal Rotation Splitting . . . . .	22
2.4.2	Two Internal Rotors . . . . .	25
2.4.3	ERHAM . . . . .	26
<b>3</b>	<b>Experimental Setup</b>	<b>28</b>
3.1	Absorption Spectrometers . . . . .	29
3.2	Double Resonance Setup . . . . .	31
<b>4</b>	<b>Analysis Process and Software</b>	<b>32</b>
4.1	Measuring the Spectrum . . . . .	32
4.2	Initial Predictions . . . . .	34
4.3	Iterative Assignment Cycle . . . . .	35
4.4	Finalizing the Analysis . . . . .	39
4.5	Advanced Steps . . . . .	39
<b>5</b>	<b>Spectroscopy of Vibrationally Excited COMs</b>	<b>40</b>
<b>6</b>	<b>A new Loomis-Wood Software at the Example of Acetone-<sup>13</sup>C<sub>1</sub></b>	<b>62</b>
<b>7</b>	<b>MM- and Sub-MM-Wave Study of C<sub>2</sub>H<sub>5</sub>CP</b>	<b>73</b>
<b>8</b>	<b>Towards Higher Frequencies and Vibrational States of <i>c</i>-C<sub>5</sub>H<sub>6</sub></b>	<b>82</b>

---

<b>9</b>	<b>Double Resonance Spectroscopy of Glycidaldehyde</b>	<b>92</b>
<b>10</b>	<b>Conclusions and Outlook</b>	<b>112</b>
<b>A</b>	<b>Appendix</b>	<b>115</b>
A.1	Higher-Order Centrifugal Distortion Constants . . . . .	115
A.2	Reduced Energy Diagrams . . . . .	116
A.3	(Sub-)Millimeter Spectrometer . . . . .	118
A.4	Examples of Residual Plots . . . . .	119
A.5	Examples of <i>pyckett_omit</i> and <i>pyckett_add</i> . . . . .	121
A.6	Graphical User Interfaces . . . . .	123
A.7	SI for MM- and Sub-MM-Wave Study of C <sub>2</sub> H <sub>5</sub> CP . . . . .	128
A.8	SI for DR Spectroscopy of Glycidaldehyde . . . . .	136
	<b>References</b>	<b>161</b>
	<b>List of Abbreviations</b>	<b>162</b>
	<b>List of Figures</b>	<b>163</b>
	<b>Acknowledgments</b>	<b>164</b>
	<b>Declaration of Originality</b>	<b>165</b>

# 1. Introduction

Molecules possess distinct energy levels for their rotational, vibrational, and electronic states in accordance with the rules of quantum mechanics. These energy levels are characteristic of the geometry of the molecule, its force field, and its electronic structure, respectively. Consequently, the transitions between the molecular energy levels are distinct and characteristic of the molecule. Therefore, the spectrum of comprising transitions is often referred to as the the molecular fingerprint because, analogously to a human fingerprint, it uniquely identifies the molecule. An advantage of molecular fingerprints over human fingerprints is that they can be used to infer physical properties (e.g., temperature, pressure, column density or velocity) of the molecule’s environment. To derive these properties from the spectroscopic fingerprint, a quantum mechanical (QM) description is required. With this, the spectrum can be simulated for different physical properties and also to some extent inter- and extrapolated to unmeasured regions of the electromagnetic (EM) spectrum. Conversely, the physical properties of astronomical regions can be derived from their spectra. For example, the temperature can be determined by measuring the relative intensities of different transitions. Some approaches foregoing QM models exist<sup>1–5</sup> but are lacking the ability to inter- or extrapolate the spectrum<sup>a</sup>.

Typically, the rotational, vibrational, and electronic transitions of a molecule are found in different regions of the EM spectrum. Rotational transitions are the lowest in energy and cover the microwave (MW; 1–30 GHz), millimeter-wavelength (MMW; 30–300 GHz), and sub-millimeter-wavelength (sub-MMW; 300 GHz – 30 THz) regions. Vibrational transitions are higher in energy, spanning from the far-infrared (FIR; 400–50 cm<sup>-1</sup>), for energetically low-lying vibrations such as torsional motions, to the infrared (IR; 4000–400 cm<sup>-1</sup>), for more energetic vibrations like bending and stretching motions. Lastly, electronic transitions are found in the optical and ultraviolet (UV) regimes.

This thesis focuses exclusively on molecular rotational spectra thereby covering the radio wave (< 3 THz) and sub-MMW regions. A great advantage, especially for the MW

---

<sup>a</sup>In principle, the double-modulation double-resonance (DM-DR) technique<sup>6</sup> could also be used without QM models. A full 2D scan of the rotational spectrum would reveal all shared energy levels between transitions. However, due to the limited frequency coverage of the setup used here, only subnetworks of the total energy term diagram can be reconstructed. Similarly, also the approach of De Lucia and coworkers, using intensity-calibrated spectra measured over a range of temperatures,<sup>1,2</sup> and approaches based on combination differences<sup>3–5</sup> rely on measuring the entire spectral range of interest.

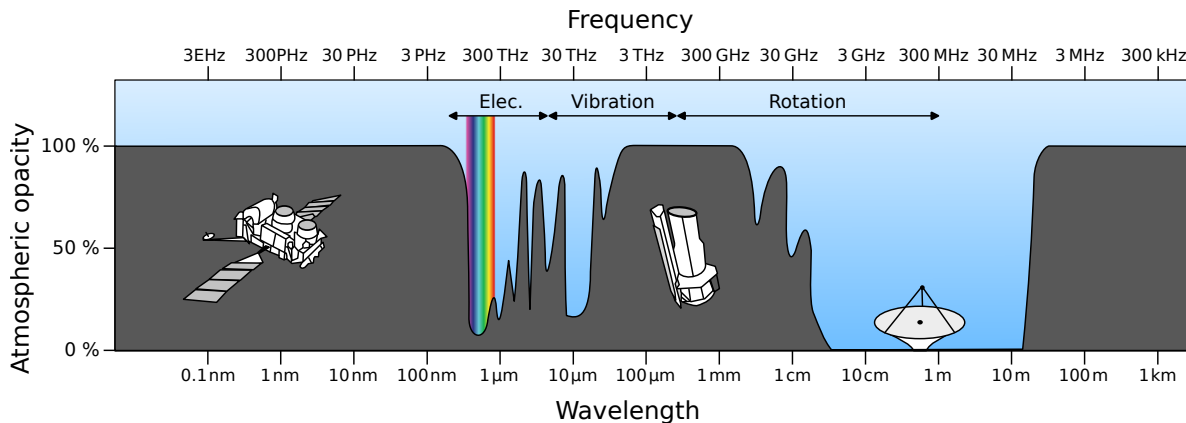


**Figure 1.1:** The opacity of Earth’s atmosphere for different frequencies (upper scale) or wavelengths (lower scale). Rotational transitions fall into the radio window of the atmosphere and can therefore be observed from Earth. For frequencies above 300 GHz, the opacity reaches up to 100 % requiring observations to be either performed at very high altitudes (e.g., ALMA) or above the troposphere (e.g., with SOFIA, the Herschel Space Observatory, JWST, or the here shown Compton Gamma Ray Observatory and Hubble Space Telescope). Figure adapted from NASA.

and MMW regions, is the transparency of Earth’s atmosphere in this frequency range (see Fig. 1.1). This makes it possible to use Earth-based telescopes to study distant regions in space. While the first molecule detected in space,  $\text{CH}^+$ ,<sup>7-9</sup> was found via electronic transitions in the UV and visible regions, most astronomical detections of molecules since then have been made using radio telescopes.<sup>10</sup> The vast majority of recent detections were made with three single-dish telescopes: The Institut de Radioastronomie Millimétrique (IRAM) 30 m telescope, the Green Bank 100 m Telescope (GBT), and the Yebes 40 m telescope.<sup>10</sup> The latter two are located at altitudes of 818 m and 931 m with the highest observable frequencies at 116 GHz and 90 GHz, respectively. In contrast, the IRAM 30 m telescope covers frequencies up to 375 GHz and is located at an altitude of 2850 m<sup>b</sup>.

The telescopes measure the EM radiation emitted<sup>c</sup> by regions in space, which can then be searched for molecular fingerprints. Once a molecule is found, appropriate models of its spectral characteristics can be used to infer the prevalent physical properties of the astronomical source which is invaluable to astronomers in understanding and modeling these regions. To identify the molecules in space, a matching fingerprint in a database is

<sup>b</sup>Going higher in altitude minimizes the attenuation of signals from space by reducing the distance through the atmosphere. The Atacama Large Millimeter/submillimeter Array (ALMA) telescope covers frequencies up to 950 GHz, which is slightly beyond the atmospheric window (compare Fig. 1.1). Located at an altitude of 5059 m in the dry Atacama Desert, observations are possible because the atmosphere is very thin and dry. Taking this even more to the extreme, the Stratospheric Observatory For Infrared Astronomy (SOFIA) covered frequencies up to 1 THz while flying at altitudes of up to 13.7 km until its decommissioning in 2022 and the James Webb Space Telescope (JWST) measures the infrared region from space, about  $1.5 \times 10^6$  km from Earth.

<sup>c</sup>In special configurations, astronomical absorption spectra are possible as well if the absorption spectrum can be measured against a continuous background source, such as a (proto)star.

required. This is where molecular spectroscopy shines by measuring and analyzing the spectra of molecules in the laboratory, building appropriate quantum chemical models, and publishing the results in astronomical databases such as the Cologne Database for Molecular Spectroscopy (CDMS).<sup>11,12</sup> In this context, molecular spectroscopy is often also referred to as laboratory astrophysics. The number of astronomical detections has been increasing steeply since the year 2020 (see Fig. 1 of Sec. 5), mainly due to complex organic molecules (COMs). This increase, driven in part by the commissioning of a new generation of receivers,<sup>13</sup> presents a challenge for laboratory spectroscopy, as the efficiency of the analysis process must be improved to keep pace with the speed of astronomical observations.<sup>14</sup>

To date, more than 340 molecules have been detected in the interstellar medium<sup>d</sup>, half of which can be classified as COMs, defined here as carbon-bearing molecules with six or more atoms.<sup>15</sup> COMs are of particular interest as they might be possible precursors of life, and thus could indicate the formation of extraterrestrial life, or at least habitable zones. They have been detected in a wide variety of astronomical objects, ranging from very cold dark clouds ( $\sim 10$  K) to star-forming regions or protoplanetary disks which easily reach temperatures of a few 100 or 1000 K, respectively.<sup>11,16-18</sup> Many of the most complex molecules ( $> 12$  atoms) have only recently been detected, especially in the cold dark cloud TMC-1,<sup>19-30</sup> but also towards high-mass star-forming regions.<sup>31</sup> In contrast, two of the three largest astronomically detected molecules, the fullerenes  $C_{60}$ , and  $C_{70}$  were detected in 2010 towards the young planetary nebula Tc 1,<sup>32</sup> and  $C_{60}^+$  was tentatively detected in 1994 near several reddened stars<sup>33</sup> but has since been found in other stars,<sup>34</sup> as well as protoplanetary and reflection nebulae.<sup>35,36</sup> This highlights the richness of astronomical chemistry, as both small and large molecules are found over a wide range of temperatures. However, rotational spectroscopy goes far beyond laboratory astrophysics as it is also immensely useful for identifying samples and quantifying concentrations on Earth, determining molecular structures and other properties<sup>e</sup>, as well as examining fundamental physics.<sup>37-39</sup> By combining the latter with radio astronomy, the variation of fundamental constants over time can be tested by analyzing data at different redshifts. The only requirements for rotational spectroscopy are that the molecule is polar and that it must be measured in the gas phase.

In this thesis, the rotational analyses of the astrophysically relevant COMs acetone- $^{13}C_1$ ,

---

<sup>d</sup>See the *Molecules in Space* section of the Cologne Database for Molecular Spectroscopy or *The Astrochymist* website at [www.astrochymist.org](http://www.astrochymist.org)

<sup>e</sup>Examples of structure determinations are given in Sec. 7 and Sec. 8. Regarding further properties that can be derived from spectroscopy, the rotational constants are directly related to the moments of inertia and results from rotational spectroscopy are usually an order of magnitude more precise than those from crystallography. The dipole moments can be derived from the Stark effect, vibrational energy separations from interactions (see Sec. 8 and Sec. 9), barriers from internal rotation, the electronic structure from fine or hyperfine structure, and the vibrational force field from both the centrifugal distortion constants and interaction parameters.

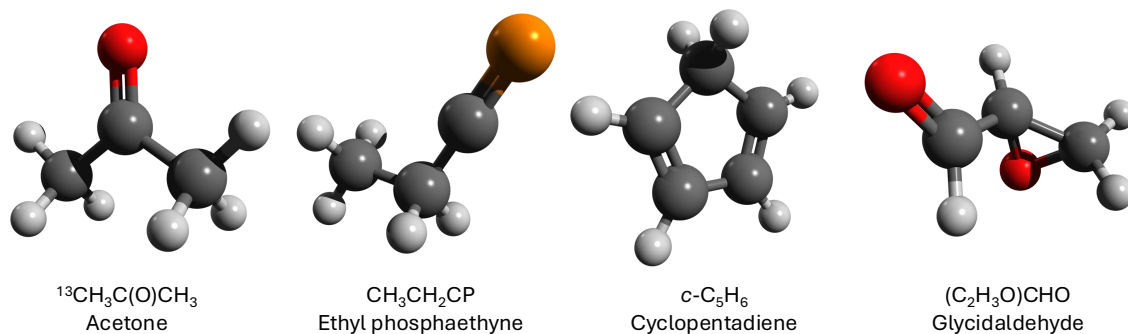


**Figure 1.2:** The four COMs analyzed in this thesis in ball-and-stick representation. Hydrogen atoms are shown in white, carbon atoms in gray, oxygen atoms in red, and the phosphorus atom in orange. The representations were created with Avogadro.<sup>40,41</sup>

ethyl phosphoethyne, cyclopentadiene, and glycidaldehyde are presented. Ball-and-stick representations of the four molecules are shown in Fig. 1.2. Acetone- $^{13}\text{C}_1$  has been tentatively detected towards Sgr B2(N2)<sup>42</sup> and cyclopentadiene was detected towards the prototypical dark cloud TMC-1.<sup>26</sup> Ethyl phosphoethyne and glycidaldehyde have not yet been detected astronomically, but are potential candidates for detections since the closely related ethyl cyanide ( $\text{CH}_3\text{CH}_2\text{CN}$ )<sup>43,44</sup> and oxirane ( $c\text{-C}_2\text{H}_4\text{O}$ )<sup>45–49</sup> are known to be ubiquitous in space.

For all four molecules, high-resolution broadband spectra over a wide frequency range were recorded with three different absorption spectrometers in the Cologne laboratories. The broad frequency coverage achieved in the studies presented here leads to accurate frequency predictions even beyond 1 THz which in turn facilitates astronomical searches in a wide range of astronomical surveys. At the same time, the high sensitivity of the experimental setups facilitates the analysis of isotopologues at natural abundance and of vibrationally excited states even high in energy. Isotopologues and vibrational states are of particular astronomical interest as they are excellent diagnostics of isotopic ratios (e.g.,  $^{12}\text{C}/^{13}\text{C}$  ratio) and the temperature, respectively. In addition, they are thought to be the origin of a large number of unassigned lines in astronomical spectra.<sup>15,50,51</sup> However, the analysis of vibrationally excited states in molecular spectra can be challenging due to their lower intensity and possible interactions between vibrational states close in energy.<sup>51</sup> This is amplified when going to higher vibrational energies, as the vibrational spectrum becomes denser making the appearance of interactions more likely.

To address these challenges, a diverse toolbox has been used, parts of which were developed during this thesis. The most important tools are Loomis-Wood plots (LWPs), quantum chemical calculations (QCC), tools for treating interactions of vibrational states, and double resonance (DR) techniques. Each of the four rotational analyses illustrates the use of one of these tools. The acetone- $^{13}\text{C}_1$  analysis (Sec. 6) describes the LLWP software which relies on LWPs for an efficient and reliable spectroscopic assignment process. The power

of QCC is demonstrated in the study of ethyl phosphoethyne (Sec. 7), where the excellent agreement between calculations and measurements allowed the immediate assignment of the experimental spectrum. For cyclopentadiene, vibrationally excited states were analyzed for the first time in addition to the ground vibrational state. The process of finding perturbed series without relying on QCC and treating the interactions between vibrational states is highlighted there (Sec. 8). Finally, the analysis of glycidaldehyde is a prime example of a powerful DM-DR technique<sup>6</sup> that precisely filters the spectrum for lines sharing an energy level (Sec. 9). Weak series were found even in the densest parts of the spectrum, perturbed series were easily followed, and multiple interstate transitions were identified. This allowed the analysis of 17 vibrationally excited states and three interaction systems of glycidaldehyde.

The outline of this thesis is as follows: First, the rotational spectrum is introduced in general (Sec. 2) by explaining the theory behind the frequency positions (Sec. 2.2) as well as the intensities and lineshapes (Sec. 2.3). In addition, the implications and treatment of internal rotation are introduced (Sec. 2.4). The experimental setups are then described in some detail (Sec. 3), followed by a brief overview of the general analysis process and software developed as part of this thesis (Sec. 4). Next, special considerations for vibrational satellite spectra are discussed (Sec. 5), before the analyses of the four molecules acetone-<sup>13</sup>C<sub>1</sub> (Sec. 6), ethyl phosphoethyne (Sec. 7), cyclopentadiene (Sec. 8), and glycidaldehyde (Sec. 9) follow. Finally, the results are summarized and an outlook is given (Sec. 10).

## 2. Theory

This chapter introduces the rotational fingerprint of molecules, which is used to uniquely identify them. First, the origin of a line spectrum is explained (Sec. 2.1) and the rotational Hamiltonian is introduced (Sec. 2.2). Since no analytical solution exists for the asymmetric top case, to which the four molecules of interest belong to, a qualitative understanding of the asymmetric top energy scheme is obtained by first introducing the analytically solvable cases of linear molecules (Sec. 2.2.1) and symmetric tops (Sec. 2.2.2). The positions in the spectrum can be derived from the rotational Hamiltonian. Then, the population, intensities and lineshapes are explained (Sec. 2.3). Finally, internal rotation is introduced phenomenologically (Sec. 2.4), the case of two internal rotors is explained (Sec. 2.4.2), followed by the Effective Rotational HAMILtonian (ERHAM) approach used to solve the internal rotation Hamiltonian in the analysis of acetone- $^{13}\text{C}_1$  (presented in Sec. 6).

Additional information on the rotational spectrum of vibrationally excited states is given later in Sec. 5. This chapter is largely based on the corresponding chapters in *Microwave Molecular Spectra* by Gordy and Cook<sup>52</sup> and, unless otherwise noted, is implicitly limited to the cases of absorption spectra of electronic dipole transitions.

### 2.1 Spectrum

Each molecule possesses distinct electronic, vibrational, and rotational states. If a transition between two states is allowed, i.e. it has a non-zero intensity, a transition between two states is possible either by absorbing a photon, going from the energetically lower to the energetically higher state, or by emitting a photon for the inverse process. The energy difference is related to the photon energy by

$$\Delta E = E' - E'' \tag{2.1}$$

$$= h\nu = h\frac{c}{\lambda} = hc\tilde{\nu} \tag{2.2}$$

where  $E'$  and  $E''$  are the energies of the upper and lower states, respectively,  $c$  is the speed of light, and  $h$  the Planck constant.

In the second row the fundamental relation

$$c = \lambda\nu = \frac{\nu}{\tilde{\nu}} \quad (2.3)$$

was used which connects the wavelength  $\lambda$ , the frequency  $\nu$ , and the wavenumber  $\tilde{\nu}$  of the photon. By measuring the absorption (or emission) for a set of different frequencies, a spectrum is obtained where each signal position is related to an energy difference by the given formulas.

## 2.2 The Rotational Hamiltonian

According to the Born-Oppenheimer approximation, the complete wavefunction  $\psi_{\text{total}}$  of a molecule can be treated as the product of an electronic, vibrational, rotational, and nuclear spin wavefunction

$$\psi_{\text{total}} = \psi_{\text{elec}}\psi_{\text{vib}}\psi_{\text{rot}}\psi_{\text{ns}} \quad (2.4)$$

The rotational energy of a state is thus given by the eigenvalues of its rotational wavefunction with the rotational Hamiltonian

$$\mathbf{H}_{\text{rot}}|\psi_i\rangle = E_{\text{rot},i}|\psi_i\rangle \quad (2.5)$$

In the classical case, the rotational energy of a rigid body with total angular momentum  $\vec{J}$  is given by

$$E_{\text{rot}} = \frac{J_a^2}{2I_a} + \frac{J_b^2}{2I_b} + \frac{J_c^2}{2I_c} \quad (2.6)$$

with the angular momentum components  $J_\alpha$  and moment of inertia components  $I_\alpha$  along the  $\alpha$ -axis, with  $\alpha = a, b$ , or  $c$ . The  $a$ -,  $b$ -, and  $c$ -axes are the principal axes of the molecule, meaning they are oriented in such a manner that the moment of inertia tensor is fully diagonal with the three diagonal components being the  $I_\alpha$ . By convention, the three principal moments of inertia are ordered to fulfill

$$I_a \leq I_b \leq I_c \quad (2.7)$$

In the literature, often the moments of inertia are specified indirectly via the inversely proportional rotational constants

$$A/B/C = \frac{h}{8\pi^2 I_{a/b/c}} \quad (2.8)$$

which are given here in units of a frequency.

The quantum mechanical Hamiltonian for a rigid rotor is defined analogously to Eq. 2.6 as

$$\mathbf{H}_{\text{rr}} = \frac{\mathbf{J}_a^2}{2I_a} + \frac{\mathbf{J}_b^2}{2I_b} + \frac{\mathbf{J}_c^2}{2I_c} \quad (2.9)$$

where the  $\mathbf{J}_\alpha$  are the angular momentum component operators. Because the bonds between atoms in a molecule are closer to springs than rigid connections, the centrifugal forces resulting from the rotation lead to a distortion of the molecular geometry. This is taken into account by adding terms for the centrifugal distortion to the rotational Hamiltonian

$$\mathbf{H}_{\text{rot}} = \mathbf{H}_{\text{rr}} + \mathbf{H}_{\text{cd}} \quad (2.10)$$

$$\mathbf{H}_{\text{cd}} = \frac{1}{4} \sum_{\alpha,\beta,\gamma,\delta} \tau_{\alpha\beta\gamma\delta} \mathbf{J}_\alpha \mathbf{J}_\beta \mathbf{J}_\gamma \mathbf{J}_\delta + \dots \quad (2.11)$$

For the centrifugal distortion Hamiltonian,  $\alpha$ ,  $\beta$ ,  $\gamma$ , and  $\delta$  are summed over  $a$ ,  $b$ , and  $c$  with the  $\tau_{\alpha\beta\gamma\delta}$  being the centrifugal distortion constants as defined by Kivelson and Wilson.<sup>53</sup> Here only the quartic order is given, but higher orders are defined analogously. The invariance of the Hamiltonian under time-reversal requires even powers of the angular momenta operators, essentially simplifying the centrifugal distortion Hamiltonian to

$$\mathbf{H}_{\text{cd}} = \frac{1}{4} \sum_{\alpha,\beta} \tau_{\alpha\alpha\beta\beta} \mathbf{J}_\alpha^2 \mathbf{J}_\beta^2 + \dots \quad (2.12)$$

Only five linear combinations of the fourth-order  $\tau$ 's are determinable, resulting in the reduced Hamiltonians – being either Watson's  $A$ -reduction<sup>54,55</sup> or the  $S$ -reduction,<sup>56,57</sup> with the latter being advantageous for very symmetric molecules. In the  $S$ -reduction, the centrifugal distortion Hamiltonian takes the form

$$\begin{aligned} \mathbf{H}_{\text{cd}} = & -D_J \mathbf{J}^4 - D_{JK} \mathbf{J}^2 \mathbf{J}_z^2 - D_K \mathbf{J}_z^4 \\ & + d_1 \mathbf{J}^2 (\mathbf{J}_+^2 + \mathbf{J}_-^2) + d_2 (\mathbf{J}_+^4 + \mathbf{J}_-^4) + \dots \end{aligned} \quad (2.13)$$

where  $\mathbf{J}_\pm = \mathbf{J}_x \pm i\mathbf{J}_y$  are the raising and lowering operators. The connection between the  $a$ ,  $b$ ,  $c$  and the  $x$ ,  $y$ ,  $z$  labels for the axes is given by the chosen representation<sup>a</sup>.

<sup>a</sup>There are six different representations, meaning six mappings from the  $a$ ,  $b$ ,  $c$  to the  $x$ ,  $y$ ,  $z$  labels of the axes:

	I <sup>r</sup>	II <sup>r</sup>	III <sup>r</sup>	I <sup>l</sup>	II <sup>l</sup>	III <sup>l</sup>
a	z	y	x	z	x	y
b	x	z	y	y	z	x
c	y	x	z	x	y	z

The representation is typically chosen such that off-diagonal elements become as small as possible. It is vital to specify the used representation as many rotational constants depend on the  $(x, y, z)$  axis system. Therefore, Hamiltonians set up in different representations will result in different values for these rotational constants.

Higher-order centrifugal distortion constants are given in both  $A$ - and  $S$ -reduction in Sec. A.1.

Molecules are divided into five molecule classes based on their moments of inertia:

Linear molecules	$I_a = 0$ , $I_b = I_c$
Spherical tops	$I_a = I_b = I_c$
Prolate symmetric tops	$I_a < I_b = I_c$
Oblate symmetric tops	$I_a = I_b < I_c$
Asymmetric tops	$I_a < I_b < I_c$

The molecules studied in this thesis are all asymmetric tops for which no analytical solutions exist except for the lowest values of the angular momentum quantum number  $J$ . Typically, their energy levels are determined numerically via matrix formalism. The degree of asymmetry of a molecule is measured by Ray's asymmetry parameter  $\kappa$  given by<sup>58</sup>

$$\kappa = \frac{2B - A - C}{A - C} \quad (2.14)$$

The two limiting cases are  $+1$  for an oblate symmetric top and  $-1$  for a prolate symmetric top. If an asymmetric molecule is fairly close to one of the symmetric limits, the spectrum shows qualitative similarities with the spectrum of the corresponding symmetric top. Therefore, the analytical solutions for linear and symmetric molecules are introduced first to provide some intuition. Spherical molecules are omitted because they have no net dipole moment and thus no allowed rotational dipole transitions.

## 2.2.1 Linear Molecules

The most simple assumption is that of a rigid linear molecule. As a linear molecule has no rotation around the  $a$ -axis and  $I_b = I_c = I$  its rotational Hamiltonian is simplified to

$$\mathbf{H}_{\text{rot}} = \frac{\mathbf{J}^2}{I} \quad (2.15)$$

and the rotational energies are its eigenvalues

$$E_{\text{rot}}/h = BJ(J+1) \quad (2.16)$$

as also shown on the left hand side of Fig. 2.1. For one-photon transitions, the change in angular momentum is limited to the photon's angular momentum of  $\pm\hbar$  resulting in  $\Delta J = \pm 1$ . The resulting spectrum consists of equidistant transitions

$$\nu_{J+1 \leftarrow J} = 2B(J+1) \quad (2.17)$$

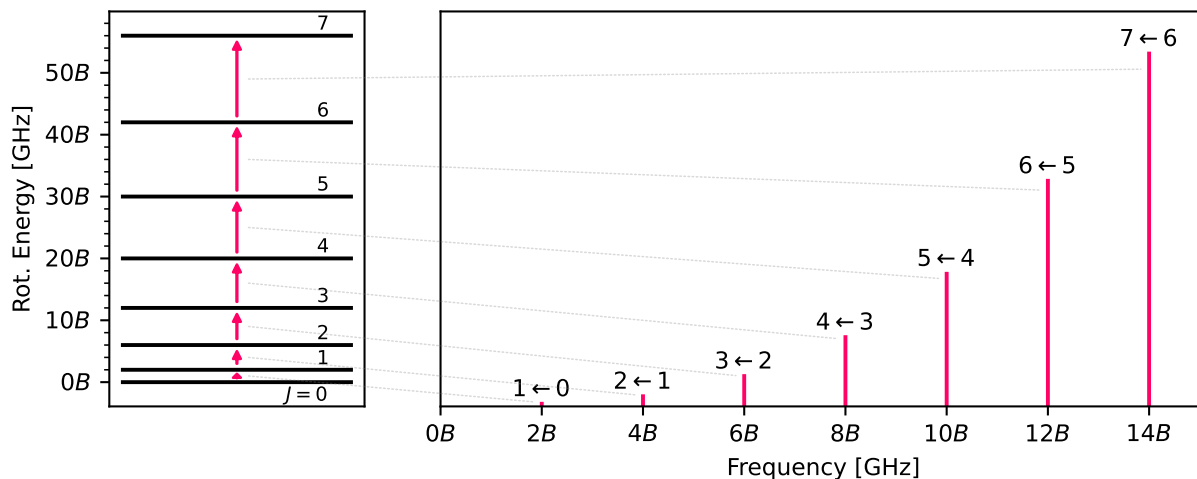


**Figure 2.1:** The calculated rotational energies (left hand side) and rotational transitions (right hand side) of a linear molecule (OCS at 300 K) up to  $J = 7$ . The energies and frequencies are given in multiples of the rotational constant  $B$ . The arrows indicating transitions in the energy diagram are connected by gray dotted lines with the transitions in the spectrum. The intensities of the transitions on the right hand side are explained in Sec. 2.3.4.

with a distance of  $2B$  as shown on the right hand side of Fig. 2.1. When adding centrifugal distortion for a non-rigid molecule, Eq. 2.16 is expanded into

$$E_{\text{rot}}/h = BJ(J+1) - D(J(J+1))^2 + \dots \quad (2.18)$$

with the centrifugal distortion constant  $D$ . For linear molecules,  $D$  is positive as the internuclear distance is increased by the centrifugal forces. As a result, the effective rotational constant  $B_{\text{eff}} = B - DJ(J+1)$  and the transition frequencies

$$\nu_{J+1 \leftarrow J} = 2B(J+1) - 4D(J+1)^3 + \dots \quad (2.19)$$

are decreased in comparison to the rigid rotor.

The main results are, that rotational spectra of linear molecules have almost equidistant patterns (as  $D$  is a few magnitudes smaller than  $B$ ) and that neglecting higher centrifugal distortion constants results in transition frequencies being predicted to slightly higher frequencies.

## 2.2.2 Symmetric Molecules

Starting again with the rigid rotor case and considering a prolate symmetric rotor, the rotational energy of a symmetric top is obtained by using  $I_b = I_c$  and Eq. 2.6. This yields

$$E_p = \frac{J_a^2}{2I_a} + \frac{J_b^2 + J_c^2}{2I_b} \quad (2.20)$$

$$= \frac{J_a^2}{2I_a} + \frac{J^2 - J_a^2}{2I_b} \quad (2.21)$$

$$= J^2 \frac{1}{2I_b} + J_a^2 \left( \frac{1}{2I_a} - \frac{1}{2I_b} \right) \quad (2.22)$$

The corresponding rotational Hamiltonian is

$$\mathbf{H} = \mathbf{J}^2 \frac{1}{2I_b} + \mathbf{J}_a^2 \left( \frac{1}{2I_a} - \frac{1}{2I_b} \right) \quad (2.23)$$

When using Eq. 2.23 and the rotational constants  $A$ ,  $B$  and  $C$  instead of the moments of inertia, the energies are found to be

$$E_p/h = BJ(J+1) + (A-B)K_a^2 \quad (2.24)$$

Analogously, the energies of an oblate symmetric top are found to be

$$E_o/h = BJ(J+1) + (C-B)K_c^2 \quad (2.25)$$

Here, the total angular momentum quantum number  $J$  and its projections on the respective molecule axes  $K_a$  and  $K_c$  are used. The projection quantum numbers have to fulfill  $J \geq K_a$  and  $J \geq K_c$  as a projection cannot be larger than the quantity itself. Eq. 2.24 and Eq. 2.25 are similar to the linear molecule case (Eq. 2.16) but have a  $K_a$  or  $K_c$  dependent offset. For a prolate symmetric top, the energy offset increases with  $K_a$  whereas it decreases for the oblate symmetric top with  $K_c$ <sup>b</sup>. This is shown in Fig. 2.2 where the energy term diagrams are compared to a linear molecule.

The selection rules for a symmetric top molecule are

$$\Delta J = \pm 1 \quad (2.26)$$

$$\Delta K = 0 \quad (2.27)$$

resulting in the same transition frequencies as for a rigid linear molecule

$$\nu_{J+1, K \leftarrow J, K} = 2B(J+1) \quad (2.28)$$

---

<sup>b</sup>From  $A \geq B \geq C$  it follows that  $A - B \geq 0$  and  $C - B \leq 0$

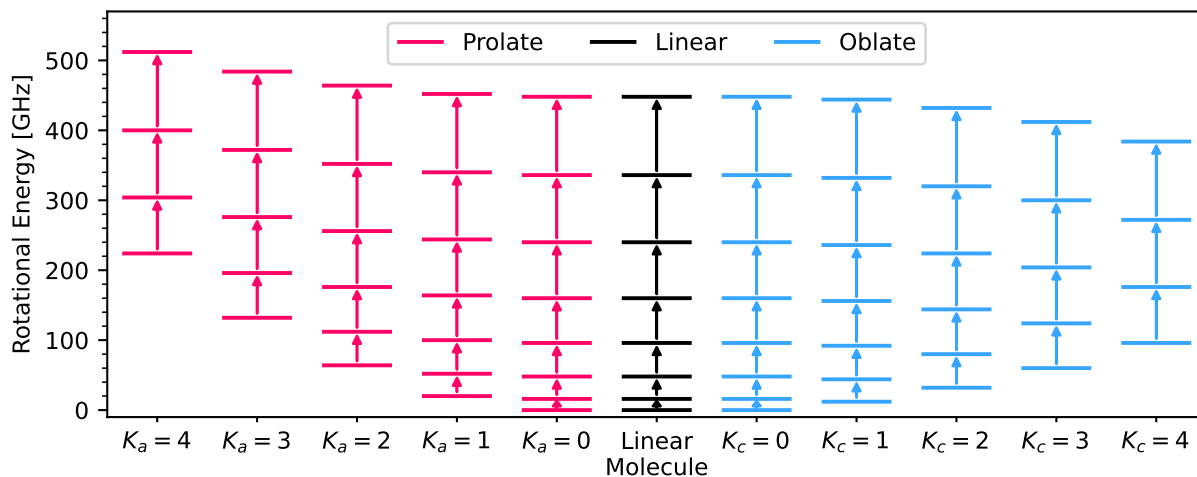


**Figure 2.2:** Simulated energy term diagrams for a prolate symmetric top (red), a linear molecule (black), and an oblate symmetric top (blue). For all molecules,  $B$  was chosen as 8 GHz and for the prolate symmetric top  $A = 12$  GHz while for the oblate symmetric top  $C = 4$  GHz. Only levels up to  $J_{\max} = 8$  and  $K_{\max} = 5$  are shown.

Only when adding centrifugal distortion effects, the degeneracy for transitions with different  $K_a$  values is lifted as Eq. 2.24 is expanded into

$$E_p/h = BJ(J+1) - D_J(J(J+1))^2 + (A-B)K_a^2 - D_K K_a^4 - D_{JK}J(J+1)K_a^2 + \dots \quad (2.29)$$

and accordingly the transition frequencies become

$$\nu_{J+1, K \leftarrow J, K} = 2B(J+1) - 4D_J(J+1)^3 - 2D_{JK}(J+1)K_a^2 + \dots \quad (2.30)$$

Two things should be noted here. First, each  $K_a$  series can be seen as a linear rotor spectrum with  $B_{\text{eff}} = (B - D_{JK}K_a^2)$ . Secondly, the parameter  $D_K$  is not determinable from the spectrum as the transition frequencies do not depend on it. This may not be a problem if only the frequency positions of the spectrum are of interest, but if the complete energy term diagram is of interest (e.g., for a partition function) this parameter has to be estimated or calculated.

### 2.2.3 Asymmetric Molecules

The energy expression for asymmetric tops has no general analytical solution as all three moment of inertia components are different  $I_a < I_b < I_c$ . Thus, the problem is solved numerically which is typically done in matrix formalism. For this, Eq. 2.9 is reformulated

as

$$\frac{h}{4\pi^2} \mathbf{H}_{\text{rot}} = A\mathbf{J}_a^2 + B\mathbf{J}_b^2 + C\mathbf{J}_c^2 \quad (2.31)$$

$$= \left(\frac{A+B}{2}\right) (\mathbf{J}_a^2 + \mathbf{J}_b^2) + C\mathbf{J}_c^2 + \frac{(A-B)}{2} (\mathbf{J}_a^2 - \mathbf{J}_b^2) \quad (2.32)$$

$$= \left(\frac{A+B}{2}\right) \mathbf{J}^2 + \left(C - \frac{A+B}{2}\right) \mathbf{J}_c^2 + \left(\frac{A-B}{4}\right) (\mathbf{J}_+^2 + \mathbf{J}_-^2) \quad (2.33)$$

and the following identities are used

$$\langle J, K | \mathbf{J}^2 | J, K \rangle = \hbar^2 J(J+1) \quad (2.34)$$

$$\langle J, K | \mathbf{J}_c^2 | J, K \rangle = \hbar^2 K^2 \quad (2.35)$$

$$\langle J, K+2 | \mathbf{J}_-^2 | J, K \rangle = \hbar^2 ((J-K)(J+K+1)(J-K-1)(J+K+2))^{1/2} \quad (2.36)$$

$$\langle J, K-2 | \mathbf{J}_+^2 | J, K \rangle = \hbar^2 ((J+K)(J-K+1)(J+K-1)(J-K+2))^{1/2} \quad (2.37)$$

As all matrix elements are diagonal in  $J$ , the energy levels for each  $J$  value can be calculated independently. This greatly reduces the size of the matrices and improves the efficiency of the calculations<sup>c</sup>.

The process is explained here for  $J = 1$ , as this case can be solved analytically. A total of three states has to be considered due to the  $2J + 1$  different values of  $K$ , which is the projection quantum number of  $J$  on the molecular  $z$ -axis. The states are written, as in the identities above, in the format  $|J, K\rangle$ . The system is then described with the following matrix

$$\mathbf{H}/h = \begin{matrix} & |1, 1\rangle & |1, 0\rangle & |1, -1\rangle \\ \begin{matrix} \langle 1, 1| \\ \langle 1, 0| \\ \langle 1, -1| \end{matrix} & \begin{pmatrix} C + \frac{A+B}{2} & 0 & \frac{A-B}{2} \\ 0 & A+B & 0 \\ \frac{A-B}{2} & 0 & C + \frac{A+B}{2} \end{pmatrix} & \end{matrix} \quad (2.38)$$

The energy values are found as the eigenvalues of the matrix

$$\lambda_1 = A + B \quad (2.39)$$

$$\lambda_2 = A + C \quad (2.40)$$

$$\lambda_3 = B + C \quad (2.41)$$

To label the corresponding states the correlation diagram of prolate and oblate symmetric

---

<sup>c</sup>The matrices for each  $J$  value can be subdivided even further. This results from the ellipsoid of inertia being symmetric to the identity operation and the three  $180^\circ$  rotations around the principal axes of inertia. The group formed by these symmetry operations is known as Four-group and the rigid asymmetric Hamiltonian is invariant under its operations. This knowledge can be used for deriving selection rules and for splitting up the energy matrices into four smaller sub-matrices.

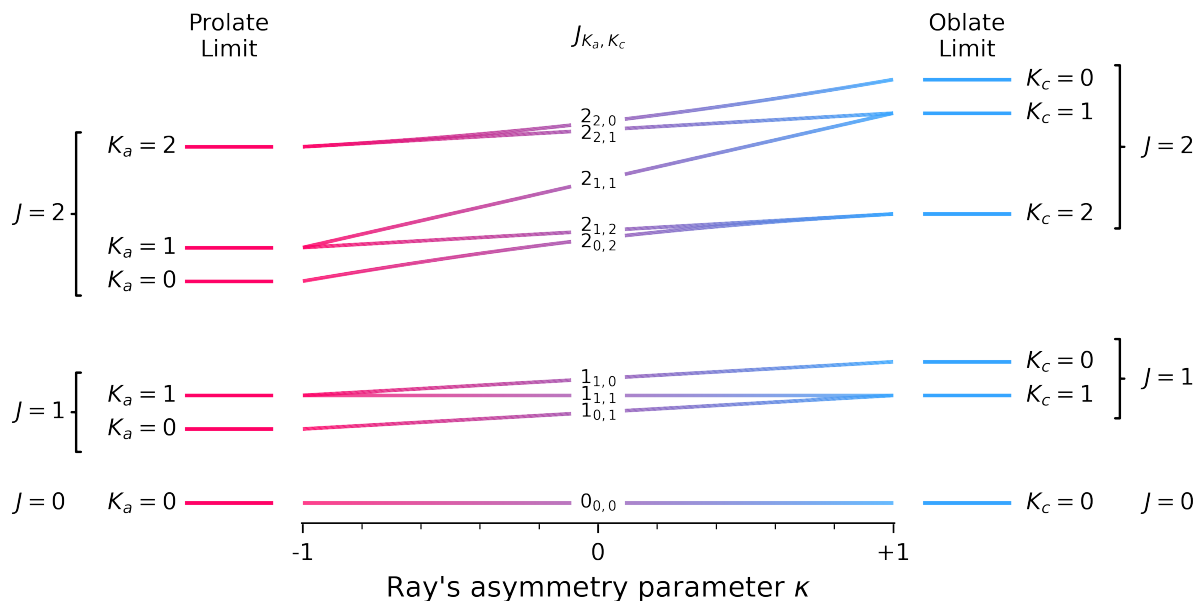


**Figure 2.3:** Correlation diagram for asymmetric top levels. The limiting cases of a prolate and oblate symmetric top are given to the left and right, respectively. The asymmetric top levels are labeled as  $J_{K_a, K_c}$ , with  $K_a$  coming from the correlated prolate energy level and  $K_c$  from the oblate energy level. The asymmetric top energy values are calculated for  $A = 10.5$  GHz,  $C = 5.5$  GHz, and  $B$  going from  $C$  (corresponding to  $\kappa = -1$ ) to  $A$  (corresponding to  $\kappa = 1$ ).

tops is introduced (see Figure 2.3). The limiting cases are the prolate symmetric top on the left-hand side and the oblate symmetric top on the right-hand side. For each limiting case, the corresponding energy levels are shown. The curves connecting prolate and oblate states display the correlation. The levels for the asymmetric top are labeled by  $J_{K_a, K_c}$ , with  $K_a$  stemming from the prolate symmetric top and  $K_c$  from the oblate symmetric top. It is important, that  $K_a$  and  $K_c$  are only good quantum numbers in their respective limiting cases, but not in between. Important restrictions on  $K_a$  and  $K_c$  are, that their sum is equal to  $J$  or  $J + 1$  and equivalently to the symmetric top case  $J \geq K_a$  and  $J \geq K_c$ . States with same  $J$  value are ordered in energy by  $\tau = K_a - K_c$ . As a result the eigenvalues are connected to the three possible states in the following manner:  $E(1_{1,0})/h = A + B$  as this is the highest energy,  $E(1_{1,1})/h = A + C$ , and  $E(1_{0,1})/h = B + C$ , as this is the lowest energy.

In Fig. 2.4, the energy term diagrams are shown for three of the four molecules analyzed in this thesis. The molecules are ordered from left to right by increasing values of  $\kappa$ . On the left hand side, glycidaldehyde with  $\kappa = -0.98$  is close to the prolate limit for which reason  $K_a$  is given on the  $x$ -axis. Accordingly, its energy term diagram matches qualitatively the prolate symmetric top energy term diagram (see left hand side of Fig. 2.2). Differences are, that for each pair of  $J$  and  $K_a$  values, two levels exist for the asymmetric top as  $K_a$  is no longer a good quantum number and levels with both  $J + 1 = K_a + K_c$  and  $J = K_a + K_c$  are possible, and that the energy offset with  $K_a$  is much more pronounced than for the simulated symmetric top in Fig. 2.2. The splitting between the asymmetry components

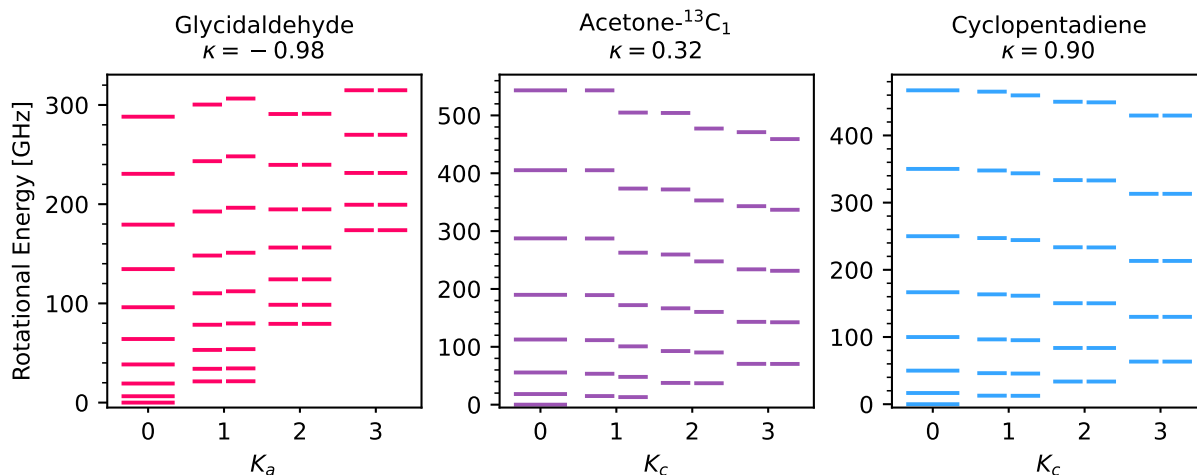


**Figure 2.4:** Energy term diagrams for three of the molecules analyzed in this thesis. Glycidaldehyde (left) is close to the prolate symmetric top limit, as indicated by its  $\kappa$  value, acetone- $^{13}\text{C}_1$  (middle) is an example for a rather asymmetric molecule, and cyclopentadiene is close to the oblate symmetric top limit. Energy levels where  $K_{a/c}$  is nonzero are split as both the  $J + 1 = K_a + K_c$  and  $J = K_a + K_c$  levels exist, with the former here being displayed to the left of the latter. The qualitative agreement with the symmetric top limit cases can be seen by comparison with Fig. 2.2.

(levels with same  $J$  and  $K_a$  value but different values of  $J - K_a - K_c$ ) increases with  $J$  but decreases with  $K_a$ . For low  $J$  values, levels with the same  $J$  and  $K_a$  values are paired in energy (so-called prolate pairing) whereas at high  $J$  values energy levels with same  $J$  and  $K_c$  values are paired in energy (so-called oblate pairing; this is shown more clearly in Fig. A.1). On the right hand side, the energy term diagram of cyclopentadiene is shown, which is quite close to the oblate limit ( $\kappa = 0.90$ ) for which reason  $K_c$  is given on the  $x$ -axis. The qualitative agreement with the oblate symmetric top energy term diagram (see right hand side of Fig. 2.2) is very high. The asymmetry splitting increases with  $J$  and decreases with  $K_c$ , similar to glycidaldehyde just that  $K_a$  and  $K_c$  are exchanged. Thus, also the pairing is inverted, going from oblate pairing for low  $J$  values to prolate pairing for high  $J$  values (see Fig. A.2). Acetone- $^{13}\text{C}_1$  is quite asymmetric ( $\kappa = 0.32$ ) which is also resembled by the strong asymmetry splitting in its energy term diagram (middle of Fig. 2.4).

More typical patterns of the molecular fingerprint are highlighted in the analyses themselves. Typical patterns of  $a$ -type transitions are shown in Fig. 2 of Sec. 7, with the top part showing the pattern for different  $J$  values and the bottom the structure within the same  $J$  value, and of both  $\Delta J = 0$  and  $\Delta J = 1$   $b$ -type transitions in Fig. 2 of Sec. 8.

### Selection Rules

The selection rules for  $J$  and  $M$ , the projection of  $J$  on the fixed space axis, are  $\Delta J = 0, \pm 1$  and  $\Delta M = 0, \pm 1$  due to the maximum angular momentum  $\hbar$  that a photon may carry. Additionally, selection rules exist for  $K_a$  and  $K_c$  that are coupled to the dipole moment

components  $\mu_a$ ,  $\mu_b$  and  $\mu_c$ <sup>d</sup>. Every non-zero dipole moment component is responsible for a set of transitions with a set of selection rules. Accordingly, the designation is *a*-, *b*- and *c*-type transitions, with the corresponding component of the dipole moment being non-zero.

*a*-type transitions follow the selection rules

$$\Delta K_a = 0 (\pm 2, \pm 4, \dots) \quad (2.42)$$

$$\Delta K_c = \pm 1 (\pm 3, \pm 5, \dots) \quad (2.43)$$

*b*-type transitions follow the selection rules

$$\Delta K_a = \pm 1 (\pm 3, \pm 5, \dots) \quad (2.44)$$

$$\Delta K_c = \pm 1 (\pm 3, \pm 5, \dots) \quad (2.45)$$

*c*-type transitions follow the selection rules

$$\Delta K_a = \pm 1 (\pm 3, \pm 5, \dots) \quad (2.46)$$

$$\Delta K_c = 0 (\pm 2, \pm 4, \dots) \quad (2.47)$$

Values in brackets indicate, that these values are possible but less likely than the first value. The different transition types are shown in Fig. 2.5.

---

<sup>d</sup>These selection rules follow from parity considerations. The transition dipole moment (see Eq. 2.54) must stay unchanged under symmetry operations. For inversion, the sign of the  $\mu$  components changes, meaning the initial and final rotational wavefunctions  $\psi_m$  and  $\psi_n$  have to have opposite parity for the transition dipole moment to stay unchanged. The  $K_a$  and  $K_c$  values specify if the respective wavefunction is symmetric (even  $K$  values) or antisymmetric (odd  $K$  values) with respect to a rotation of  $180^\circ$  around the respective axis. Four possible combinations arise (ee, eo, oe, oo) with the resulting group being the Four-group. Six different transitions are possible, with  $\mu_a \neq 0$  permitting  $ee \leftrightarrow eo$  and  $oe \leftrightarrow oo$ ,  $\mu_b \neq 0$  permitting  $ee \leftrightarrow oo$  and  $oe \leftrightarrow eo$ , and  $\mu_c \neq 0$  permitting  $ee \leftrightarrow oe$  and  $eo \leftrightarrow oo$ . This is easily translated into the changes in  $K_a$  and  $K_c$  given in equations 2.42 - 2.47.

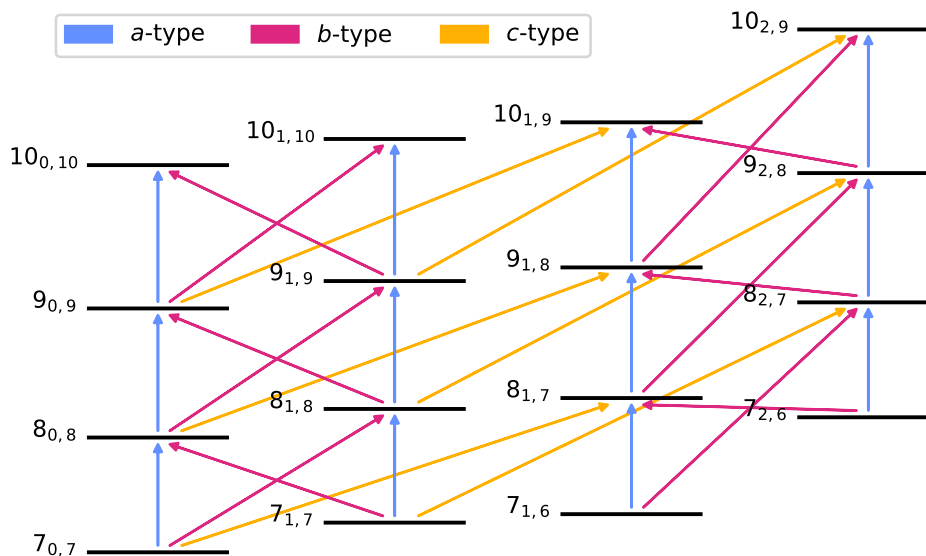


**Figure 2.5:** Different transition types are shown in the energy term diagram of glycidaldehyde. For clarity, only transitions with  $\Delta J = 1$ ,  $\Delta K_a = 0, \pm 1$ , and  $\Delta K_c = 0, \pm 1$  are shown.

## 2.3 Lineshape, Population and Intensity

With the knowledge of Sec. 2.2, the frequency positions of transitions in the rotational spectrum can be explained. For a full interpretation of the spectrum, the lineshape and the intensity of each transition need to be understood. First, the lineshape is explained (Sec. 2.3.1), followed by the population distribution (Sec. 2.3.2), transition dipole moment (Sec. 2.3.3), and finally the intensity (Sec. 2.3.4).

### 2.3.1 Lineshape

The absorption features have a width that is connected to their lifetime in the observed state as well as their translational speed in the direction of the source. The lifetime of the observed state is limited with the most important factors being the time between two collisions (which might change the rotational state), the Rabi frequency (if the source is powerful), and the natural lifetime. This limited lifetime  $\Delta\tau$  is connected via the Heisenberg uncertainty principle

$$\Delta E \Delta\tau \geq \hbar/2 \quad (2.48)$$

to an energy uncertainty  $\Delta E$  and results in a Lorentzian lineshape. For the molecules and experimental setups used in this thesis, the most prominent effect arises from the time between two collisions which is inversely proportional to the pressure  $p$ . Hence, this

broadening effect is called pressure broadening and the Full Width at Half Maximum (FWHM) is proportional to the pressure

$$\Delta\nu_T \propto \frac{1}{\Delta\tau} \propto p \quad (2.49)$$

The second contribution results from the velocity component parallel to the direction of the incoming radiation which causes a Doppler shift. This velocity component is a heterogenous quantity, leading to a broadening in the form of a Gaussian with a FWHM of

$$\Delta\nu_D = 2\nu_0 \sqrt{\frac{2kT \ln(2)}{mc^2}} \quad (2.50)$$

with the frequency of the source  $\nu_0$ , the Boltzmann constant  $k$ , the temperature  $T$ , and the rest energy of the molecule  $mc^2$ . For measurements at room temperature, and the masses of the molecules examined in this thesis, Gaussians with FWHM ranging from about 100 kHz at 75 GHz to 1.5 MHz at 1 THz are expected.

The combination of the aforementioned effects results in a Voigt profile being the convolution of the Gaussian and Lorentzian.

### 2.3.2 Population and Degeneracy

The intensity of a transition also depends on the population of the initial state  $m$  which is given in thermal equilibrium by the Boltzmann distribution, depending on the total number of molecules  $N$ , the energy of the state  $E_m$ , and the degeneracy of the state  $g_m$ . The population in state  $m$  is then

$$N_m = N \cdot g_m \frac{e^{-E_m/kT}}{Q} \quad (2.51)$$

where  $Q$  is the partition function

$$Q = \sum_m g_m e^{-E_m/kT} \approx \frac{kT}{\sigma B} \quad (2.52)$$

In the last step, the symmetry number  $\sigma$  was introduced, which is 1 for symmetric and 2 for asymmetric molecules. For the case of a linear molecule, the sum can just run over  $J$  whereas for an asymmetric top molecule the sum has to run over  $J$  and  $K$  as states with the same  $J$  value have different energies. The relative population  $\frac{N_m}{N}$  and the Boltzmann factor  $\frac{N_m}{N g_m}$  are shown in Fig. 2.6 for a linear rigid rotor.

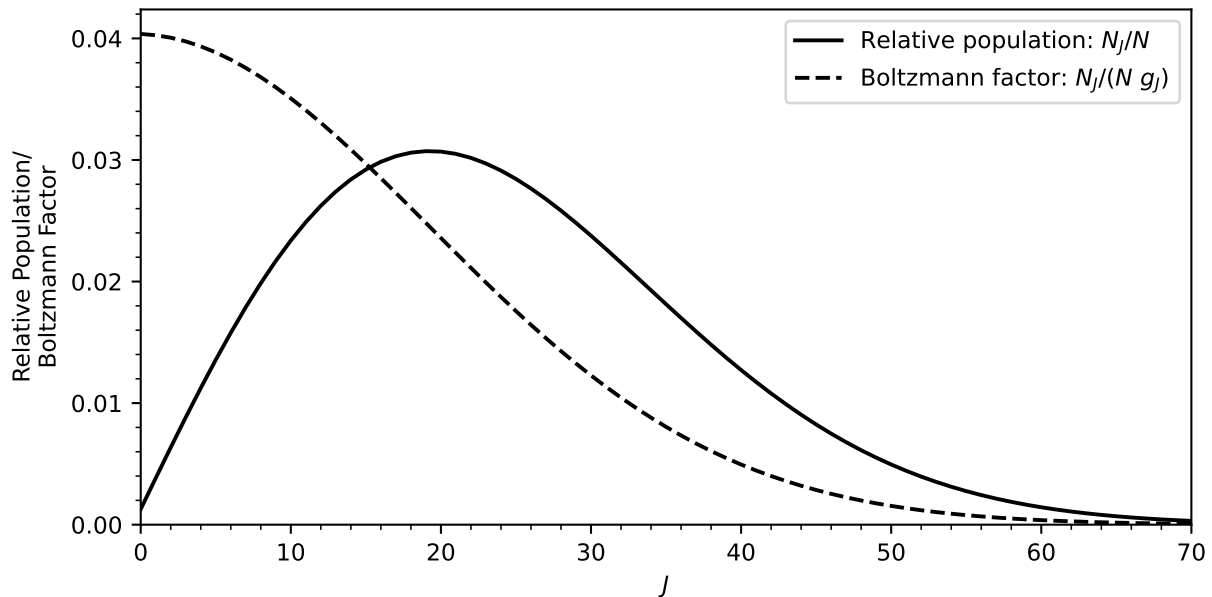


**Figure 2.6:** The relative population  $\frac{N_m}{N}$  (solid line) and the Boltzmann factor  $\frac{N_m}{N g_m}$  (dashed line) against the angular momentum quantum number  $J$  for a linear top with  $B = 8$  GHz at  $T = 300$  K. The relative population is equal to the product of the Boltzmann factors and the degeneracies ( $g_J = 2 \cdot J + 1$ ) with subsequent normalization.

### 2.3.3 Transition Dipole Moment and Einstein Coefficient

The probability of a transition is given by its Einstein coefficient

$$B_{mn} = B_{m \rightarrow n} = B_{m \leftarrow n} = \left( \frac{8\pi^3}{3h^2} \right) |M_{mn}|^2 \quad (2.53)$$

where  $M_{mn}$  is the transition dipole moment between the two states  $m$  and  $n$

$$\vec{M}_{mn} = \int \psi_m \vec{\mu} \psi_n d\tau = \langle \psi_m | \vec{\mu} | \psi_n \rangle \quad (2.54)$$

Here,  $\psi_m$  and  $\psi_n$  are the wavefunctions of the initial and final states and  $\vec{\mu}$  is the dipole moment

$$\vec{\mu} = \sum_i q_i \vec{r}_i \quad (2.55)$$

with  $q_i$  being the charges and the  $\vec{r}_i$  their respective positions. The transition dipole moment can be calculated from the eigenvectors, which are obtained when calculating the energies as the eigenvalues of the rotational Hamiltonian, and knowledge of the dipole moment. The transition dipole matrix is Hermitian, meaning  $\langle \psi_m | \vec{\mu} | \psi_n \rangle = \langle \psi_n | \vec{\mu} | \psi_m \rangle^*$ .

### 2.3.4 Intensity

In the laboratory, the intensity is measured as the transmitted power  $P$  after passing an absorption cell

$$P = P_0 e^{-\alpha_{mn}d} \quad (2.56)$$

with the incoming power  $P_0$  and the absorption path length  $d$ . The absorption coefficient  $\alpha$  is given by

$$\alpha_{mn} = \frac{N_m}{c} \left(1 - e^{-h\nu_{mn}/kT}\right) B_{mn} h\nu_{mn} S(\nu, \nu_0) \quad (2.57)$$

$$\approx \frac{N_m (h\nu_{mn})^2}{ckT} B_{mn} S(\nu, \nu_0) \quad (2.58)$$

where in the second row  $h\nu \ll kT$  was assumed. Therefore, the intensity depends on the population of the initial state  $N_m$ , the transition frequency  $\nu_{mn}$ , the temperature  $T$ , the Einstein  $B$  coefficient, and the normalized lineshape function  $S(\nu, \nu_0)$ .

Often the absorption coefficient is also specified with the matrix dipole moment  $M_{mn}$  as

$$\alpha_{mn} = \frac{8\pi^3 N_m}{3hc} \nu_{mn} |M_{mn}|^2 \left(1 - e^{-h\nu_{mn}/kT}\right) S(\nu, \nu_0) \quad (2.59)$$

which resembles more closely the equation for the intensities calculated by the SPCAT<sup>59,60</sup> software (see Eq. 1 of the original publication<sup>60</sup>)

$$I_{mn} = \frac{8\pi^3}{3hc} \nu_{mn} S\mu^2 \left(e^{-E_m/kT} - e^{-E_n/kT}\right) / Q \quad (2.60)$$

$$= \frac{8\pi^3}{3hc} \frac{e^{-E_m/kT}}{Q} \nu_{mn} S\mu^2 \left(1 - e^{-h\nu_{mn}/kT}\right) \quad (2.61)$$

where  $S$  is the line strength<sup>e</sup>. When also accounting for degeneracy<sup>f</sup>, the resulting line strength calculated by SPCAT

$$I_{mn} = \frac{8\pi^3}{3hc} \frac{N_m}{N} \nu_{mn} |M_{mn}|^2 \left(1 - e^{-h\nu_{mn}/kT}\right) \quad (2.62)$$

is connected to the absorption coefficient by  $I_{mn} \cdot N = \alpha_{mn}$ . The simulated spectrum of glycinaldehyde is shown in Fig. 2.7 to highlight some of the contributions to the total intensity. For example, the dependency on the population and degeneracy is seen by comparison with Fig. 2.6. The weak  $c$ -type transitions highlight the influence of the dipole moment component ( $I_{mn} \approx \mu_\alpha^2$ ), and the fact that the  $b$ -type spectrum ( $\mu_b = 1.5$  D) shows stronger peaks than the  $a$ -type spectrum ( $\mu_a = 1.9$  D) highlights the dependence on the

<sup>e</sup>If wavefunction mixing occurs, e.g., due to strong interactions,  $S\mu^2$  is calculated as the sum over all three principal axes  $S\mu^2 = \sum_\alpha S_\alpha \mu_\alpha^2$  with  $\alpha = x, y, z$

<sup>f</sup>From the documentation it is unclear, if the degeneracy is included in the line strength  $S$  or is accomplished by summation over all degenerate levels.

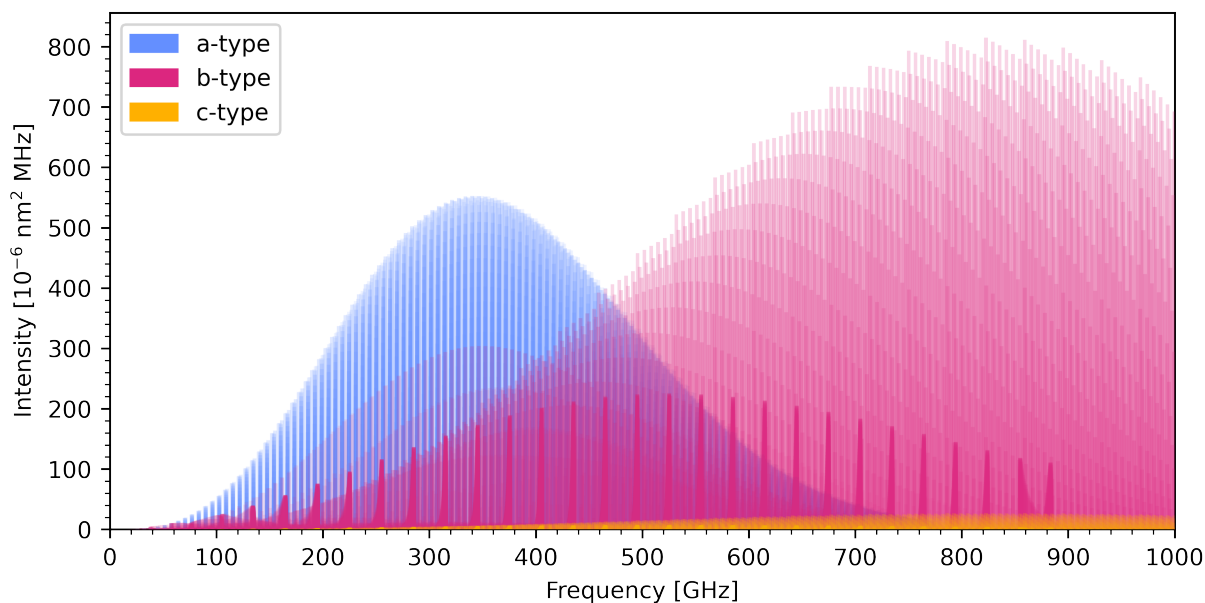


**Figure 2.7:** Simulated stick spectrum of glycidaldehyde’s rotational spectrum. *a*-type transitions (blue), *b*-type transitions (red), and *c*-type transitions (yellow) are plotted with slight transparency. Different aspects can be understood by different factors of the line strength as defined in Eq. 2.60. The *c*-type spectrum is much weaker than the *a*- and *b*-type spectra due to its small dipole moment of  $\mu_c = 0.3\text{D}$  (compared to  $\mu_a = 1.9\text{D}$  and  $\mu_b = 1.5\text{D}$ ). Multiple series of transitions are visible, with their curvature being the product of the relative population (Fig. 2.6) and the frequency dependence. The comb-like structure of *b*-type transitions are  $\Delta J = 0$  transitions where each teeth consists of transitions with the same  $K_a$  value.

transition frequency  $\nu_{mn}$  (and the  $1 - \exp(-h\nu_{mn}/kT)$  factor). Transitions with  $\Delta J = 0$  are visible as a comb-like structure in the *b*-type spectrum.

## 2.4 Internal Rotation and ERHAM

If two groups of a molecule are connected only by a single bond, e.g., as is the case for the methyl groups in acetone and ethyl phosphoethyne, the two groups can rotate around this bond. While for a double bond the relative rotation requires uncoupling of the  $\pi$ -electrons, which is quite difficult, the relative rotation about a single bond is only hindered by a potential barrier.<sup>61</sup> The coupling between the internal-rotation and the overall rotation splits the transitions in the spectrum. The magnitude of the relative rotation is of large amplitude (similar to the order of magnitude of the molecular parameters), classifying it as a large amplitude motion (LAM). Two other examples of LAMs are inversion, as in ammonia,<sup>62</sup> or ring puckering.<sup>63–66</sup>

The outline of this section is as follows. First, a qualitative understanding of the origin of the splitting is given by examining the two extreme cases of no and an infinitely high potential barrier (Sec. 2.4.1). Then, this qualitative description is extended to two threefold internal rotors (Sec. 2.4.2). Lastly, the ERHAM approach is explained which is used in

Sec. 6 for the analysis of acetone- $^{13}\text{C}_1$  having two non-equivalent rotors. For more detailed explanations the reader is referred to the literature.<sup>52,67-73</sup>

### 2.4.1 Internal Rotation Splitting

The two limiting cases of a single threefold internal rotor are an infinitely high and no potential barrier. For an infinitely high barrier, each level is triply degenerate (due to the three equivalent potential wells) and the internal motion of the methyl group corresponds to a simple harmonic torsional oscillation whereas for no barrier the internal rotor spins freely.

The symmetry of the internal rotor and the frame (the molecule without the internal rotor) is essential for the description. The potential is periodic in the angle of internal rotation  $\alpha$  with periodicity  $2\pi/N$ . Hence, the potential can be expressed as a Fourier series

$$V(\alpha) = \sum_{k=0}^{\infty} \frac{V_{kN}}{2} (1 - \cos(kN\alpha)) \quad (2.63)$$

For methyl rotors,  $N = 3$  and hence the Fourier series of the potential is given by

$$V(\alpha) = \frac{V_3}{2}(1 - \cos(3\alpha)) + \frac{V_6}{2}(1 - \cos(6\alpha)) + \dots \quad (2.64)$$

As the Fourier series is rapidly converging, often only the first term is sufficient (shown in Fig. 2.8), which is also supported by experimental findings.<sup>74-77</sup> The energies are found

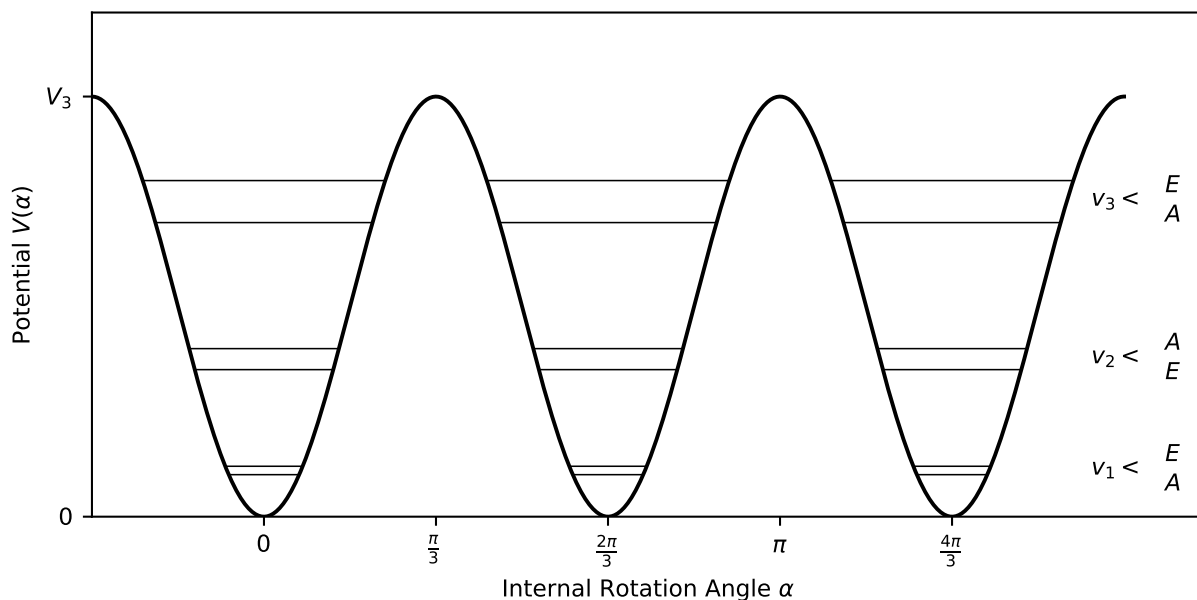


**Figure 2.8:** Potential function for internal rotation with threefold degenerate potential. Horizontal lines indicate the sublevels of the vibrational states due to internal rotation. The splitting between sublevels is increasing with increasing vibrational energy. This figure is adapted from *Microwave Molecular Spectra* by Gordy and Cook.<sup>52</sup>

via the time-independent one-dimensional Schrödinger equation, which results in the wave equation for internal rotation

$$-F \frac{d^2 U(\alpha)}{d\alpha^2} + \left[ \frac{V_3}{2} (1 - \cos(3\alpha)) - E \right] U(\alpha) = 0 \quad (2.65)$$

with the eigenfunctions  $U(\alpha)$ , the internal rotation constant  $F = \hbar^2/2I_r$ , and the reduced moment of inertia for the relative motion of the two groups  $I_r$ .

When considering the previously mentioned extreme case of a very small barrier,  $V_3 \rightarrow 0$ , Eq. 2.65 simplifies to

$$\frac{d^2 U(\alpha)}{d\alpha^2} + \frac{E}{F} U(\alpha) = 0 \quad (2.66)$$

This equation is easily solved analogously to a spatial rotator with a fixed axis of rotation

$$U(\alpha) = A e^{im\alpha} = A (\cos(m\alpha) + i \sin(m\alpha)) \quad (2.67)$$

where  $A$  is an appropriate normalization factor resulting in

$$E = F m^2 \quad (2.68)$$

$$m = 0, \pm 1, \pm 2, \dots \quad (2.69)$$

where the values for  $m$  directly follow from the boundary condition  $U(\alpha) = U(\alpha + 2\pi)$ . Except for  $m = 0$ , all energies are doubly degenerate.

When considering the opposite case of a very high barrier,  $V_3 \rightarrow \infty$ ,  $\alpha$  is restricted to very small changes and thus the small angle approximation can be used for the potential, simplifying Eq. 2.65 to

$$\frac{d^2 U(\alpha)}{d\alpha^2} + \frac{1}{F} \left( E - \frac{9}{4} V_3 \alpha^2 \right) U(\alpha) = 0 \quad (2.70)$$

This equation is solved analogously to a harmonic oscillator resulting in

$$E = 3\sqrt{V_3 F} \left( v + \frac{1}{2} \right) \quad (2.71)$$

$$v = 0, 1, 2, 3, \dots \quad (2.72)$$

Because there are three equivalent potential wells, all solutions of this limiting case are triply degenerate. Additionally, the frequency of the torsional oscillation can be derived as

$$\nu = \frac{3}{2\pi} \sqrt{\frac{V_3}{2I_r}} \quad (2.73)$$

As the frequency depends on the barrier height  $V_3$ , the barrier height can be determined

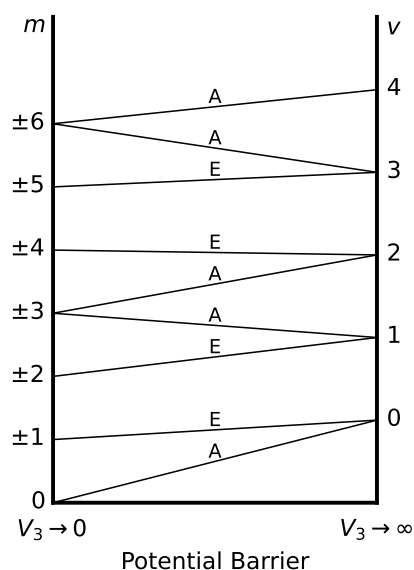


**Figure 2.9:** Correlation diagram for the two limiting cases of internal rotation, being the free rotor on the left and the harmonic oscillator on the right. The free rotor levels are doubly degenerate whereas the harmonic oscillator levels are triply degenerate. The degeneracy is split for finite barrier heights. This figure is adapted from *Microwave Molecular Spectra* by Gordy and Cook.<sup>52</sup>

by infrared studies or microwave intensity studies.

The internal motion of a real molecule lies somewhere in between the two extreme cases. For the quantitative solution, the reader is referred to the literature as it is quite involved and requires numerical evaluation (e.g., chapter 12 of *Microwave Molecular Spectra* by Gordy and Cook<sup>52</sup>). Instead, the qualitative behavior for a finite barrier ( $0 < V_3 < \infty$ ) is discussed in the following. The first consequence is, that a non-zero chance of tunneling is introduced with the value depending on the height and width of the potential barrier. As can be seen by the correlation diagram in Fig. 2.9, each of the triply degenerate levels of the high-barrier extreme case splits into two levels labeled as  $A$  and  $E$ . The  $A$  levels are singly degenerate while the  $E$  levels are doubly degenerate. In a classical sense, even though not quantum mechanically correct, the  $E$  levels can be understood as the two equivalent tunneling motions in clockwise and anti-clockwise direction while the  $A$  level corresponds to the vibrational motion within a potential well. The correlation diagram shows that for even  $v$  the  $E$  levels are higher in energy than the  $A$  level and for odd  $v$  the  $A$  level is higher in energy than the  $E$  levels. If  $m$  is a multiple of three, the  $\pm m$  degeneracy is lifted but remains for all other values of  $m$ . The splitting between the  $A$  and  $E$  levels increases with  $v$ , as does the rate of tunneling. If the torsional energy surpasses the potential height, the internal rotor can spin freely and the energy levels go to the free rotor case.

Just adding the two energies of internal and overall rotation is not sufficient for describing spectra with internal rotation as no splitting would occur.<sup>78</sup> Therefore, the complete

internal rotation Hamiltonian is required incorporating the rotation-internal rotation interaction. The Hamiltonian for a single internal rotor in the rigid-rotor approximation is in the principal axis system (PAS) given by

$$\mathbf{H} = F(\vec{p}_\alpha - \rho_a J_a - \rho_b J_b - \rho_c J_c)^2 + V(\alpha) + A J_a^2 + B J_b^2 + C J_c^2 \quad (2.74)$$

which follows from classical considerations. The three last terms are the rigid rotor Hamiltonian (see Eq. 2.9), the second term is the internal rotation potential (see Eq. 2.63), and in the first term  $\vec{p}_\alpha$  is the internal rotation angular momentum conjugate to the torsion angle  $\alpha$ , the  $\rho_{a/b/c}$  are the components of the  $\rho$  vector, and  $F$  is the internal rotation constant introduced earlier. The components of the  $\rho$ -vector are given by

$$\rho_g = \frac{\lambda_g I_\alpha}{I_g} \quad (2.75)$$

where  $I_\alpha$  is the moment of inertia of the internal top and  $\lambda_{a/b/c}$  are the direction cosines of the internal rotation axis  $i$  of the internal top in the principal axis system

$$\lambda_g = \cos(\Theta(i, g)) \quad (2.76)$$

As the axis of internal rotation is typically not coinciding with one of the principal axes of rotation, evaluation of Eq. 2.74 results in three quadratic terms of the form  $J_i J_j + J_j J_i$  and three quadratic cross terms in  $\vec{p}_\alpha J_i$ . With today's computational power, this does not pose a problem but historically different approaches were used to overcome these problems. Quite a few different approaches were successfully used, including the principal axis method, the rho-axis method, and the internal-axis method. These methods were implemented in different programs, with JB95,<sup>79,80</sup> SPFIT/SPCAT/IAMCALC,<sup>59,81</sup> XIAM,<sup>82</sup> BELGI,<sup>83,84</sup> RAM36<sup>85</sup>/RAM36hf,<sup>86,87</sup> and ERHAM<sup>88,89</sup> being the most proven codes but also new codes being developed, e.g., westerfit<sup>90</sup> which combines the spin-coupling treatment of SPFIT with an expanded version of the internal rotor treatment of BELGI. In the following, only the working principle of ERHAM is described in detail as the other programs were not used in this thesis. For more detailed information on the other codes, the reader is referred to the review papers by Kleiner<sup>69,73</sup> or the respective publications given above.

## 2.4.2 Two Internal Rotors

A single internal methyl rotor splits each level into an  $A$  and two degenerate  $E$  levels where the  $E$  levels may be thought of as the rotation in clockwise/anti-clockwise direction and the  $A$  level as the vibration within the potential well. The states can also be labelled by the symmetry number  $\sigma = 0, 1, \dots, N - 1$  which is more convenient for the case of

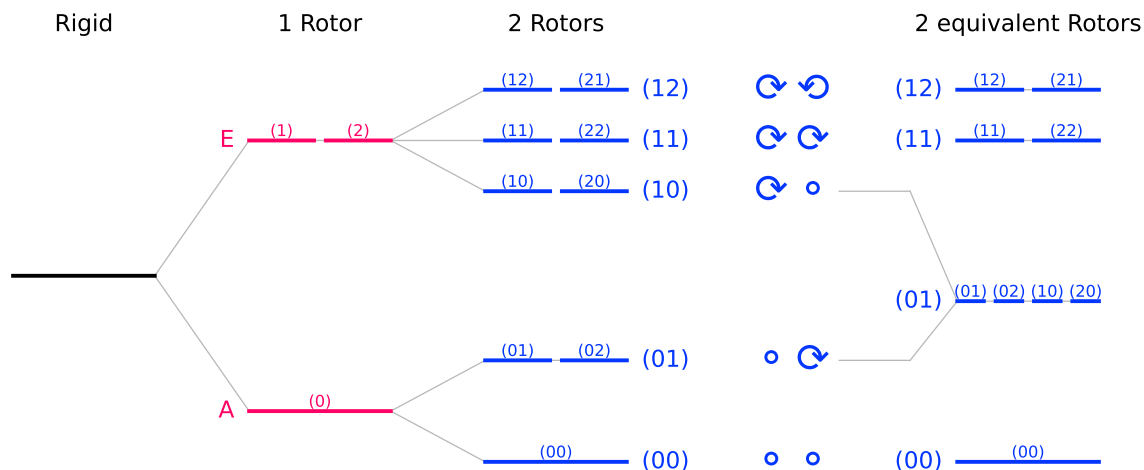


**Figure 2.10:** Schematic energy term diagram for molecules with (from left to right) no internal rotor, one internal rotor, two internal rotors, and two equivalent internal rotors. For all internal rotors  $N = 3$  is assumed. A circle indicates a  $\sigma = 0$  state whereas the clockwise and anti-clockwise arrows indicate the  $\sigma = \pm 1$  states. For one internal rotor, the levels split into an  $A$  and  $E$  level. Adding a second rotor leads to a splitting into five sublevels which for the case of two equivalent rotors reduces to four, as the (10) and (01) levels are indistinguishable.

two internal methyl rotors<sup>g</sup>. The  $A$  level corresponds to  $\sigma = 0$  and the degenerate  $E$  levels correspond to  $\sigma = 1$  and 2. The addition of a second methyl rotors splits these levels even further into nine levels, labelled with the two symmetry numbers ( $\sigma_1\sigma_2$ ) as shown in Fig. 2.10. Except for (00), all levels are doubly degenerate resulting in the five resolvable sublevels (00), (01), (10), (11), and (12). With two internal rotors, the cases of rotation into the same or different directions, being the (11) and (12) levels, respectively, are distinguishable due to top-top interactions. If the two rotors are equivalent, the (01) and (10) components are equivalent, resulting in only four components.

For acetone- $^{13}\text{C}_1$ , the two rotors are not equivalent as in one methyl rotor a  $^{12}\text{C}$  atom is substituted by a  $^{13}\text{C}$  atom. Out of the five components, the (11) and (12) components as well as the (10) and (01) components converge for transitions with all but the lowest values of  $J$ . The result is a trident pattern in the spectrum with an intensity distribution (due to nuclear spin statistics) of  $(1 + 1) : (2 + 2) : 2 = 1 : 2 : 1$ . More in detail information on two internal rotors is found in the literature.<sup>78,91–97</sup>

### 2.4.3 ERHAM

ERHAM stands for Effective Rotational HAMiltonian<sup>88</sup> and is used both for the Hamiltonian and the software implementing it. ERHAM has been applied successfully to molecules with one<sup>98–101</sup> or two<sup>102–104</sup> internal rotors. Whereas many other programs try to determine the potential function, ERHAM takes a different approach by exploiting the symmetry

<sup>g</sup>For two internal methyl rotors, the symmetry of the sublevels depends also on the symmetry of the molecule and the two internal rotors.<sup>91</sup>

considerations with a phenomenological Hamiltonian instead of actually solving the internal rotation Hamiltonian. This makes the program considerably faster than programs solving the internal rotation Hamiltonian.<sup>105</sup> The idea is based on previous work by Ohashi, Hougen, and coworkers on phenomenological Hamiltonians<sup>106–111</sup> and is described just very briefly here with a more detailed description being given in the respective literature.<sup>88,89,112</sup> The overall wave function is constructed as a product of the symmetric rotor eigenfunctions (as is typical for asymmetric rotors) and the eigenfunctions of the internal Hamiltonian set up in a rho-axis system. Due to the periodicity of the internal rotation, the internal rotation eigenfunctions and eigenvalues can be expressed as Fourier series. In the resulting effective Hamiltonian, the potential energy terms appear only in the tunneling coefficients  $\epsilon$  which are fitting parameters. As a result of this approach, ERHAM is very fast but the potential barrier is not given explicitly, as the internal rotation Hamiltonian is not solved. However, the barrier can be calculated from the  $F$  constant and the splitting of the torsional sublevels.<sup>89</sup>

The high efficiency of ERHAM is required for the large datasets, resulting from the broad frequency coverage explained in Sec. 3, and especially for testing possible parameter additions to the model, as explained in Sec. 4.

### 3. Experimental Setup

All measurements in this thesis were performed using three different experimental setups in Cologne. The three experimental setups are absorption spectrometers covering different frequency ranges, which are shown in Fig. 3.1 together with the respective multiplication factors of the amplifier-multiplier chains (AMCs).

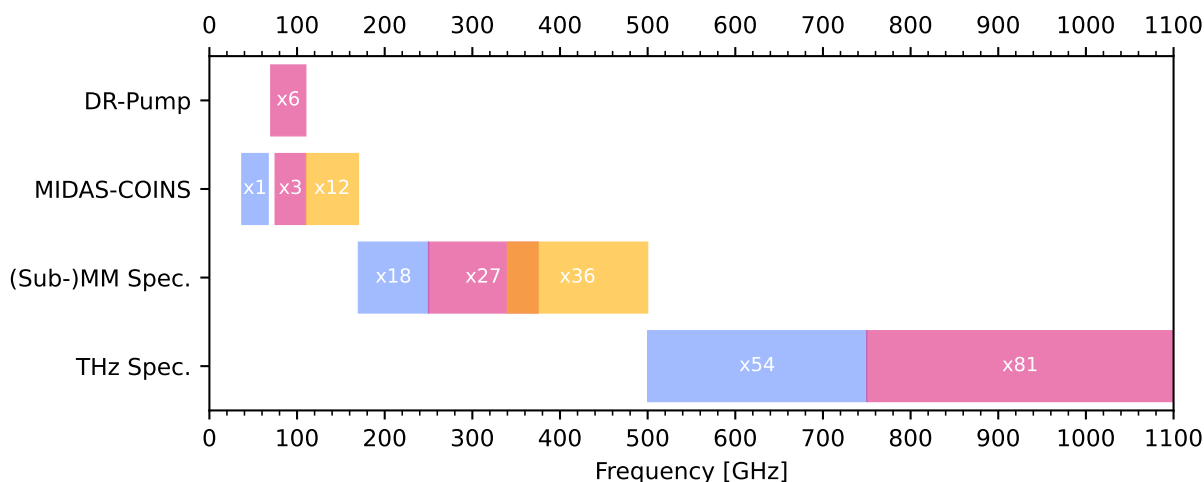


**Figure 3.1:** The frequency coverage of the three experimental setups and the pump source for DR measurements. For each frequency range, the corresponding multiplication factor is given.

Starting at low frequencies, the Millimeter-wave Double-pass Absorption Spectrometer for COMplex INTERstellar Species (MIDAS-COINS) covers the frequency ranges 37–67 GHz, and 75–170 GHz.<sup>42</sup> Additionally, MIDAS-COINS can be used to perform double-resonance spectroscopy by adding a second, more powerful source operating in the 70–110 GHz frequency range.<sup>6,113</sup> Next, the Cologne (Sub-)millimeter-wave spectrometer covers the frequency range of 170–510 GHz with three different multiplication setups.<sup>114</sup> It has the ability to produce unstable molecules *in situ* by means of a pyrolysis setup or an RF-discharge. In this work, the pyrolysis setup was used to produce cyclopentadiene from dicyclopentadiene via thermolysis. Finally, the Cologne THz spectrometer covers the frequency range 500–1100 GHz. This results in a total frequency coverage of 1055 GHz, excluding any overlap. Running all three experiments in parallel with typical integration times and frequency resolutions, the full coverage of over 1 THz can be measured in less than a month. The specified frequency limits can also be slightly exceeded to for example

measure down to 70 GHz. However, the signal-to-noise ratio (SNR) drops quite drastically toward the specified limits as the sources become less powerful and the detectors become less sensitive.

In the following, the conventional absorption spectrometer setups are introduced first (Sec. 3.1) followed by a description of the updated DR setup (Sec. 3.2).

### 3.1 Absorption Spectrometers

The three experimental setups share the same working principle (see Fig. 3.2). The source generates radiation of a specified frequency which is guided through the absorption cell containing the gaseous molecule. After the cell, the transmitted radiation is measured by the detector. Repeating this for different frequencies results in a spectrum.

The radiation sources consist of synthesizers, subsequent AMCs to reach higher frequencies, and matching horn antennas. The synthesizer models are an Agilent E8257D synthesizer with an upper frequency limit of 67 GHz, and Rohde & Schwarz SMF100A's with upper frequency limits of either 22 GHz or 43.5 GHz. The subsequent AMCs are different commercial options from Virginia Diodes Inc. and RPG Radiometer Physics. Only for the frequency range of 37–67 GHz no AMC is used but the RF output of the Agilent E8257D synthesizer is used directly without further multiplication. This is the only limitation on the synthesizer usage which are otherwise completely interchangeable between the experimental setups. All synthesizers are locked to a 10 MHz reference signal from a rubidium atomic clock to ensure a frequency accuracy of  $\frac{\Delta\nu}{\nu} = 10^{-11}$ .

The radiation enters and exits the absorption cells through Teflon (polytetrafluoroethylene) windows. HDPE lenses are used between the source and the absorption cell entrance to parallelize the beam and between the cell exit and the detector to focus the beam onto the detector. The absorption cells themselves consist of Pyrex glass tubes with diameters of about 10 cm and different lengths. For MIDAS-COINS, two 7 m cells are used in a (contrary to its name) single-pass setup, resulting in an absorption path of 14 m. The THz and (Sub-)MM spectrometers both use single 5 m cells. The latter uses a double-pass configuration in which the radiation is reflected on one side at a rooftop mirror, doubling the absorption path to 10 m (see Fig. A.3). Thus, the incoming and outgoing beams are superimposed and a polarization filter is used to outcouple the outgoing beam onto the detector while transmitting the orthogonally oriented radiation of the source. Each absorption cell has a sample inlet and is connected to a vacuum pumping system consisting of a turbo molecular pump and a backing pump.

On the detection side, Schottky detectors are used for the lower frequency ranges with bias voltages applied ( $< 170$  GHz) or as zero-bias detectors ( $170 \text{ GHz} < \nu < 500 \text{ GHz}$ ). For frequencies above 500 GHz, a cryogenically cooled bolometer (QMC QNbB/PTC(2+XBI)) is utilized. A  $2f$ -frequency modulation (FM) scheme is used to improve the SNR. The

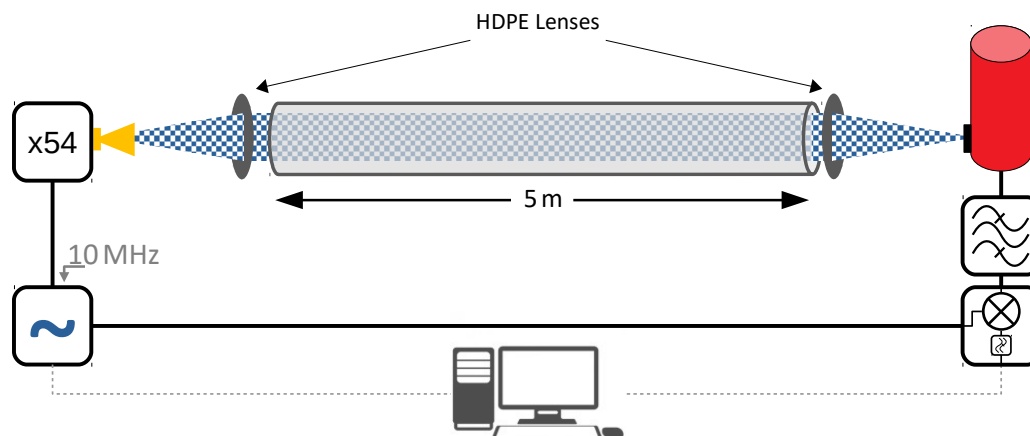


**Figure 3.2:** Schematic view of the THz spectrometer setup. On the left, the synthesizer generates the radio frequency (RF), which is then multiplied by a factor of 54 in several stages. Horn antennas and high-density polyethylene (HDPE) lenses are used to guide the beam through the absorption cell and onto the bolometer. A bandpass filter and a lock-in amplifier are used to increase the SNR.

output frequency of the synthesizer is modulated over time and the detector signal is demodulated at  $2f$  by a lock-in amplifier<sup>a</sup>. All lock-in amplifiers used here, being the models Signal Recovery 7260, 7265, and 7270, digitize the detector signal after analog pre-processing and perform the multiplication with the  $2f$  signal and the subsequent integration digitally. The modulation scheme can be seen as a very narrow bandpass filter that rejects noise at all other frequencies and phases, resulting in a considerably better SNR. Depending on the detector signal level, preamplifiers and analog bandpass filters (set to a frequency of  $2f$ ) were used in front of the lock-in amplifiers to allow for optimal digitization. The frequency of the FM is chosen such that the noise spectrum of the total spectrometer is low at this frequency.

The FM amplitude should roughly match the width of the absorption lines. Too small or too large FM amplitudes result in weak signals or very broad lineshapes after demodulation, respectively, with the latter making it difficult to distinguish close-by lines. However, the chosen FM amplitude is always a compromise between the strongest possible signal and the narrowest linewidth with the goal of the measurement dictating the right mixture. The resulting lineshapes look similar to the second derivative of a Voigt profile.

Broadband measurements are typically performed in segments of about 1 GHz, with each segment scanned once for increasing and once for decreasing frequencies, and the intensities averaged for each frequency. This procedure greatly reduces any memory effects in the setups (e.g., due to exponential moving averages in the lock-in amplifiers) and intensity variations due to the pressure in the absorption cells increasing with time.

<sup>a</sup>The demodulation is performed with twice the modulation frequency because the symmetry of an absorption peak doubles the FM frequency of the detector signal relative to the incoming RF radiation.

## 3.2 Double Resonance Setup

For double resonance (DR) measurements, two sources are simultaneously resonant with transitions of the molecule. Therefore, a second, more powerful source, the so-called pump source, is added to the conventional absorption setup described in Sec. 3.1. The two beams are co-spatially aligned in the absorption cell by using two polarization filters and the polarization of the pump source being orthogonal to the polarization of the probe source, see Fig. 3.3.

As explained later in Sec. 5 and Sec. 9, the Autler-Townes effect then splits all transitions sharing an energy level with the pumped transition. The affected lines can be identified by measuring the spectrum once with and once without the pump source and calculating the difference. The subtraction of the on- and off-intensities for each frequency should be performed on short time scales to minimize fluctuations in experimental conditions, for which different implementations exist.<sup>6,115</sup> Here, a single modulation of the pump source was used while operating the probe source in continuous wave mode. The single FM of the pump source simultaneously realizes a difference spectrum and increases the SNR analogously to the conventional case. A more detailed explanation of the working principle is given in Sec. 9. If all additional components (pump source, polarization filters) are kept on the optical table, switching between the conventional and DR setup is as easy as changing a single connection, going from the lock-in amplifier to either the probe synthesizer (conventional) or the pump synthesizer (DR).

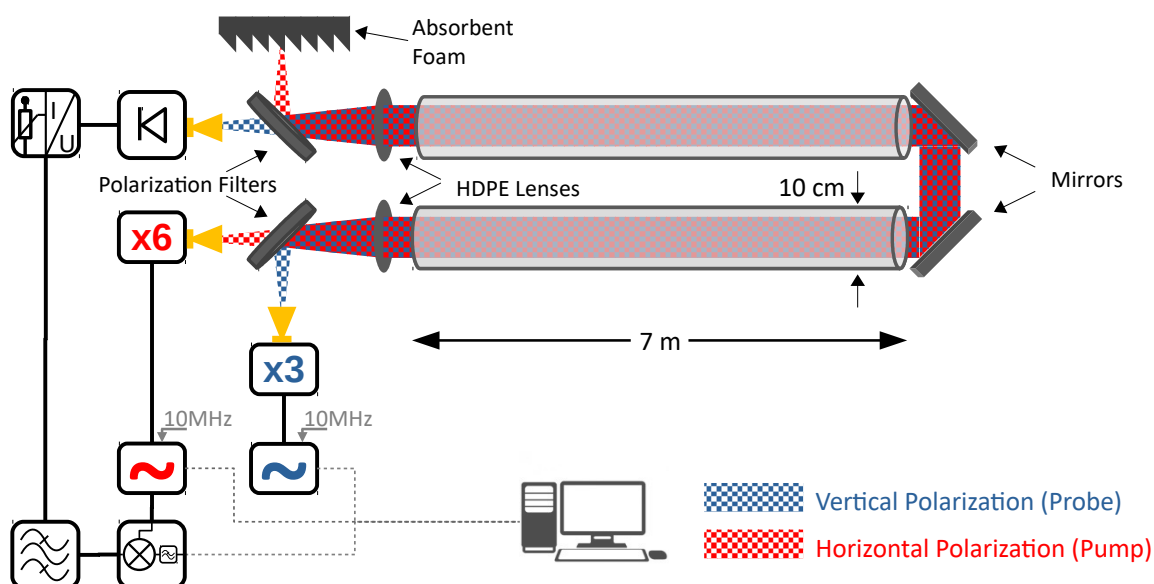


**Figure 3.3:** DR setup used at MIDAS-COINS. The orthogonally polarized probe (blue) and pump source (red) are aligned co-spatially via a polarization filter. While the probe beam is recorded by the detector, the pump beam is outcoupled by another polarization filter and sent into absorber foam. In contrast to the conventional setup, the probe source is operated in continuous wave mode and the pump radiation is frequency modulated.

## 4. Analysis Process and Software

This chapter describes the analysis process and the software used. An overview of the analysis process is given in Fig. 4.1, consisting of measuring the spectrum (Sec. 4.1), creating initial predictions (Sec. 4.2), multiple loops of the iterative assignment process (Sec. 4.3), and finalizing the dataset for publication (Sec. 4.4). The iterative assignment process consists of assigning predictions to the experimental spectrum, improving the model by fitting it to the assignments, and generating new predictions to assign more spectra, bringing the process full circle. Finally, some more advanced steps are presented (Sec. 4.5). All software mentioned in this chapter, unless specified otherwise, was developed as part of this thesis.

### 4.1 Measuring the Spectrum

High-resolution broadband spectra are recorded at the different experimental setups introduced in Sec. 3. The required samples can either be purchased commercially, synthesized (which was the case for acetone- $^{13}\text{C}_1$  in Sec. 6, ethyl phosphoethyne in Sec. 7, and glycid-aldehyde in Sec. 9), or created *in situ* which is necessary when the molecule is not stable or is very short-lived (cyclopentadiene was created via thermolysis in Sec. 8). Molecules produced *in situ* are measured in a flow setup, which means that the target molecule is constantly produced while at the same time the cell is pumped. For flow measurements, the pressure in the cell is controlled by adjusting the production and pumping speed. Establishing a stable equilibrium can be difficult and requires frequent supervision and adjustments. In contrast, for static measurements, the cell is filled only in the beginning and after the pressure in the cell has risen to a certain limit<sup>a</sup>. The supervision requirements for static measurements are very low, only requiring intervention when the cell needs to be refilled.

The low supervision requirements are made possible by the measurement software Tool for Remotely Accessing and Controlling Experiments (TRACE)<sup>b</sup>. The software is written

---

<sup>a</sup>The pressure increases due to tiny leaks and diffusion from the walls and windows. The increasing pressure causes the lineshapes to broaden (see Sec. 2.3.1). This causes the linewidth and FM amplitude to mismatch, resulting in a decreasing signal. Typically, the cells are refilled when the signal reaches half its initial value.

<sup>b</sup>Available at <https://github.com/Ltotheo1s/TRACE>

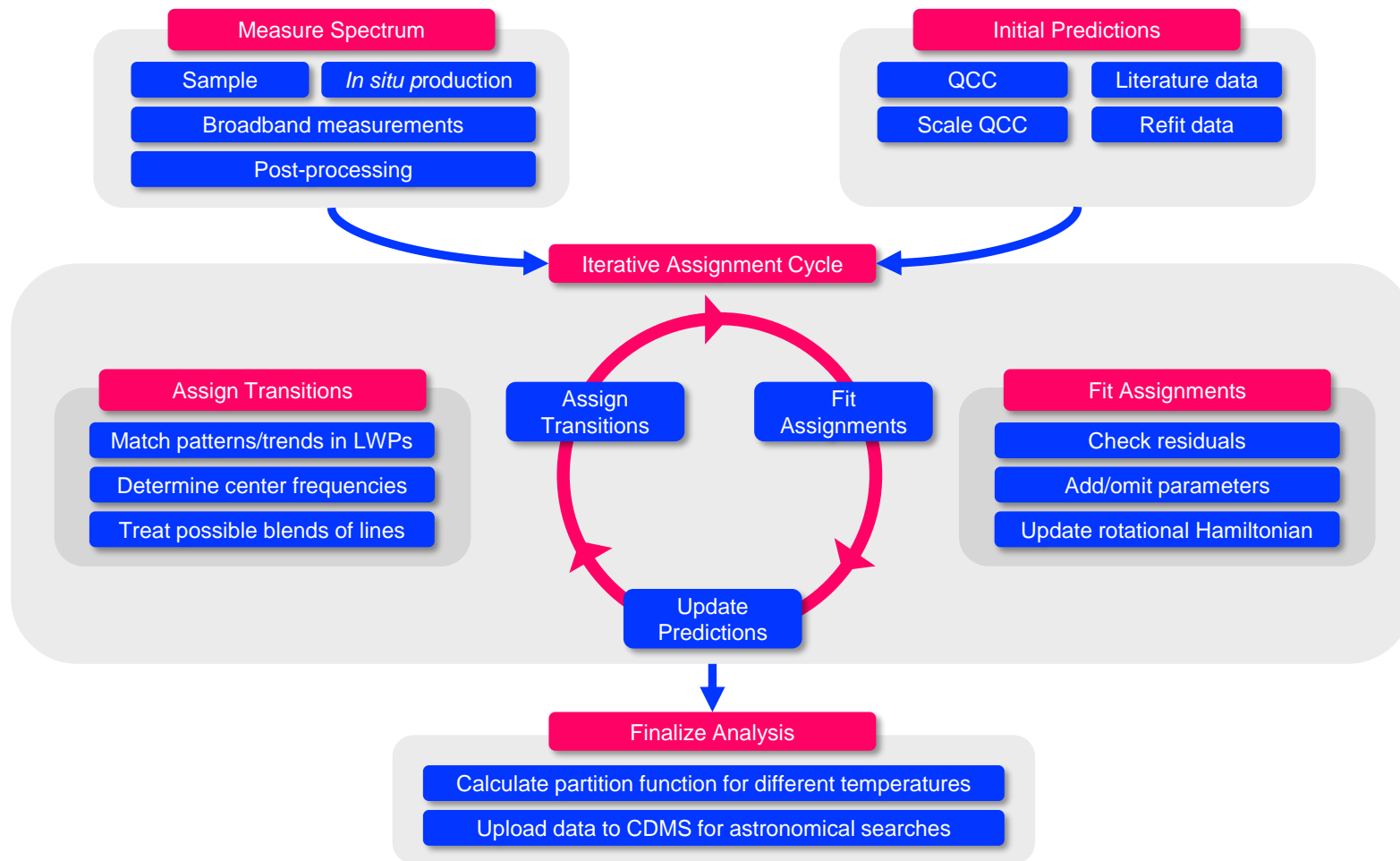


**Figure 4.1:** Flowchart of the analysis process. The process begins with measuring the spectrum (top left) and initial predictions (top right), which can either come from QCC, literature data, or even very simple assumptions. With these two prerequisites, the iterative assignment cycle begins. In each round, lines from the experimental spectrum are assigned to the predicted transitions by matching their patterns. Then, the initial model is updated with the new assignments, improved predictions are created, which in turn facilitate more assignments, starting the next round of the iterative assignment cycle. When the quantum or frequency coverage is sufficient and the model matches the experimental accuracy, the data are finalized by calculating the partition function and making the data publicly available, e.g., in the CDMS.<sup>11,12</sup>

in Python3 and its graphical user interface (GUI) is shown in detail in Fig. A.11 and Fig. A.12. Different measurement types, including broadband measurements and different DR measurement techniques, can be started or queued quickly and easily. The ability to perform reproducibility measurements after a user-defined number of scans is used to monitor the performance of the spectrometer over the entire broadband measurement. This facilitates to check the overall functionality of the experimental setup, the signal degradation due to pressure increase, or to determine the frequency uncertainty of the spectrometer (see Sec. A.7). Additionally, the software reports any errors to the user, e.g., if the synthesizer loses the 10 MHz reference signal of the atomic clock.

TRACE saves for each frequency the in-phase and quadrature components of the lock-in amplifier. Hence, the phase of the demodulated spectrum can be checked and modified afterwards with the software *retrophase*<sup>c</sup>, which is highlighted in Fig. A.9. Additionally, standing waves are removed from each measurement by Fourier filtering with the software *fftfilter*<sup>d</sup> shown in Fig. A.10. These post-processing steps greatly facilitate the detection of very weak signals, which is the case for (most) isotopologues in natural abundance and vibrationally excited states high in energy.

## 4.2 Initial Predictions

The second prerequisite is an initial model of the rotational spectrum. For the simplest molecules, such as a linear molecule, just some rough approximations of the  $B$  rotational constant may be sufficient. As the complexity of the molecule increases, so do the requirements for the initial predictions. A good starting point are previous analyses from the literature. If available, their data are re-fitted to confirm the molecular parameters. Another option are QCC, which allow to predict the molecular constants *ab initio* with good accuracy. All QCC presented in this work were performed with the Coupled-Cluster techniques for Computational Chemistry (CFOUR)<sup>116–118</sup> software at the CCSD(T) level of theory.<sup>119</sup> The reader is referred to the respective chapters for the choice of basis sets<sup>120–123</sup> and the techniques used to determine the equilibrium geometries<sup>124</sup> as well as the harmonic and anharmonic force fields.<sup>125–128</sup> If an isoelectronic molecule with a similar structure (e.g., an isotopologue) is known from previous studies, the rotational constants obtained from the QCC can also be scaled by the exp/calc ratio of the known species, often improving the agreement for the unknown species considerably (see e.g., Table S2 in Sec. A.7, but also the literature on ions<sup>129–134</sup>). In some cases, even the exp/calc ratios of the neutral and ion species show good agreement.<sup>135</sup> This technique is so powerful, that a handful of linear molecules were detected astronomically without laboratory data.<sup>131–135</sup> However, even in these cases, laboratory data from similar molecules are essential to derive

---

<sup>c</sup>Available at <https://pypi.org/project/retrophase/>

<sup>d</sup>Available at <https://pypi.org/project/fftfilter/>

accurate exp/calc ratios.

Similarly, the rotational constants of vibrationally excited states can be significantly improved by applying the rotation-vibration interaction constants to the experimental ground state values.

Although the precision of modern QCC is very high, it does not match the precision of rotational spectroscopy (especially for larger molecules). Similarly, literature data may show deviations if the frequency or quantum number coverage is limited. Therefore, the initial predictions often reproduce the spectrum very well qualitatively, but not quantitatively. This qualitative agreement is then used in the iterative assignment cycle to also achieve quantitative agreement.

### 4.3 Iterative Assignment Cycle

The goal of the iterative assignment cycle is to go from predictions that capture the patterns in the experimental spectrum qualitatively but not quantitatively, to a model that matches both qualitatively and quantitatively. Patterns between the predicted and the experimental spectrum are matched to assign quantum numbers to the experimental lines. Depending on the molecule, patterns can result from prolate or oblate pairing (see Sec. 2.2.3), splitting due to hyperfine structure, internal rotation or other LAMs.

The patterns are especially easy to follow when viewed in LWPs.<sup>136</sup> LWPs show sections of the experimental broadband spectrum of the same width on top of each other. The predicted positions of the target series are used as the center frequencies of the different subplots. Deviations between the experimental and predicted spectrum appear then as smooth trends. This increases at the same time the efficiency and reliability of the spectroscopic assignment process. LWPs are implemented in the LLWP software<sup>e</sup> along with additional features. LLWP provides functionality to determine the center frequency of experimental lines by least squares fitting of different model lineshapes (including a second derivative Voigt profile) to the experimental data, blended lines are either separated in multi-component fits or assigned as a blend of lines, which is then handled accordingly by the Hamiltonian fitting software (SPFIT<sup>59</sup> or ERHAM<sup>88,89</sup>). The full feature set of LLWP is described in more detail in Sec. 6. Two recent changes to the software are worth highlighting here. First, to make the assignment process more efficient, a feature was implemented to automatically assign all transitions of a series given a few initial assignments. The center position of the next unassigned transition is predicted by a polynomial fitted to the  $\nu_{\text{exp}} - \nu_{\text{calc}}$  deviations of the already assigned transitions of the series. The exact center frequency is determined by least-square fitting the selected lineprofile to the experimental data around the predicted center frequency. This process is repeated, until all transitions of the series have been assigned. Especially series that are

---

<sup>e</sup>Available at <https://pypi.org/project/llwp/>

straight-forward to assign, meaning transitions that are not blended with other transitions or heavily influenced by interactions, are assigned quickly with this procedure – leaving more time for series that are challenging to analyze. Second, the Automated Spectral Assignment Procedure (ASAP)<sup>137</sup> was implemented which makes assigning rovibrational bands very efficient if one of the two vibrational states is known to sufficient accuracy. A more detailed description of ASAP is given in Sec. 5.

When no more transitions can be assigned, the assignments are checked for integrity. A very helpful tool are residual plots, where the  $\nu_{\text{obs}} - \nu_{\text{calc}}$  deviations are plotted against  $J$ ,  $K_a$ ,  $K_c$  or the frequency  $\nu$ . Correctly assigned series should form continuous trends (see Fig. A.4) while misassignments are typically visible as individual outliers (see Fig. A.6), making them easy to correct. The effective Hamiltonian is then fitted to the assigned transitions. For the analysis of acetone-<sup>13</sup>C<sub>1</sub>, Groner’s ERHAM<sup>88,89</sup> was used, while Pickett’s SPFIT<sup>59</sup> was used for all other analyses. Both programs take the assignments and the initial parameter values as input.

ERHAM relies on a single input file containing all assignments, rotational constants, dipole moments, and other settings. The output file provides a summary of the input data, the updated parameter values and their standard errors, in addition to statistics on the assignments. If specified, the predicted transitions are saved in the *\*.cat* format.<sup>60</sup>

In contrast, the SPFIT software takes as input a *\*.lin* file containing the assignments and a *\*.par* file containing the initial parameter values and some additional settings. Its output includes the updated parameter values and standard errors in the *\*.var* file (the *\*.par* input file is also overwritten with the new updated parameters), a summary of the input data and statistics on the assignments in the *\*.fit* file, and a backup of the initial *\*.par* file in the *\*.bak* file. The updated predictions are obtained by running SPCAT<sup>60</sup> on the resulting *\*.var* file and an *\*.int* file specifying the dipole moments, partition function, in addition to frequency and intensity limits.

The agreement between the model and the experimental data can be evaluated by a combination of several quality criteria. Two factors are the root mean square (RMS) and weighted root mean square (WRMS) values which are defined as

$$\text{RMS} = \sqrt{\frac{1}{N} \sum_i (\nu_i - \nu_{i,0})^2} \quad (4.1)$$

and

$$\text{WRMS} = \sqrt{\frac{1}{N} \sum_i \left( \frac{\nu_i - \nu_{i,0}}{\Delta\nu_i} \right)^2} \quad (4.2)$$

with the experimental frequencies  $\nu_i$ , the experimental uncertainties  $\Delta\nu_i$ , the calculated frequencies  $\nu_{i,0}$ , and the number of lines  $N$ . The RMS value has the dimensions of a

frequency and is independent of the assigned uncertainties. In contrast, the WRMS value is dimensionless and depends on the assigned uncertainties. The RMS value is only meaningful if the uncertainties of the entire dataset are similar. Then, a good agreement between model and experiment is achieved if the RMS value is close to the experimental uncertainty. Similarly, a WRMS value of about unity indicates good agreement. The WRMS value is also meaningful if the dataset consists of subsets of varying quality but relies on well-determined frequency uncertainties<sup>f</sup>.

Both the RMS and WRMS values are statistical values, meaning that very few blatant outliers can greatly influence them. Such outliers can be identified in the aforementioned residual plots which are another quality criterion. The distribution in the residual plots should be Gaussian around zero. In addition to outliers, trends can be quickly identified in residual plots (see Fig. A.5). Examples of these cases are shown in Sec. A.4. If the trends persist after updating the Hamiltonian with the new assignments, they typically indicate missing rotational constants or other deficiencies in the model. Two further quality criteria are whether lines are rejected from the model<sup>g</sup> and whether the fit converges or not.

Once all misassignments have been removed, additional parameters can be added to the model. For all but the simplest cases, several different rotational parameters are potential candidates<sup>h</sup>. To determine the best additional parameter, it is very helpful to test the influence of each candidate parameter on the dataset. Since doing this manually is both slow and error-prone, this procedure was automated for both ERHAM and SPFIT/SPCAT. For SPFIT/SPCAT, the Python3 package *Pyckett*<sup>i</sup> provides a command line interface (CLI) to automatically test all candidate parameters. Their influence on the fit is reported in terms of the RMS value, number of rejected lines, whether the fit is/was diverging, and the initial and final parameter values. An example is given for the analysis of the vibrationally excited state  $\nu_{27}$  of cyclopentadiene. For this example, the Hamiltonian was reduced to the quadratic rotational constants only. Running the *pyckett\_add* command to test additional parameters then produced the output shown in Fig. 4.2.

<sup>f</sup>Both the RMS and WRMS values have cases where they can be misleading. The RMS value will have little meaning if rotational and rovibrational data are used in a combined fit. The rovibrational data will typically have much higher uncertainties than the rotational data. As a result, the deviations of the rovibrational data will dominate the RMS value making it hard to spot problems in the rotational data. For the WRMS value, the accurate determination of the experimental uncertainties is critical, as by overestimating the uncertainties the WRMS value will reach unity before the model is actually matching the experimental accuracy. Therefore, it is important to never rely solely on a single quality criterion but to evaluate them in combination.

<sup>g</sup>In SPFIT a threshold can be set for the  $|\nu_{\text{obs}} - \nu_{\text{calc}}|/\Delta\nu$  value. Assignments surpassing that threshold will not be considered when fitting the Hamiltonian to the assignments.

<sup>h</sup>A very simple case is a linear molecule where the parameter hierarchy is just determined by the rank of  $J$ . For example, if the model for a linear molecule consists of only the  $B$  rotational constant, the centrifugal distortion constant  $D$  is the obvious parameter to test next. Similarly for asymmetric molecules, all parameters that are obtained by multiplying either  $\mathbf{J}^2$ ,  $\mathbf{J}_z^2$ , or  $\mathbf{J}_+^2 + \mathbf{J}_-^2$  to an already included parameter are good candidates. This corresponds to increasing either  $j$ ,  $k$ , or  $l$  by 1 in the SPFIT/SPCAT parameter codes, see Eq. 1 from *Practical uses of SPFIT* by B. Drouin.<sup>138</sup>

<sup>i</sup>Available at <https://pypi.org/project/pyckett>

```
>>> pyckett_add Analysis_v27 --skipfixed --sreduction
```

ID	RMS [kHz]	RejLines	Diverging	Init Value	Final Value
40100	190.94	0	NEVER	1.00e-37	6.28e-06
200	255.92	0	NEVER	1.00e-37	-1.35e-06
1100	265.94	0	NEVER	1.00e-37	-1.06e-06
50000	234.18	0	NEVER	1.00e-37	2.42e-06
2000	271.79	0	NEVER	1.00e-37	-7.75e-07

Initial values were an RMS of 277.10 kHz, 0 rejected lines, and diverging NEVER.

Best run is parameter 40100 with a final parameter value of 6.28e-06, RMS of 190.94 kHz, 0 rejected lines, and diverging NEVER.

**Figure 4.2:** Example of the *pyckett\_add* command. The first line is the command invocation and the subsequent lines are the generated output. The parameter candidates are automatically determined by the command. The output represents a table of the specified metrics when adding the parameter specified in the first column to the model. For more information, see the text.

The first line is how to invoke the CLI. *pyckett\_add* is the command name, *Analysis\_v27* the path (without the file extension) of the *\*.par* and *\*.lin* files of the corresponding analysis, *--skipfixed* specifies that fixed parameters (parameters that are not floated in the fit) should be ignored, and *--sreduction* specifies that the *S*-reduction (see Sec. 2.2) should be used. The following lines are the output generated by the program, representing a table. It is evident, that the parameter  $d_1$  with the parameter ID 40100 would improve the model the most (as indicated by its RMS value in the first row). The parameter is a good choice to add to the model because its final parameter value is physically reasonable and its addition does not lead to the rejection of any lines nor to the fit diverging. Furthermore, its addition would improve the RMS value much more significantly than the addition of any other parameter. It is important to note that although *Pyckett* greatly improves the workflow by eliminating tedious manual and error-prone work, it does not eliminate the necessity of checking the results for spectroscopic meaningfulness. Similarly, the influence of omitting already added parameters can be tested with *pyckett\_omit* (see Sec. A.5). Combined with the ability to quickly and interactively check residuals in LLWP, determining the right parameters to add to or omit from the model becomes very efficient. Once the set of rotational parameters has been updated and there are no more outliers or trends visible in the residuals, new predictions are generated. These are then used to assign more transitions, marking the first full cycle. This is repeated until all experimental/predicted transitions are assigned or the desired quantum number range is covered.

## 4.4 Finalizing the Analysis

After leaving the assignment cycle, the model is finalized by calculating the partition function at different temperatures and making the data publicly available to astronomers by uploading it together with the generated documentation to a spectroscopic database, for example the CDMS.<sup>11,12</sup>

## 4.5 Advanced Steps

This very general procedure can be extended by more advanced steps, some of which are described in the following.

The uncertainties of the determined center frequencies may be obtained with semi-automatic procedures. In the analyses presented here, the RMS deviation between the best-fit lineprofile and the experimental data was divided by the amplitude  $A$  of the best-fit lineprofile. The resulting  $\text{RMS}/A$  values were used to group the assignments and assign uncertainties (see Sec. A.7).

There are several additional methods to improve the identification of low-intensity patterns. The intensities of the experimental data can be re-calibrated with the results of an initial fit, e.g., the spectrum can be re-calibrated with the vibrational ground state data to facilitate the detection of weaker spectra such as vibrationally excited states or isotopologues (see Sec. 9). Furthermore, already assigned transitions can be removed from the spectrum, which also facilitates the detection of low-intensity patterns (see Sec. 8).

If interactions between vibrationally excited states are significant, the analysis process must be extended by identifying the interacting energy levels and describing the interactions explicitly in combined fits. Interactions also pose additional challenges, as e.g., the correct choice of parameters is difficult due to possible high correlations between interaction and rotational parameters. In certain cases, a detour via the rovibrational spectrum can simplify the analysis of vibrationally excited states, e.g., by using ASAP.<sup>137</sup> Methods concerning vibrationally excited states are discussed in more detail in Sec. 5.

Finally, additional experimental techniques such as DR measurements can be used to alleviate some of the aforementioned difficulties by unambiguously confirming shared energy levels between transitions in the spectrum.

In summary, the analysis process was explained and a broad range of tools has been introduced, ranging from very universal tools, like QCC or LWPs, to more powerful tools, like ASAP or DM-DR, which also require more upfront preparation. Some more detailed information about LWPs, ASAP, and DR measurements follow in Sec. 5.

# 5. Spectroscopy of Vibrationally Excited COMs

## Bibliographic Information

L. Bonah, S. Schlemmer, S. Thorwirth, Spectroscopy of Vibrationally Excited Complex Organic Molecules for Radio Astronomy, *in prep.*

## Author's contribution

The author of this thesis wrote the original draft and provided the visualization.

## Context

This paper reviews procedures, experimental techniques, and tools for the treatment of vibrationally excited states of COMs. The advantages of LWPs, ASAP, and DM-DR measurements are highlighted and worked examples are presented. In addition, a brief guide to identifying and analyzing interactions is given. Thus, this paper provides the theoretical background for understanding vibrational satellite spectra and explains their analysis process.

# Spectroscopy of Vibrationally Excited Complex Organic Molecules for Radio Astronomy

Luis Bonah<sup>a</sup>, Stephan Schlemmer<sup>a</sup>, Sven Thorwirth<sup>a</sup>

<sup>a</sup>*I. Physikalisches Institut, Universität zu Köln, Zùlpicher Str. 77, Köln, 50937, Germany*

---

## Abstract

The rotational spectra of molecules in vibrationally excited states (vibrational satellites) are astronomically very interesting but may be difficult to analyze. Their astronomical importance results from them being excellent temperature (and energy) probes. In addition, they are suspected to be a major source of unidentified lines in astronomical line surveys. Vibrational satellites are more difficult to analyze because the vibrational Boltzmann factors result in weaker spectra and due to the high number of possible vibrational states per species. If vibrational states are lying close in energy, interactions between them may occur, requiring an explicit description of the interactions in combined fits. Therefore, the analysis of vibrationally excited states can benefit from tools catered to these challenges, three of which are presented here.

Loomis-Wood plots (Loomis & Wood, 1928) use series of related lines as reference to make assigning weak spectra more confident and efficient. The Automated Spectral Assignment Procedure (Martin-Drumel *et al.*, 2015) uses a detour via the rovibrational spectrum to assign even series with perturbations seamlessly. Lastly, double resonance measurements can filter the spectrum for lines sharing an energy level. Especially the combination of these tools makes deciphering vibrational satellite spectra efficient and reliable.

*Keywords:* Vibrational Satellites, Double Resonance Spectroscopy, ASAP, Loomis-Wood Plots

---

## 1. Introduction

More than 340 molecules have been detected in the interstellar medium to date<sup>1</sup>. Since 2020, the detection rate has been increasing significantly (see Fig. 1) due to the commissioning of a new receiver generation [3] causing an increase in the detection rate of complex organic molecules (COMs), defined in this context as carbon-bearing molecules with six or more atoms [4]. The analysis process in the laboratory must be accelerated to match the detection speed and demands of astronomical observations [5]. While modern laboratory spectroscopic experimental techniques, like FASSST [6] or

chirped-pulse spectroscopy [7, 8], can record large broadband spectra within hours, the analysis process is usually the bottleneck. Assigning quantum numbers to the experimental lines is predominantly performed in a manual bootstrapping process which limits the efficiency of the laboratory analyses.

Vibrational satellite spectra of COMs are astronomically interesting as tracers for the excitation conditions of the corresponding interstellar regions and are thought to be the origin of many so-far unidentified lines (U-lines) in astronomical line survey spectra, especially in hot regions. An example has been given e.g. by Herbst and van Dishoeck [4] for a 80–280 GHz line survey of Orion-KL with the IRAM-30 m telescope [9]. Only half of the 16 000 detected lines could be assigned initially. After

---

<sup>1</sup>See the *Molecules in Space* section of the Cologne Database for Molecular Spectroscopy [1, 2] or *The Astrochemist* webpage at [www.astrochemist.org](http://www.astrochemist.org)

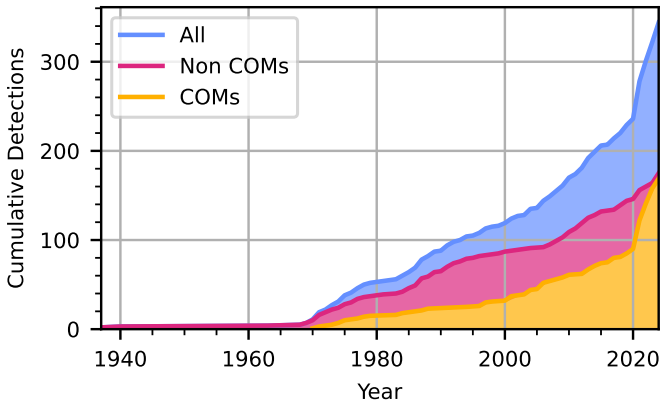


Figure 1: Cumulative detections of astronomical molecules over time.

two years, this number was significantly reduced to about 6000 U-lines by laboratory measurements of only two COMs, ethyl cyanide ( $\text{CH}_3\text{CH}_2\text{CN}$ ) and vinyl cyanide ( $\text{CH}_2\text{CHCN}$ ), and their isotopologues and vibrationally excited states. Despite their importance, data on vibrationally excited states are still missing for many COMs [5]. One reason is the increased difficulty in analyzing vibrational satellite spectra. To begin with, every COM has by definition at least 12 vibrational fundamentals. When also accounting for linear combinations, this results in a plethora of vibrational states requiring analysis. In addition, the spectra of vibrational states are lower in intensity due to their vibrational Boltzmann factor. This is complicated even more by the fact, that many COMs already have quite dense and weak spectra due to large rotational partition functions, splittings caused by internal rotation or other large amplitude motions, and/or hyperfine splitting. Hence, the weak vibrational satellite spectra are often considerably more challenging to identify. Last, vibrationally excited states close in energy can interact with each other (via e.g., Coriolis or Fermi resonances) leading to strong perturbations in their spectral patterns and rendering single-state fits useless. To describe such interaction systems, the interacting states have to be identified and their resonances have to be treated explicitly in multi-state fits. Even though not the main focus here, the situation is similar for isotopologues. They are astronomically interesting as tracers of isotope ratios and carriers of U-lines but

often have weak intensities in natural abundance.

A wide variety of sophisticated tools exist to speed up the spectroscopic analysis. For the assignment process, these include brute-force approaches like the AUTOFIT algorithm [10, 11], approaches based on neural networks [12] or genetic algorithms [13], codes exploiting the combination differences in purely rotational transitions [14], and approaches using computational optimal transport [15]. However, most of these tools require a peak list as input, which can be especially difficult to generate for low intensity patterns. On the experimental side, the energy term diagram can be reconstructed by measuring the spectrum at different temperatures [16, 17]. This requires to cover the complete frequency range of interest, as quantum mechanical models are foregone and with that the ability to inter- or extrapolate the spectrum.

In this paper, three methods are presented that can be used separately from each other but are especially powerful when combined: Loomis-Wood plots (LWPs) are a visual aid using adjacent transitions of a series as reference for a more efficient assignment process [18]. The Automated Spectral Assignment Procedure (ASAP) uses a detour via the rovibrational spectrum in combination with previous knowledge about one vibrational state to massively simplify the spectroscopic analysis of the unknown (target) state [19]. The resulting quantum mechanical model for the unknown vibrational state can then be used to guide the rotational analysis. Double resonance (DR) measurements can filter the spectrum for transitions sharing an energy level. As a result, subnetworks of the energy term diagram can be reconstructed unambiguously, which is especially useful for very weak spectra, and/or spectra affected by interactions.

In the following, the theory of vibrational satellite spectra is briefly summarized (Sec. 2). Then, the conventional analysis process is introduced (Sec. 3.1) to highlight how LWPs (Sec. 3.2), ASAP (Sec. 3.3), and DR measurements (Sec. 3.4) extend and improve it. Additionally, the identification and treatment of interaction systems is described (Sec. 4). Together, this results in an efficient and confident process for deciphering the rotational fingerprints of vibrationally excited states of COMs.

## 2. Theory - Vibrational Satellite Spectra

The rotational Hamiltonian  $\mathcal{H}_{\text{rot}}$  of a molecule is generally given as

$$\mathcal{H}_{\text{rot}} = \mathcal{H}_{\text{rr}} + \mathcal{H}_{\text{cd}} \quad (1)$$

$$\mathcal{H}_{\text{rr}} = A\hat{J}_a^2 + B\hat{J}_b^2 + C\hat{J}_c^2 \quad (2)$$

$$\mathcal{H}_{\text{cd}} = \frac{1}{4} \sum_{\alpha, \beta, \gamma, \delta} \tau_{\alpha\beta\gamma\delta} \hat{J}_\alpha \hat{J}_\beta \hat{J}_\gamma \hat{J}_\delta + \dots \quad (3)$$

being the sum of the rigid-rotor Hamiltonian  $\mathcal{H}_{\text{rr}}$  and the Hamiltonian considering the centrifugal distortion of the molecules geometry due to the rotation  $\mathcal{H}_{\text{cd}}$  [20]. The rigid-rotor Hamiltonian is found analogous to the classical description, where  $\hat{J}$  is the angular momentum operator, and  $A/B/C = \hbar^2/(2I_{a/b/c})$  are the effective rotational constants depending on the moment of inertia components  $I_\alpha$  along the three principal axes  $\alpha = a, b$ , or  $c$ . For the centrifugal distortion Hamiltonian,  $\alpha, \beta, \gamma$ , and  $\delta$  are summed over  $a, b$ , and  $c$  and the  $\tau_{\alpha\beta\gamma\delta}$  are the centrifugal distortion constants as defined by Kivelson and Wilson [21]. Here, only the quartic order is given, but higher orders are defined analogously. The invariance of the Hamiltonian under time-reversal requires even powers of the angular momenta operators, simplifying Eq. 3 to

$$\mathcal{H}_{\text{cd}} = \frac{1}{4} \sum_{\alpha, \beta} \tau_{\alpha\alpha\beta\beta} \hat{J}_\alpha^2 \hat{J}_\beta^2 + \dots \quad (4)$$

Only five linear combinations of the fourth-order  $\tau$ 's are determinable, leading to the reduced Hamiltonians – being either Watson's  $A$ -reduction [22, 23] or the  $S$ -reduction [24, 25] with the latter typically being advantageous for very symmetric molecules<sup>2</sup>. In the  $S$ -reduction, the effective centrifugal distortion Hamiltonian has the form

$$\mathcal{H}_{\text{cd}}^{(4)} = -D_J \hat{J}^4 - D_{JK} \hat{J}^2 \hat{J}_z^2 - D_K \hat{J}_z^4 + d_1 \hat{J}^2 \hat{J}_\pm^2 + d_2 \hat{J}_\pm^4 + \dots \quad (5)$$

with the raising and lowering operators  $\hat{J}_\pm = \hat{J}_x \pm i\hat{J}_y$ , the imaginary unit  $i$ , and the connection between the  $a, b, c$  and  $x, y, z$  labels for the axes being

<sup>2</sup>An asymmetric molecule is said to be symmetric if its Ray's asymmetry parameter  $\kappa = (2B - A - C)/(A - C)$  is close to the oblate limit of +1 or the prolate limit of -1 [26].

given by the chosen representation<sup>3</sup>. Consequently, the transition frequencies depend on the rotational constants and the centrifugal distortion constants.

When additionally considering the vibration of the molecule, the complete vibration-rotation Hamiltonian [27] can be approximated as two almost independent sums of rotation and vibration

$$\mathcal{H}_{\text{rovib}} = \mathcal{H}_{\text{rot}} + \mathcal{H}_{\text{vib}} \quad (6)$$

The vibrational excitation results in slightly changed rotational parameters, given here exemplarily for the  $B$  rotational constant

$$B_v = B_e - \sum_r \alpha_r^B \left( v_r + \frac{1}{2} \right) + \sum_{r \geq s} \gamma_{rs}^B \left( v_r + \frac{1}{2} \right) \left( v_s + \frac{1}{2} \right) + \dots \quad (7)$$

The  $\alpha$ 's and  $\gamma$ 's are the so-called rotation-vibration interaction constants and  $\gamma$  is small compared to  $\alpha$ .  $B_e$  is the rotational constant along the  $b$ -axis in the equilibrium configuration.  $r$  and  $s$  are running indices over the vibrational modes of the molecules with the respective vibrational quantum numbers  $v_r$  and  $v_s$ .

The  $\alpha$ 's consist of three terms accounting for the harmonic dependence of  $B$  on the normal coordinate  $Q_r$ , the Coriolis interaction between the vibrational mode  $r$  and any other vibrational mode  $s$ , and the anharmonicity of the potential [28]

$$\alpha_r^B = -\frac{2B_0^2}{\omega_r} \left[ \sum_\xi \frac{3 \left( a_r^{(b\xi)} \right)^2}{4I_\xi} + \sum_s (\zeta_{rs}^B)^2 \frac{3\omega_r^2 + \omega_s^2}{\omega_r^2 - \omega_s^2} + \pi \sqrt{\frac{c}{\hbar}} \sum_s \phi_{rrs} a_s^{(bb)} \frac{\omega_r}{\omega_s^{3/2}} \right] \quad (8)$$

Here,  $\omega_r$  is the harmonic wavenumber of the  $r$ th normal mode,  $a_r^{(b\xi)} = (\partial I_{b\xi} / \partial Q_r)_e$  (with  $\xi = a, b, c$ )

<sup>3</sup>There are six different representations, i.e., six mappings from the  $a, b, c$  to the  $x, y, z$  labels of the axes. The representation is typically chosen such that off-diagonal elements become as small as possible.

are the derivatives of the moment of inertia products with respect to the normal coordinate  $Q_r$ , the  $\zeta_{rs}^B$  are the Coriolis zeta constants, and the  $\phi$ 's are the anharmonic force constants. Each term within the brackets will be roughly of order of unity<sup>4</sup> meaning the magnitude of  $\alpha$  is  $2B_0^2/\omega_r$ , which is typically small compared to  $B_0$ . For example, the lowest vibrational modes of cyclopentadiene ( $\nu_{27}$  at  $350\text{ cm}^{-1}$  [29],  $B_0 \approx 8\text{ GHz}$  [30]) or glycidaldehyde ( $\nu_{21}$  at  $123\text{ cm}^{-1}$  [31],  $B_0 \approx 3\text{ GHz}$  [32]) each result in  $\alpha/B_0 \approx 0.17\%$ .

As a last consideration, the intensity of a rotational transition within a vibrational state will be compared to the same rotational transition in the ground vibrational state for an absorption experiment. For this approximation, similar transition frequencies, transition dipole moments and line-shapes are assumed for the two transitions. Hence, their intensities  $I$  will differ mainly due to the populations  $N$  of their respective initial levels, resulting in

$$\frac{I_v}{I_0} \approx \frac{N_v}{N_0} \approx \exp(-\Delta E_{\text{vib}}/kT) \quad (9)$$

where  $\Delta E_{\text{vib}}$  is the vibrational energy separation,  $k$  the Boltzmann constant, and  $T$  the temperature.

To summarize, rotational energy levels are described by effective Hamiltonians that are power series in the angular momentum (component) operators. Vibrational satellite spectra differ from the ground vibrational state in their frequency positions (Eq. 7) but in general not by very much (Eq. 8). Therefore, spectra are expected that qualitatively match the ground vibrational state spectrum with a relative intensity that is given by their vibrational Boltzmann factor (Eq. 9).

### 3. Tools for Vibrational Satellite Analysis

The goal of the spectral analysis process is to reconstruct the energy level diagram. Fig. 2 shows the connection between the energy level diagram (left hand side) and the spectrum (red transitions on the right hand side) for the  $K_a = 0$  levels of

<sup>4</sup>The Coriolis term can get significantly bigger than unity if  $\omega_r \approx \omega_s$ . This resonant case is described in more detail in Sec. 4

cyclopentadiene ( $v = 0$  up to  $J = 8$ ). For single-photon absorption, only  $\Delta J = +1$  transitions are allowed resulting in the eight possible transitions that are highlighted by the red arrows in the energy level diagram and by the respective red sticks in the spectrum. In the spectral analysis, this process is reversed by assigning the correct quantum numbers to the lines in the spectrum and using these assignments to reconstruct the energy term diagram. Transitions with other values of  $K_a$  are shown in Fig. 2 in blue to indicate that following a series in asymmetric top spectra is much more challenging than for a single  $K_a$  ladder, which would be comparable to the case of a simple linear molecule. While for linear molecules the energy term diagram could be easily reconstructed by measuring the complete rotational spectrum and calculating the cumulative sums of the transition positions, this is not feasible for more complicated molecules as identifying the correct transitions is not straight-forward and usually the frequency coverage is limited.

A more robust approach is to model an effective Hamiltonian (see Eq. 1) to the assigned transitions. The effective Hamiltonian in turn allows to inter- and (within limits) to extrapolate the energy term diagram.

#### 3.1. Conventional Analysis

Conventionally, the assignment process is based on matching the patterns of initial predictions to the experimental spectrum. Therefore, the initial predictions should predict the spectrum qualitatively but quantitative agreement is not required. The predictions can be based on previous analyses (if available) or quantum chemical calculations (QCC). The accuracy of QCC may be improved if previous data from isoelectronic molecules similar in geometry are available. Then, the derived exp/calc ratio for the parameters of the known molecule can be used to scale the parameters of the unknown molecule. This works so well that some linear molecules not known from laboratory studies have been detected astronomically solely based on scaled parameters from QCC [33–37].

The rotational energy levels are described by power series, as described in Sec. 2. If the rotational constants used for the predictions deviate

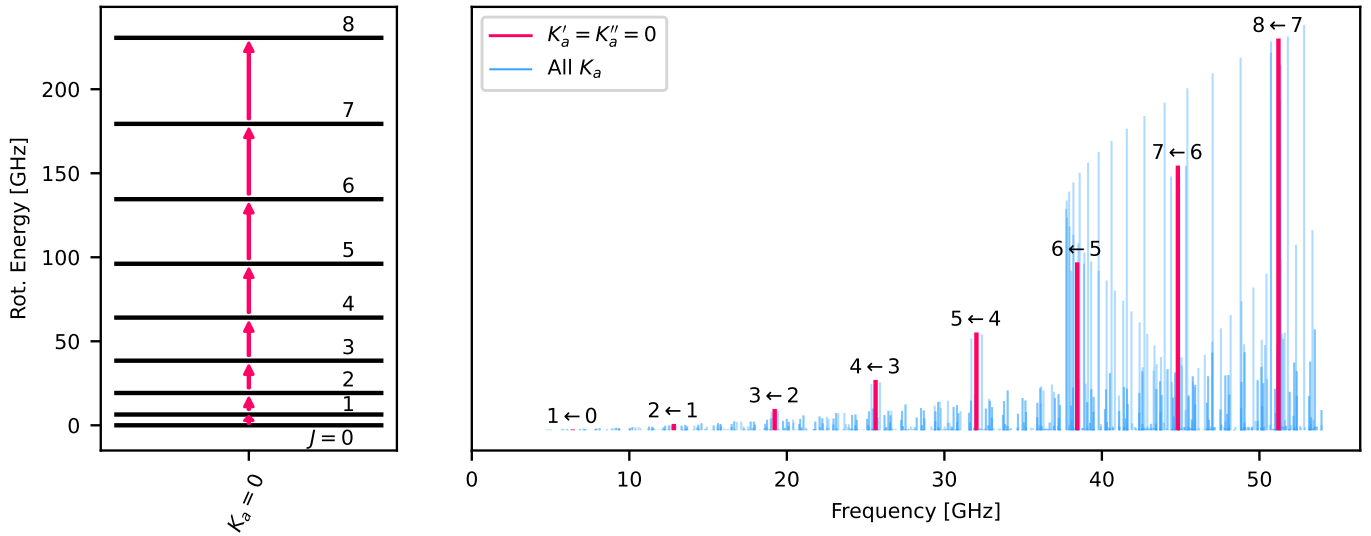


Figure 2: Simulated rotational energy levels (left) and spectrum (right) of the ground vibrational state of cyclopentadiene for  $K_a = 0$  up to  $J = 8$ . The nine allowed one-photon transitions are highlighted by red arrows in the energy term diagram and as red sticks in the simulated spectrum. The transition frequencies are almost equidistant. The goal of the spectroscopic analysis is to recognize the patterns in the spectrum and assign the correct quantum numbers. Then, the energy term diagram can be reconstructed via an effective Hamiltonian.

from their true values, the deviations between experimental and predicted positions of a series of transitions also form a power series, which converges quickly for low values of  $J$ . This behaviour is exploited in Loomis-Wood plots [18] which are presented in Sec. 3.2, but can also be followed manually. In combination with other patterns, e.g., from internal rotation, hyperfine splitting, and prolate or oblate pairing, this can be used to assign the quantum numbers from the predictions to the matching patterns in the experimental spectrum. The model Hamiltonian is then improved by fitting it to the assignments. Predictions from the improved Hamiltonian facilitate more assignments, starting a bootstrapping cycle.

Unfortunately, this process becomes more difficult for patterns which are weak and less prominent, as is the case for vibrationally excited states and isotopologues in natural abundance. This can be accommodated experimentally by measuring at higher temperatures, to increase the population of vibrationally excited states, or by using isotopically enriched samples. Furthermore, post-processing steps can emphasize weaker patterns in the spectrum, e.g., by removing already known patterns from the spectrum [38]. As already mentioned,

LWPs greatly improve the identification of even low-intensity patterns, while ASAP and DR measurements can identify series without relying on well-behaved trends in the deviations.

### 3.2. Loomis-Wood Plots

Loomis-Wood plots (LWPs) are a visual aid for identifying series of transitions in spectra and were first employed by Loomis and Wood in 1928 [18]. An example is shown in Fig. 3 for a series of transitions of the vibrational mode  $\nu_{27}$  of cyclopentadiene [38]. The full experimental spectrum from 170 to 250 GHz is shown in the plot on the right hand side (rotated by  $90^\circ$ ). In this broadband view, strong patterns formed by the  $b$ -type  $\Delta J = 1$  transitions repeat every 8.5 GHz. The areas highlighted in red are the parts of the spectrum that are shown in the vertically aligned plots on the left hand side. All rows have the same width and each row is centered around the respective predicted position (red sticks) for the  $K_a = 1 \leftarrow 0$  series of  $\nu_{27} = 1$ . The corresponding experimental transitions are highlighted in blue and form an almost straight line with the absolute deviation ( $\nu_{\text{obs}} - \nu_{\text{calc}}$ ) increasing with increasing  $J$  value. This Loomis-Wood representation makes assigning the series very efficient

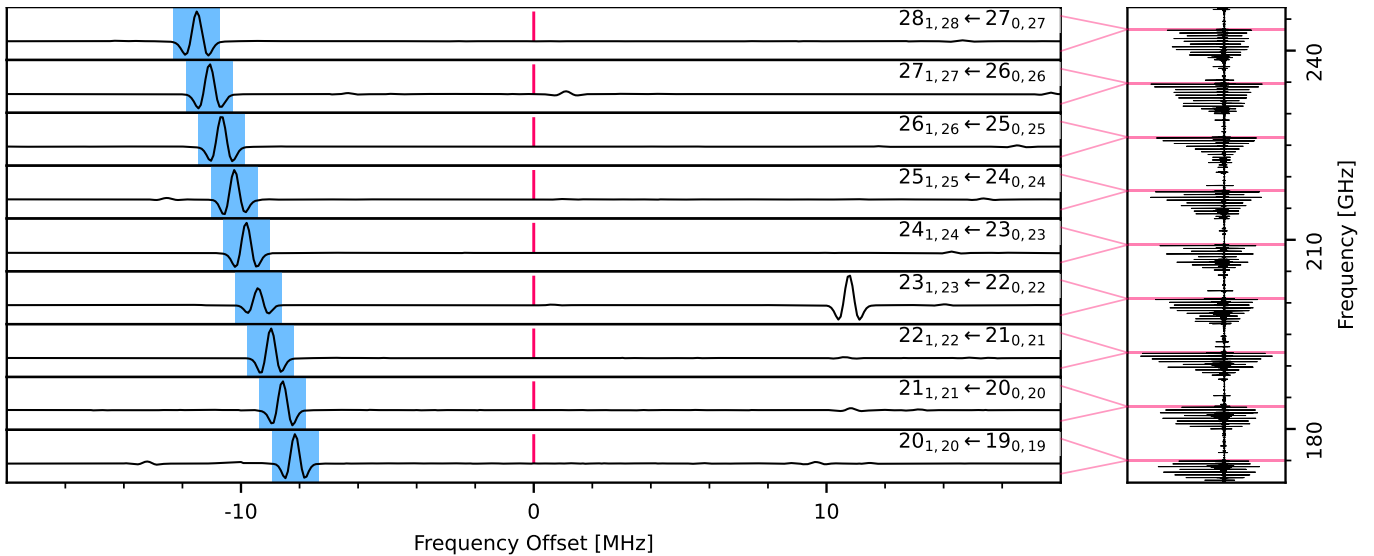


Figure 3: Loomis-Wood plot for the vibrational mode  $\nu_{27}$  of cyclopentadiene [38]. The reference positions (red sticks in the center) are calculated by applying rotation-vibration interaction constants from QCC to the experimental ground state model.

and reliable as the well-behaved deviation trend is easy to identify and follow. The adjacent rows basically act as mutual references for each other.

For the example shown in Fig. 3, the predicted positions were calculated by using the rotational parameters of the final ground vibrational state model and adding the rotation-vibration interaction constants from quantum-chemical calculations performed at CCSD(T) level with CFOUR [39–41]. The small deviations (only 8 to 12 MHz at 175 to 243 GHz, respectively) for transitions already quite high in  $J$  highlight the accuracy of combining the rotation-vibration interaction constants with experimental ground state rotational constants. However, also much simpler approaches can be chosen for the reference positions, e.g., the ground vibrational state predictions often suffice to identify vibrationally excited states (Fig. A.1). Basically the predictions just have to deviate following well-behaved trends (see Appendix A). When interactions are present, this may not be the case anymore and LWPs will be of limited use requiring more powerful methods like ASAP or DR measurements. However, for the vast majority of assignments, LWPs increase the reliability and efficiency dramatically.

LWPs have been used manually (e.g., Ref. [42]) and computer-aided (e.g., Ref. [43]) to simplify

spectral analyses. Some popular codes that are routinely used are the AABS package [44], LWW [45], Pgopher [46], and LLWP [47].

### 3.3. ASAP

The rotational analysis can benefit from a detour via the rovibrational spectrum. Reasons can be low signal-to-noise ratios in the pure-rotational spectrum, due to low population of the vibrational states or small permanent dipole moments, or strong interactions, that make it hard to identify patterns in LWPs. If certain prerequisites are met, the *Automated Spectral Assignment Procedure* (ASAP) [19] can significantly speed up the rovibrational assignment process. ASAP requires the experimental spectrum to be background-corrected, meaning areas with no transitions have a zero baseline. Additionally, the rotational spectrum of one of the two vibrational states and the selection rules have to be known. The second set of requirements is met quite frequently when the ground vibrational state is known from pure rotation. Then, the second state can be easily approximated by combining the ground state results with rotation-vibration interaction constants, for example from QCC.

ASAP’s working principle is described in Fig. 4 at the example of  $S_2O$  where the ground vibrational state  $\nu_0$  was already known from pure ro-

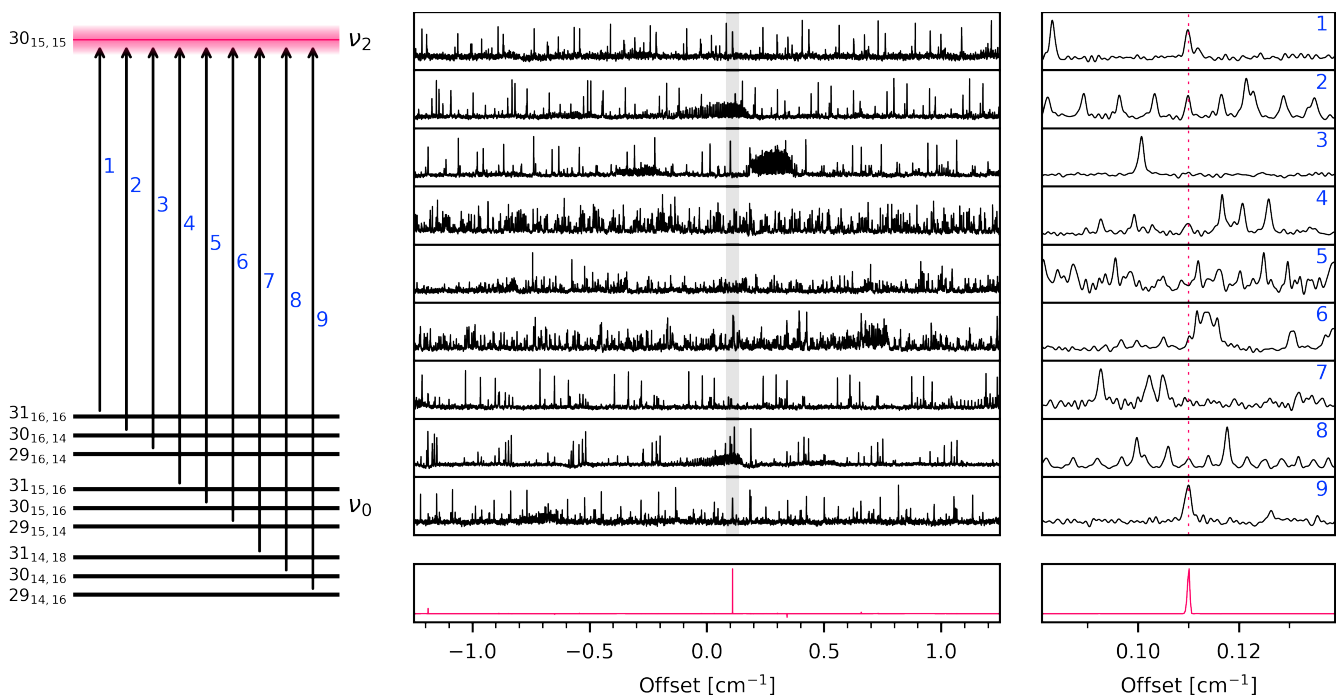


Figure 4: The working principle of the *Automated Spectral Assignment Procedure* (ASAP) explained exemplarily for the target state  $J_{K_a, K_c} = 30_{15,15}$  of the vibrational mode  $\nu_2$  of  $S_2O$  [19]. The ground vibrational state  $\nu_0$  is known to high accuracy from a previous rotational analysis [48]. Hence, all nine allowed transitions from  $\nu_0$  into the target state (left column) have the same offset from their predicted positions (middle and right column). By multiplying the offset plots with each other, the cross-correlation plot (red spectrum on bottom) results with only a single feature, the offset of the target level. The figure is adapted from Fig. 5 of the original ASAP publication [19].

tation to high accuracy [48]. The procedure is shown for the assignment of a single energy level, the  $J_{K_a, K_c} = 30_{15,15}$  energy level of  $\nu_2$ , which will be called *target level* hereafter. The left column of the figure shows the target level in red on top, and the nine  $\nu_0$  rotational levels that have an allowed transition into the target level. The actual and predicted energy of the target level will differ by  $\Delta E = E_{\text{obs}} - E_{\text{calc}}$ . Consequently, all nine transitions will deviate from their predicted positions  $\tilde{\nu}_{\text{calc},i}$  by the same amount  $\Delta\tilde{\nu}_i = \Delta\tilde{\nu} = \Delta E/hc$ . The predicted positions are used as the reference positions in a Loomis-Wood plot resulting in the actual transitions being vertically aligned at an offset of exactly  $\Delta\tilde{\nu}$  as shown in the middle and right columns of Fig. 4 (the right column is a zoom-in of the middle column).

Identification of this pattern can be massively simplified by computing the cross-correlation of the Loomis-Wood plot by multiplying all rows with each other (red spectrum at the bottom of the

middle and right columns in Fig. 4). The transitions into the target level all have the same offset resulting in a strong cross-correlation signal at this position. At all other offset frequencies, there should be no cross-correlation signal. This simplifies the analysis immensely as typically only a single strong feature remains in the cross-correlation plot. By determining its center frequency, the true energy of the target state can be calculated as  $E_{\text{obs}} = E_{\text{calc}} + \Delta\tilde{\nu} \cdot hc$  as well as the positions of the nine contributing transitions  $\tilde{\nu}_i = \tilde{\nu}_{\text{calc},i} + \Delta\tilde{\nu}$ .

In some cases, there can be accidental cross-correlation signals, especially if the number of rovibrational transitions into the target state is low or the quality of the background-correction is not optimal. This can be addressed by weighting the signals according to their predicted intensity before calculating the cross-correlation plots and by plotting the cross-correlation plots for a series of target states in Loomis-Wood fashion. An example of the latter is shown in Fig. 5 for the  $J_{15,J}$  series of states.

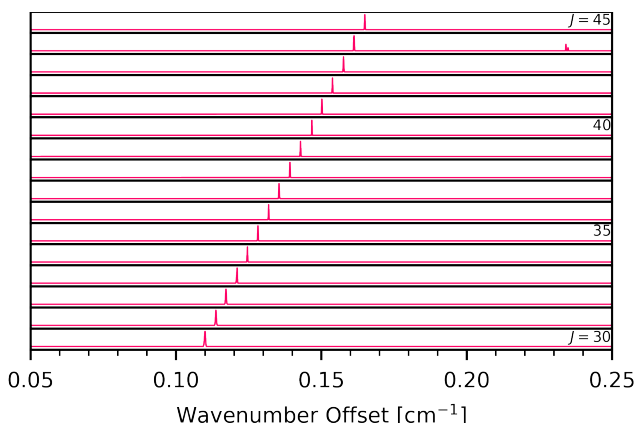


Figure 5: Loomis-Wood type representation of cross-correlation plots for a series of target states, the  $J_{15,J}$  series of the  $\nu_2$  vibrational mode of  $S_2O$ . Each row is an ASAP cross-correlation plot as explained in Fig. 4. The Loomis-Wood representation allows to easily spot accidental cross-correlation signals, like for  $J = 44$  at about  $0.24 \text{ cm}^{-1}$ , and makes the assignment process very efficient.

Each row is a cross-correlation plot similar to Fig. 4 and the series of transitions is easily identified and followed by the trend in the deviations. The cross-correlation peak for  $J = 44$  at a wavenumber offset of about  $0.24 \text{ cm}^{-1}$  is clearly identified as an accidental cross-correlation peak by not matching the trend of the cross-correlation peaks for other values of  $J$ .

The results of the rovibrational analysis performed with ASAP subsequently guide the pure-rotational analysis. Even though ASAP greatly improves the rovibrational analysis, there are only a handful of worked examples as of yet [19, 49–53]. ASAP could also be of special interest for interacting vibrational states, as the energy of the target level only needs to be known very roughly, which could significantly simplify the identification of perturbed series and thereby the interaction analysis.

### 3.4. Double Resonance Techniques

Double resonance (DR) techniques use two radiation fields that are resonant with different transitions of the molecule. While the probe radiation is used to scan the spectrum (similar to the conventional case), the pump radiation induces changes in the spectrum that can be monitored with the probe radiation. DR is used routinely in a wide variety of frequency ranges (see the introductions

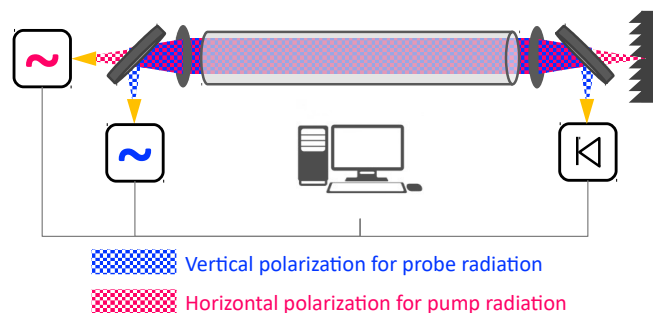


Figure 6: Schematic depiction of a double resonance setup. The probe radiation (blue) and the pump radiation (red) are orthogonally polarized to align them colinearly with the help of a polarization filter. After the absorption cell, the probe radiation is coupled out into a detector and the pump radiation is sent into an absorber. Additional equipment to synchronize the timing and to improve the signal-to-noise ratio, like modulations schemes, are omitted here for improved clarity.

of Refs. [54, 55]). If the two radiations cover significantly different frequency ranges, DR methods can be used to extend the frequency range [56–58], or populate higher vibrational states [59]. The other case, where the two radiations cover (approximately) the same frequency ranges, is called two-dimensional (2D) spectroscopy and is well established, for example in NMR [60–63] and ESR [64–66] techniques. For rotational transitions, the microwave (MW) and (sub-)millimeter regions are of special interest. In the MW, 2D and 3D techniques are established for quite some time [67–70] with recent work combining the strengths of chirped-pulse and cavity FTMW spectroscopy [71, 72]. For the sub-MMW region, 2D spectroscopy is a rather recent development [31, 55, 73–75]. An exemplary experimental setup is shown in Fig. 6.

2D spectroscopy can verify the relationships between transitions, which is especially useful if perturbations are present [78–80]. The pump radiation only modifies transitions sharing an energy level with the pumped transition, which can be identified by subtracting the spectra with and without pump source (see Fig. 7). The underlying effects are population changes and the Autler-Townes effect (ATE; also known as AC Stark effect) [76, 77].

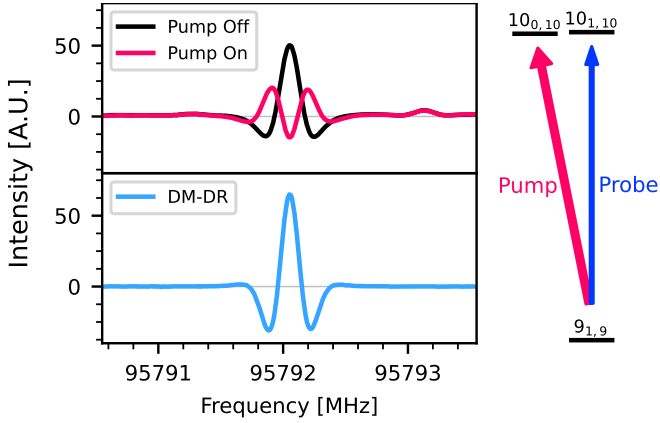


Figure 7: Example of a double resonance measurement for *syn*-propanal. The  $10_{1,10} \leftarrow 9_{1,9}$  transition is probed and the  $10_{0,10} \leftarrow 9_{1,9}$  transition is pumped. If the pump radiation is applied, the probe transition splits due to the Autler-Townes effect from a single line (black trace in top plot) into two half as intense lines (red trace in top plot) [76, 77]. The DM-DR spectrum is the difference of the pump-off and pump-on spectrum. The lineshapes are close to second derivatives due to the employed frequency modulation and  $2f$ -demodulation of the detector signal.

The population ratio of two states

$$\frac{N_i}{N_j} = \frac{g_i}{g_j} \exp(-\Delta E/kT) \quad (10)$$

depends on their degeneracies  $g$ , their energy difference  $\Delta E$ , and the temperature  $T$ . When assuming  $g_i \approx g_j$ , room temperature, and a transition frequency of 100 GHz, the intensity ratio is  $N_i/N_j = 98.4\%$ , which is very close to unity. As will be shown in the following, the changes that can be realized with the ATE are often dominating, especially if powerful sources are available.

The ATE is most easily explained by considering a three-level system and two fields in a fully quantum mechanical picture. Here, a conventional absorption spectrometer is considered foregoing any phase dependency as this is discussed in more detail elsewhere [81]. The three levels  $a$ ,  $b$ , and  $c$  have energies  $E_a < E_b < E_c$  and the transitions  $a \leftrightarrow b$  and  $b \leftrightarrow c$  are allowed. The pump field  $\omega_p$  is quasi-resonant to the transition  $b \leftarrow a$  meaning its detuning  $\delta = \omega_p - \omega_{ab}$  is small compared to  $\omega_{ab}$  and  $\omega_{bc}$ . At the same time, the pump field is non-resonant for the transition  $c \leftarrow b$  meaning the difference between  $\omega_{ab}$  and  $\omega_{bc}$  is sufficiently large.

Therefore, in an initial description the level  $c$  and the probe field  $\omega$  can be excluded. The remaining two-level system is described by

$$\mathcal{H} = \mathcal{H}_{\text{mol}} + \mathcal{H}_{\text{field}} + \mathcal{H}_{\text{int}} \quad (11)$$

where the three terms are the respective Hamiltonians for the molecular levels, the pump field, and the interaction

$$\mathcal{H}_{\text{mol}} = \hbar\omega_{ab}\sigma^+\sigma^- \quad (12)$$

$$\mathcal{H}_{\text{field}} = \hbar\omega_p a^\dagger a \quad (13)$$

$$\mathcal{H}_{\text{int}} = \frac{\hbar\Omega_n}{2} \hat{E} \hat{S} \quad (14)$$

with the reduced Planck constant  $\hbar$ . The molecular Hamiltonian describes the simple two-level system consisting of levels  $a$  and  $b$  where  $\sigma^+ = |b\rangle\langle a|$  is the raising operator and  $\sigma^- = |a\rangle\langle b|$  is the lowering operator. The Hamiltonian for the pump field consists of a single bosonic mode with the creation operator  $a^\dagger$  and the annihilation operator  $a$ . The interaction Hamiltonian describes the coupling of the molecule to the electric field  $\hat{E} = E_0(a^\dagger + a)$  by its polarization  $\hat{S} = \sigma^+ + \sigma^-$ . The  $n$ -photon Rabi frequency  $\Omega_n$  is proportional to the transition dipole moment and the power of the pump source. The interaction Hamiltonian can be simplified by applying the rotating wave approximation resulting in

$$\mathcal{H}_{\text{int}} = \frac{\hbar\Omega_n}{2} (a^\dagger\sigma^- + \sigma^+a) \quad (15)$$

When describing this system in the dressed-atom model (also known as Jaynes-Cummings model) each dressed state is described by a quantum number for the molecular level and one for the number of photons [82]. The two dressed states  $|b, n\rangle$  and  $|a, n+1\rangle$  can be expressed in matrix representation (with respect to the lowest molecule level  $a$ ) as

$$\frac{\hat{H}}{\hbar} = \begin{array}{cc} & \begin{array}{c} |a, n+1\rangle \\ |b, n\rangle \end{array} \\ \begin{array}{c} \langle a, n+1| \\ \langle b, n| \end{array} & \begin{pmatrix} (n+1)\omega_p & \Omega_n/2 \\ \Omega_n/2 & n\omega_p + \omega_{ab} \end{pmatrix} \end{array} \quad (16)$$

The resulting eigenvalues are

$$E_n^\pm = \frac{1}{2}\hbar \left( \pm\sqrt{\delta^2 + \Omega_n^2} - \delta \right) + (n+1)\hbar\omega_p \quad (17)$$

with the normalized eigenvectors

$$|n, +\rangle = \cos(\vartheta)|a, n+1\rangle - \sin(\vartheta)|b, n\rangle \quad (18)$$

$$|n, -\rangle = \sin(\vartheta)|a, n+1\rangle + \cos(\vartheta)|b, n\rangle \quad (19)$$

where  $\cos(\vartheta)$  and  $\sin(\vartheta)$  are mixing coefficients. The two states  $|n, \pm\rangle$  are linear combinations of the initial unperturbed states  $|b, n\rangle$  and  $|a, n+1\rangle$ <sup>5</sup>. Hence, both  $|n, +\rangle$  and  $|n, -\rangle$  have an allowed transition into the level  $|c, n\rangle$  as they consist to some amount of  $|b, n\rangle$ . As the resonant case ( $\delta = 0$ ) is ideal for the spectroscopic application, the reader is referred to the literature for the implications of the off-resonant case [55]. For  $\delta = 0$ , the two mixing coefficients are equal  $\cos(\vartheta) = \sin(\vartheta) = 1/\sqrt{2}$ , and the energies of the new states are

$$E_n^\pm = \omega_{bc} \pm \hbar\Omega_n/2 \quad (20)$$

Consequently, the transition  $c \leftarrow b$  splits into two half as intense transitions that are symmetrically shifted from their initial position  $\omega_{bc}$  by  $\pm\hbar\Omega_n/2$ , compare the right spectrum of Fig. 8. Generalizing this to an actual molecule, all transitions sharing an energy level with the pumped transition will show this splitting. By subtracting the spectrum with and without pump radiation, a baseline free spectrum is obtained consisting of only transitions sharing an energy level with the pumped transition (see Fig. 7 and Fig. 9).

In the following, some implications for real experiments are discussed. The splitting of the transitions is proportional to the transition dipole moment and the electric field, which in turn is proportional to the square root of the power of the source. Thus, the splitting of the transitions can be smaller than their FWHM resulting in a wider and less intense lineshape but no clear splitting (see the middle spectrum of Fig. 8). If the splitting is small, the influence from population changes has to be considered also. When the pump and probe transition share the same upper or lower level (so-called regressive arrangement; shown in Fig. 7), the population changes also decrease the intensity of

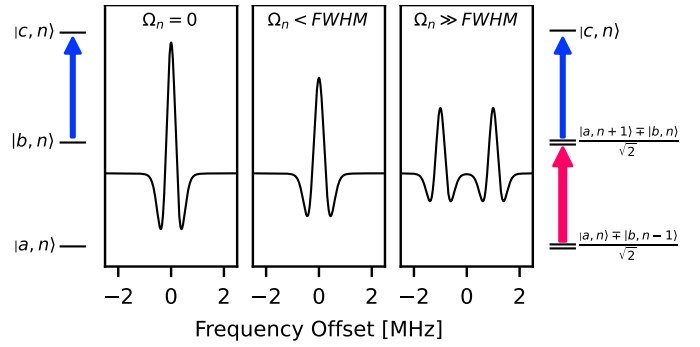


Figure 8: The Autler-Townes effect [76, 77] explained with a simple three-level system and simulated spectra. The probe radiation is indicated as a blue arrow and the pump radiation as a red arrow. When no pump radiation is present (left side), only the probed transition  $c \leftarrow b$  appears in the spectrum. When a strong pump source is resonant with the transition  $b \leftarrow a$ , the unperturbed dressed-states  $|b, n\rangle$  and  $|a, n+1\rangle$  mix to create the two perturbed states  $(|a, n+1\rangle \pm |b, n\rangle)/\sqrt{2}$  which are offset by  $\pm\hbar\Omega_n/2$  from the unperturbed level  $|b, n\rangle$ , resulting in a splitting of the transition in the spectrum (right side). If  $\Omega_n$  is smaller than the FWHM, the line appears broader but less intense (middle).

the probe transition, whereas they increase the intensity if the shared level is the upper level of one and the lower level of the other transition (progressive arrangement; shown in Fig. 9). Therefore, for small  $\Omega_n$  and similar transition dipole moments, it is advantageous to use regressive energy level arrangements. Additionally, it is advisable to perform the subtraction on a short timescale to mitigate fluctuations of the experimental conditions. One possible way is to add a second modulation resulting in a double-modulation double-resonance (DM-DR) setup [55] where for each frequency the measurement with and without pump field are performed in rapid succession before switching to the next frequency.

The advantage of DR measurements is that they unambiguously confirm shared energy levels between transitions. With unlimited frequency coverage, a complete 2D scan would immediately yield the energy term diagram. Even with limited frequency coverage, subnetworks of the energy term diagram can be reconstructed, which in turn can be used to build an initial model and extrapolate the network to areas where no DR spectroscopy but conventional measurements are available. Often, these predictions suffice in combination with

<sup>5</sup>Equivalent results are obtained for the states  $|a, n\rangle$  and  $|b, n-1\rangle$ .

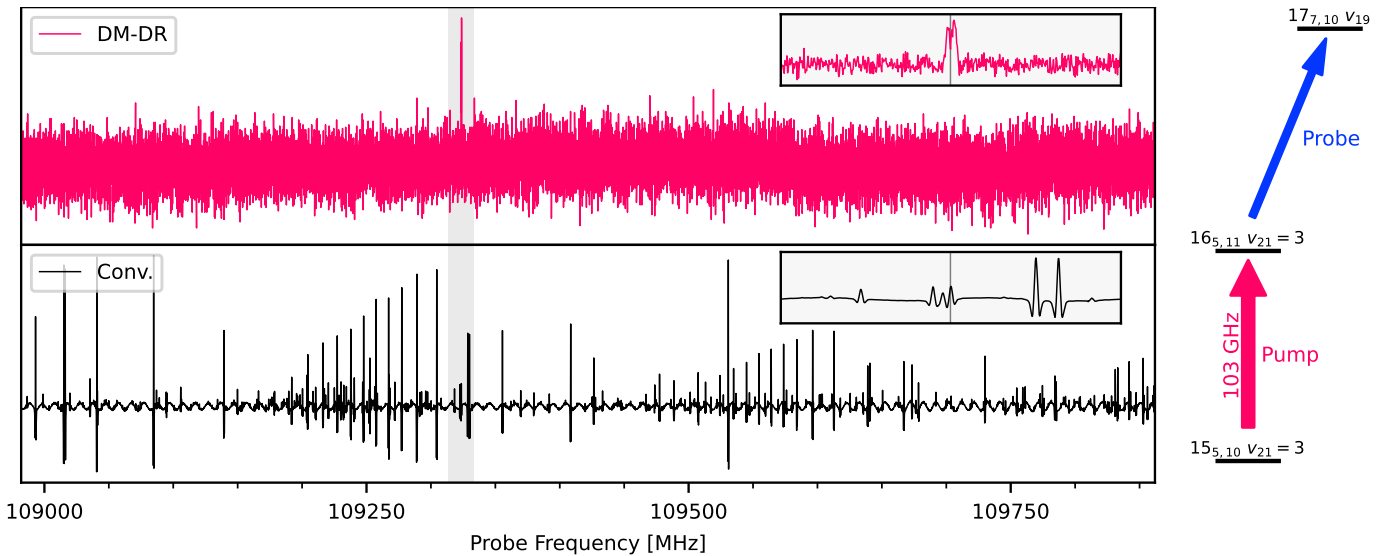


Figure 9: Double-modulation double-resonance (DM-DR) spectrum of glycidaldehyde for the interstate transition from  $16_{5,11}$  of  $v_{21} = 3$  to  $17_{7,10}$  of  $v_{19} = 1$ . Only a single line of the conventional spectrum (black spectrum on bottom) remains in the DM-DR spectrum (red spectrum on top) if the  $16_{5,11} \leftarrow 15_{5,10}$  transition of  $v_{21} = 3$  is pumped. The rotational transition between two vibrational states is possible due to their interaction which leads to wavefunction mixing, meaning the levels are actually linear combinations of both vibrational states (see Appendix C). Identifying these transitions is immensely helpful for the analysis of the interaction as the vibrational energy difference is determined with rotational precision.

LWPs to assign all measured transitions of the series.

Cases where DR measurements are especially powerful are i) blended or very weak transitions that can only be identified by removing all transitions not sharing an energy level with the pump transition from the spectrum (see Fig. B.1), ii) series of transitions that are heavily perturbed, or iii) (nominal) interstate transitions coupling different vibrational states (see Fig. 9) or tunneling states (see Fig. B.1) as they depend on the energy separation of the two states which often is not known with sufficient accuracy, making these transitions very difficult to identify by conventional means. Fig. 9 shows the identification of a nominal interstate transition between two vibrationally excited states of glycidaldehyde due to wavefunction mixing [31]. The two vibrational states  $v_{21} = 3$  and  $v_{19} = 1$  are interacting via Fermi and Coriolis interactions with each other. The resulting interacting states are linear combinations of the unperturbed  $v_{21} = 3$  and  $v_{19} = 1$  levels (see Fig. C.2). Therefore, rotational transitions between nominally different vibrational modes become possible (see Appendix

C). Because there was no experimental value for the vibrational energy separation between  $v_{21} = 3$  and  $v_{19} = 1$ , the frequency position of the interstate transition was very uncertain. By pumping an already known transition of  $v_{21} = 3$  (red arrow in Fig. 9), the DM-DR measurement reveals the interstate transition unambiguously, being the only line within 1 GHz to share an energy level with the pumped transition. Thereby, the vibrational energy separation is determined with rotational precision, which greatly facilitates the quantum mechanical modeling of the interaction system.

Another example of a DM-DR measurement is given in Fig. B.1 for a transition between the two tunneling states  $v = 0^+$  and  $v = 0^-$  of propanal [74]. The transition is split into  $A$  and  $E$  components due to internal rotation of the methyl rotor. Again, the energy separation between the two tunneling states was tough to determine experimentally as the transition is highly blended with other, stronger lines, making their assignment in the conventional spectrum impossible (see zoom-in in bottom plot of Fig. B.1). Measuring transitions between the tunneling states was essential to derive

their energy separation accurately which in turn was important to describe the interactions with the energetically low-lying  $\nu_{24}$  aldehyde torsion.

In summary, DR measurements are extremely powerful for finding transitions that are important for the quantum mechanical description but poorly predicted. At the same time, they speed up the analysis process by unambiguously constructing subnetworks, shifting work from the analysis process to the measurements.

#### 4. Interactions

Often it is sufficient to analyze each vibrationally excited state separately in a single-state fit. Then, for each vibrational state a unique set of rotational parameters is obtained. This is no longer possible if the coupling between vibrational modes is strong, which can happen if their energies are (nearly) degenerate. An example for such an interaction is introduced by the second term in Eq. 8, which describes the influence of Coriolis coupling on the rotational constants. For  $\omega_r \approx \omega_s$ , the denominator goes to zero, the term increases in magnitude, and gains first-order significance. Then, the applied perturbation treatment is no longer sufficient and the Coriolis resonance has to be treated explicitly by using a combined fit and exactly diagonalizing the Hamiltonian. Exemplarily for two vibrational states  $v_a$  and  $v_b$ , the combined Hamiltonian has the form

$$\mathcal{H} = \begin{pmatrix} \mathcal{H}_{\text{rot}}^{v_a} & \mathcal{H}_{\text{int}}^{v_a v_b} \\ \mathcal{H}_{\text{int}}^{v_b v_a} & \mathcal{H}_{\text{rot}}^{v_b} \end{pmatrix} \quad (21)$$

where the diagonal terms represent the rotational Hamiltonians (Eq. 1) and the off-diagonal terms are the interaction Hamiltonians. The complete Hamiltonian is Hermitian, hence,  $\mathcal{H}_{\text{int}}^{v_a v_b}$  is the Hermitian transpose of  $\mathcal{H}_{\text{int}}^{v_b v_a}$ . In the following, Coriolis and Fermi resonances will be introduced. For higher-order resonances, like Darling-Dennison [83] resonances or higher-order Coriolis resonances [84] the reader is referred to the literature. All mentioned resonance types have in common, that they are diagonal in the total angular momentum  $J$ , meaning only energy levels with the same  $J$  value interact, and that the effects get stronger the closer the interacting energy levels are energetically to each other.

Coriolis interactions were first described by Ebers and Nielsen [85] in 1937. They can already be seen in the harmonic potential and are a result of the coupling of rotation and vibration via the Coriolis operator. There can be  $a$ -,  $b$ -, and  $c$ -type Coriolis interactions corresponding to the rotations around each of the three principal axes. They occur only if the two vibrational levels  $\langle v_a, v_b |$  and  $\langle v_a \pm 1, v_b \mp 1 |$  are close in energy<sup>6</sup> and the product of their symmetries  $\Gamma(v_a) \times \Gamma(v_b)$  is equal to the symmetry of the rotation around the respective axis  $\Gamma(R_\alpha)$  [86]. An easy example is the water molecule where the asymmetric-stretch will induce the bending motion (and vice versa) for a rotation around the out-of-plane axis. This can be verified by simply applying the right-hand rule for the respective motions to each atom. The Coriolis interaction Hamiltonian has the form

$$\begin{aligned} \mathcal{H}_{\text{Cor}} = & iG_a \hat{J}_a + iG_b \hat{J}_b + iG_c \hat{J}_c \\ & + F_{bc} \left( \hat{J}_b \hat{J}_c + \hat{J}_c \hat{J}_b \right) \\ & + F_{ca} \left( \hat{J}_c \hat{J}_a + \hat{J}_a \hat{J}_c \right) \\ & + F_{ab} \left( \hat{J}_a \hat{J}_b + \hat{J}_b \hat{J}_a \right) + \dots \end{aligned} \quad (22)$$

Fermi resonances were first described by Fermi [87] in 1931. They result from the anharmonicity of the cubic potential and couple vibrational states with the same symmetry. Two types of resonance are possible, between  $\langle v_a, v_b, v_c |$  and  $\langle v_a \pm 1, v_b \pm 1, v_c \mp 1 |$  or between  $\langle v_a, v_b |$  and  $\langle v_a \pm 2, v_b \mp 1 |$ . As Fermi resonances are a purely vibrational effect, the absolute energy shift is the same for levels with the same  $J$  value. The Fermi resonance interaction Hamiltonian has the form

$$\begin{aligned} \hat{\mathcal{H}}_{\text{Fer}} = & W_0 + W_J \hat{J}^2 + W_k \hat{J}_z^2 \\ & + 2W_\pm \left( \hat{J}_x^2 - \hat{J}_y^2 \right) + \dots \end{aligned} \quad (23)$$

Unfortunately, the nomenclature for the Coriolis and Fermi interaction parameters is not always consistent in the literature.

<sup>6</sup>In this notation only the changing vibrational quantum numbers are specified. Any unspecified vibrational quantum numbers are assumed to remain constant.

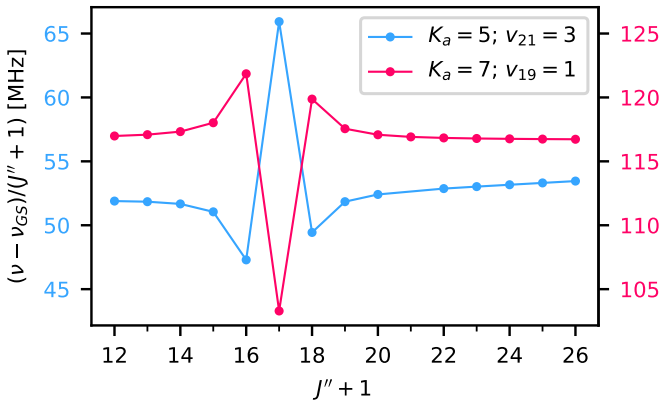


Figure 10: Resonance plot for  $\Delta J_{\Delta K_a, \Delta K_c} = 1_{0,1}$  transitions of glycidaldehyde for  $K_a = 5$  of  $v_{21} = 3$  (blue) and  $K_a = 7$  of  $v_{19} = 1$  (red). Here, the  $J = K_a + K_c$  asymmetry components are shown. The respective  $y$ -axes are shifted to highlight the mirror-image nature of the two series which indicates that the two series are interaction partners with the center of the interaction between  $J = 16$  and  $J = 17$ . See Fig. C.2 for the corresponding reduced energy diagram.

Resonances can be identified in so-called resonance plots which display  $(\nu - \nu_{\text{GS}})/(J'' + 1)$  for a series of transitions against  $J'' + 1$ , where  $\nu$  is the frequency of the transition and  $\nu_{\text{GS}}$  the frequency of the respective ground vibrational state transition. An example is given for the interacting vibrational states  $v_{21} = 3$  and  $v_{19} = 1$  of glycidaldehyde in Fig. 10. Whereas for states without interactions smooth curves are expected (see Fig. C.1), interactions lead to mirror-like deviations. To treat the resonances, first, the possible interaction types between the involved vibrational states should be derived from the mentioned symmetry considerations. Next, the energy difference of the two states has to be determined accurately. If no accurate value is available, the energy difference can be approximated from the involved energy levels and single-state fits. In the example of Fig. 10, the center of the resonance is between  $J = 16$  and  $J = 17$ . The pattern suggests that the two energy level series are crossing each other at this position, with the  $v_{19} = 1$  energy levels being energetically higher for  $J \leq 16$  and energetically lower for  $J \geq 17$ . By comparing the rotational energies of the single state fits, the vibrational energy separation can be approximated to give a sensible initial value. Then, the different interaction parameters have to be tested.

Initial parameter values can either be calculated, estimated from similar systems in other molecules, or different magnitudes are tested. It is not always sufficient to set the initial interaction parameter values to zero, as this can result in the model not converging toward the correct solution. This procedure is both tedious and error prone, especially when testing different starting values for multiple interaction parameters. Therefore, the inclusion of different interaction parameters can be automatically tested with the *Pyckett* library<sup>7</sup> [88], a Python 3 wrapper around Pickett’s SPFIT/SPCAT [89]. Once the correct interaction parameters are added to the model, it should reach about experimental uncertainty.

In summary, this approach allows to fit simple interaction systems, especially with two interacting states, with little to no *a priori* knowledge.

## 5. Conclusions and Outlook

Three methods were presented to speed up and simplify the analysis of rotational spectra of COMs – especially for vibrational satellite spectra but also isotopologues in natural abundance. As mentioned in the beginning, this increase in efficiency is highly desirable as weak satellite spectra are more challenging to analyze, and the capabilities of the latest generation of state-of-the-art radio astronomical instrumentation have significantly upped the rate of spectroscopic information. Many of the molecular fingerprints found in astronomical data cannot be assigned yet, even with the most comprehensive databases, like the Cologne Database for Molecular Spectroscopy, CDMS [1, 2]. However, their identification is important to better understand and model the corresponding astronomical regions. Vibrationally excited states are excellent tracers for the temperature of warm astronomical medium, while isotopologues are used to determine isotope ratios, e.g., the important  $^{12}\text{C}/^{13}\text{C}$  ratio.

Possible future steps should be taken toward extending the frequency coverage of DR measurements. A full 2D coverage of the rotational spectrum would immediately yield the complete energy term diagram, as regressive and progressive

<sup>7</sup>Available at <https://pypi.org/project/pyckett>

arrangements are distinguishable, only the intensities would require additional attention. Measuring large 2D spectra could be sped up by combining the DR approach with fast-scanning techniques, like chirped-pulse spectroscopy. On a similar note, vibrational states high in energy might benefit from an infrared laser as the pump source. The laser could increase their population, resulting in a stronger signal and would provide the ability to filter the spectrum for lines only belonging to the targeted vibrational state. This would make the analysis of these vibrational satellite spectra as simple as for the ground vibrational state.

Even though ASAP is a powerful technique, it has been rarely used yet, which may be endorsed by a user-friendly and well documented implementation.

Lastly, the analysis of easily recognizable patterns may be automated further. Neural networks can be trained to identify patterns in the spectra [12]. Possibly, also patterns of interactions could be identified with machine learning to speed up their analysis.

Together with the other tools mentioned earlier, the methods highlighted here provide a powerful toolbox to tackle the analysis of challenging rotational spectra more efficiently and reliably in the future.

## Acknowledgments

The authors gratefully acknowledge the Collaborative Research Center 1601 (SFB 1601 subproject A4) funded by the Deutsche Forschungsgemeinschaft (DFG, German Research Foundation) – 500700252.

## Appendix A. Additional LWPs

Loomis-Wood plots can be used with a wide range of predictions for the reference positions. In Fig. 3, predictions were generated by combining the ground vibrational state analysis with rotation-vibration interaction constants from quantum chemical calculations. This resulted in an excellent agreement, with only very small deviations between predicted and experimental positions. An

example of a much simpler approach is shown in Fig. A.1. The ground vibrational state data is used as reference without applying any corrections for the vibrational states. Nonetheless, the rotational patterns of many vibrational modes can be identified in the Loomis-Wood plots, as is highlighted exemplarily for  $\nu_{27}$  (blue),  $\nu_{14}$  (red), and  $\nu_{13}$  (orange). The deviations from the reference position are of course significantly higher for the simpler approach than for the more sophisticated approach (for  $\nu_{27}$  about 100–145 GHz compared to 8–12 MHz in Fig. 3, respectively).

Another point of reference comes from the fact, that the deviation trends are not only well-behaved in  $J$  but also in  $K_a$  or  $K_c$ . This is highlighted in Fig. A.2 where three Loomis-Wood plots of cyclopentadiene are shown next to each other. The  $K_a''$  values increase from left to right, being  $K_a'' = 0, 1, \text{ and } 2$ .

Combining these two approaches, vibrational satellite spectra can be identified in Loomis-Wood plots without any *a priori* knowledge of the vibrational modes, simply with the ground vibrational state as reference positions. The Loomis-Wood plot shown in Fig. A.1 will show the same qualitative pattern for the next higher value of  $K_a$ , as highlighted in Fig. A.2. This can be used to identify series belonging to the same vibrational mode. Especially for students, this can provide the opportunity to explore and assign vibrational satellite spectra without having to resort to QCC.

## Appendix B. DM-DR for Energy Separation of Tunneling States

*gauche*-propanal has two tunneling states as a result of the low barrier between the two *gauche* configurations. The energy differences are essential for accurately modeling the interactions and thereby the spectrum [74]. Similar to the example of vibrational states of glycidaldehyde in Sec. 3.4, the transitions of interest are weak in intensity and their positions are poorly predicted. Fig. B.1 shows how a transition between the two tunneling states of the ground vibrational state,  $\nu_0^+$  and  $\nu_0^-$ , could be identified. On the bottom (in black), the conventional spectrum is shown while on top the DM-DR

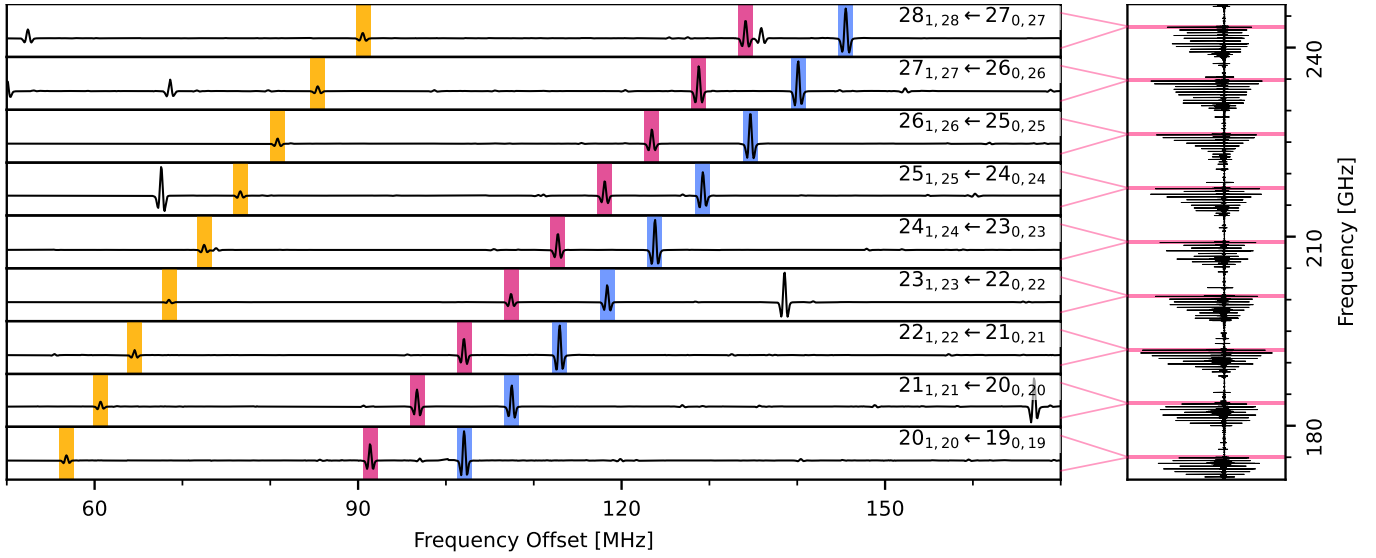


Figure A.1: Loomis-Wood plot for the  $\nu_{27}$  (blue),  $\nu_{14}$  (red), and  $\nu_{13}$  (orange) vibrational modes of cyclopentadiene [38]. The respective ground vibrational state transitions are chosen as reference positions which are at lower frequencies compared to the region shown here. The different relative intensities due to the vibrational Boltzmann factor (Eq. 9) are visible ( $\tilde{\nu}_{27} = 350 \text{ cm}^{-1}$ ,  $\tilde{\nu}_{14} = 516 \text{ cm}^{-1}$ ,  $\tilde{\nu}_{13} = 700 \text{ cm}^{-1}$  [29]).

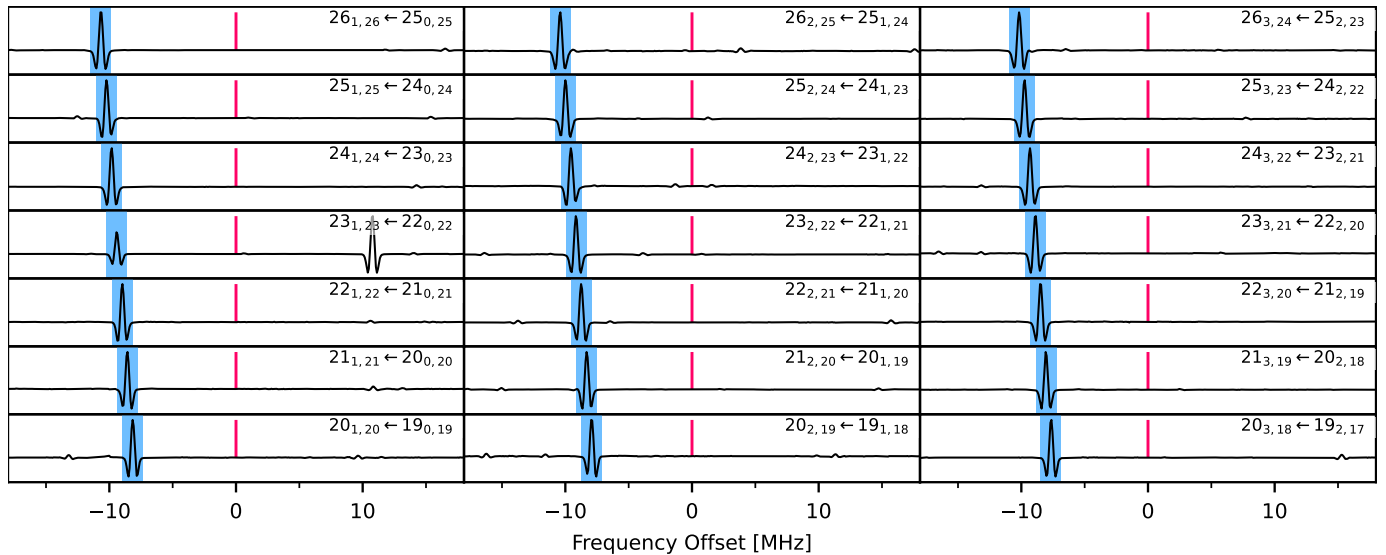


Figure A.2: Loomis-Wood plot for three subsequent  $b$ -type transition series of cyclopentadiene's  $\nu_{27} = 1$  vibrational state. The deviation progression is smooth in  $J$  but also in  $K_a$ , giving another point of reference when assigning transitions.

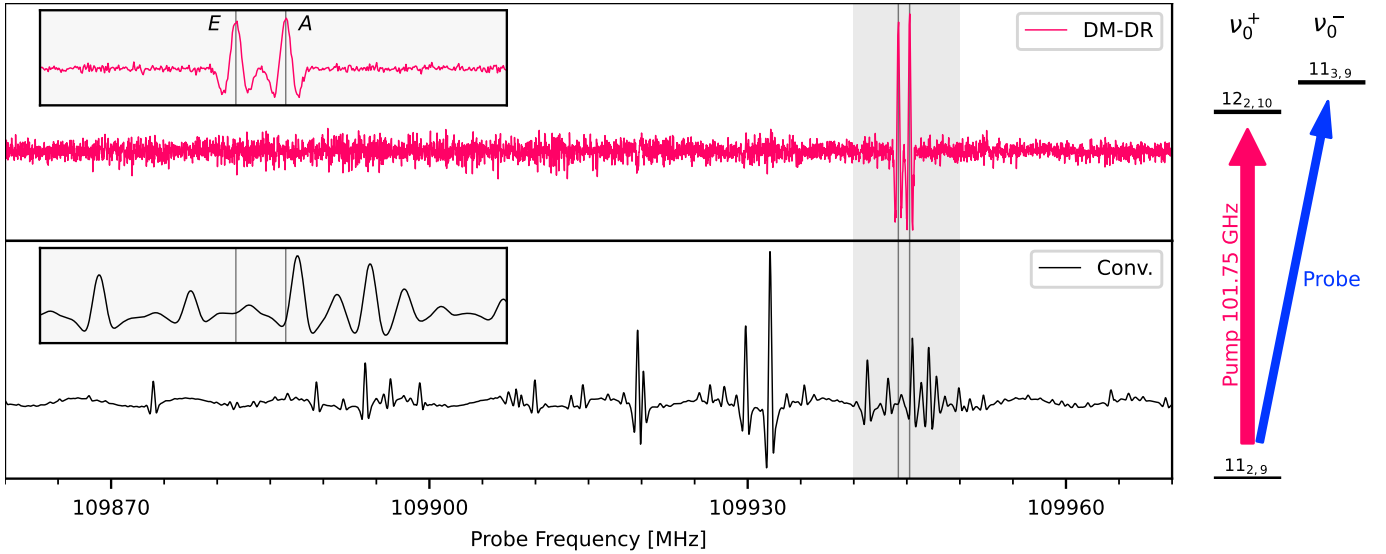


Figure B.1: Double-modulation double-resonance (DM-DR) measurement of *gauche*-propanal to determine the energy difference of the two tunneling states  $\nu_0^+$  and  $\nu_0^-$ . The conventional spectrum is shown in black on the bottom. When pumping the  $12_{2,10} \leftarrow 11_{2,9}$  transition of the  $\nu_0^+$  state, only two transitions remain in the DM-DR spectrum (red spectrum on top). These are the *A* and *E* components (due to internal rotation) of the targeted transition from  $11_{2,9}$  of  $\nu_0^+$  to  $11_{3,9}$  of  $\nu_0^-$ . The zoom-ins highlight the importance of DM-DR measurements for the correct assignment as the two components are heavily blended in the conventional spectrum, making it almost impossible to assign them by conventional means.

spectrum is shown for pumping the  $12_{2,10} \leftarrow 11_{2,9}$  transition of the  $\nu_0^+$  tunneling state. Only two lines are left in the DM-DR spectrum, being the *A* and *E* internal rotation components of the transition from the  $11_{2,9}$  level of  $\nu_0^+$  to the  $11_{3,9}$  level of  $\nu_0^-$ . Even with accurate predictions, the two transitions were almost impossible to identify in the conventional spectrum as they are heavily blended with much stronger transitions. The DM-DR spectrum removes all contributions from lines that do not share an energy level with the pumped transition. As a result, the two components of the targeted transitions are easily visible in the DM-DR spectrum. Thereby, the energy separation of the tunneling states could be determined accurately which was essential for analyzing the interactions with the aldehyde torsion  $\nu_{24}$ .

This is another example of DM-DR measurements greatly facilitating the analysis by identifying transitions that otherwise could not be found and by determining crucial energy differences for the analysis process, here the energy separation between the tunneling states.

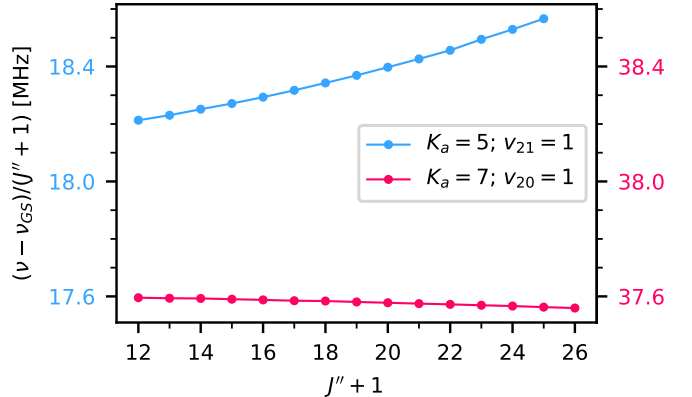


Figure C.1: Resonance plot for *a*-type transitions of glycidaldehyde for the two non-interacting series  $K_a = 5$  of  $v_{21} = 1$  and  $K_a = 7$  of  $v_{20} = 1$ . In contrast to Fig. 10, where two interacting series are shown, the two non-interacting series show no mirror-like deviations and form smooth trends.

## Appendix C. Details on the Interaction System

In Sec. 4 and in Fig. 9, the interaction system between  $v_{21} = 3$  and  $v_{19} = 1$  of glycidaldehyde is used as an example. Here, this interaction system is looked at in more detail.

First, the interaction system was identified via

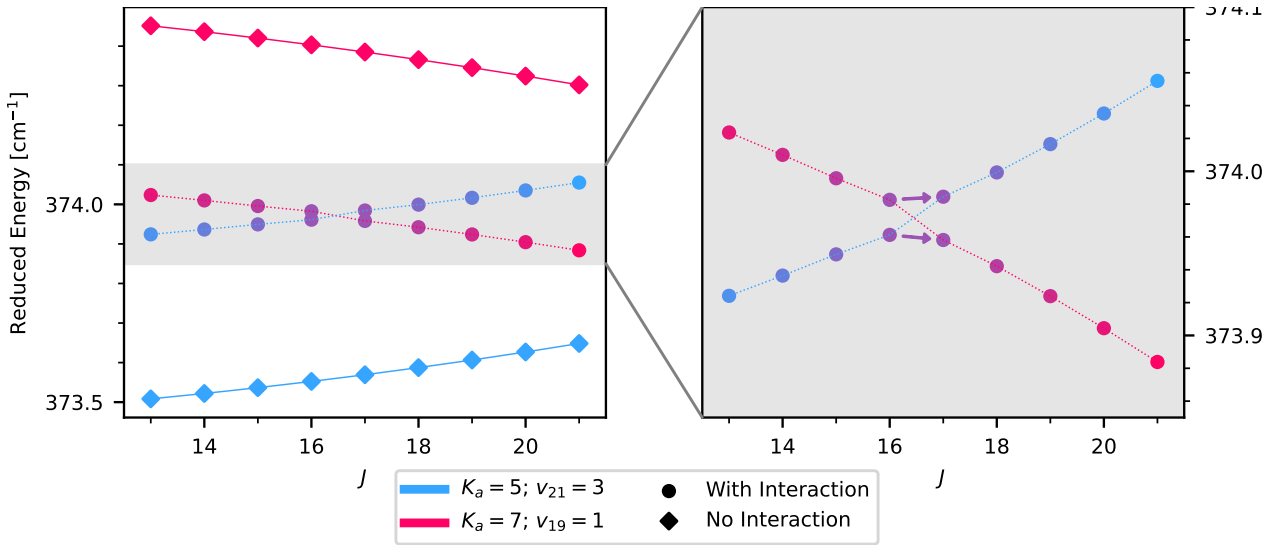


Figure C.2: Reduced energy diagram with and without interactions for energy levels with  $K_a = 5$  of  $v_{21} = 3$  (blue) and  $K_a = 7$  of  $v_{19} = 1$  (red) of glycidaldehyde. The  $J = K_a + K_c$  asymmetry components are shown. Without interactions, the two series are far apart (diamonds). Due to the interactions the two series are crossing each other (circles). The states close to the crossing are linear combination of the unperturbed states (as indicated by their colors). As a result, new transitions (purple arrows in the zoom in) become allowed, which connect nominally different vibrational states.

resonance plots, as shown in Fig. 10. The resonance plots of the  $K_a = 5$  transitions of  $v_{21} = 3$  and the  $K_a = 7$  transitions of  $v_{19} = 1$  are almost perfect mirror-images of each other. This is an indication, that the two series are interacting with each other. In contrast, Fig. C.1 shows the resonance plot of two non-interacting series, the  $K_a = 5$  transitions of  $v_{21} = 1$  and the  $K_a = 7$  transitions of  $v_{20} = 1$ . Both series form almost straight-lines, as is expected from Sec. 2. This highlights, how strong the deviations in the resonance plot are in Fig. 9 and what an interaction looks like in comparison to no interaction.

Second, the reduced energy plots for the  $v_{21} = 3$   $K_a = 5$  and  $v_{19} = 1$   $K_a = 7$  energy levels are shown in Fig. C.2. For glycidaldehyde, a near prolate asymmetric top, the reduced energy is given by

$$E_{\text{red}} = E - \frac{B + C}{2} J(J + 1) \quad (\text{C.1})$$

where  $B$  and  $C$  are the rotational constants of the ground vibrational state. As a result, energy levels belonging to the same series (levels with the same values of  $K_a$  and  $J - K_a - K_c$ ) are displayed roughly as horizontal lines. Circles show the energy levels for the real case with interactions and diamonds

for the simulated case of no interactions. Without the interactions, the two series are far apart from each other. With interactions, the two series cross each other between  $J = 16$  and  $17$ . The right side shows a zoom in  $y$ -direction. As mentioned beforehand, only levels with the same value of  $J$  can interact with each other and the interactions are stronger the closer the interacting levels are to each other. Therefore, the energy levels with  $J = 16$  and  $17$  are influenced the most by the interactions as can be seen from their deviations from the trend of the remaining levels. Similar to the explanation of the ATE in Sec. 3.4, the interaction shifts the positions of the levels and the resulting levels are linear combinations of the unperturbed levels. This is indicated in Fig. C.2 by the interacting levels being more purple than pure red or blue. The red- and blue-dotted lines trace the labeling of SPFIT/SPCAT [89], which labels them by the unperturbed level with the biggest contribution to the mixed levels. Due to this wavefunction mixing, new transitions are allowed between the levels indicated by purple arrows. These transitions are nominally interstate transitions, but are actually allowed because both levels are linear combination of the respective  $v_{19} = 1$  and  $v_{21} = 3$  levels.

Nominal interstate transitions are often very difficult to find, as their intensity also depends on the mixing coefficients of the involved levels, and their frequency prediction depends highly on the interaction strength and the energy separation. DM-DR techniques greatly simplify their identification (see Fig. 9), which in turn drastically simplifies the analysis process by determining the vibrational energy separation with rotational accuracy.

## References

- [1] C. P. Endres, S. Schlemmer, P. Schilke, J. Stutzki, H. S. P. Müller, The Cologne Database for Molecular Spectroscopy, CDMS, in the Virtual Atomic and Molecular Data Centre, VAMDC, *J. Mol. Spectrosc.* 327 (2016) 95–104. doi:10.1016/j.jms.2016.03.005.
- [2] H. S. P. Müller, S. Thorwirth, D. A. Roth, G. Winnewisser, The Cologne Database for Molecular Spectroscopy, CDMS, *Astron. Astrophys.* 370 (2001) L49–L52. doi:10.1051/0004-6361/20010367.
- [3] F. Tercero, J. A. López-Pérez, J. D. Gallego, F. Beltrán, O. García, M. Patino-Esteban, I. López-Fernández, G. Gómez-Molina, M. Diez, P. García-Carreño, I. Malo, R. Amils, J. M. Serna, C. Albo, J. M. Hernández, B. Vaquero, J. González-García, L. Barbas, J. A. López-Fernández, V. Bujarrabal, M. Gómez-Garrido, J. R. Pardo, M. Santander-García, B. Tercero, J. Cernicharo, P. de Vicente, Yebes 40m radio telescope and the broad band nanocosmos receivers at 7mm and 3mm for line surveys, *Astron. Astrophys.* 645 (2021) A37. doi:10.1051/0004-6361/202038701.
- [4] E. Herbst, E. F. van Dishoeck, Complex organic interstellar molecules, *Annu. Rev. Astron. Astrophys.* 47 (2009) 427–480. doi:10.1146/annurev-astro-082708-101654.
- [5] S. M. Fortman, I. R. Medvedev, C. F. Neese, F. C. De Lucia, How complete are astrophysical catalogs for the millimeter and submillimeter spectral region?, *Astrophys. J.* 725 (2010) L11–L14. doi:10.1088/2041-8205/725/1/L11.
- [6] S. Albert, F. C. De Lucia, Fast Scan Submillimeter Spectroscopy Technique (FASST): A new analytical tool for the gas phase, *Chimia* 55 (2001) 29. doi:10.2533/chimia.2001.29.
- [7] G. G. Brown, B. C. Dian, K. O. Douglass, S. M. Geyer, B. H. Pate, The rotational spectrum of epifluorohydrin measured by chirped-pulse Fourier transform microwave spectroscopy, *J. Mol. Spectrosc.* 238 (2006) 200–212. doi:10.1016/j.jms.2006.05.003.
- [8] G. G. Brown, B. C. Dian, K. O. Douglass, S. M. Geyer, S. T. Shipman, B. H. Pate, A broadband Fourier transform microwave spectrometer based on chirped pulse excitation, *Rev. Sci. Instrum.* 79 (2008). doi:10.1063/1.2919120.
- [9] B. Tercero, J. Cernicharo, J. R. Pardo, J. R. Goicoechea, A line confusion limited millimeter survey of Orion KL I. Sulfur carbon chains, *Astron. Astrophys.* 517 (2010) A96. doi:10.1051/0004-6361/200913501.
- [10] N. A. Seifert, I. A. Finneran, C. Perez, D. P. Zaleski, J. L. Neill, A. L. Steber, R. D. Suenram, A. Lesarri, S. T. Shipman, B. H. Pate, AUTOFIT, an automated fitting tool for broadband rotational spectra, and applications to 1-hexanal, *J. Mol. Spectrosc.* 312 (2015) 13–21. doi:10.1016/j.jms.2015.02.003.
- [11] C. M. Western, B. E. Billinghurst, Automatic assignment and fitting of spectra with PGOPHER, *Phys. Chem. Chem. Phys.* 19 (2017) 10222–10226. doi:10.1039/c7cp00266a.
- [12] D. P. Zaleski, K. Prozument, Automated assignment of rotational spectra using artificial neural networks, *J. Chem. Phys.* 149 (2018). doi:10.1063/1.5037715.
- [13] W. Leo Meerts, M. Schmitt, Application of genetic algorithms in automated assignments of high-resolution spectra, *Int. Rev. Phys. Chem.* 25 (2006) 353–406. doi:10.1080/01442350600785490.
- [14] L. Yeh, L. Satterthwaite, D. Patterson, Automated, context-free assignment of asymmetric rotor microwave spectra, *J. Chem. Phys.* 150 (2019). doi:10.1063/1.5085794.
- [15] N. A. Seifert, K. Prozument, M. J. Davis, Computational optimal transport for molecular spectra: The fully continuous case, *J. Chem. Phys.* 159 (2023). doi:10.1063/5.0166469.
- [16] I. R. Medvedev, F. C. De Lucia, An experimental approach to the prediction of complete millimeter and submillimeter spectra at astrophysical temperatures: Applications to confusion-limited astrophysical observations, *Astrophys. J.* 656 (2007) 621–628. doi:10.1086/510379.
- [17] S. M. Fortman, I. R. Medvedev, C. F. Neese, F. C. De Lucia, A new approach to astrophysical spectra: The complete experimental spectrum of ethyl cyanide ( $\text{CH}_3\text{CH}_2\text{CN}$ ) between 570 and 645GHz, *Astrophys. J.* 714 (2010) 476–486. doi:10.1088/0004-637x/714/1/476.
- [18] F. W. Loomis, R. W. Wood, The rotational structure of the blue-green bands of  $\text{Na}_2$ , *Phys. Rev.* 32 (1928) 223–236. doi:10.1103/physrev.32.223.
- [19] M. A. Martin-Drumel, C. P. Endres, O. Zingsheim, T. Salomon, J. van Wijngaarden, O. Pirali, S. Gruet, F. Lewen, S. Schlemmer, M. C. McCarthy, S. Thorwirth, The SOLEIL view on sulfur rich oxides: The  $\text{S}_2\text{O}$  bending mode  $\nu_2$  at  $380\text{ cm}^{-1}$  and its analysis using an Automated Spectral Assignment Procedure (ASAP), *J. Mol. Spectrosc.* 315 (2015) 72–79. doi:10.1016/j.jms.2015.02.014.
- [20] W. Gordy, R. L. Cook, *Microwave molecular spectra*, Wiley, New York, NY, 1984.
- [21] D. Kivelson, E. B. Wilson, Approximate treatment of the effect of centrifugal distortion on the rotational en-

- ergy levels of asymmetric-rotor molecules, *J. Chem. Phys.* 20 (1952) 1575–1579. doi:10.1063/1.1700219.
- [22] J. K. G. Watson, Centrifugal corrections for asymmetric-top molecules, *J. Chem. Phys.* 45 (1966) 1360–1361. doi:10.1063/1.1727763.
- [23] J. K. G. Watson, Determination of centrifugal distortion coefficients of asymmetric-top molecules, *J. Chem. Phys.* 46 (1967) 1935–1949. doi:10.1063/1.1840957.
- [24] G. Winnewisser, Millimeter wave rotational spectrum of HSSH and DSSD. II. Anomalous  $K$  doubling caused by centrifugal distortion in DSSD, *J. Chem. Phys.* 56 (1972) 2944–2954. doi:10.1063/1.1677629.
- [25] B. P. van Eijck, Reformulation of quartic centrifugal distortion Hamiltonian, *J. Mol. Spectrosc.* 53 (1974) 246–249. doi:10.1016/0022-2852(74)90129-5.
- [26] B. S. Ray, Über die Eigenwerte des asymmetrischen Kreisels, *Z. Phys.* 78 (1932) 74–91. doi:10.1007/bf01342264.
- [27] J. K. G. Watson, Simplification of the molecular vibration-rotation Hamiltonian, *Mol. Phys.* 15 (1968) 479–490. doi:10.1080/00268976800101381.
- [28] I. M. Mills, Vibration-rotation structure in asymmetric and symmetric-top molecules, in: K. N. Rao, C. W. Mathews (Eds.), *Molecular Spectroscopy: Modern Research*, Academic Press, 1972, Ch. 3.2, pp. 115–140.
- [29] E. Castellucci, P. Manzelli, B. Fortunato, E. Gallinella, P. Mirone, Vibrational spectra and normal-coordinate treatment of cyclopentadiene and its deuterated derivatives, *Spectrochim. Acta A* 31 (1975) 451–461. doi:10.1016/0584-8539(75)80037-7.
- [30] V. W. Laurie, Microwave spectrum and dipole moment of cyclopentadiene, *J. Chem. Phys.* 24 (1956) 635–636. doi:10.1063/1.1742585.
- [31] L. Bonah, J.-C. Guillemin, A. Belloche, S. Thorwirth, H. S. P. Müller, S. Schlemmer, Leveraging mmw-mmw double-resonance spectroscopy to understand the pure rotational spectrum of trans-glycidaldehyde and 17 of its vibrationally excited states, *ACS Earth Space Chem.* submitted (2025).
- [32] R. A. Creswell, P. J. Manor, R. A. Assink, R. H. Schwendeman, Microwave spectrum, torsional excitation energy, partial structure, and dipole moment of oxiranecarboxaldehyde, *J. Mol. Spectrosc.* 64 (1977) 365–375. doi:10.1016/0022-2852(77)90222-3.
- [33] N. Marcelino, M. Agúndez, B. Tercero, C. Cabezas, C. Bermúdez, J. D. Gallego, P. deVicente, J. Cernicharo, Tentative detection of  $\text{HC}_5\text{NH}^+$  in TMC-1, *Astron. Astrophys.* 643 (2020) L6. doi:10.1051/0004-6361/202039251.
- [34] C. Cabezas, Y. Endo, E. Roueff, N. Marcelino, M. Agúndez, B. Tercero, J. Cernicharo, Space and laboratory observation of the deuterated cyanomethyl radical HDCCN, *Astron. Astrophys.* 646 (2021) L1. doi:10.1051/0004-6361/202040210.
- [35] C. Cabezas, M. Agúndez, N. Marcelino, B. Tercero, S. Cuadrado, J. Cernicharo, Interstellar detection of the simplest aminocarbyne  $\text{H}_2\text{NC}$ : an ignored but abundant molecule, *Astron. Astrophys.* 654 (2021) A45. doi:10.1051/0004-6361/202141491.
- [36] C. Cabezas, M. Agúndez, N. Marcelino, B. Tercero, R. Fuentetaja, P. de Vicente, J. Cernicharo, Discovery of a new molecular ion,  $\text{HC}_7\text{NH}^+$ , in TMC-1, *Astron. Astrophys.* 659 (2022) L8. doi:10.1051/0004-6361/202142972.
- [37] J. Cernicharo, M. Agúndez, C. Cabezas, R. Fuentetaja, B. Tercero, N. Marcelino, Y. Endo, J. R. Pardo, P. de Vicente, Discovery of  $\text{C}_5\text{H}^+$  and detection of  $\text{C}_3\text{H}^+$  in TMC-1 with the QUIJOTE line survey, *Astron. Astrophys.* 657 (2022) L16. doi:10.1051/0004-6361/202142992.
- [38] L. Bonah, B. Helmstaedter, J.-C. Guillemin, S. Schlemmer, S. Thorwirth, Extending the rotational spectrum of cyclopentadiene towards higher frequencies and vibrational states, *J. Mol. Spectrosc.* 408 (2025).
- [39] J. F. Stanton, J. Gauss, L. Cheng, M. E. Harding, D. A. Matthews, P. G. Szalay, CFOUR, coupled-cluster techniques for computational chemistry, a quantum-chemical program package, With contributions from A. Asthana, A.A. Auer, R.J. Bartlett, U. Benedikt, C. Berger, D.E. Bernholdt, S. Blaschke, Y. J. Bomble, S. Burger, O. Christiansen, D. Datta, F. Engel, R. Faber, J. Greiner, M. Heckert, O. Heun, M. Hilgenberg, C. Huber, T.-C. Jagau, D. Jonsson, J. Jusélius, T. Kirsch, M.-P. Kitsaras, K. Klein, G.M. Kopper, W.J. Lauderdale, F. Lipparini, J. Liu, T. Metzroth, L. Monzel, L.A. Mück, D.P. O’Neill, T. Nottoli, J. Oswald, D.R. Price, E. Prochnow, C. Puzzarini, K. Ruud, F. Schiffmann, W. Schwalbach, C. Simmons, S. Stopkowicz, A. Tajti, T. Uhlířová, J. Vázquez, F. Wang, J.D. Watts, P. Yergün, C. Zhang, X. Zheng, and the integral packages MOLECULE (J. Almlöf and P.R. Taylor), PROPS (P.R. Taylor), ABACUS (T. Helgaker, H.J. Aa. Jensen, P. Jørgensen, and J. Olsen), and ECP routines by A. V. Mitin and C. van Wüllen. For the current version, see <http://www.cfour.de>.
- [40] M. E. Harding, T. Metzroth, J. Gauss, A. A. Auer, Parallel calculation of CCSD and CCSD(T) analytic first and second derivatives, *J. Chem. Theory Comput* 4 (2008) 64–74. doi:10.1021/ct700152c.
- [41] D. A. Matthews, L. Cheng, M. E. Harding, F. Lipparini, S. Stopkowicz, T.-C. Jagau, P. G. Szalay, J. Gauss, J. F. Stanton, Coupled-cluster techniques for computational chemistry: The CFOUR program package, *J. Chem. Phys.* 152 (2020). doi:10.1063/5.0004837.
- [42] J. F. Scott, K. Narahari Rao, “Loomis-Wood” diagrams for polyatomic infrared spectra, *J. Mol. Spectrosc.* 20 (1966) 461–463. doi:10.1016/0022-2852(66)90016-6.
- [43] A. W. Mantz, K. N. Rao, L. H. Jones, R. M. Potter, Vibration rotation bands of  $^{15}\text{N}_2^{18}\text{O}$  effects of Fermi resonance and  $l$ -type doubling, *J. Mol. Spectrosc.* 30 (1969)

- 513–530. doi:10.1016/0022-2852(69)90283-5.
- [44] Z. Kisiel, L. Pyszczółkowski, I. R. Medvedev, M. Winnewisser, F. C. De Lucia, E. Herbst, Rotational spectrum of trans–trans diethyl ether in the ground and three excited vibrational states, *J. Mol. Spectrosc.* 233 (2005) 231–243. doi:10.1016/j.jms.2005.07.006.
- [45] W. Lodyga, M. Kreglewski, P. Pracna, S. Urban, Advanced graphical software for assignments of transitions in rovibrational spectra, *J. Mol. Spectrosc.* 243 (2007) 182–188. doi:10.1016/j.jms.2007.02.004.
- [46] C. M. Western, GOPHER: A program for simulating rotational, vibrational and electronic spectra, *J. Quant. Spectrosc. Radiat. Transf.* 186 (2017) 221–242. doi:10.1016/j.jqsrt.2016.04.010.
- [47] L. Bonah, O. Zingsheim, H. S. P. Müller, J.-C. Guillemin, F. Lewen, S. Schlemmer, LLWP—A new Loomis-Wood software at the example of acetone-<sup>13</sup>C<sub>1</sub>, *J. Mol. Spectrosc.* 388 (2022) 111674. doi:10.1016/j.jms.2022.111674.
- [48] S. Thorwirth, P. Theulé, C. A. Gottlieb, H. S. P. Müller, M. C. McCarthy, P. Thaddeus, Rotational spectroscopy of S<sub>2</sub>O: Vibrational satellites, <sup>33</sup>S isotopomers, and the sub-millimeter-wave spectrum, *J. Mol. Struct.* 795 (2006) 219–229. doi:10.1016/j.molstruc.2006.02.055.
- [49] S. Thorwirth, M. A. Martin-Drumel, C. P. Endres, T. Salomon, O. Zingsheim, J. van Wijngaarden, O. Pirali, S. Gruet, F. Lewen, S. Schlemmer, M. C. McCarthy, An ASAP treatment of vibrationally excited S<sub>2</sub>O: The  $\nu_3$  mode and the  $\nu_3+\nu_2-\nu_2$  hot band, *J. Mol. Spectrosc.* 319 (2016) 47–49. doi:10.1016/j.jms.2015.12.009.
- [50] M.-A. Martin-Drumel, J. P. Porterfield, M. Goubet, P. Asselin, R. Georges, P. Soulard, M. Nava, P. B. Changala, B. Billingham, O. Pirali, M. C. McCarthy, J. H. Baraban, Synchrotron-based high resolution far-infrared spectroscopy of trans-butadiene, *J. Phys. Chem. A* 124 (2020) 2427–2435. doi:10.1021/acs.jpca.0c00623.
- [51] C. P. Endres, G. C. Mellau, M. E. Harding, M.-A. Martin-Drumel, H. Lichau, S. Thorwirth, High-resolution infrared study of vinyl acetylene: The  $\nu_{13}$  (214 cm<sup>-1</sup>) and  $\nu_{18}$  (304 cm<sup>-1</sup>) fundamentals, *J. Mol. Spectrosc.* 379 (2021) 111469. doi:10.1016/j.jms.2021.111469.
- [52] C. P. Endres, M.-A. Martin-Drumel, O. Zingsheim, L. Bonah, O. Pirali, T. Zhang, A. Sánchez-Monge, T. Möller, N. Wehres, P. Schilke, M. C. McCarthy, S. Schlemmer, P. Caselli, S. Thorwirth, SOLEIL and ALMA views on prototypical organic nitriles: C<sub>2</sub>H<sub>5</sub>CN, *J. Mol. Spectrosc.* 375 (2021) 111392. doi:10.1016/j.jms.2020.111392.
- [53] D. Herberth, K. M. T. Yamada, T. F. Giesen, The torsion–rotation spectrum of deuterated hydrogen peroxide HOOD — the first torsional state, *J. Mol. Spectrosc.* 389 (2022) 111700. doi:10.1016/j.jms.2022.111700.
- [54] K. M. Roenitz, B. M. Hays, C. R. Powers, M. N. McCabe, H. Smith, S. L. Widicus Weaver, S. T. Shipman, AC Stark effect observed in a microwave–millimeter/submillimeter wave double-resonance experiment, *J. Phys. Chem. A* 122 (2018) 6321–6327. doi:10.1021/acs.jpca.8b02116.
- [55] O. Zingsheim, L. Bonah, F. Lewen, S. Thorwirth, H. S. P. Müller, S. Schlemmer, Millimeter-millimeter-wave double-modulation double-resonance spectroscopy, *J. Mol. Spectrosc.* 381 (2021) 111519. doi:10.1016/j.jms.2021.111519.
- [56] V. N. Markov, Y. Xu, W. Jäger, Microwave-submillimeter wave double-resonance spectrometer for the investigation of van der Waals complexes, *Rev. Sci. Instrum.* 69 (1998) 4061–4067. doi:10.1063/1.1149251.
- [57] K. Suma, Y. Sumiyoshi, Y. Endo, Fourier transform microwave spectroscopy and Fourier transform microwave–millimeter wave double resonance spectroscopy of the ClOO radical, *J. Chem. Phys.* 121 (2004) 8351–8359. doi:10.1063/1.1792591.
- [58] K. Suma, W. Funato, Y. Sumiyoshi, Y. Endo, Microwave and millimeter-wave spectroscopy of the open-shell van der Waals complex Ar–HO<sub>2</sub>, *J. Chem. Phys.* 122 (2005). doi:10.1063/1.1889429.
- [59] H. Jones, J. M. Brown, Infrared-microwave double-resonance spectroscopy of the ClO<sub>2</sub> radical: A textbook example, *J. Mol. Spectrosc.* 90 (1981) 222–248. doi:10.1016/0022-2852(81)90343-x.
- [60] C. Griesinger, O. W. Sorensen, R. R. Ernst, Three-dimensional Fourier spectroscopy. Application to high-resolution NMR, *J. Magn. Reson.* 84 (1989) 14–63. doi:10.1016/0022-2364(89)90004-8.
- [61] I. Pelczer, S. Szalma, Multidimensional NMR and data processing, *Chem. Rev.* 91 (1991) 1507–1524. doi:10.1021/cr00007a012.
- [62] R. R. Ernst, Kernresonanz-Fourier-Transformations-Spektroskopie (Nobel-Vortrag), *Angew. Chem.* 104 (1992) 817–836. doi:10.1002/ange.19921040704.
- [63] M. Sattler, Heteronuclear multidimensional NMR experiments for the structure determination of proteins in solution employing pulsed field gradients, *Prog. Nucl. Magn. Reson. Spectrosc.* 34 (1999) 93–158. doi:10.1016/s0079-6565(98)00025-9.
- [64] J. Gorcester, J. H. Freed, Two-dimensional Fourier transform ESR spectroscopy, *J. Chem. Phys.* 85 (1986) 5375–5377. doi:10.1063/1.451158.
- [65] J. Gorcester, J. H. Freed, Two-dimensional Fourier transform ESR correlation spectroscopy, *J. Chem. Phys.* 88 (1988) 4678–4693. doi:10.1063/1.453782.
- [66] J. D. Hybl, A. Albrecht Ferro, D. M. Jonas, Two-dimensional Fourier transform electronic spectroscopy, *J. Chem. Phys.* 115 (2001) 6606–6622. doi:10.1063/1.1398579.
- [67] D. A. Andrews, J. G. Baker, B. G. Blundell, G. C.

- Petty, Spectroscopic applications of three-level microwave double resonance, *J. Mol. Struct.* 97 (1983) 271–283. doi:10.1016/0022-2860(83)90203-x.
- [68] W. Stahl, E. Fliege, H. Dreizler, Two-dimensional microwave Fourier transform spectroscopy, *Z. Naturforsch. Teil A* 39 (1984) 858–864. doi:10.1515/zna-1984-0906.
- [69] B. Vogelsanger, A. Bauder, Two-dimensional microwave Fourier transform spectroscopy, *J. Chem. Phys.* 92 (1990) 4101–4114. doi:10.1063/1.457770.
- [70] D. S. Wilcox, K. M. Hotopp, B. C. Dian, Two-dimensional chirped-pulse Fourier transform microwave spectroscopy, *J. Phys. Chem. A* 115 (2011) 8895–8905. doi:10.1021/jp2043202.
- [71] K. N. Crabtree, M.-A. Martin-Drumel, G. G. Brown, S. A. Gaster, T. M. Hall, M. C. McCarthy, Microwave spectral taxonomy: A semi-automated combination of chirped-pulse and cavity Fourier-transform microwave spectroscopy, *J. Chem. Phys.* 144 (2016). doi:10.1063/1.4944072.
- [72] M.-A. Martin-Drumel, M. C. McCarthy, D. Patterson, B. A. McGuire, K. N. Crabtree, Automated microwave double resonance spectroscopy: A tool to identify and characterize chemical compounds, *J. Chem. Phys.* 144 (2016). doi:10.1063/1.4944089.
- [73] S. Herbers, O. Zingsheim, H. V. L. Nguyen, L. Bonah, B. Heyne, N. Wehres, S. Schlemmer, Internal rotation arena: Program performances on the low barrier problem of 4-methylacetophenone, *J. Chem. Phys.* 155 (2021). doi:10.1063/5.0070298.
- [74] O. Zingsheim, H. S. P. Müller, L. Bonah, F. Lewen, S. Thorwirth, S. Schlemmer, (Sub-)millimeter-wave spectroscopy of gauche-propanal, *J. Mol. Spectrosc.* 384 (2022) 111565. doi:10.1016/j.jms.2021.111565.
- [75] O. Zingsheim, J. Maßen, H. S. P. Müller, B. Heyne, M. Fatima, L. Bonah, A. Belloche, F. Lewen, S. Schlemmer, Rotational spectroscopy of *n*-propanol: *aa* and *ag* conformers, *Astron. Astrophys.* 662 (2022) A111. doi:10.1051/0004-6361/202243571.
- [76] S. H. Autler, C. H. Townes, Stark effect in rapidly varying fields, *Phys. Rev.* 100 (1955) 703–722. doi:10.1103/physrev.100.703.
- [77] C. Cohen-Tannoudji, J. Dupont-Roc, G. Grynberg, *The Dressed Atom Approach*, John Wiley & Sons, Ltd, 2008, Ch. 6, pp. 407–514. doi:10.1002/9783527617197.ch6.
- [78] D. Christen, L. H. Coudert, R. D. Suenram, F. J. Lovas, The rotational/concerted torsional spectrum of the *g'Ga* conformer of ethylene glycol, *J. Mol. Spectrosc.* 172 (1995) 57–77. doi:10.1006/jmsp.1995.1155.
- [79] D. Christen, L. H. Coudert, J. A. Larsson, D. Cremer, The rotational-torsional spectrum of the *g'Gg* conformer of ethylene glycol: Elucidation of an unusual tunneling path, *J. Mol. Spectrosc.* 205 (2001) 185–196. doi:10.1006/jmsp.2000.8263.
- [80] S. Twagirayezu, T. N. Clasp, D. S. Perry, J. L. Neill, M. T. Muckle, B. H. Pate, Vibrational coupling pathways in methanol as revealed by coherence-converted population transfer Fourier transform microwave infrared double-resonance spectroscopy, *J. Phys. Chem. A* 114 (2010) 6818–6828. doi:10.1021/jp1019735.
- [81] D. Schmitz, V. A. Shubert, D. Patterson, A. Krin, M. Schnell, Phase dependence of double-resonance experiments in rotational spectroscopy, *J. Phys. Chem. Lett.* 6 (2015) 1493–1498. doi:10.1021/acs.jpcllett.5b00494.
- [82] E. T. Jaynes, F. W. Cummings, Comparison of quantum and semiclassical radiation theories with application to the beam maser, *Proc. IEEE* 51 (1963) 89–109. doi:10.1109/proc.1963.1664.
- [83] B. T. Darling, D. M. Dennison, The water vapor molecule, *Phys. Rev.* 57 (1940) 128–139. doi:10.1103/physrev.57.128.
- [84] A. R. Hoy, High order Coriolis interactions in NO<sub>2</sub>, *J. Mol. Spectrosc.* 86 (1981) 55–64. doi:10.1016/0022-2852(81)90105-3.
- [85] E. S. Ebers, H. H. Nielsen, Two bands in the infrared spectrum of formaldehyde, *J. Chem. Phys.* 5 (1937) 822–827. doi:10.1063/1.1749947.
- [86] H. A. Jahn, Note on Coriolis Coupling Terms in Polyatomic Molecules, *Phys. Rev.* 56 (1939) 680–683. doi:10.1103/physrev.56.680.
- [87] E. Fermi, Über den Ramaneffekt des Kohlendioxyds, *Z. Phys.* 71 (1931) 250–259. doi:10.1007/bf01341712.
- [88] L. Bonah, S. Schlemmer, J.-C. Guillemin, M. E. Harding, S. Thorwirth, On the spectroscopy of phosphalkynes: Millimeter- and submillimeter-wave study of C<sub>2</sub>H<sub>5</sub>CP, *J. Phys. Chem. A* 128 (2024) 4859–4866. doi:10.1021/acs.jpca.4c02566.
- [89] H. M. Pickett, The fitting and prediction of vibration-rotation spectra with spin interactions, *J. Mol. Spectrosc.* 148 (1991) 371–377. doi:10.1016/0022-2852(91)90393-o.

# 6. A new Loomis-Wood Software at the Example of Acetone- $^{13}\text{C}_1$

## Bibliographic Information

L. Bonah, O. Zingsheim, H. S. P. Müller, J.-C. Guillemin, F. Lewen, S. Schlemmer, LLWP–A new Loomis-Wood software at the example of Acetone- $^{13}\text{C}_1$ , *J. Mol. Spectrosc.* 388 (2022) 111674. doi:10.1016/j.jms.2022.111674.

## Author's contribution

The author of this thesis performed the measurements together with the second author. Furthermore, he performed the analysis, developed the software, wrote the original draft and provided the visualization.

## Context

This study analyzes the rotational spectrum of acetone- $^{13}\text{C}_1$  ( $^{13}\text{CH}_3\text{C}(\text{O})\text{CH}_3$ ), a COM with two internal rotors that has already been tentatively detected in space.<sup>42</sup> Over 1 THz of high-resolution broadband spectra were measured with an isotopically enriched sample. LWPs in the newly developed LLWP software were used to follow the characteristic trident pattern (intensity distribution of 1:2:1) resulting from the two internal rotors. The efficiency and reliability of LWPs is demonstrated by the high number of assigned transitions and the quality of the resulting model.

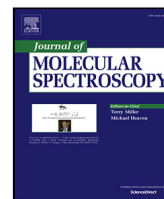
## Copyright Notice

Reprinted with permission from *J. Mol. Spectrosc.* 2022, **388**, 111674. © 2022 Elsevier.



Contents lists available at ScienceDirect

## Journal of Molecular Spectroscopy

journal homepage: [www.elsevier.com/locate/jmmsp](http://www.elsevier.com/locate/jmmsp)LLWP—A new Loomis-Wood software at the example of Acetone- $^{13}\text{C}_1$ Luis Bonah<sup>a,\*</sup>, Oliver Zingsheim<sup>a</sup>, Holger S.P. Müller<sup>a</sup>, Jean-Claude Guillemin<sup>b</sup>, Frank Lewen<sup>a</sup>, Stephan Schlemmer<sup>a</sup><sup>a</sup> I. Physikalisches Institut, Universität zu Köln, Zùlpicher Str. 77, Köln, 50937, Germany<sup>b</sup> Univ Rennes, Ecole Nationale Supérieure de Chimie de Rennes, ISCR-UMR 6226, Rennes, 35000, France

## ARTICLE INFO

## Keywords:

Acetone- $^{13}\text{C}_1$ 

Software

Rotational spectroscopy

Loomis-Wood plots

## ABSTRACT

Acetone- $^{13}\text{C}_1$  is a complex organic molecule with two internal methyl ( $-\text{CH}_3$ ) rotors having relatively low effective barriers to internal rotation of about  $249\text{ cm}^{-1}$ . This leads to two low-lying torsional modes and five internal rotation components resulting in a dense and complicated spectrum. In this study, measurements of acetone- $^{13}\text{C}_1$  were performed with an isotopically enriched sample in the frequency range 37–1102 GHz. Predicted spectra of acetone- $^{13}\text{C}_1$  created with ERHAM allow for future radio astronomical searches.

Loomis-Wood plots are one approach to improve and fasten the analysis of such crowded spectra. In this study, the new Loomis-Wood software LLWP was used for fast and confident assignments. LLWP focuses on being user-friendly, intuitive, and applicable to a broad range of assignment tasks. The software is presented here and can be downloaded from [llwp.astro.uni-koeln.de](http://llwp.astro.uni-koeln.de).

## 1. Introduction

Acetone was first detected in Sgr B2(N) by Combes et al. [1] and later confirmed by Snyder et al. [2]. In the laboratory, first lines up to 31 GHz were found by Bak et al. [3] and Weatherly and Williams [4]. Swalen and Costain presented a structural study based on microwave spectroscopy [5]. Several subsequent studies investigated the spectrum of acetone, its isotopologs, and vibrationally excited states of the main isotopolog [6–15].

For the asymmetric  $^{13}\text{C}_1$  isotopolog ( $^{13}\text{CH}_3\text{C}(\text{O})\text{CH}_3$ ), an initial analysis was presented by Lovas and Groner [12] consisting of 55 transitions up to 25 GHz. Their results were extended by Ordu et al. [15] to 110 transitions up to 355 GHz. The low number of assigned transitions in Ref. [15], compared to 9715 assigned transitions for an enriched sample of the symmetric  $\text{CH}_3^{13}\text{C}(\text{O})\text{CH}_3$  isotopolog in the same study, resulted from the lack of an enriched sample of the asymmetric species. We revisited the spectrum with an enriched sample to circumvent difficulties tied to the low 2.2% natural abundance of acetone- $^{13}\text{C}_1$  (see Fig. 1).

Acetone- $^{13}\text{C}_1$  has two inequivalent internal methyl ( $-\text{CH}_3$ ) rotors with relatively low effective barriers to internal rotation. A value of  $249.232\text{ cm}^{-1}$  was derived for the parent species<sup>1</sup> [14]. In comparison to the main isotopolog, one methyl  $^{12}\text{C}$  atom is substituted by a  $^{13}\text{C}$  atom. The coupling of the two distinguishable internal rotors with the overall rotation results in five internal rotation components labeled (following

the nomenclature of Ref. [12]) as (0,0), (0,1), (1,0), (1,1), and (1,2) which will be introduced in more detail later.

The internal rotation components and two energetically low-lying torsional modes lead to a dense and complicated spectrum. Similar conditions can be found for many other complex molecules, with isotopologs, hyperfine structure, and other interactions being additional factors for a complex and line-rich spectrum. Analyzing spectra close to the confusion limit, i.e., assigning lines unambiguously, proves to be cumbersome with conventional methods. Approaches to accommodate this challenge include on the software side e.g., Loomis-Wood plots (LWPs) [16], Fortrat diagrams, and for infrared data the Automated Spectral Assignment Procedure [17] as well as on the experimental side e.g., double-resonance spectroscopy [18,19] and its advancement the double-modulation double-resonance spectroscopy [20].

LWPs display adjacent transitions of a series on top of each other. This makes it easy to follow series and identify deviations by using adjacent transitions as reference. This results in more confident and efficient assignments. Several programs using this approach exist in the literature, with Pgopher [21], the AABS package [22], and LWW [23] being three popular options. These programs are valuable tools, but unfortunately, they either lack different methods to determine center frequencies, use of experimental spectrum instead of peak lists, easy setup, support for multiple operating systems, documentation, or combinations of these. In addition, the advancement in graphical

\* Corresponding author.

E-mail address: [bonah@ph1.uni-koeln.de](mailto:bonah@ph1.uni-koeln.de) (L. Bonah).<sup>1</sup> Variations for Acetone- $^{13}\text{C}_1$  are assumed to be negligible.

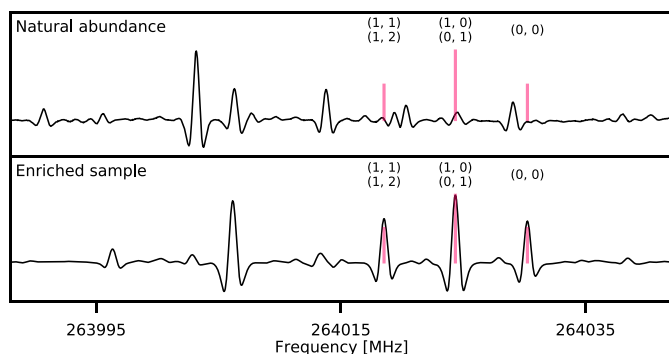


Fig. 1. Spectrum and predictions (red sticks) of acetone- $^{13}\text{C}_1$  at natural abundance (2.2%, top) and for the enriched sample (98%, bottom). The internal rotation components of the oblate paired transitions  $27_{0,27} \leftarrow 26_{1,26}$  and  $27_{1,27} \leftarrow 26_{0,26}$  are shown. For the enriched sample, the typical triplet pattern is clearly visible whereas at natural abundance all three peaks are blended and the pattern is not visible.

user interface (GUI) libraries and computational power of personal computers alleviates some of the restrictions that previous generations of programs faced.

Here LLWP is presented, a newly written Loomis-Wood plotting software for fast and confident assignment of real spectra. It focuses on being intuitive and user-friendly while being proficient for a wide range of assignment tasks. The analysis of the dense and complicated spectrum of acetone- $^{13}\text{C}_1$  benefited immensely from the use of LLWP.

First, the experimental details are described (Section 2), next the newly developed LLWP program is presented (Section 3), then the analysis of spectra of acetone- $^{13}\text{C}_1$  is explained (Section 4), and finally the results are discussed and an outlook is given (Section 5).

## 2. Experimental details

Measurements were performed with a synthesized sample of acetone- $^{13}\text{C}_1$ . High-resolution broadband spectra were measured in the frequency ranges 37–67 GHz, 70–129 GHz, and 167–1102 GHz using different experiments in Cologne, resulting in a total broadband coverage of 1024 GHz. First, the synthesis is described (Section 2.1) then the different experimental setups are presented (Section 2.2).

### 2.1. Synthesis of Acetone- $^{13}\text{C}_1$

The sample was synthesized using a procedure described by Winkel et al. [24]. In a 50 mL round-bottomed flask equipped with a reflux condenser, a dropping funnel and a nitrogen inlet were introduced magnesium turnings (0.4 g, 16.8 mmol, 1.2 equiv.) and 15 ml of diethyl ether.  $^{13}\text{C}$ -methyl iodide (2.0 g, 14 mmol, 1 equiv.) diluted in 10 ml of diethyl ether was added dropwise at such a rate that a gentle reflux was maintained. The mixture was refluxed for 10 min and then cooled at  $-10^\circ\text{C}$ . Freshly distilled acetaldehyde (0.74 g; 16.8 mmol; 1.2 equiv.) was slowly added, to give a white slurry and the mixture was stirred at room temperature for 30 min. The ether was evaporated and 5 ml of water were carefully added. Hydrochloric acid (6N) was added until pH 6. The low boiling point compounds containing 2-propanol and water were distilled in vacuo (0.1 mbar) and then slowly added to a cold solution of sodium bichromate dihydrate (5.4 g, 18 mmol, 1.3 equiv.) and sulfuric acid at 96% (2.1 g) in 3 ml of water. The temperature should not exceed  $50^\circ\text{C}$ . After 10 min at room temperature, the acetone was purified by distillation in a vacuum line equipped with two U-traps. The first immersed in a cold bath at  $-60^\circ\text{C}$  removed the high boiling point compounds and the second immersed in a liquid nitrogen bath selectively trapped the acetone. This procedure yielded 0.74 g (90% yield) with 98% enrichment of acetone- $^{13}\text{C}_1$ .

### 2.2. Experimental setups

Broadband measurements of the synthesized acetone- $^{13}\text{C}_1$  sample were performed using three different experimental setups in Cologne [15,25]. Additionally, single measurements with longer integration times were performed in frequency ranges with low source output power.<sup>2</sup> Especially the frequency range 37–67 GHz was important as in this low-frequency range the five internal rotation components are often resolved. All experiments share a general structure, consisting of a source, an absorption cell, and a detector [15,25]. Horn antennas, lenses, and mirrors are used to guide the beam through the absorption cells and onto the detector. The absorption cells are made out of borosilicate glass. They are connected with a pump for evacuating the cell and with an inlet for the sample. Different detector techniques, being Schottky detectors (<500 GHz) and a cryogenically cooled bolometer (>500 GHz), were used to optimize the SNR. Lock-in amplifiers with a  $2f$ -demodulation scheme were used. As a result, lineshapes look similar to the second derivative of a Voigt profile. All measurements were performed at room temperature and with gas pressures around 10  $\mu\text{bar}$ .

For 37–67 GHz, the signal is guided directly to the antenna and not multiplied, for 70–129 GHz a tripler is used. For both frequency ranges, Schottky detectors are employed and connected to an in-house made bias box. The absorption cell consists of two 7 m glass cells in single-pass mode adding up to a total absorption path length of 14 m. The experimental setup is described in greater detail in Ref. [15].

The frequency range 167–515 GHz was covered with a commercially available source from Virginia Diodes Inc. (VDI) with three different setups consisting of cascaded doublers and triplers. As in the previous experiment, Schottky detectors were utilized. The absorption cell of 5 m length was used in double-pass mode resulting in a total absorption path length of 10 m. More detailed information can be found in Refs. [15,25].

The frequency range 500–1100 GHz was measured with two different setups of cascaded multipliers (VDI) and a QMC QNbB/PTC(2+XBI) hot-electron bolometer. A single 5 m cell was used in single-pass mode.

Standing waves were removed from the spectra by Fourier filtering using a self-written script.<sup>3</sup>

## 3. The LLWP program

LLWP is presented, a newly developed software based on LWPs for exploring and assigning spectra. It aims to be efficient, easy to handle, and in particular user-friendly. Additionally, LLWP offers great customizability and flexibility. Distinguishing factors from previous programs [21–23] are the use of real spectra instead of peak lists, and most importantly the simple setup and the improved user experience that is tied to the advancement in graphical user interface (GUI) libraries. The software, its documentation, and contact information for feedback as well as feature requests can be found on LLWP's website.<sup>4</sup>

First, the technical details are summarized (Section 3.1), then the core functionality is described in some detail to highlight the main advantages for potential users (Section 3.2), and last a selection of additional features that support a thorough analysis are introduced to highlight the variety of tools provided by LLWP (Section 3.3).

<sup>2</sup> Transitions were ordered by the predicted intensity and the top 98 transitions in the frequency range 750–790 GHz as well as the top 1008 transitions in the frequency range 37–67 GHz were measured.

<sup>3</sup> Download at <https://github.com/Ltotheois/SnippetsForSpectroscopy/tree/main/FFTCorrection>

<sup>4</sup> Visit <https://llwp.astro.uni-koeln.de/>

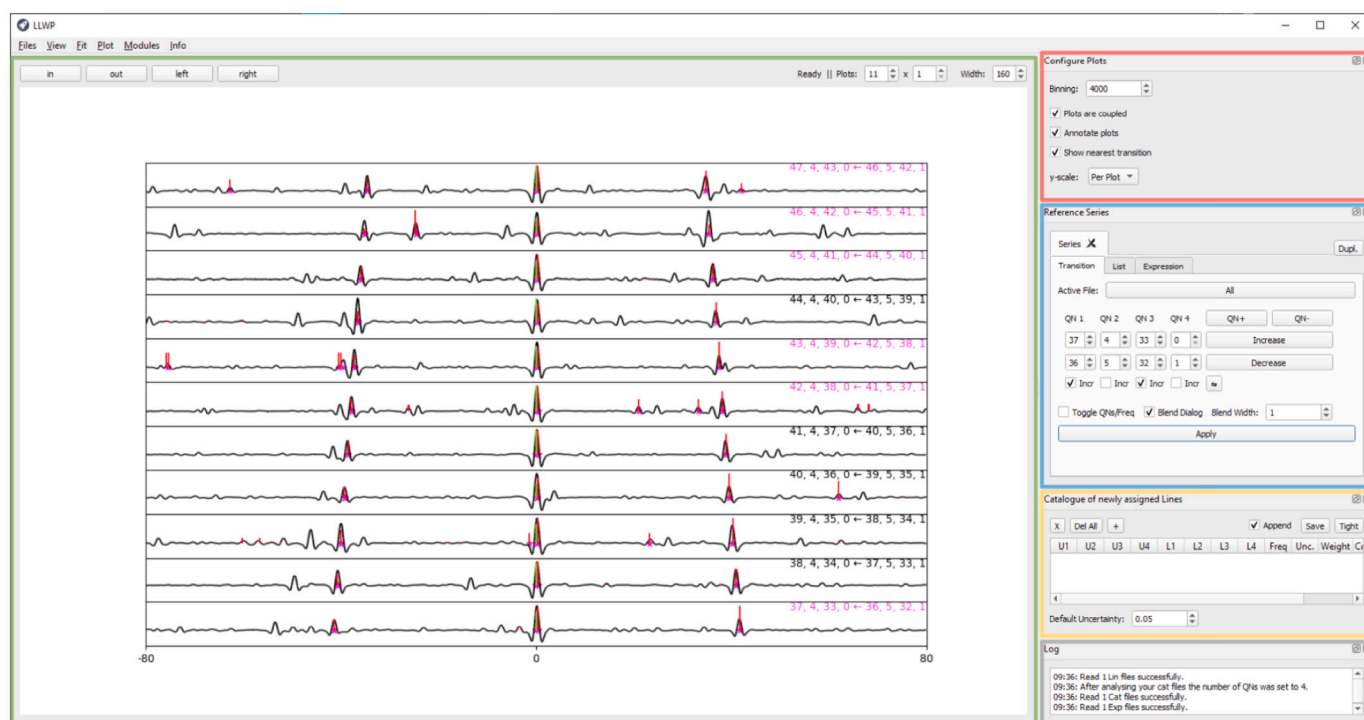


**Fig. 2.** The GUI of the newly developed LLWP program. The five areas of the main window are highlighted by colored rectangles. The Loomis-Wood plot window (green rectangle) shows the experimental spectrum (black lines), the predictions (red sticks), and the reference series (pink sticks). Already assigned transitions are indicated by pink stars and pink-colored transitions (top right corner of the respective subplot). To the right of the LWP are the **Configure Plots** window (red rectangle) for options regarding the LWP, the **Reference Series** window (blue rectangle) which specifies the center positions of the LWP, the **Catalogue of newly assigned Lines** (yellow rectangle) showing the assigned lines, and the **Log** window (gray rectangle) for messages, warnings, and errors. See the text for more information.

### 3.1. Technical details

LLWP is written in Python 3. Therefore it runs on all operating systems that support Python 3 and the required libraries. For good performance, Pandas [26] and NumPy [27] are used for data handling as they are written in C/C++. The GUI uses PyQt5 and the fitting uses SciPy [28]. Plots are created with Matplotlib [29]. For the handling of Pickett's *\*.cat*, *\*.lin*, and *\*.egy* formats [30] our own Pyckett library was used.<sup>5</sup> In addition to the Python code, a Windows executable is provided on the website, making installation on Windows machines as simple as downloading a single file.

Certain tasks that are either computationally or I/O intensive are threaded to not block the user interface resulting in a responsive experience. To keep performant with large datasets, each subplot plots only its currently visible data.<sup>6</sup> Additionally, even these subsets are downsampled if they exceed a user-selectable value.

### 3.2. Core functionality

LLWP's core functionality is assigning center frequencies from a real spectrum to quantum numbers of predicted transitions. LLWP

<sup>5</sup> See <https://pypi.org/project/pyckett/> or install with pip via `pip install pyckett`

<sup>6</sup> The important step is to reduce the complete dataset to only the visible dataset before handing it to the plot function of the used library. For typical use cases, this drastically decreases computation time and memory consumption. However, for the user, apart from the mentioned performance benefits, there is no tangible difference between plotting all data but only showing an excerpt and only plotting the data in the excerpt

relies on Loomis-Wood plots for increased confidence and speed. The LWP consists of multiple subplots arranged in a vertical fashion. Each subplot shows a region of the spectrum with the same width around its predicted center frequency. The series of predicted center frequencies of all subplots is called reference series. The easiest example would be a linear rotor which usually shows only small deviations from equidistantly spaced transitions with a distance of  $2B$ . When using these ideal frequencies as the reference series, the LWP shows the deviations of the real transitions from this idealized model. The trend in the LWP makes it easy to identify and follow the series and the row number corresponds to the  $J$  quantum number of the upper state and makes assignment straightforward. The software is not opinionated, meaning it is not limited to specific units or formats and works with 1–6 quantum numbers (or even no quantum numbers at all). Additionally, LLWP can display multiple Loomis-Wood plots next to each other (see Fig. A.1). Possible use cases are infrared data, e.g., examining  $P$ -,  $Q$ -, and  $R$ -branch series simultaneously, heavily perturbed systems, e.g., showing interaction partners side by side, or even as simple cases as comparing predictions from two different methods. On the other extreme, LLWP can be used with only a single row and column to explore and assign spectra in a single plot, basically neglecting the Loomis-Wood character. In summary, LLWP is a versatile tool for fast and confident assignments.

In the following, the most basic workflow is described, consisting of (I) loading data, (II) setting the reference series, (III) assigning, and (IV) saving the results.<sup>7</sup> Simultaneously, the five areas of the main window (see Fig. 2) are introduced.

<sup>7</sup> This basic workflow is presented in video format at <https://llwp.astro.uni-koeln.de/videos/QuickGuide.mp4>.

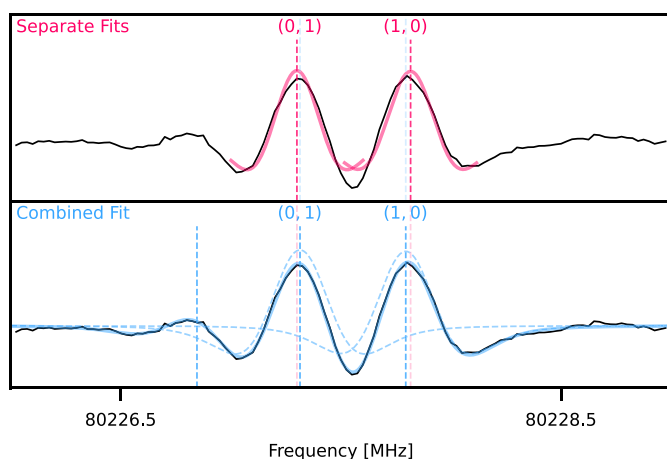


**Fig. 3.** Example of the combined fit performed by the blended lines module (bottom in blue) in comparison with separate fits for each peak (top in red). The visible transitions are the  $7_{2,6} \leftarrow 6_{1,5}$  transitions for the (0,1) and (1,0) internal rotation components. For the combined fit, an additional unknown peak at a lower frequency was included and the widths of the three peaks were coupled together. The center frequencies for each fit are indicated by dotted lines in the corresponding color and for the combined fit, the two components of interest are shown as dotted profiles. The center frequencies of the separate fit deviate by about 20 kHz, emphasizing the advantage of a combined fit. For the analysis of acetone it was fundamental to accurately determine the splitting between (0,1) and (1,0) as well as between (1,1) and (1,2). However, even at low frequencies, these transitions overlap partly making a combined fit indispensable.

(I) The first step is to load data into the program. Three different types of data can be used in the program: (i) files providing the experimental measurements, (ii) files providing predictions, and (iii) files providing already assigned lines. All three data types can be added via the *Files* menu or per drag-and-drop. After this step, the **Loomis-Wood plot** (green rectangle in Fig. 2) shows a default series. Important controls for the LWP are available on top, controlling the number of rows and columns as well as the width of the subplots.

(II) In the second step, a user-defined reference series is selected in the **Reference Series** window (blue rectangle in Fig. 2). Three options are available for specifying the center frequencies of the series, either by (i) using catalog files and selecting a series, (ii) via a list of frequencies, or (iii) by entering a custom equation depending on  $N$  (index of the subplot) and  $N_0$  (offset index). For the catalog files, Pickett's *\*.cat* format is supported by default but all fixed-width-formats (FWF) can be used.

(III) Next, transitions of the reference series are assigned by selecting an area around the peak and the selected profile is fit to the selected data. Currently available line profiles are a Gaussian, Lorentzian, and Voigt profile as well as their first and second derivatives. Additionally, a polynomial with a selectable rank, a procedure testing polynomials with different ranks and using the best one, or a center-of-mass procedure adapted from Pgoopher [21] are available. The determined center frequency and, if a catalog file is used, also the quantum numbers are added to the **Catalog of newly assigned Lines** window (yellow rectangle in Fig. 2). Additionally, the uncertainty is set as (i) a user-defined default value, (ii) the absolute value of obs-calc, (iii) user input to a dialog, or (iv) the uncertainty from the fitting routine.<sup>8</sup> In the **Catalog of newly assigned Lines** window, the assignments can be edited or deleted. Already assigned lines are highlighted in the program to reduce confusion and prevent the user from unintentionally assigning

the same line multiple times. Steps (II) and (III) can be repeated for any desired reference series.

(IV) When all targeted transitions are assigned, they are saved to a file, with Pickett's *\*.lin* format as the default format but all FWFs are available.

Additionally, the **Configure Plots** window (red rectangle in Fig. 2) provides further options for the appearance of the plot, with the most important being the scale of the LWP. Either (i) each plot is scaled individually, (ii) all plots are scaled by the minimum and maximum of the whole spectrum, or (iii) the user can set a custom scale. For (i) the predictions are also scaled individually whereas for (ii) and (iii) the predictions are scaled relative to the experimental spectrum. Furthermore, the **Log** window (gray rectangle in Fig. 2) shows messages, warnings, and errors.

For convenience, all options can be set as default and the references to all currently opened files can be saved into a project eliminating the need of reloading all files individually.

### 3.3. Additional features

Several modules extend LLWP's core functionality. Here, selected modules for an extended analysis, being the (i) blended lines module, (ii) seriesfinder module, (iii) peakfinder module, and (iv) residuals module, are presented with a short example of their respective use. For more information on the modules visit the online documentation.

(i) A major inconvenience for the assignment process are blended lines, as they make it complicated to determine precise center frequencies. Many programs (e.g., ERHAM [31,32] and SPFIT [30]) have built-in mechanisms to deal with blended lines. For these cases, LLWP provides the ability to assign all blended lines to the center frequency of the blend and give each line its respective weight. If this feature is activated and other predicted transitions are within a user-defined distance of the assigned transition, a dialogue window opens and the close-by transitions that should be assigned to the same blend can be selected. On the other hand, partly blended lines can be resolved with the **blended lines module**. It allows to fit multiple peaks simultaneously and thereby determine an individual center frequency for each transition. The widths of the peaks can be independent or coupled (e.g., if all peaks are from the same molecule and measurement and therefore are expected to have the same linewidth). Additionally, a baseline can be subtracted in the form of a polynomial. In the majority of cases, this results in more accurate center frequencies of partly blended transitions, see Fig. 3.

(ii) The **seriesfinder module** allows to filter the predictions and display them ordered by intensity. Predefined filters are present for the transition type, the frequency range, and to hide already assigned predictions. One major use case is finding the strongest predicted, but so far unassigned transitions in the frequency range of the experiment. For convenience, the transitions can be chosen as the reference series of the Loomis-Wood plot with a single click.

(iii) The **peakfinder module** finds peaks in the real spectrum. The peaks are shown in the spectrum and can be saved to a *\*.csv* file. In addition, the peaks can be limited to so far unassigned peaks by providing a distance that peaks have to deviate from assigned transitions. This allows to find the experimentally strongest, but yet unassigned peaks.

(iv) Assigned transitions can be compared with predicted transitions in the **residuals module**. By default, the residuals  $\nu_{\text{Obs}} - \nu_{\text{Calc}}$  are shown against  $\nu_{\text{Obs}}$  (see Fig. A.3). The residuals allow to assess the performance of the model and visually detect deviation patterns. However, the x- and y-axis quantities can be chosen freely. Therefore, a multitude of different plots can be created by the user, e.g., quantum number coverage plots (see Fig. A.2) or weighted residuals (see Fig. A.4). For greater control, the transitions can be filtered and subgroups can be colored to highlight them in the plot.

<sup>8</sup> Not all fitting routines support this option. Use with caution.

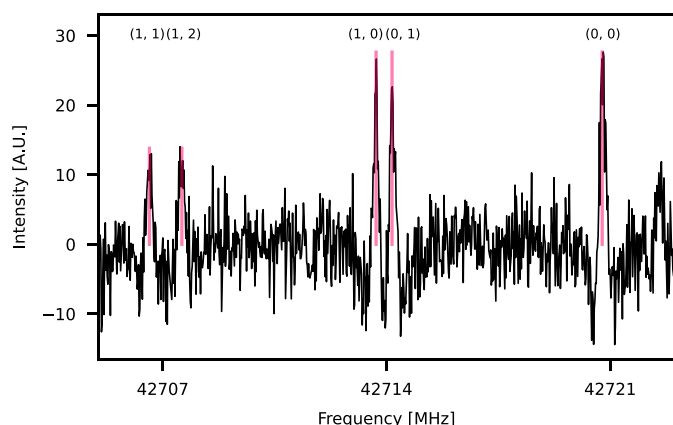


Fig. 4. Acetone- $^{13}\text{C}_1$  spectrum and predictions (red sticks) with resolved symmetry states. The  $4_{0,4} \leftarrow 3_{1,3}$  transition is split into its five internal rotation components (1, 1), (1, 2), (1, 0), (0, 1), and (0, 0) with an intensity ratio of 1:1:2:2:2.

To summarize, the modules complement the program's core capabilities and focus on more specific tasks.

#### 4. Spectroscopic fingerprint of acetone

Acetone- $^{13}\text{C}_1$  ( $^{13}\text{CH}_3\text{C}(\text{O})\text{CH}_3$ ) is an asymmetric rotor with  $\kappa = (2B - A - C)/(A - C) = 0.3150$ , meaning acetone is an oblate rotor but far from the symmetric limit of +1. The only nonzero dipole moment component of the main isotopolog is along the  $b$ -inertial axis with a value of  $2.93(3)\text{D}^9$  [7]. This results in a strong  $b$ -type spectrum with the selection rules  $\Delta J = 0, \pm 1$  and  $\Delta K_a = \pm 1, (\pm 3, \dots)$  and  $\Delta K_c = \pm 1, (\pm 3, \dots)$ .

The two distinguishable internal methyl rotors lead to five internal rotation components which are labeled as  $(\sigma_1, \sigma_2)$  with  $\sigma_1$  and  $\sigma_2$  being the symmetry numbers. The nomenclature is adapted from Lovas and Groner [12], see their work for more information.

The five components are (0, 0), (0, 1), (1, 0), (1, 1), and (1, 2). For transitions with low frequencies, often all five internal rotation components are resolved with an intensity ratio of 1:1:2:2:2 (see Fig. 4). Single measurements of such resolved transitions were essential to accurately determine the energy tunneling parameters  $\epsilon$  of the ERHAM model [31, 32]. For transitions with high quantum numbers, the internal rotation components (0, 1) and (1, 0) as well as (1, 1) and (1, 2) become degenerate, resulting in a typical triplet pattern with an intensity ratio of  $(1+1):(2+2):2 = 1:2:1$  (see LWP of Fig. 2).

First assignments were straightforward due to the characteristic patterns and previous literature work [12,15]. An iterative fitting procedure was used. In each cycle, the model was updated and new improved predictions were calculated, which led to more assignments. Assigning with LLWP was confident and efficient as multiple trends were visible in the LWPs. The two most used trends were systematic deviation patterns ( $\nu_{\text{obs}} - \nu_{\text{calc}}$ ) for adjacent rows and trends in typical patterns (see e.g., the typical triplet pattern becoming narrower with increasing frequency in Fig. 2). These trends allowed to confidently assign transitions, even if they showed strong deviations from the initial predictions.

<sup>9</sup> Acetone- $^{13}\text{C}_1$  is expected to have a small non-zero  $a$ -type dipole moment due to the  $^{13}\text{C}$ -atom. Thus, also  $a$ -type transitions are allowed. However, the  $a$ -type dipole moment is negligibly small in comparison to the  $b$ -type dipole moment. Therefore,  $a$ -type transitions were neglected in the analysis.

All literature transitions in the here measured frequency range were reassigned, especially as the transitions from Ordu et al. [15] for the  $^{13}\text{C}_1$ -acetone isotopolog were misassigned above 200 GHz. For lower frequency areas that were not measured here, literature data were used consisting of 55 transitions in the frequency range 10–25 GHz [12]. Together with the here assigned lines, this resulted in a total of 16 208 transitions with due to blends 8958 unique line frequencies, see Table A.1 for the transition type coverage. Fits and predictions were performed with a modified version of ERHAM [31,32]. Due to the size of the dataset, multiple array sizes were increased from the version available on the PROSPE webpage,<sup>10</sup> e.g., the maximum of transitions was increased from 8191 to 16 383, the number of tunneling parameters per state was increased from 37 to 199 and the number of predicted lines was increased from 50 000 to 1 000 000.

An inconvenience for the assignment process was label switching [33–35], which occurred especially for high  $J$  values. This behavior is described in ERHAM's manual and appears due to oblate paired transitions being degenerate. A random phase is introduced to nonetheless diagonalize the matrix which randomly spreads the intensity between two allowed  $b$ -type transitions and two forbidden  $a$ -type transitions. The  $a$ -type transitions were filtered out before fitting the assigned lines. However, the randomly spread intensity can influence the center frequency of blends because LLWP automatically sets the weight according to the intensity from the \*.cat file. This was corrected by manually setting the weights of affected transitions. Another complication arose due to transitions affected by label switching changing between different fits. Thus, certain transitions were not assigned in otherwise assigned series (see unassigned transitions in Fig. 2). Additionally, specific lines were excluded from the fit due to either poor signal-to-noise ratio or being inseparably blended with unknown transitions. However, the great majority of blends could be treated with LLWP's blended lines module (see Fig. 3 and Section 3.3) or ERHAM's blend functionality.

Due to the high number of assignments, the uncertainties were assigned automatically. A single second derivative Voigt profile was fit to the experimental spectrum for each assignment. The mean deviation between the experimental and simulated lineshape was calculated via the root mean square (RMS). To normalize the deviation, this value was divided by the amplitude  $A$  resulting in<sup>11</sup>

$$RMS/A = \frac{1}{A} \sqrt{\frac{\sum_i (I_{\text{exp},i} - I_{\text{fit},i})^2}{N}} \quad (1)$$

$I_{\text{exp},i}$  and  $I_{\text{fit},i}$  are the intensities at frequency  $i$  of the experimental lineshape and fit function respectively,  $N$  is the number of frequencies  $i$  in the fit range, and  $A$  the amplitude of the fit function. This resulted in a quantity, which incorporates the SNR, the asymmetry of the line, and possible blends – all being aspects that are taken into account when assigning uncertainties manually. The calculated  $RMS/A$  value was used to group the transitions into three classes with uncertainties of 30 kHz, 50 kHz, and 70 kHz.

Different approaches were tested for the fit. First, a fit was created step-by-step with a script that added in every cycle the next best parameter to the fit. However, a better result was obtained by adding whole sets of parameters at once and afterward removing parameters with high relative uncertainties.

Up to 500 GHz, fitting was straightforward. The previous step-by-step fit up to 500 GHz was used to get an approximation for which orders of parameters were needed. Except for fundamental parameters,<sup>12</sup> all other parameters were given an initial value of zero. Different sets of interaction parameters were tested. The resulting fit includes 8125 transitions (5819 unique lines) with the covered quantum numbers

<sup>10</sup> Visit <http://www.ifpan.edu.pl/~kisiel/prospe.htm>

<sup>11</sup> A direct implementation in LLWP is planned for the future.

<sup>12</sup> For both fits  $\alpha_1$  and  $\alpha_2$  were fixed to zero while  $\rho_1, \rho_2, \beta_1, \beta_2, A, B, C, \epsilon_{01}$  and  $\epsilon_{10}$  had sensible initial values from previous fits.

**Table 1**  
Molecular parameters for the ground state of  $^{13}\text{CH}_3\text{C}(\text{O})\text{CH}_3$  up to 500 GHz.

Parameter		Rotor 1	Rotor 2
$\rho_1$		0.059 925 9(97)	0.061 394(20)
$\beta_1$	/°	29.3671(35)	21.1451(93)
$A$	/MHz	10 083.034 62(12)	
$B$	/MHz	8277.507 38(10)	
$C$	/MHz	4811.469 122(77)	
$\Delta_K$	/kHz	9.430 44(76)	
$\Delta_{JK}$	/kHz	-2.739 03(43)	
$\Delta_J$	/kHz	4.585 14(10)	
$\delta_K$	/kHz	-0.346 59(24)	
$\delta_J$	/kHz	1.915 380(46)	
$\Phi_K$	/Hz	0.0324(10)	
$\Phi_{KJ}$	/Hz	0.0315(1)	
$\Phi_{JK}$	/Hz	-0.027 32(36)	
$\Phi_J$	/Hz	0.005 127(51)	
$\phi_K$	/Hz	-0.075 04(35)	
$\phi_{JK}$	/Hz	0.035 41(19)	
$\phi_J$	/Hz	0.002 596(25)	
$\epsilon_{11}$	/MHz	1.0306(75)	
$\epsilon_{1-1}$	/MHz	0.0944(13)	
$\epsilon_{10}$	/MHz	-758.019(36)	-763.230(32)
$\epsilon_{20}$	/MHz	0.7627(26)	0.7721(23)
$[A - (B + C)/2]_{10}$	/MHz	0.031 97(49)	0.037 11(62)
$[(B + C)/2]_{10}$	/kHz	3.37(25)	-3.68(43)
$[(B - C)/4]_{10}$	/kHz	9.01(13)	5.12(22)
$[-\Delta_K]_{10}$	/kHz	0.024 31(36)	0.013 49(34)
$[-\Delta_{JK}]_{10}$	/kHz	-0.025 76(37)	-0.015 84(36)
$[-\Delta_J]_{10}$	/Hz	1.66(12)	2.24(13)
$[-\delta_{KJ}]_{10}$	/kHz	-0.018 20(11)	-0.011 76(10)
$[-\delta_{JK}]_{10}$	/Hz	0.782(62)	1.272(65)
$[B_{001}^-]_{10}$	/MHz	-0.3298(54)	-0.3140(88)
$[B_{010}^-]_{10}$	/MHz	-0.641(14)	0.861(30)
$[B_{012}^-]_{10}$	/kHz	0.1784(48)	-0.0683(66)
$[B_{030}^-]_{10}$	/kHz	0.3080(99)	-0.723(12)
$[B_{210}^-]_{10}$	/kHz	-0.5487(79)	0.740(12)
Transitions		8125	
Lines		5819	
RMS	/MHz	0.053 938	
WRMS		1.136 331	

**Note.** Fits performed with ERHAM in A-reduction. Standard errors are given in parentheses. Parameters are given in notation for the first rotor. Interaction parameters are given in  $B_{kpr}^-$  notation. The minus sign indicates, that  $\omega = -1$ , while  $k$ ,  $p$ , and  $r$  are the powers of the operators  $P^k$ ,  $P_p^p$ , and  $P_r^r + P_{-r}^-$ , respectively.

being shown in Fig. A.2(a). The WRMS is 1.14 and the highest parameter uncertainty is about 11 %, so all parameters were kept. The resulting parameters are shown in Table 1 and the residuals of the final fit are shown in Fig. A.3(a).

For frequencies higher than 500 GHz, LLWP's residuals module was used to identify a group of transitions with high quantum numbers that showed strong deviations. The affected transitions with  $94 > J' > 67$  and  $K'_a > 3$  were excluded from the final fit. Their deviation patterns look similar to patterns caused by interactions but were not further examined here (see Fig. A.3(b)). We expect more transitions with high quantum numbers to be perturbed and thus the fit to be effective. Consequentially, it should not be used for structure determination. The resulting fit up to 1100 GHz includes 12 403 transitions (8602 unique lines) with a quantum number coverage as shown in Fig. A.2(b). As with the previous fit, sets of parameters were added together, resulting in a fit with many parameters having high uncertainties, some even greater than 100 %. Parameters were then omitted symmetrically for the two rotors. Their uncertainty and influence on the goodness of the fit were the two criteria for choosing the next parameter to omit. This

**Table 2**  
Molecular parameters for the ground state of  $^{13}\text{CH}_3\text{C}(\text{O})\text{CH}_3$  up to 1100 GHz.

Parameter		Rotor 1	Rotor 2
$\rho$		0.059 539 9(39)	0.061 028 6(83)
$\beta$	/°	29.4232(18)	21.2920(63)
$A$	/MHz	10 083.033 461(80)	
$B$	/MHz	8277.506 507(96)	
$C$	/MHz	4811.468 723(58)	
$\Delta_K$	/kHz	9.428 16(24)	
$\Delta_{JK}$	/kHz	-2.739 86(25)	
$\Delta_J$	/kHz	4.585 316(65)	
$\delta_K$	/kHz	-0.343 17(13)	
$\delta_J$	/kHz	1.915 325(32)	
$\Phi_K$	/Hz	0.028 83(19)	
$\Phi_{KJ}$	/Hz	0.031 41(27)	
$\Phi_{JK}$	/Hz	-0.026 95(14)	
$\Phi_J$	/mHz	5.531(26)	
$\phi_K$	/Hz	-0.068 43(11)	
$\phi_{JK}$	/Hz	0.035 616(50)	
$\phi_J$	/mHz	2.749(13)	
$[I_{JK}]_{00}$	/μHz	0.3461(47)	
$\epsilon_{11}$	/MHz	1.0891(92)	
$\epsilon_{1-1}$	/MHz	0.1064(16)	
$\epsilon_{10}$	/MHz	-758.174(26)	-763.253(22)
$\epsilon_{20}$	/MHz	0.7862(30)	0.7568(27)
$[A - (B + C)/2]_{10}$	/MHz	0.018 92(27)	0.032 41(36)
$[(B + C)/2]_{10}$	/MHz	0.010 29(13)	-0.003 67(30)
$[(B - C)/4]_{10}$	/MHz	0.012 297(69)	0.004 91(15)
$[\Delta_K]_{10}$	/kHz	0.017 66(21)	0.011 19(21)
$[\Delta_{JK}]_{10}$	/kHz	-0.017 09(17)	-0.012 93(21)
$[\Delta_J]_{10}$	/Hz	-2.005(59)	1.964(84)
$[\delta_{KJ}]_{10}$	/kHz	-0.016 669(56)	-0.010 033(57)
$[\delta_{JK}]_{10}$	/Hz	-0.824(30)	1.153(43)
$[\Phi_K]_{10}$	/mHz	5.877(66)	1.357(59)
$[\Phi_{KJ}]_{10}$	/Hz	-0.011 108(67)	-0.002 679(58)
$[\Phi_{JK}]_{10}$	/mHz	5.139(29)	1.143(26)
$[\phi_{JK}]_{10}$	/mHz	2.032(18)	0.098(17)
$[B_{001}^-]_{10}$	/MHz	-0.4125(59)	-0.3087(76)
$[B_{010}^-]_{10}$	/MHz	-1.1989(55)	1.498(10)
$[B_{012}^-]_{10}$	/kHz	0.3800(15)	-0.2079(20)
$[B_{030}^-]_{10}$	/kHz	0.0375(63)	-0.4358(60)
$[B_{210}^-]_{10}$	/kHz	-0.2595(28)	0.3991(37)
$[B_{050}^-]_{10}$	/Hz	-0.2818(24)	0.0493(22)
$[B_{230}^-]_{10}$	/Hz	0.3100(15)	-0.0632(15)
$[B_{310}^-]_{10}$	/Hz	-0.029 92(44)	0.027 23(45)
Transitions		12 403	
Lines		8602	
RMS	/MHz	0.068 270	
WRMS		1.452 576	

**Note.** Fits performed with ERHAM in A-reduction. Standard errors are given in parentheses. Parameters are given in notation for the first rotor. Interaction parameters are given in  $B_{kpr}^-$  notation. The minus sign indicates, that  $\omega = -1$ , while  $k$ ,  $p$ , and  $r$  are the powers of the operators  $P^k$ ,  $P_p^p$ , and  $P_r^r + P_{-r}^-$ , respectively.

allowed to reduce the number of parameters to 66 and improve the relative uncertainties. For the final fit, the highest relative uncertainty is 17 % and only 2 parameters have uncertainties higher than 10 %. The resulting WRMS is 1.45. The resulting parameters are shown in Table 2 and the residuals of the final fit are shown in Fig. A.3(b).

Selected spectroscopic parameters for the two fits from this work and for the analyses of  $\text{CH}_3\text{C}(\text{O})\text{CH}_3$ ,  $\text{CH}_3^{13}\text{C}(\text{O})\text{CH}_3$ , and  $^{13}\text{CH}_3\text{C}(\text{O})\text{CH}_3$  from Ordu et al. [15] are shown in Table 3. For these parameters, the two fits from this work show good agreement as the relative deviations, except for some energy tunneling parameters  $\epsilon$ , are below 1 %. For the energy tunneling parameters the two highest relative deviations are seen for  $\epsilon_{1-1}$  (~ 13 %) and  $\epsilon_{11}$  (~ 6 %). The  $^{13}\text{CH}_3\text{C}(\text{O})\text{CH}_3$  fit from Ordu et al. agrees for low parameters but shows

**Table 3**

Selected spectroscopic parameters for the fits of  $\text{CH}_3\text{C}(\text{O})\text{CH}_3$ ,  $\text{CH}_3^{13}\text{C}(\text{O})\text{CH}_3$ , and  $^{13}\text{CH}_3\text{C}(\text{O})\text{CH}_3$  from Ordu et al. [15] as well as the two fits for  $^{13}\text{CH}_3\text{C}(\text{O})\text{CH}_3$  from this work.

Parameter	Ordu et al. [15]			This work	
	$\text{CH}_3\text{C}(\text{O})\text{CH}_3$	$\text{CH}_3^{13}\text{C}(\text{O})\text{CH}_3$	$^{13}\text{CH}_3\text{C}(\text{O})\text{CH}_3$	$^{13}\text{CH}_3\text{C}(\text{O})\text{CH}_3$	$^{13}\text{CH}_3\text{C}(\text{O})\text{CH}_3$
$\rho_1$	0.061 954(12)	0.061 485 8(41)	0.060 458(57)	0.059 925 9(97)	0.059 539 9(39)
$\rho_2$			0.061 811(58)	0.061 394(20)	0.061 028 6(83)
$\beta_1$ /°	25.5065(76)	25.7140(31)	29.5967(77)	29.3671(35)	29.4232(18)
$\beta_2$ /°			21.2614(76)	21.1451(93)	21.2920(63)
$A$ /MHz	10 165.217 78(28)	10 164.005 78(15)	10 083.032 18(58)	10 083.034 62(12)	10 083.033 461(80)
$B$ /MHz	8515.163 07(25)	8516.083 09(10)	8277.506 17(44)	8277.507 38(10)	8277.506 507(96)
$C$ /MHz	4910.198 78(21)	4910.235 40(11)	4811.468 97(17)	4811.469 122(77)	4811.468 723(58)
$\Delta_K$ /kHz	9.791 05(88)	9.850 55(33)	9.456(60)	9.430 44(76)	9.428 16(24)
$\Delta_{JK}$ /kHz	-3.170 67(60)	-3.192 45(19)	-2.865(74)	-2.739 03(43)	-2.739 86(25)
$\Delta_J$ /kHz	4.854 45(22)	4.852 046(73)	4.556(15)	4.585 14(10)	4.585 316(65)
$\delta_K$ /kHz	-0.607 20(39)	-0.619 62(13)	-0.226(31)	-0.346 59(24)	-0.343 17(13)
$\delta_J$ /kHz	2.038 605(99)	2.038 100(27)	1.8855(77)	1.915 380(46)	1.915 325(32)
$\epsilon_{10}$ /MHz	-764.737(38)	-763.9260(53)	-759.25(81)	-758.019(36)	-758.174(26)
$\epsilon_{01}$ /MHz			-766.18(79)	-763.230(32)	-763.253(22)
$\epsilon_{20}$ /MHz	0.7749(28)	0.7661(17)	0.574(45)	0.7627(26)	0.7862(30)
$\epsilon_{02}$ /MHz			0.574(45) <sup>a</sup>	0.7721(23)	0.7568(27)
$\epsilon_{11}$ /MHz	1.0902(95)	1.1059(61)	1.000(21)	1.0306(75)	1.0891(92)
$\epsilon_{1-1}$ /MHz	0.0735(26)	0.0885(18)	0.0863(14)	0.0944(13)	0.1064(16)
Transitions	2181	9715	110	8125	12 403
Lines	1862	5870	72	5819	8602
RMS /kHz	104	111	29	54	68
WRMS	0.93	1.28	0.75	1.14	1.45
Standard Deviation <sup>b</sup>	0.95	1.29	0.93	1.11	1.46

**Note.** Fits performed with ERHAM in A-reduction. Standard errors are given in parentheses.

<sup>a</sup>Parameter of  $(q, q') = (0, 2)$  is fixed to its counterpart equivalent parameter with  $(2, 0)$ .

<sup>b</sup>Weighted unitless value for the entire fit.

already clear deviations for  $\Delta_{JK}$  ( $\sim 5\%$ ) and  $\delta_K$  ( $\sim 35\%$ ). Additionally, the energy tunneling parameters  $\epsilon_{20}$  and  $\epsilon_{02}$ , which are fixed to each other in the analysis from Ordu et al. show strong deviations of about 25% each. This is expected, as Ordu et al. assigned only 72 lines, suffered from misassignments, and, in contrast to this work, were severely limited in frequency and quantum number coverage.

## 5. Conclusion

The microwave spectrum of an enriched sample of acetone- $^{13}\text{C}_1$  was recorded for the first time. More than 1 THz of high-resolution spectra were recorded up to 1102 GHz. Previous analyses of the rotational ground state were extended, with the number of assigned transitions increasing by more than a factor of 100. The quantum number coverage was increased to  $J''_{\text{max}} = 98$  and  $K''_{a,\text{max}} = 44$ . Two fits are presented. The fit up to 500 GHz should be used for structure determination as the fit up to 1100 GHz is expected to be effective. The latter fit allows for astronomical searches up to the THz region, especially due to the high number of assigned lines, but caution is required for the here excluded quantum numbers above 500 GHz.

For the analysis, the new LLWP software was used successfully. It raised the efficiency and confidence of assignments in the dense and complicated spectrum. Additionally, LLWP facilitated the analysis by providing a multitude of important metrics. Due to its general and unopinionated approach, molecular fingerprints of various molecules can be analyzed in various frequency ranges.

LLWP is expected to speed up and facilitate the assignment of many more complex molecular fingerprints in the future.

## Declaration of competing interest

The authors declare that they have no known competing financial interests or personal relationships that could have appeared to influence the work reported in this paper.

## Data availability

Data will be provided as supplementary material

## Acknowledgments

This work has been supported via Collaborative Research Centre 956, sub-project B3, funded by the Deutsche Forschungsgemeinschaft, Germany (DFG; project ID 184018867) and DFG SCHL, Germany 341/15-1 (“Cologne Center for Terahertz Spectroscopy”). J.-C.G. thanks the Centre National d’Etudes Spatiales (CNES), France and the “Programme National Physique et Chimie du Milieu Interstellaire” (PCMI) of CNRS/INSU with INC/INP co-funded by CEA, France and CNES, France for a grant.

## Appendix A. Complementary material

First, the GUI of LLWP is shown with multiple columns (Fig. A.1) to highlight the possibilities that this offers. Next, different important metrics of the final analyses are provided. The quantum number coverage plots (Fig. A.2) of the two final fits give an overview of the quantum numbers of the included transitions. The residuals (Fig. A.3) and weighted residuals (Fig. A.4) are a measure of the goodness of the fit and highlight the need to exclude specific transitions with high deviations for the fit up to 1100 GHz. Additionally, the assignments per transition type are displayed in Table A.1.



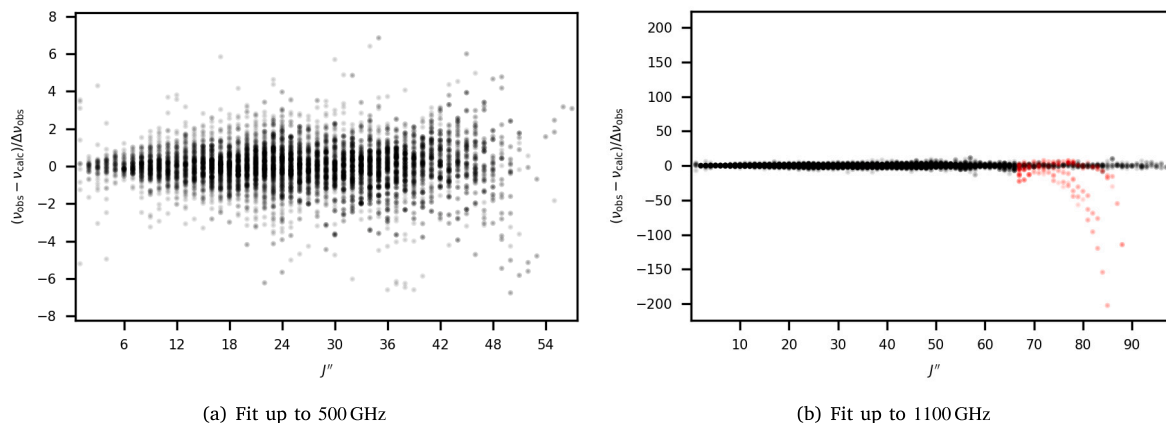


Fig. A.4. Weighted residuals of the two final fits (Tables 1 and 2) against  $J''$ . The assignments that were excluded from the fit up to 1100 GHz (being the transitions with  $94 > J' > 67$  and  $K'_a > 3$ ) are highlighted in red in Fig. A.3(b).

Table A.1

Assignments per transition type for the two final fits (Table 1 and Table 2). Only transitions with a nonzero weight are listed here (252 transitions with zero weight together with the 15956 here listed transitions result in the 16208 assigned lines). For the fits, the  $a$ -type transitions were excluded as they are a product of label switching (Section 4). An additional 225 lines were excluded for the fit up to 1100 GHz (transitions with  $94 > J' > 67$  and  $K'_a > 3$ ).

Fit up to 500 GHz (Table 1)				Fit up to 1100 GHz (Table 2)			
$J' - J''$	$K'_a - K''_a$	$K'_c - K''_c$	No. transitions	$J' - J''$	$K'_a - K''_a$	$K'_c - K''_c$	No. transitions
0	0	-1	92 <sup>a</sup>	0	0	-1	92 <sup>a</sup>
0	1	-2	26	0	1	-2	26
0	1	-1	3280	0	1	-1	3280
0	1	0	31	0	1	0	31
0	2	-1	89 <sup>a</sup>	0	2	-1	89 <sup>a</sup>
0	3	-3	-	0	3	-3	2
1	-1	1	1868	1	-1	1	2926
1	-1	3	1	1	-1	3	1
1	0	1	1073 <sup>a</sup>	1	0	1	3147 <sup>a</sup>
1	1	-1	211	1	1	-1	554
1	1	0	612	1	1	0	2023
1	1	1	2095	1	1	1	3783
1	3	-2	-	1	3	-2	1
1	3	-1	1	1	3	-1	1
$a$ -type transitions			1254 <sup>a</sup>	$a$ -type transitions			3328 <sup>a</sup>
$b$ -type transitions			7456	$b$ -type transitions			10547
$c$ -type transitions			669	$c$ -type transitions			2081
Total transitions			9379	Total transitions			15956

Note. Primes indicate the upper level and double primes indicate the lower level.

<sup>a</sup> $a$ -type transitions were excluded from all fits, see Section 4.

## References

- [1] F. Combes, M. Gerin, A. Wootten, G. Wlodarczyk, F. Clausset, P.J. Encrenaz, Acetone in interstellar space, *Astron. Astrophys.* 180 (1987) L13–L16.
- [2] L.E. Snyder, F.J. Lovas, D.M. Mehringer, N.Y. Miao, Y.-J. Kuan, J.M. Hollis, P.R. Jewell, Confirmation of interstellar acetone, *Astrophys. J.* 578 (2002) 245–255, <http://dx.doi.org/10.1086/342273>.
- [3] B. Bak, E.S. Knudsen, E. Madsen, Microwave absorption of some organic vapors, *Phys. Rev.* 75 (1949) 1622–1623, <http://dx.doi.org/10.1103/physrev.75.1622>.
- [4] T.L. Weatherly, D. Williams, The microwave absorption spectrum of acetone vapor, *J. Chem. Phys.* 20 (1952) 755, <http://dx.doi.org/10.1063/1.1700546>.
- [5] J.D. Swalen, C.C. Costain, Internal rotation in molecules with two internal rotors: Microwave spectrum of acetone, *J. Chem. Phys.* 31 (1959) 1562–1574, <http://dx.doi.org/10.1063/1.1730653>.
- [6] R. Nelson, L. Pierce, Microwave spectrum, structure, and barrier to internal rotation of acetone, *J. Mol. Spectrosc.* 18 (1965) 344–352, [http://dx.doi.org/10.1016/0022-2852\(65\)90144-x](http://dx.doi.org/10.1016/0022-2852(65)90144-x).
- [7] R. Peter, H. Dreizler, Das Mikrowellenspektrum von Aceton im Torsionsgrundzustand, *Z. Naturforsch. A* 20 (1965) 301–312, <http://dx.doi.org/10.1515/zna-1965-0224>.
- [8] J.M. Vacherand, B.P. van Eijck, J. Burie, J. Demaison, The rotational spectrum of acetone: Internal rotation and centrifugal distortion analysis, *J. Mol. Spectrosc.* 118 (1986) 355–362, [http://dx.doi.org/10.1016/0022-2852\(86\)90175-x](http://dx.doi.org/10.1016/0022-2852(86)90175-x).
- [9] P. Groner, S. Albert, E. Herbst, F.C. De Lucia, F.J. Lovas, B.J. Drouin, J.C. Pearson, Acetone: Laboratory assignments and predictions through 620 GHz for the vibrational-torsional ground state, *Astrophys. J. Suppl. Ser.* 142 (2002) 145–151, <http://dx.doi.org/10.1086/341221>.
- [10] P. Groner, E. Herbst, F.C. De Lucia, B.J. Drouin, H. Mäder, Rotational spectrum of acetone,  $\text{CH}_3\text{COCH}_3$ , in the first torsional excited state, *J. Mol. Struct.* 795 (2006) 173–178, <http://dx.doi.org/10.1016/j.molstruc.2006.02.028>.
- [11] P. Groner, I.R. Medvedev, F.C. De Lucia, B.J. Drouin, Rotational spectrum of acetone,  $\text{CH}_3\text{COCH}_3$ , in the  $\nu_{17}$  torsional excited state, *J. Mol. Spectrosc.* 251 (2008) 180–184, <http://dx.doi.org/10.1016/j.jms.2008.02.018>.
- [12] F.J. Lovas, P. Groner, Microwave spectra of mono- $^{13}\text{C}$  substituted acetone,  $(\text{CH}_3)_2\text{CO}$ , *J. Mol. Spectrosc.* 236 (2006) 173–177, <http://dx.doi.org/10.1016/j.jms.2006.01.009>.
- [13] V.V. Ilyushin, J.T. Hougen, A fitting program for molecules with two equivalent methyl tops and  $C_{2v}$  point-group symmetry at equilibrium: Application to existing microwave, millimeter, and sub-millimeter wave measurements of acetone, *J. Mol. Spectrosc.* 289 (2013) 41–49, <http://dx.doi.org/10.1016/j.jms.2013.05.012>.
- [14] V. Ilyushin, I. Armieieva, O. Dorovskaya, I. Krapivin, E. Alekseev, M. Tudorie, R.A. Motienko, L. Margulès, O. Pirali, E.S. Bekhtereva, S. Bauerecker, C. Maul, C. Sydow, B.J. Drouin, The torsional fundamental band and high- $J$  rotational spectra of the ground, first and second excited torsional states of acetone, *J. Mol. Spectrosc.* 363 (2019) 111169, <http://dx.doi.org/10.1016/j.jms.2019.06.008>.
- [15] M.H. Ordu, O. Zingsheim, A. Belloche, F. Lewen, R.T. Garrod, K.M. Menten, S. Schlemmer, H.S.P. Müller, Laboratory rotational spectroscopy of isotopic acetone,  $\text{CH}_3^{13}\text{C}(\text{O})\text{CH}_3$  and  $^{13}\text{CH}_3\text{C}(\text{O})\text{CH}_3$ , and astronomical search in Sagittarius B2(N2), *Astron. Astrophys.* 629 (2019) A72, <http://dx.doi.org/10.1051/0004-6361/201935887>.
- [16] F.W. Loomis, R.W. Wood, The rotational structure of the blue-green bands of  $\text{Na}_2$ , *Phys. Rev.* 32 (1928) 223–236, <http://dx.doi.org/10.1103/physrev.32.223>.
- [17] M.A. Martin-Drumel, C.P. Endres, O. Zingsheim, T. Salomon, J. van Wijngaarden, O. Pirali, S. Gruet, F. Lewen, S. Schlemmer, M.C. McCarthy, S. Thorwirth, The

- SOLEIL view on sulfur rich oxides: The  $S_2O$  bending mode  $\nu_2$  at  $380\text{ cm}^{-1}$  and its analysis using an automated spectral assignment procedure (ASAP), *J. Mol. Spectrosc.* 315 (2015) 72–79, <http://dx.doi.org/10.1016/j.jms.2015.02.014>.
- [18] W. Stahl, E. Fliege, H. Dreizler, Two-dimensional microwave Fourier transform spectroscopy, *Z. Naturforsch. A* 39 (1984) 858–864, <http://dx.doi.org/10.1515/zna-1984-0906>.
- [19] D. Christen, L.H. Coudert, R.D. Suenram, F.J. Lovas, The rotational/concerted torsional spectrum of the  $g'$ Ga conformer of ethylene glycol, *J. Mol. Spectrosc.* 172 (1995) 57–77, <http://dx.doi.org/10.1006/jmsp.1995.1155>.
- [20] O. Zingsheim, L. Bonah, F. Lewen, S. Thorwirth, H.S.P. Müller, S. Schlemmer, Millimeter-millimeter-wave double-modulation double-resonance spectroscopy, *J. Mol. Spectrosc.* 381 (2021) 111519, <http://dx.doi.org/10.1016/j.jms.2021.111519>.
- [21] C.M. Western, PGOPHER: A program for simulating rotational, vibrational and electronic spectra, *J. Quant. Spectrosc. Radiat. Transf.* 186 (2017) 221–242, <http://dx.doi.org/10.1016/j.jqsrt.2016.04.010>.
- [22] Z. Kisiel, L. Pszczółkowski, I.R. Medvedev, M. Winniewisser, F.C. De Lucia, E. Herbst, Rotational spectrum of trans–trans diethyl ether in the ground and three excited vibrational states, *J. Mol. Spectrosc.* 233 (2005) 231–243, <http://dx.doi.org/10.1016/j.jms.2005.07.006>.
- [23] W. Łodyga, M. Kręglewski, P. Pracna, Ś. Urban, Advanced graphical software for assignments of transitions in rovibrational spectra, *J. Mol. Spectrosc.* 243 (2007) 182–188, <http://dx.doi.org/10.1016/j.jms.2007.02.004>.
- [24] C. Winkel, M.W.M.M. Aarts, F.R. van der Heide, E.G. Buitenhuis, J. Lugtenburg, Synthesis and NMR spectroscopy of stable isotope-labelled phenols and L-tyrosines, *Recl. Trav. Chim. Pays-Bas.* 108 (1989) 139–146, <http://dx.doi.org/10.1002/recl.19891080405>.
- [25] M.A. Martin-Drumel, J. van Wijngaarden, O. Zingsheim, F. Lewen, M.E. Harding, S. Schlemmer, S. Thorwirth, Millimeter- and submillimeter-wave spectroscopy of disulfur dioxide, OSSO, *J. Mol. Spectrosc.* 307 (2015) 33–39, <http://dx.doi.org/10.1016/j.jms.2014.11.007>.
- [26] W. McKinney, Data structures for statistical computing in Python, in: S. van der Walt, J. Millman (Eds.), *Proceedings of the 9th Python in Science Conference*, 2010, pp. 56–61, <http://dx.doi.org/10.25080/Majora-92bf1922-00a>.
- [27] C.R. Harris, K.J. Millman, S.J. van der Walt, R. Gommers, P. Virtanen, D. Cournapeau, E. Wieser, J. Taylor, S. Berg, N.J. Smith, R. Kern, M. Picus, S. Hoyer, M.H. van Kerkwijk, M. Brett, A. Haldane, J.F. del Río, M. Wiebe, P. Peterson, P. Gérard-Marchant, K. Sheppard, T. Reddy, W. Weckesser, H. Abbasi, C. Gohlke, T.E. Oliphant, Array programming with NumPy, *Nature* 585 (2020) 357–362, <http://dx.doi.org/10.1038/s41586-020-2649-2>.
- [28] P. Virtanen, R. Gommers, T.E. Oliphant, M. Haberland, T. Reddy, D. Cournapeau, E. Burovski, P. Peterson, W. Weckesser, J. Bright, S.J. van der Walt, M. Brett, J. Wilson, K.J. Millman, N. Mayorov, A.R.J. Nelson, E. Jones, R. Kern, E. Larson, C.J. Carey, I. Polat, Y. Feng, E.W. Moore, J. VanderPlas, D. Laxalde, J. Perktold, R. Cimrman, I. Henriksen, E.A. Quintero, C.R. Harris, A.M. Archibald, A.H. Ribeiro, F. Pedregosa, P. van Mulbregt, A. Vijaykumar, A.P. Bardelli, A. Rothberg, A. Hilboll, A. Kloeckner, A. Scopatz, A. Lee, A. Rokem, C.N. Woods, C. Fulton, C. Masson, C. Häggström, C. Fitzgerald, D.A. Nicholson, D.R. Hagen, D.V. Pasechnik, E. Olivetti, E. Martin, E. Wieser, F. Silva, F. Lenders, F. Wilhelm, G. Young, G.A. Price, G.-L. Ingold, G.E. Allen, G.R. Lee, H. Audren, I. Probst, J.P. Dietrich, J. Silterra, J.T. Webber, J. Slavič, J. Nothman, J. Buchner, J. Kulick, J.L. Schönberger, J.V. de Miranda Cardoso, J. Reimer, J. Harrington, J.L.C. Rodríguez, J. Nunez-Iglesias, J. Kuczynski, K. Tritz, M. Thoma, M. Newville, M. Kümmeler, M. Bolingbroke, M. Tartre, M. Pak, N.J. Smith, N. Nowaczyk, N. Shebanov, O. Pavlyk, P.A. Brodtkorb, P. Lee, R.T. McGibbon, R. Feldbauer, S. Lewis, S. Tytgier, S. Sievert, S. Vigna, S. Peterson, S. More, T. Pudlik, T. Oshima, T.J. Pingel, T.P. Robitaille, T. Spura, T.R. Jones, T. Cera, T. Leslie, T. Zito, T. Krauss, U. Upadhyay, Y.O. Halchenko, Y. Vázquez-Baeza, SciPy 1.0 Contributors, SciPy 1.0: fundamental algorithms for scientific computing in Python, *Nat. Methods* 17 (2020) 261–272, <http://dx.doi.org/10.1038/s41592-019-0686-2>.
- [29] J.D. Hunter, Matplotlib: A 2D graphics environment, *Comput. Sci. Eng.* 9 (2007) 90–95, <http://dx.doi.org/10.1109/mcse.2007.55>.
- [30] H.M. Pickett, The fitting and prediction of vibration-rotation spectra with spin interactions, *J. Mol. Spectrosc.* 148 (1991) 371–377, [http://dx.doi.org/10.1016/0022-2852\(91\)90393-o](http://dx.doi.org/10.1016/0022-2852(91)90393-o).
- [31] P. Groner, Effective rotational Hamiltonian for molecules with two periodic large-amplitude motions, *J. Chem. Phys.* 107 (1997) 4483–4498, <http://dx.doi.org/10.1063/1.474810>.
- [32] P. Groner, Effective rotational Hamiltonian for molecules with internal rotors: Principles, theory, applications and experiences, *J. Mol. Spectrosc.* 278 (2012) 52–67, <http://dx.doi.org/10.1016/j.jms.2012.06.006>.
- [33] P. Groner, S. Albert, E. Herbst, F.C. De Lucia, Dimethyl ether: Laboratory assignments and predictions through 600 GHz, *Astrophys. J.* 500 (1998) 1059–1063, <http://dx.doi.org/10.1086/305757>.
- [34] M. Koerber, S.E. Bisschop, C.P. Endres, M. Kleshcheva, R.W.H. Pohl, A. Klein, F. Lewen, S. Schlemmer, Laboratory rotational spectra of the dimethyl ether  $^{13}\text{C}$ -isotopologues up to 1.5 THz, *Astron. Astrophys.* 558 (2013) A112, <http://dx.doi.org/10.1051/0004-6361/201321898>.
- [35] C.P. Endres, B.J. Drouin, J.C. Pearson, H.S.P. Müller, F. Lewen, S. Schlemmer, T.F. Giesen, Dimethyl ether: laboratory spectra up to 2.1 THz, *Astron. Astrophys.* 504 (2009) 635–640, <http://dx.doi.org/10.1051/0004-6361/200912409>.

# 7. MM- and Sub-MM-Wave Study of $C_2H_5CP$

## Bibliographic Information

L. Bonah, S. Schlemmer, J.-C. Guillemin, M. E. Harding, S. Thorwirth, On the Spectroscopy of Phosphaalkynes: Millimeter- and Submillimeter-Wave Study of  $C_2H_5CP$ , *J. Phys. Chem. A* 128 (2024) 4859–4866. doi:10.1021/acs.jpca.4c02566.

The supporting information is provided in Sec. A.7.

## Author's contribution

The author of this thesis performed the measurements and the analysis. Furthermore, he wrote the original draft and provided the visualization.

## Context

This study is the first rotational analysis of ethyl phosphoethyne ( $CH_3CH_2CP$ ), the phosphoalkyne analog of the astronomically ubiquitous ethyl cyanide ( $C_2H_5CN$ ).<sup>43,44,142</sup> The assignment process was guided by QCC, which made initial assignments straightforward (see the TOC Figure or Fig. 2). The singly  $^{13}C$  substituted isotopologues could be assigned in natural abundance by scaling their calculated rotational constants with the exp/calc ratio of the parent isotopologue. This highlights the power of using (scaled) QCC for the initial assignment process and for the identification of weak patterns in LWPs.

## Copyright Notice

Reprinted with permission from *J. Phys. Chem. A* 2024, **128**, 4859-4866. © 2024 American Chemical Society.

# On the Spectroscopy of Phosphaalkynes: Millimeter- and Submillimeter-Wave Study of $C_2H_5CP$

Luis Bonah, Stephan Schlemmer, Jean-Claude Guillemin, Michael E. Harding, and Sven Thorwirth\*

Cite This: *J. Phys. Chem. A* 2024, 128, 4859–4866

Read Online

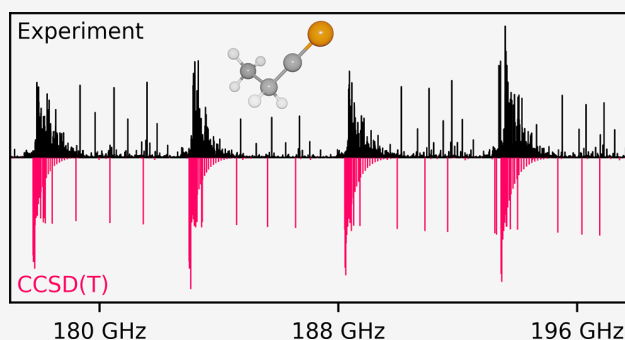
ACCESS |

Metrics & More

Article Recommendations

Supporting Information

**ABSTRACT:** Ethyl phosphoethyne,  $C_2H_5CP$ , has been characterized spectroscopically in the gas phase for the first time, employing millimeter- and submillimeter-wave spectroscopy in the frequency regime from 75 to 760 GHz. Spectroscopic detection and analysis was guided by high-level quantum-chemical calculations of molecular structures and force fields performed at the coupled-cluster singles and doubles level extended by a perturbative correction for the contribution from triple excitations, CCSD(T), in combination with large basis sets. Besides the parent isotopologue, the three singly substituted  $^{13}C$  species were observed in natural abundance up to frequencies as high as 500 GHz. Despite the comparably low astronomical abundance of phosphorus, phosphaalkynes,  $R-CP$ , such as  $C_2H_5CP$  are promising candidates for future radio astronomical detection.



## INTRODUCTION

Nitriles, chemical species of the general formula  $R-CN$ , are one, if not the most prominent, class of molecules found in space. Over the last 50 years, many nitriles have been detected by their pure rotational spectra using radio astronomical techniques. Here, species range from simple prototypical  $HCN$ ,<sup>1</sup> over metal-bearing variants like  $FeCN$ <sup>2</sup> and  $CN$ -bearing molecular ions,<sup>3,4</sup> up to complex and heavy benzenoid variants such as cyanonaphthalene<sup>5</sup> and cyanoindene,<sup>6</sup> just to name a few.

Owing to intrinsically strong dipole moments, numerous nitriles have also been studied in the laboratory using microwave and millimeter-wave spectroscopy. In contrast, comparable studies of phosphaalkynes, where the  $CN$  functional group is replaced by an isovalent  $CP$  unit, are rather scarce, which may in part be attributed to their pronounced transient character and also more challenging synthetic routes. Since the first microwave spectroscopic studies of prototypical phosphoethyne ( $HCP$ ),<sup>7</sup> and a handful of other selected species studied by Kroto and collaborators ( $HC_3P$ ,  $CH_3CP$ ,  $NCCP$ ,  $C_2H_3CP$ ,  $PhCP$ ; see Burckett-St. Laurent et al.<sup>8</sup> and references therein), only a small number of additional phosphaalkynes have been characterized employing high-resolution (rotational) spectroscopy. For detailed accounts on the available laboratory spectroscopic data of individual species, the interested reader may consult the reports on phosphoethyne,  $HCP$ ,<sup>9,10</sup>  $HC_3P$ ,<sup>9,11</sup>  $HC_5P$ ,<sup>12,13</sup>  $NCCP$ ,<sup>9</sup>  $NC_4P$ ,<sup>14,15</sup>  $C_2H_3CP$ ,<sup>16</sup>  $CH_3CP$ ,<sup>17,18</sup>  $PhCP$ ,<sup>19</sup> and  $C_3H_5CH_2CP$ .<sup>20</sup>

It should be noted that while to this day, spectroscopic signatures of only two phosphaalkynes,  $HCP$  and  $NCCP$ , have been found in space,<sup>21,22</sup> not all of the above species have yet been characterized in the laboratory at a level meeting the needs of radio astronomy. In addition, other potentially astronomically relevant phosphaalkynes still await laboratory (high-resolution) spectroscopic characterization. One such species is ethyl phosphoethyne,  $C_2H_5CP$  (also known as propylidynephosphine or phosphabutyne).

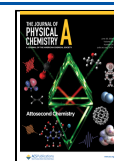
$C_2H_5CP$ , the phosphorus variant of the astronomically ubiquitous ethyl cyanide,  $C_2H_5CN$  (e.g., Endres et al.<sup>23</sup>), has been known in the laboratory for many years and characterized by its  $^1H$ ,  $^{31}P$ , and  $^{13}C$  NMR spectra in solution.<sup>24,25</sup> However, so far, there does not seem to be any account of its spectroscopic properties in the gas phase. In the present study, high-level quantum-chemical calculations were performed at the coupled-cluster (CC) singles and doubles level extended by a perturbative correction for the contribution from triple excitations, CCSD(T). Based on these results, the pure rotational spectrum of  $C_2H_5CP$  has been detected for the first time and observed in selected frequency ranges between 75 and 760 GHz. A detailed account of the experimental and

Received: April 19, 2024

Revised: May 22, 2024

Accepted: May 24, 2024

Published: June 10, 2024



theoretical work as well as the analysis of the rotational spectrum of  $C_2H_5CP$  in its ground vibrational state are given in the following.

## THEORETICAL AND EXPERIMENTAL METHODS

**Quantum-Chemical Calculations.** Quantum-chemical calculations to guide the spectroscopic search of  $C_2H_5CP$  were performed at the CC singles and doubles level extended by a perturbative correction for the contribution from triple excitations (CCSD(T)).<sup>26</sup> All calculations were performed using the quantum-chemical program package CFOUR.<sup>27–29</sup> Correlation-consistent polarized valence and polarized core valence basis sets were used throughout. Within the frozen core (fc) approximation, the tight-*d*-augmented basis set cc-pV(T+d)Z was used for the phosphorus atom, and the corresponding cc-pVTZ basis sets for carbon and hydrogen<sup>30,31</sup> as well as the atomic natural orbital basis set ANO1.<sup>32</sup> The ANO1 set consists of 18s13p6d4f2g to 5s4p2d1f, 13s8p6d4f2g to 4s3p2d1f, and 8s6p4d3f to 4s2p1d contractions for P, C, and H, respectively.

The cc-pwCVXZ (X = T and Q) basis sets were used when considering all electrons in the correlation treatment.<sup>33</sup> Equilibrium geometries were obtained using analytic gradient techniques.<sup>34</sup> For molecules comprising first- and second-row elements, the ae-CCSD(T)/cc-pwCVQZ level of theory has been shown on many occasions to yield molecular equilibrium structures of very high quality (e.g., Coriani et al.<sup>35</sup>). The corresponding structure of  $C_2H_5CP$  is shown in Figure 1. Full sets of internal coordinates of both the ground-state molecular structure and the transition state to methyl internal rotation are collected in the Supporting Information.

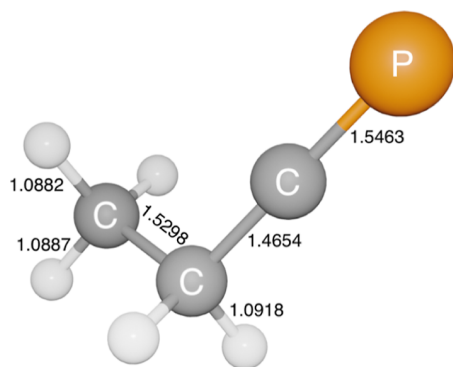


**Figure 1.** Bond lengths of  $C_2H_5CP$  calculated at the ae-CCSD(T)/cc-pwCVQZ level of theory (in Å). Full structure in internal coordinates is given in the Supporting Information.

Harmonic and anharmonic force fields were calculated in the fc approximation using the cc-pV(T+d)Z and ANO1 basis sets using analytic second-derivative techniques,<sup>36,37</sup> followed by additional numerical differentiation to calculate the third and fourth derivatives needed for the anharmonic force field.<sup>37,38</sup> Theoretical ground-state rotational constants were then estimated from the equilibrium rotational constants (calculated at the CCSD(T)/cc-pwCVQZ level of theory) and the zero-point vibrational corrections  $\Delta A_0$ ,  $\Delta B_0$ , and  $\Delta C_0$  (calculated at the fc-CCSD(T)/ANO1 level; see Table 1). In addition, the fc-CCSD(T)/ANO1 force-field calculation yields the quartic and sextic centrifugal distortion parameters. Spin-rotation constants, owing to the presence of  $^{31}P$  ( $I = 1/2$ ), were

**Table 1.** Calculated and Experimental Molecular Parameters of  $C_2H_5CP$  in Its Ground Vibrational State<sup>a</sup>

parameter	calculations	experimental
$A_e$ /MHz	25374.531	
$B_e$ /MHz	2719.663	
$C_e$ /MHz	2532.995	
$\Delta A_0$ /MHz	158.770	
$\Delta B_0$ /MHz	12.603	
$\Delta C_0$ /MHz	14.132	
$A_0$ /MHz	25215.761	25216.12285(35)
$B_0$ /MHz	2707.060	2709.143447(22)
$C_0$ /MHz	2518.863	2520.638536(21)
$-D_J$ /Hz	-879.142	-900.7695(38)
$-D_{JK}$ /kHz	23.760	24.101222(85)
$-D_K$ /kHz	-536.855	-547.7691(34)
$d_1$ /Hz	-147.802	-153.7099(23)
$d_2$ /Hz	-7.414	-8.11625(97)
$H_J$ /mHz	1.461	1.50407(31)
$H_{JK}$ /mHz	-14.470	-14.8371(54)
$H_{KJ}$ /Hz	-1.374	-1.37747(40)
$H_K$ /Hz	36.623	36.895(11)
$h_1$ /μHz	469.5	490.70(24)
$h_2$ /μHz	65.5	69.37(13)
$h_3$ /μHz	6.8	6.570(15)
$L_J$ /nHz		-3.0130(87)
$L_{JK}$ /μHz		-2.446(11)
$L_{KJ}$ /μHz		71.50(53)
$l_1$ /nHz		-1.3244(74)
$l_2$ /pHz		-259.3(5.0)
$C_{aa}(P)$ /kHz	7.42	
$C_{bb}(P)$ /kHz	5.02	
$C_{cc}(P)$ /kHz	4.92	
$C_{ab}(P)$ /kHz	12.51	
$C_{ba}(P)$ /kHz	1.06	
$\mu_a$ /D	1.53	
$\mu_b$ /D	0.29	
$V_3$ /kcal/mol	2.8	
transitions		6016
lines		4010
RMS/kHz		29.7
WRMS		1.00

<sup>a</sup>Fits performed with SPFIT in the S-reduction and the I<sup>r</sup> representation. Standard errors are given in parentheses. Lines that were rejected from the fit are excluded from the statistics. Equilibrium rotational constants, phosphorus spin rotation constants, dipole moment components, and barrier of internal rotation calculated at the ae-CCSD(T)/cc-pwCVQZ level, zero-point vibrational contributions to the rotational constants, centrifugal distortion constants, and barrier of internal rotation calculated at the fc-CCSD(T)/ANO1 level. Ground-state rotational constants are estimated as  $B_0 = B_e - \Delta B_0$ . For further details, see the text.

calculated at the CCSD(T)/cc-pwCVQZ level of theory using rotational London orbitals.<sup>39</sup>

At the ae-CCSD(T)/cc-pwCVQZ level of theory and corrected for harmonic zero-point effects at the fc-CCSD(T)/ANO1 level of theory, the barriers of internal rotation  $V_3$  of both  $C_2H_5CP$  and isovalent  $C_2H_5CN$  are estimated as about 2.8 kcal/mol, suggesting that torsional splitting will not be significant for the ground-state rotational spectrum obtained here.

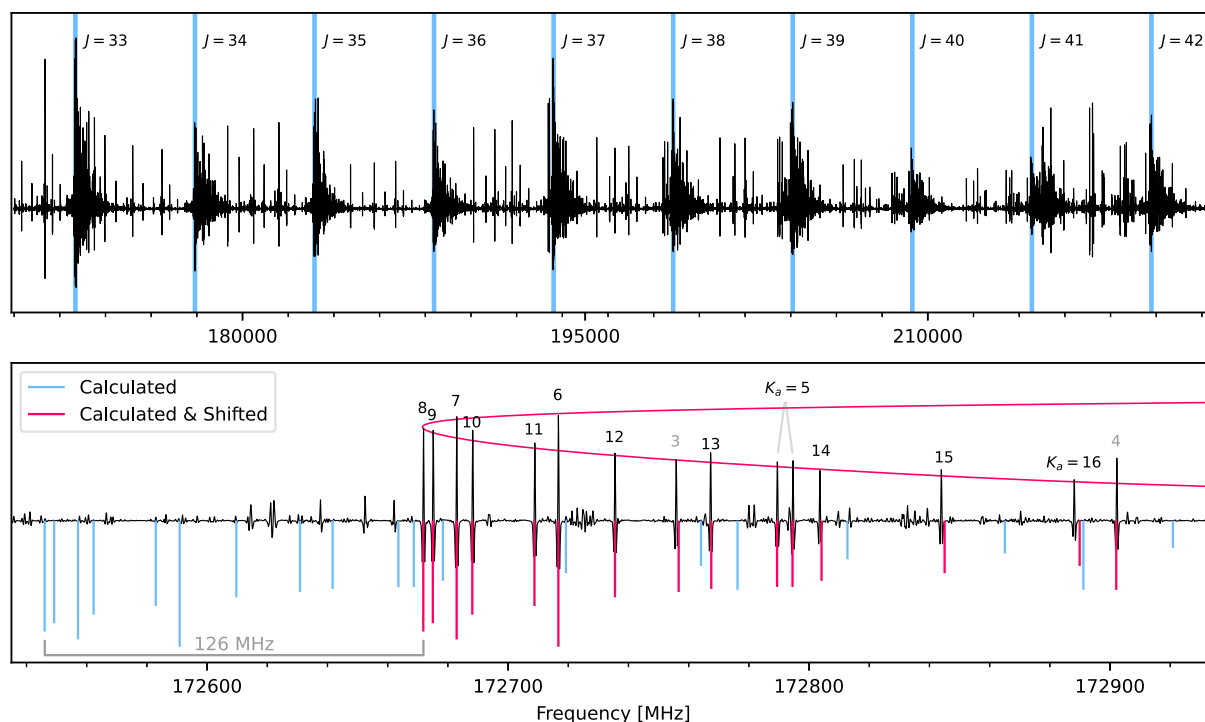


**Figure 2.** Top: pure rotational spectrum of  $C_2H_5CP$  from 170 to 216 GHz. The typical pattern determined by consecutive  $a$ -type rotational transitions is clearly visible. Transitions of the  $J_{7,J-7} \leftarrow J - 1_{7,J-8}$  series are highlighted in blue and the respective  $J$  values are given. The intensities vary due to the frequency dependence of the source power and pressure in the cell increasing over time. Bottom: one of the first scans taken at 172.7 GHz. The initial theoretical predictions (blue sticks) reproduce the experimental pattern nearly quantitatively when shifted by about +126 MHz, making spectroscopic assignment a straightforward procedure. The red trendline highlights the pattern of the  $33_{K_a,33-K_a} \leftarrow 32_{K_a,32-K_a}$  and  $33_{K_a,34-K_a} \leftarrow 32_{K_a,33-K_a}$  transitions. For  $K_a > 5$ , the asymmetry components are overlapping, whereas the splitting is still resolved for  $K_a = 5$  (indicated by the gray lines). For  $K_a = 3$  and  $K_a = 4$ , the second asymmetry components lie outside the shown region.

Puzzarini et al.<sup>40</sup> may be consulted for further insight into the theoretical approaches used in the present context.

**Experiment.** Broadband measurements were recorded with a synthesized sample by using three different experimental setups in Cologne. The three measured frequency ranges of 75–120, 170–255, and 340–760 GHz resulted in a total frequency coverage of 550 GHz.

**Synthesis.**  $C_2H_5CP$  was prepared following the synthesis published by Guillemin et al.<sup>25</sup> The three-step sequence involves the synthesis of 1,1-dichloropropylphosphonic acid diisopropyl ester, which was reduced to 1,1-dichloropropylphosphine followed by a bis-dehydrochlorination using 1,8-diazabicyclo[5,4,0]undec-7-ene as a base to generate  $C_2H_5CP$ . The two last steps of the synthesis were performed in tetraethylene glycol dimethyl ether (tetraglyme) as solvent.  $C_2H_5CP$  was purified by vaporization, condensed under vacuum at  $-100$  °C, and finally introduced into a cell containing degassed tetraglyme for storage at dry ice temperature.

**Broadband Measurements.** Spectra were obtained through broadband scans by utilizing three different absorption experiments sharing a common basic structure consisting of a source, an absorption cell, and a detector. The sources consist of synthesizers and subsequent commercial amplifier-multiplier chains to reach the desired frequency range. For the absorption cells, different lengths of borosilicate tubes were used. The resulting radiation was propagated via horn antennas, mirrors, and polarization filters through the absorption cells and onto the detectors. These are either

Schottky detectors ( $<500$  GHz) or a cryogenically cooled bolometer ( $>500$  GHz). All experiments utilized frequency modulation with a  $2f$ -demodulation scheme to increase the SNR. The resulting lineshapes look similar to the second derivative of a Voigt profile. More in-depth descriptions of the setups have been given earlier in Martin-Drumel et al.<sup>41</sup> and Zingsheim et al.<sup>42</sup>

All measurements were performed at room temperature and static pressure. This was deemed safe, as a time series of the same calibration line showed no significant degradation of the sample over time. Before each filling of the absorption cells, the sample was frozen out. Then,  $C_2H_5CP$  was selectively removed from the solution in vacuo while keeping the sample container at a temperature of about  $-40$  °C. The filling pressures were in the range of 10–40  $\mu$ bar. Reproducibility lines were measured before and after each batch of measurements as sanity checks (Supporting Information). Standing waves were removed from the broadband spectra via Fourier filtering with an in-house-written script.<sup>a</sup>

## RESULTS AND DISCUSSION

$C_2H_5CP$  is an asymmetric top molecule with Ray's asymmetry parameter of  $\kappa = (2B - A - C)/(A - C) = -0.98$ . Thus,  $C_2H_5CP$  is a highly prolate rotor close to the symmetric limit of  $-1$ . Its two nonzero dipole moments  $\mu_a = 1.5$  D and  $\mu_b = 0.3$  D (see Table 1) result in a strong  $a$ -type spectrum and a considerably weaker  $b$ -type spectrum, with the methyl group potentially allowing for internal rotation splitting and energeti-

cally low-lying vibrational states giving rise to rather intense vibrational satellite spectra.

**Parent Isotopologue.** Initial scans of the millimeter-wave regime were performed around a wavelength of 2 mm in search of the characteristic *a*-type line pattern. Indeed, strong transitions were observed soon and were found to be fully compatible with the theoretical predictions on both large and small frequency scales. As can be seen in the top spectrum of Figure 2, the broadband scan around 200 GHz clearly features harmonically related line series, as expected for the *a*-type spectrum of a prolate asymmetric rotor. From coarse visual inspection of this scan alone, the separation between consecutive transitions is about 5 GHz, in very good agreement with the theoretical estimate of  $(B + C) = 5.25$  GHz calculated for  $C_2H_5CP$  (Table 1). At smaller scales, see the bottom spectrum in Figure 2, the assignment of  $C_2H_5CP$  to the carrier of the molecular absorption is secured immediately: As can be seen, the theoretical spectrum can be brought into near-perfect agreement with the dominant transitions of the experimental spectrum when a small shift of only 126 MHz is applied, identifying the experimental lines as belonging to the  $J = 33 \leftarrow 32$  transition. The spectroscopic offset of 126 MHz translates into a deviation of merely  $126 \text{ MHz}/33 \approx 4 \text{ MHz}$  in  $B + C$  between prediction and experiment, corresponding to an effective agreement on the order of one per mill. This small empirical correction permitted immediate detection and assignment of many lines from adjacent rotational transitions over a sizable quantum number regime.

Comprehensive spectroscopic analysis was finally carried out using the 75–120, 170–255, and 340–760 GHz broadband spectra and by tracing line series in Loomis-Wood plots employing the LLWP software.<sup>43</sup> Besides the capabilities of LLWP to facilitate spectroscopic assignment and (multi-component) spectral line profile fitting to evaluate transition frequencies accurately, it has also been designed as a frontend to Pickett's SPFIT/SPCAT program suite,<sup>44</sup> hence speeding up the spectroscopic analysis as a whole significantly. Owing to the high quality and predictive power of the CCSD(T) model (Table 1), spectral assignment was a rather straightforward procedure. Furthermore, consistency of line fitting was evaluated and supported using our Python package *Pyckett*, which is a Python wrapper around Pickett's SPFIT and SPCAT program suite, adding some very useful functionality.<sup>b</sup> Rather than estimating uniform transition frequency uncertainty, uncertainties of either 20, 30, or 40 kHz were assigned via an automated process, which is described in greater detail in the Supporting Information.

The final fit comprises 6041 ground-state transitions with 4024 unique frequencies spanning quantum number ranges of  $4 \leq J \leq 140$  and  $0 \leq K_a \leq 25$ . The majority of these lines are *a*-type transitions (4340 transitions with 2856 unique frequencies) complemented with *b*-type transitions (1701 transitions with 1223 unique frequencies) that proved more difficult to assign due to their lower intensities. However, LLWP's Blended Lines Window allowed us to derive accurate line positions even for weak or moderately blended lines. No *A/E*-splitting from internal rotation of the methyl group was observed. The final fit parameters are collected in Table 1. As can be seen, the full set of sextic and five octic centrifugal distortion parameters were needed to reproduce the transition frequencies within their experimental uncertainties ( $RMS = 30$  kHz,  $WRMS = 1.00$ ). The agreement between the calculated and the experimental molecular parameters is excellent.

Only a very small number of 25 transitions at 14 unique frequencies were omitted from the fit due to  $(\nu_{\text{obs}} - \nu_{\text{calc}})/\Delta\nu_{\text{obs}}$  values greater than 5. Clearly, at values of about  $109 \leq J \leq 114$ , the ground vibrational state shows signs of a local perturbation (see Figure 3). From a rudimentary Boltzmann

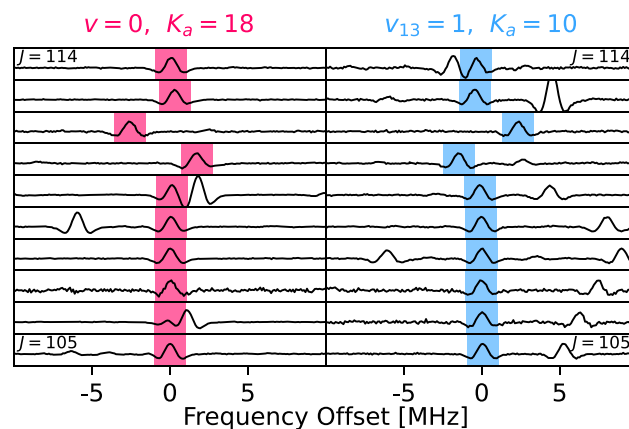


**Figure 3.** Side-by-side Loomis-Wood plots for the  $J_{18,J-17} \leftarrow J - 1_{18,J-18}$  series of the vibrational ground state  $\nu = 0$  (left side in red) and the  $J_{10,J-9} \leftarrow J - 1_{10,J-10}$  series of the energetically lowest vibrationally excited state  $\nu_{13} = 1$  (right side in blue). The two sides are almost perfect mirror images with strong deviations for  $J = 111$  and  $J = 112$ . This indicates interactions between the two states centered around the respective  $J = 111$  energy levels. The predictions from this work were used as the center frequencies for  $\nu = 0$ , while for  $\nu_{13} = 1$ , a polynomial of degree 2 was fitted to the ten here seen assignments as its preliminary analysis is not sufficiently accurate.

analysis performed through intensity comparison of vibrational satellites and ground state lines, the vibrational wavenumber is estimated as  $170 \text{ cm}^{-1}$ , hinting toward the energetically lowest state  $\nu_{13} = 1$ , the first excited in-plane C–C–P bending mode (see Supporting Information). While a quantitative perturbation treatment is beyond the scope of the present paper, a preliminary fit of the vibrational satellite lines compared against the ground-state parameters yields rotation-vibration interaction constants in good agreement with values obtained from the anharmonic force field calculations,<sup>c</sup> substantiating this assignment. Further yet preliminary inspection of the  $\nu_{13}$  vibrational satellite pattern with LLWP provides evidence that the state is not just part of a dyad with the ground vibrational state but part of a polyad with other vibrational states. A comprehensive treatment of the vibrational satellite spectrum will be the subject of future analysis.

Additionally, *a*-type transitions of the vibrational ground state with  $K_a = 22$  and  $K_a \geq 26$  show systematic deviations for high  $J$  values, which are most-likely also a result of the interaction with the  $\nu_{13}$  vibrational state. Thus, the analysis of the parent isotopologue was limited to transitions with  $K_a < 26$ .

**Singly Substituted  $^{13}C$  Isotopologues.** While the detection of the singly substituted  $^{13}C$  species proved challenging due to low line intensities as well as the overall high line density and line blending (see Figure 4), spectroscopic assignment was finally feasible based on empirically improved predictions obtained by scaling the theoretical rotational parameters of the minor species with correction factors obtained from the parent species (see Supporting Information). This procedure finally enabled the detection of  $K_a = 0, 1$  line series very close to the scaled

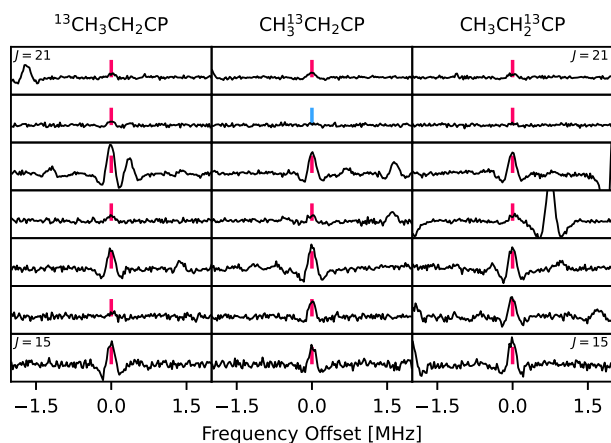


**Figure 4.** Loomis-Wood plot of the  $J_{0J} \leftarrow J - 1_{0J-1}$  transitions for the three singly substituted  $^{13}\text{C}$  species of  $\text{C}_2\text{H}_5\text{CP}$ . Predictions are shown as sticks in red if the transition is assigned or blue if unassigned. The measured intensity of the lines is highly dependent on the power of the source at the respective frequencies. The overall signal-to-noise ratio is very low for these isotopologues, severely limiting the number of possible assignments.

predictions using the LLWP program. Once a valid spectroscopic assignment had been accomplished, assignment of additional series was much easier; however, only  $a$ -type spectra up to 500 GHz were assigned with confidence. Many transitions were found blended with close-by strong lines. This was especially severe for  $\text{CH}_3\text{CH}_2^{13}\text{CP}$  as its  $B$  and  $C$  constants are very similar to those of the parent isotopologue. As a result,

the quantum number coverage of  $\text{CH}_3\text{CH}_2^{13}\text{CP}$  is significantly more limited compared with that of the other two species.

For all rare isotopologues, full quadratic and quartic parameter sets were used. For the sextic parameters, only  $H_J$ ,  $H_{JK}$ ,  $H_{KJ}$ , and  $h_1$  were determined, which is a result of having only  $a$ -type transitions assigned. To provide more accurate predictions outside the covered quantum number range, undetermined parameters were set to the main isotopologue values. The resulting molecular parameters are listed in Table 2. The parameters match the scaled predictions very well (see Supporting Information).

While the isotopic data obtained in the present study are by far not sufficient to derive an unconstrained empirical molecular structure of  $\text{C}_2\text{H}_5\text{CP}$ , they may be used to derive structural information about the carbon backbone. If the experimental ground-state rotational constants of all four isotopologues available are first corrected for the effects of zero-point vibration (calculated here at the fc-CCSD(T)/ANO1 level of theory, Table 1 and Supporting Information) prior to structural refinement, then semi-experimental equilibrium structural parameters  $r_e^{\text{SE}}$  are obtained<sup>45,46</sup> that may be compared directly to their ab initio values. Using this strategy and keeping the majority of structural parameters fixed at their ae-CCSD(T)/cc-pwCVQZ values, the two C–C bond lengths as well as the C–C–C angle are determined as  $r_{\text{H}_3\text{C}-\text{CH}_2} = 1.5293(2)$  Å,  $r_{\text{H}_2\text{C}-\text{CP}} = 1.4647(2)$  Å, and  $\alpha_{\text{CCC}} = 112.20(1)^\circ$ . These values are in excellent agreement with their ae-CCSD(T)/cc-pwCVQZ counterparts (Supporting Information). Any extension of the empirical structure determination in the future will require the experimental characterization of a

**Table 2.** Molecular Parameters of  $\text{C}_2\text{H}_5\text{CP}$  and Its Singly Substituted  $^{13}\text{C}$  Isotopologues<sup>b</sup>

parameter	$\text{CH}_3\text{CH}_2\text{CP}$	$^{13}\text{CH}_3\text{CH}_2\text{CP}$	$\text{CH}_3^{13}\text{CH}_2\text{CP}$	$\text{CH}_3\text{CH}_2^{13}\text{CP}$
$A/\text{MHz}$	25216.12285(35)	24834.81(19)	24696.03(15)	25115.37(19)
$B/\text{MHz}$	2709.143447(22)	2641.07228(69)	2686.01405(83)	2708.97088(95)
$C/\text{MHz}$	2520.638536(21)	2457.88562(70)	2495.32816(71)	2519.45345(67)
$-D_J/\text{Hz}$	−900.7695(38)	−883.46(13)	−861.16(15)	−897.91(23)
$-D_{JK}/\text{kHz}$	24.101222(85)	24.6990(22)	22.2244(20)	24.467(13)
$-D_K/\text{kHz}$	−547.7691(34)	−552(19)	−505(20)	−563(18)
$d_1/\text{Hz}$	−153.7099(23)	−149.84(20)	−149.67(24)	−155.40(23)
$d_2/\text{Hz}$	−8.11625(97)	−7.635(45)	−8.242(74)	−8.133(43)
$H_J/\text{mHz}$	1.50407(31)	1.507(25)	1.363(25)	1.582(45)
$H_{JK}/\text{mHz}$	−14.8371(54)	−17.12(51)	−11.89(45)	−14.1(3.3)
$H_{KJ}/\text{Hz}$	−1.37747(40)	−1.3748(89)	−1.3072(70)	−1.34(11)
$H_K/\text{Hz}$	36.895(11)	<i>a</i>	<i>a</i>	<i>a</i>
$h_1/\mu\text{Hz}$	490.70(24)	518(44)	503(53)	549(49)
$h_2/\mu\text{Hz}$	69.37(13)	<i>a</i>	<i>a</i>	<i>a</i>
$h_3/\mu\text{Hz}$	6.570(15)	<i>a</i>	<i>a</i>	<i>a</i>
$L_J/\text{nHz}$	−3.0130(87)	<i>a</i>	<i>a</i>	<i>a</i>
$L_{JK}/\mu\text{Hz}$	−2.446(11)	<i>a</i>	<i>a</i>	<i>a</i>
$L_{KJ}/\mu\text{Hz}$	71.50(53)	<i>a</i>	<i>a</i>	<i>a</i>
$l_1/\text{nHz}$	−1.3244(74)	<i>a</i>	<i>a</i>	<i>a</i>
$l_2/\text{pHz}$	−259.3(5.0)	<i>a</i>	<i>a</i>	<i>a</i>
transitions	6016	417	556	163
lines	4010	282	366	133
RMS/kHz	29.7	26.5	25.3	27.7
WRMS	1.00	0.75	0.71	0.77

<sup>a</sup>Parameter was fixed to the parent isotopologue value. <sup>b</sup>Fits performed with SPFIT in the S-reduction and I' representation. Standard errors are given in parentheses.

much larger sample of isotopologues, most notably deuterated variants.

## CONCLUSIONS

Ethyl phosphalkyne,  $C_2H_5CP$ , has been detected spectroscopically in the gas phase for the first time. The pure rotational spectrum of the parent isotopic species could be detected, assigned, and analyzed, covering frequencies as high as 760 GHz. In addition, the three singly substituted  $^{13}C$ -species were also observed and characterized up to 500 GHz. The experimental findings agree very well with the results of the high-level CCSD(T) calculations.

Future analysis of the vibrational satellite spectrum will be an interesting and challenging task.  $C_2H_5CP$  possesses a sizable number of energetically low-lying vibrational modes. Consequently, the vibrational satellite spectrum will comprise contributions not only from fundamental vibrations but also from overtone and combination modes additionally, providing ample opportunity for interactions and hence perturbed spectra. As has been shown here, even the ground vibrational state is subject to perturbation at high values of  $J$  and  $K_a$ .

Now that the pure rotational spectrum of  $C_2H_5CP$  in the ground vibrational state has been studied to high accuracy, astronomical searches for this phosphalkyne in suitable sources are feasible. Frequency predictions along with all relevant data (line lists, fit files) will be provided and archived through the Cologne Database for Molecular Spectroscopy (CDMS).<sup>47,48</sup>

## ASSOCIATED CONTENT

### Supporting Information

The Supporting Information is available free of charge at <https://pubs.acs.org/doi/10.1021/acs.jpca.4c02566>.

Minimum and transition-state structure as well as vibrational wavenumbers and zero-point vibrational contributions to the rotational constants resulting from the quantum-chemical calculations, calculated and scaled rotational constants for the singly  $^{13}C$  substituted isotopologues, more in-detail descriptions of the reproducibility measurements, and the automated transition frequency uncertainty assignment procedure (PDF)

## AUTHOR INFORMATION

### Corresponding Author

Sven Thorwirth – I. Physikalisches Institut, Universität zu Köln, Köln 50937, Germany; [orcid.org/0000-0001-8200-6710](https://orcid.org/0000-0001-8200-6710); Email: [sthorwirth@ph1.uni-koeln.de](mailto:sthorwirth@ph1.uni-koeln.de)

### Authors

Luis Bonah – I. Physikalisches Institut, Universität zu Köln, Köln 50937, Germany; [orcid.org/0000-0001-5686-7883](https://orcid.org/0000-0001-5686-7883)

Stephan Schlemmer – I. Physikalisches Institut, Universität zu Köln, Köln 50937, Germany; [orcid.org/0000-0002-1421-7281](https://orcid.org/0000-0002-1421-7281)

Jean-Claude Guillemin – Université de Rennes, Ecole Nationale Supérieure de Chimie de Rennes, CNRS, ISCR—UMR6226, Rennes 35000, France; [orcid.org/0000-0002-2929-057X](https://orcid.org/0000-0002-2929-057X)

Michael E. Harding – Institut für Nanotechnologie, Karlsruher Institut für Technologie (KIT), Karlsruhe 76131, Germany; [orcid.org/0000-0002-3633-493X](https://orcid.org/0000-0002-3633-493X)

Complete contact information is available at: <https://pubs.acs.org/doi/10.1021/acs.jpca.4c02566>

## Notes

The authors declare no competing financial interest.

## ACKNOWLEDGMENTS

L.B., S.S., and S.T. gratefully acknowledge the Collaborative Research Center 1601 (SFB 1601 subproject A4) funded by the Deutsche Forschungsgemeinschaft (DFG, German Research Foundation)—500700252. M.E.H. acknowledges support by the Bundesministerium für Bildung und Forschung (BMBF) through the Helmholtz research program “Materials Systems Engineering” (MSE). J.-C.G. thanks the CNRS national program PCMI (Physics and Chemistry of the Interstellar Medium) and the University of Rennes for a grant.

## ADDITIONAL NOTES

<sup>a</sup>Available at <https://github.com/Ltotheois/SnippetsForSpectroscopy/tree/main/FFTCorrection>.

<sup>b</sup>This work made extensive use of Pyckett's CLI tools `pyckett_add` and `pyckett_omit` to analyze the influence of adding sensible additional parameters to the Hamiltonian or omitting any of the included parameters from the Hamiltonian. See <https://pypi.org/project/pyckett/> for more information or install with pip via `pip install pyckett`

<sup>c</sup>Calculations yield  $\alpha_{\nu_{13}}^A = 146.32$  MHz,  $\alpha_{\nu_{13}}^B = -8.28$  MHz, and  $\alpha_{\nu_{13}}^C = -3.61$  MHz while a preliminary fit yields  $\alpha_{\nu_{13}}^A = 180(3)$  MHz,  $\alpha_{\nu_{13}}^B = -8.280(7)$  MHz, and  $\alpha_{\nu_{13}}^C = -3.613(7)$  MHz.

## REFERENCES

- (1) Snyder, L. E.; Buhl, D. Observations of Radio Emission from Interstellar Hydrogen Cyanide. *Astrophys. J.* **1971**, *163*, L47.
- (2) Zack, L. N.; Halfen, D. T.; Ziurys, L. M. Detection of FeCN ( $X^4\Delta$ ) in IRC+10216: A New Interstellar Molecule. *Astrophys. J. Lett.* **2011**, *733*, L36.
- (3) Cernicharo, J.; Marcelino, N.; Pardo, J. R.; Agúndez, M.; Tercero, B.; de Vicente, P.; Cabezas, C.; Bermúdez, C. Interstellar nitrile anions: Detection of  $C_3N^-$  and  $C_5N^-$  in TMC-1. *Astron. Astrophys.* **2020**, *641*, L9.
- (4) Cernicharo, J.; Cabezas, C.; Pardo, J. R.; Agúndez, M.; Roncero, O.; Tercero, B.; Marcelino, N.; Guélin, M.; Endo, Y.; de Vicente, P. The magnesium paradigm in IRC+10216: Discovery of  $MgC_4H^+$ ,  $MgC_3N^+$ ,  $MgC_6H^+$ , and  $MgC_5N^+$ . *Astron. Astrophys.* **2023**, *672*, L13.
- (5) McGuire, B. A.; Loomis, R. A.; Burkhardt, A. M.; Lee, K. L. K.; Shingledecker, C. N.; Charnley, S. B.; Cooke, I. R.; Cordiner, M. A.; Herbst, E.; Kalenskii, S.; et al. Detection of two interstellar polycyclic aromatic hydrocarbons via spectral matched filtering. *Science* **2021**, *371*, 1265–1269.
- (6) Sita, M. L.; Changala, P. B.; Xue, C.; Burkhardt, A. M.; Shingledecker, C. N.; Lee, K. L. K.; Loomis, R. A.; Momjian, E.; Siebert, M. A.; Gupta, D.; et al. Discovery of Interstellar 2-Cyanoindene ( $2-C_9H_7CN$ ) in GOTHAM Observations of TMC-1. *Astrophys. J. Lett.* **2022**, *938*, L12.
- (7) Tyler, J. K. Microwave Spectrum of Methinophosphide, HCP. *J. Chem. Phys.* **1964**, *40*, 1170–1171.
- (8) Burckett-St. Laurent, J. C. T. R.; Cooper, T. A.; Kroto, H. W.; Nixon, J. F.; Ohashi, O.; Ohno, K. The detection of some new phosphalkynes,  $RC\equiv P$ , using microwave spectroscopy. *J. Mol. Struct.* **1982**, *79*, 215–220.
- (9) Bizzocchi, L.; Thorwirth, S.; Müller, H. S. P.; Lewen, F.; Winnewisser, G. Submillimeter-Wave Spectroscopy of Phosphal-

kynes: HCCCP, NCCP, HCP, and DCP. *J. Mol. Spectrosc.* **2001**, *205*, 110–116.

(10) Bizzocchi, L.; Degli Esposti, C.; Dore, L.; Puzzarini, C. Lamb-dip millimeter-wave spectroscopy of HCP: Experimental and theoretical determination of  $^{31}\text{P}$  nuclear spin–rotation coupling constant and magnetic shielding. *Chem. Phys. Lett.* **2005**, *408*, 13–18.

(11) Bizzocchi, L.; Degli Esposti, C.; Botschwina, P. Millimeter-wave spectroscopy of  $\text{HC}_3\text{P}$  isotopomers and coupled-cluster calculations: the molecular structure of phosphabutadiyne. *Chem. Phys. Lett.* **2000**, *319*, 411–417.

(12) Bizzocchi, L.; Degli Esposti, C.; Botschwina, P. Millimeter-wave spectroscopy and coupled cluster calculations for a new phosphorus-carbon chain:  $\text{HC}_3\text{P}$ . *J. Chem. Phys.* **2003**, *119*, 170–175.

(13) Bizzocchi, L.; Degli Esposti, C.; Botschwina, P. Vibrationally excited states of  $\text{HC}_3\text{P}$ : millimetre-wave spectroscopy and coupled cluster calculations. *Phys. Chem. Phys.* **2003**, *5*, 4090–4095.

(14) Bizzocchi, L.; Degli Esposti, C. Pyrolysis of ortho-cyanotoluene and  $\text{PCl}_3$  mixtures: the millimeter and submillimeter-wave spectrum of NCCCCP. *J. Mol. Spectrosc.* **2003**, *221*, 186–191.

(15) Bizzocchi, L.; Degli Esposti, C.; Botschwina, P. Vibrationally excited states of  $\text{NC}_4\text{P}$ : millimetre-wave spectroscopy and coupled cluster calculations. *Phys. Chem. Phys.* **2004**, *6*, 46–50.

(16) Ohno, K.; Kroto, H. W.; Nixon, J. F. The Microwave Spectrum of 1-Phosphabut-3-ene-1-yne,  $\text{CH}_2=\text{CHC}\equiv\text{P}$ . *J. Mol. Spectrosc.* **1981**, *90*, 507–511.

(17) Transue, W. J.; Yang, J.; Nava, M.; Sergeev, I. V.; Barnum, T. J.; McCarthy, M. C.; Cummins, C. C. Synthetic and Spectroscopic Investigations Enabled by Modular Synthesis of Molecular Phosphaalkyne Precursors. *J. Am. Chem. Soc.* **2018**, *140*, 17985–17991.

(18) Degli Esposti, C.; Melosso, M.; Bizzocchi, L.; Tamassia, F.; Dore, L. Determination of a semi-experimental equilibrium structure of 1-phosphapropyne from millimeter-wave spectroscopy of  $\text{CH}_3\text{CP}$  and  $\text{CD}_3\text{CP}$ . *J. Mol. Struct.* **2020**, *1203*, 127429.

(19) Burckett-St. Laurent, J. C. T. R.; Kroto, H. W.; Nixon, J. F.; Ohno, K. The Microwave Spectrum of 1-Phenylphosphaethyne,  $\text{C}_6\text{H}_5\text{C}\equiv\text{P}$ . *J. Mol. Spectrosc.* **1982**, *92*, 158–161.

(20) Samdal, S.; Møllendal, H.; Guillemin, J.-C. Synthesis, Microwave Spectrum, Quantum Chemical Calculations, and Conformational Composition of the Novel Compound Cyclopropylethylidynephosphine ( $\text{C}_3\text{H}_5\text{CH}_2\text{C}\equiv\text{P}$ ). *J. Phys. Chem. A* **2014**, *118*, 9994–10001.

(21) Agúndez, M.; Cernicharo, J.; Guélin, M. Discovery of Phosphaethyne (HCP) in Space: Phosphorus Chemistry in Circumstellar Envelopes. *Astrophys. J.* **2007**, *662*, L91–L94.

(22) Agúndez, M.; Cernicharo, J.; Guélin, M. New molecules in IRC +10216: confirmation of  $\text{C}_3\text{S}$  and tentative identification of  $\text{MgCCH}$ , NCCP, and  $\text{SiH}_3\text{CN}$ . *Astron. Astrophys.* **2014**, *570*, A45.

(23) Endres, C. P.; Martin-Drumel, M.-A.; Zingsheim, O.; Bonah, L.; Piralí, O.; Zhang, T.; Sánchez-Monge, A.; Möller, T.; Wehres, N.; Schilke, P.; et al. SOLEIL and ALMA views on prototypical organic nitriles:  $\text{C}_2\text{H}_5\text{CN}$ . *J. Mol. Spectrosc.* **2021**, *375*, 111392.

(24) Guillemin, J.-C.; Janati, T.; Guenot, P.; Savignac, P.; Denis, J. M. Synthesis of Nonstabilized Phosphaalkynes by Vacuum Gas-Solid HCl Elimination. *Angew. Chem. Int. Ed. Engl.* **1991**, *30*, 196–198.

(25) Guillemin, J.-C.; Janati, T.; Denis, J.-M. A simple route to kinetically unstabilized phosphaalkynes. *J. Org. Chem.* **2001**, *66*, 7864–7868.

(26) Raghavachari, K.; Trucks, G. W.; Pople, J. A.; Head-Gordon, M. A fifth-order perturbation comparison of electron correlation theories. *Chem. Phys. Lett.* **1989**, *157*, 479–483.

(27) CFOUR, Coupled-Cluster techniques for Computational Chemistry, a quantum-chemical program package with contributions from Stanton, J. F.; Gauss, J.; Cheng, L.; Harding, M. E.; Matthews, D. A.; Szalay, P. G.; Auer, A.; Bartlett, R. J.; Benedikt, U.; Berger, C.; Bernholdt, D. E.; Bomble, Y. J.; Christiansen, O.; Engel, F.; Faber, R.; Heckert, M.; Heun, O.; Hilgenberg, M.; Huber, C.; Jagau, T.-C.; Jonsson, D.; Jusélius, J.; Kirsch, T.; Klein, K.; Lauderdale, W. J.; Lipparini, F.; Metzroth, T.; Mück, L. A.; O'Neill, D. P.; Price, D. R.; Prochnow, E.; Puzzarini, C.; Ruud, K.; Schiffmann, F.; Schwalbach,

W.; Simmons, C.; Stopkowitz, S.; Tajti, A.; Vázquez, J.; Wang, F.; Watts, J. D. and the integral packages MOLECULE. (J. Almlöf and P.R. Taylor), PROPS (P.R. Taylor), ABACUS (T. Helgaker, H.J. Aa. Jensen, P. Jørgensen, and J. Olsen), and ECP routines by A. V. Mitin and C. van Wüllen. For the current version, see <http://www.cfour.de>. (visited on 08/15/2019).

(28) Matthews, D. A.; Cheng, L.; Harding, M. E.; Lipparini, F.; Stopkowitz, S.; Jagau, T.-C.; Szalay, P. G.; Gauss, J.; Stanton, J. F. Coupled-cluster techniques for computational chemistry: The CFOUR program package. *J. Chem. Phys.* **2020**, *152*, 214108.

(29) Harding, M. E.; Metzroth, T.; Gauss, J.; Auer, A. A. Parallel calculation of CCSD and CCSD(T) analytic first and second derivatives. *J. Chem. Theory Comput.* **2008**, *4*, 64–74.

(30) Dunning, T. H. Gaussian basis sets for use in correlated molecular calculations. I. The atoms boron through neon and hydrogen. *J. Chem. Phys.* **1989**, *90*, 1007–1023.

(31) Dunning, T. H.; Peterson, K. A.; Wilson, A. K. Gaussian basis sets for use in correlated molecular calculations. X. The atoms aluminum through argon revisited. *J. Chem. Phys.* **2001**, *114*, 9244–9253.

(32) Almlöf, J.; Taylor, P. R. General contraction of Gaussian basis sets. I. Atomic natural orbitals for first- and second-row atoms. *J. Chem. Phys.* **1987**, *86*, 4070–4077.

(33) Peterson, K. A.; Dunning, T. H. Accurate correlation consistent basis sets for molecular core-valence correlation effects: The second row atoms Al–Ar, and the first row atoms B–Ne revisited. *J. Chem. Phys.* **2002**, *117*, 10548–10560.

(34) Watts, J. D.; Gauss, J.; Bartlett, R. J. Open-shell analytical energy gradients for triple excitation many-body, coupled-cluster methods: MBPT(4), CCSD+T(CCSD), CCSD(T), and QCISD(T). *Chem. Phys. Lett.* **1992**, *200*, 1–7.

(35) Coriani, S.; Marchesan, D.; Gauss, J.; Hättig, C.; Helgaker, T.; Jørgensen, P. The accuracy of ab initio molecular geometries for systems containing second-row atoms. *J. Chem. Phys.* **2005**, *123*, 184107.

(36) Gauss, J.; Stanton, J. F. Analytic CCSD(T) second derivatives. *Chem. Phys. Lett.* **1997**, *276*, 70–77.

(37) Stanton, J. F.; Gauss, J. Analytic second derivatives in high-order many-body perturbation and coupled-cluster theories: computational considerations and applications. *Int. Rev. Phys. Chem.* **2000**, *19*, 61–95.

(38) Stanton, J. F.; Lopreore, C. L.; Gauss, J. The equilibrium structure and fundamental vibrational frequencies of dioxirane. *J. Chem. Phys.* **1998**, *108*, 7190–7196.

(39) Gauss, J.; Ruud, K.; Helgaker, T. Perturbation-dependent atomic orbitals for the calculation of spin-rotation constants and rotational g tensors. *J. Chem. Phys.* **1996**, *105*, 2804–2812.

(40) Puzzarini, C.; Stanton, J. F.; Gauss, J. Quantum-chemical calculation of spectroscopic parameters for rotational spectroscopy. *Int. Rev. Phys. Chem.* **2010**, *29*, 273–367.

(41) Martin-Drumel, M. A.; van Wijngaarden, J.; Zingsheim, O.; Lewen, F.; Harding, M. E.; Schlemmer, S.; Thorwirth, S. Millimeter- and submillimeter-wave spectroscopy of disulfur dioxide, OSSO. *J. Mol. Spectrosc.* **2015**, *307*, 33–39.

(42) Zingsheim, O.; Bonah, L.; Lewen, F.; Thorwirth, S.; Müller, H. S. P.; Schlemmer, S. Millimeter-millimeter-wave double-modulation double-resonance spectroscopy. *J. Mol. Spectrosc.* **2021**, *381*, 111519.

(43) Bonah, L.; Zingsheim, O.; Müller, H. S. P.; Guillemin, J.-C.; Lewen, F.; Schlemmer, S. LLWP—A new Loomis-Wood software at the example of Acetone- $^{13}\text{C}_1$ . *J. Mol. Spectrosc.* **2022**, *388*, 111674.

(44) Pickett, H. M. The fitting and prediction of vibration-rotation spectra with spin interactions. *J. Mol. Spectrosc.* **1991**, *148*, 371–377.

(45) Vázquez, J.; Stanton, J. F. *Equilibrium Molecular Structures—From Spectroscopy to Quantum Chemistry*; Demaison, J., Boggs, J. E., Császár, A. G., Eds.; CRC Press, 2011; pp 53–87.

(46) Kisiel, Z. Least-squares mass-dependence molecular structures for selected weakly bound intermolecular clusters. *J. Mol. Spectrosc.* **2003**, *218*, 58–67.

(47) Müller, H. S. P.; Thorwirth, S.; Roth, D. A.; Winnewisser, G. The Cologne Database for Molecular Spectroscopy, CDMS. *Astron. Astrophys.* **2001**, 370, L49–L52.

(48) Endres, C. P.; Schlemmer, S.; Schilke, P.; Stutzki, J.; Müller, H. S. P. The Cologne Database for Molecular Spectroscopy, CDMS, in the Virtual Atomic and Molecular Data Centre, VAMDC. *J. Mol. Spectrosc.* **2016**, 327, 95–104.

# 8. Towards Higher Frequencies and Vibrational States of *c*-C<sub>5</sub>H<sub>6</sub>

## Bibliographic Information

L. Bonah, B. Helmstaedter, J.-C. Guillemin, S. Schlemmer, S. Thorwirth, Extending the rotational spectrum of cyclopentadiene towards higher frequencies and vibrational states, *J. Mol. Spectrosc.* 408 (2025) 111967. doi:10.1016/j.jms.2024.111967.

## Author's contribution

The author of this thesis performed the measurements together with the second author. Furthermore, he performed the analysis, wrote the original draft and provided the visualization.

## Context

This study analyzes the rotational spectrum of cyclopentadiene (*c*-C<sub>5</sub>H<sub>6</sub>), a polar cyclic hydrocarbon that has already been found in space.<sup>26</sup> All vibrational states below 850 cm<sup>-1</sup> were analyzed, and two interaction systems were identified and explicitly described in combined fits. This makes the work a case study in the identification and analysis of vibrationally excited states and interactions between them.

## Copyright Notice

Reprinted with permission from *J. Mol. Spectrosc.* 2025, **408**, 111967. © 2025 Elsevier.



# Extending the rotational spectrum of cyclopentadiene towards higher frequencies and vibrational states

Luis Bonah <sup>a</sup>,\* , Benedikt Helmstaedter <sup>a</sup> , Jean-Claude Guillemin <sup>b</sup>, Stephan Schlemmer <sup>a</sup>, Sven Thorwirth <sup>a</sup>

<sup>a</sup> I. Physikalisches Institut, Universität zu Köln, Zùlpicher Str. 77, Köln, 50937, Germany

<sup>b</sup> Univ Rennes, Ecole Nationale Supérieure de Chimie de Rennes, ISCR-UMR 6226, Rennes, 35000, France

## ARTICLE INFO

### Keywords:

Rotational spectroscopy  
Vibrationally excited states  
Coriolis interaction  
Absorption spectroscopy

## ABSTRACT

Cyclopentadiene ( $c\text{-C}_5\text{H}_6$ ) is a cyclic pure hydrocarbon that was already detected astronomically towards the prototypical dark cloud TMC-1 (Cernicharo et al., 2021). However, accurate predictions of its rotational spectrum are still limited to the microwave region and narrow quantum number ranges. In the present study, the pure rotational spectrum of cyclopentadiene was measured in the frequency ranges 170–250 GHz and 340–510 GHz to improve the number of vibrational ground state assignments by more than a factor of 20, resulting in more accurate rotational parameters and the determination of higher-order centrifugal distortion parameters. Additionally, vibrational satellite spectra of cyclopentadiene in its eight energetically lowest vibrationally excited states were analyzed for the first time. Coriolis interactions between selected vibrational states were identified and treated successfully in combined fits. Previous microwave work on the three singly  $^{13}\text{C}$  substituted isotopologues was extended significantly also covering frequency ranges up to 250 GHz. The new data sets permit reliable frequency predictions for the isotopologues and vibrational satellite spectra far into the sub-mm-wave range. Finally, the experimental rotational constants of all available isotopologues and calculated zero-point vibrational contributions to the rotational constants were used to derive a semi-experimental equilibrium structure of this fundamental ring molecule.

## 1. Introduction

Cyclopentadiene ( $c\text{-C}_5\text{H}_6$ ) is a polar cyclic hydrocarbon with an appreciable dipole moment of 0.419(4) D [1]. In the laboratory, its rotational spectrum was first studied in the microwave by Laurie in 1956 [2]. Later studies measured more microwave transitions [1,3] and extended the frequency coverage into the mm-wave region up to 390 GHz [4]. However, even in the most recent work by Bogey et al. [4] only 99 lines were reported. The resulting parameters have high uncertainties and no sextic or higher-order parameters were fitted. Therefore, the accuracy for predictions outside the measured frequency and quantum number range leaves much room for improvement. In addition to the main isotopologue, the three singly  $^{13}\text{C}$  substituted isotopologues and different deuterium-substituted isotopologues were examined [1,5] in the microwave regime, but no mm-wave data are available. No vibrational satellite spectra have been reported so far for any isotopic species and only one vibrational band has been studied at high spectral resolution, the  $\nu_{26}$  fundamental mode of the parent isotopologue [6]. However, eight vibrational states lie below  $850\text{ cm}^{-1}$  with the methylene-rocking motion being the lowest at about  $350\text{ cm}^{-1}$

(see Fig. 1) [7]. The narrow spacing between some vibrational levels suggests they might be subject to considerable interactions.

Cyclopentadiene was detected astronomically towards TMC-1 [8] via five lines with low quantum numbers ( $2 \leq J \leq 5$  and  $K_a \leq 3$ ) around 38 GHz and 46 GHz, all of which belong to the vibrational ground state of the main isotopologue.

This work aims at extending the frequency and quantum number coverage of the main isotopologue and the singly  $^{13}\text{C}$  substituted isotopologues. Additionally, for the parent isotopic species, rotational analyses of all vibrationally excited states below  $850\text{ cm}^{-1}$  are presented, including a treatment of two resonance systems identified for the first time.

## 2. Experimental details

High-resolution broadband spectra of cyclopentadiene were recorded with an absorption spectrometer in the frequency ranges 170–250 GHz and 340–510 GHz. A commercially available radiation

\* Corresponding author.

E-mail address: [bonah@ph1.uni-koeln.de](mailto:bonah@ph1.uni-koeln.de) (L. Bonah).

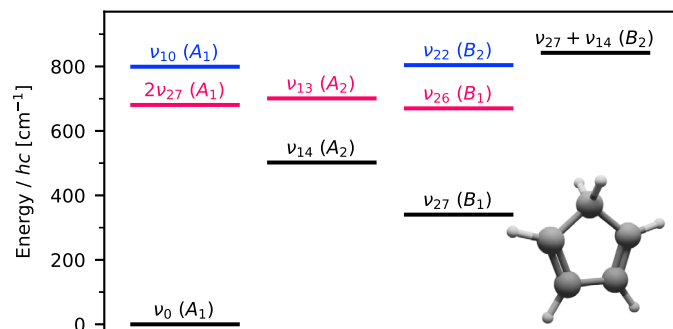


Fig. 1. The vibrational states of cyclopentadiene below  $850\text{ cm}^{-1}$ . The respective symmetries are given in parentheses. The two interaction systems are indicated by blue and red color.

source from Virginia Diodes was combined with two different amplifier-multiplier chains to reach the desired frequency ranges. A 5 m absorption cell was used in a double-pass setup for a total absorption path of 10 m. On the detection side, a Schottky detector was employed with subsequent preamplifiers and a lock-in amplifier. The radio frequency was frequency modulated by the synthesizer and a  $2f$  demodulation of the detector signal was performed by the lock-in amplifier to increase the signal-to-noise ratio (SNR). The resulting lineshapes look similar to a second derivative Voigt profile. The spectrometer was described in greater detail elsewhere previously [9].

Commercially, cyclopentadiene is not available in monomeric form but as a Diels–Alder adduct, dicyclopentadiene. It may however be produced from the adduct through a thermally induced retro-Diels–Alder reaction. In the present study, the thermolysis used a quartz tube, an oven with a 10 cm heating zone and a temperature of about  $560\text{ }^\circ\text{C}$  which was determined to yield optimal production for this specific setup [10]. A needle valve attached to the sample container allowed to precisely set the precursor flow. To increase the vapor pressure of dicyclopentadiene and prevent clogging of the needle valve, the sample container and the valve were resistively heated to about  $55\text{ }^\circ\text{C}$ . The rotational temperature in the absorption cell was room temperature as is apparent from the rotational spectrum (see e.g. the good agreement between the experimental intensities and the predictions performed at  $300\text{ K}$  in Fig. 2). Due to the thermolysis, all measurements were performed under mild flow conditions while keeping the pressure in the cell in the range of  $20\text{--}30\text{ }\mu\text{bar}$ . Standing waves were removed from the raw spectral data via Fourier filtering with a self-written script.<sup>1</sup>

### 3. Spectroscopic fingerprint of cyclopentadiene

Cyclopentadiene is an asymmetric top rotor close to the oblate limit as seen from its Ray's asymmetry parameter  $\kappa = (2B - A - C)/(A - C) = 0.90$ . The main isotopologue has  $C_{2v}$  symmetry<sup>2</sup> resulting in the two spin species ortho ( $K_a + K_c$  odd) and para ( $K_a + K_c$  even) with statistical weights of 9 and 7, respectively [6,8]. Only the  $b$ -type dipole moment is non-zero ( $0.419(4)\text{ D}$  [1]) and the rotational spectrum mainly comprises two characteristic patterns for  $\Delta J = 1$  ( $R$ -branch) and  $\Delta J = 0$  ( $Q$ -branch) transitions which are highlighted in Fig. 2.

The  $R$ -branch line series consist of  $\Delta J_{\Delta K_a, \Delta K_c} = 1_{\pm 1, 1}$  transitions. For high  $J$  values the  $\Delta K_a = +1$  transitions are blended with the respective  $\Delta K_a = -1$  transitions. Transitions with the same  $J + K_a$  value form patterns (see red lines in Fig. 2) that increase in  $J$  with increasing frequency. When  $K_a$  is far from  $J$ , the lines are spaced almost

<sup>1</sup> <https://github.com/Ltotheois/SnippetsForSpectroscopy/tree/main/FFTCorrection>.

<sup>2</sup> The naming of the symmetry species  $B_1$  and  $B_2$  is swapped in this work compared to some older works, e.g. Castellucci et al. [7].

Table 1

The resulting rotational parameters for the vibrational ground states of the main isotopologue and the three singly  $^{13}\text{C}$  substituted isotopologues.

Parameter	$c\text{-C}_5\text{H}_6$	$1\text{-}^{13}\text{C}$	$2\text{-}^{13}\text{C}$	$3\text{-}^{13}\text{C}$
$A$ /MHz	8426.108825(35)	8226.0534(18)	8420.04351(98)	8345.13300(94)
$B$ /MHz	8225.640352(33)	8219.4832(18)	8040.4326(14)	8108.7105(12)
$C$ /MHz	4271.437296(30)	4217.75907(40)	4219.40981(37)	4219.06493(33)
$-D_J$ /kHz	-2.692726(21)	-2.6502(22)	-2.6318(19)	-2.6357(17)
$-D_{JK}$ /kHz	4.059634(34)	3.9985(49)	3.9703(41)	3.9771(38)
$-D_K$ /kHz	-1.682765(22)	-1.6585(26)	-1.6472(22)	-1.6498(21)
$d_1$ /Hz	-42.220(10)	<sup>a</sup>	-17.2(1.3)	-12.7(1.3)
$d_2$ /Hz	-0.6014(36)	<sup>a</sup>	-5.06(60)	1.90(51)
$H_J$ /mHz	1.0208(37)	<sup>a</sup>	<sup>a</sup>	<sup>a</sup>
$H_{JK}$ /mHz	-4.0297(71)	<sup>a</sup>	<sup>a</sup>	<sup>a</sup>
$H_{KJ}$ /mHz	5.0425(73)	<sup>a</sup>	<sup>a</sup>	<sup>a</sup>
$H_K$ /mHz	-2.0316(41)	<sup>a</sup>	<sup>a</sup>	<sup>a</sup>
Transitions	3510	228	228	235
Lines	1992	120	143	145
RMS /kHz	21.40	14.97	16.72	16.31
WRMS	0.79	0.44	0.49	0.46

Fits performed with SPFIT in the S-reduction and III<sup>1</sup> representation. Standard errors are given in parentheses. Parameters of the vibrational ground state are applied to all vibrationally excited states and difference values are fitted.

<sup>a</sup> Parameter was fixed to the global value.

equidistantly (about  $430\text{ MHz}$ ). These patterns repeat every  $8.54\text{ GHz}$  corresponding to  $2(B + C - A) = 2C$  for the limiting case of an oblate symmetric top.

$Q$ -branches comprise  $\Delta J_{\Delta K_a, \Delta K_c} = 0_{1,-1}$  transitions and again the two asymmetry components are typically blended. Lines belonging to a single pattern (see blue lines in Fig. 2) share the same  $K_c$  value. Going from high to low frequencies, the pattern starts with the  $K_a'' = 0$  transition and its respective blended  $K_a'' = 1$  transition. Subsequent lines (at lower frequencies) increase in  $J$  and  $K_a$ . Similarly, the distance between lines increases slightly when  $J$  values increase. These  $Q$ -type patterns repeat about every  $8.1\text{ GHz}$ , which for the limiting case of an oblate symmetric top would be given by  $2(2B - A - C) = 2(B - C)$ .

Spectroscopic assignment was carried out via Loomis-Wood plots as implemented in the LLWP software [11]. Pickett's SPFIT was used for least squares fitting to an asymmetric top Hamiltonian in the S-reduction and III<sup>1</sup> representation [12]. Line uncertainties were determined with a semi-automatic procedure described previously [13].

Complementary quantum chemical calculations in support of the spectroscopic analysis were performed using the CFOUR suite of programs [14,15] using strategies outlined elsewhere [16]. Most importantly, the rotation-vibration interaction constants  $\alpha_i^{A,B,C}$  as well as vibrational wavenumbers  $\tilde{\nu}_i$  were derived from an anharmonic force field computed at the coupled-cluster (CC) singles and doubles level extended by a perturbative correction for the contribution from triple excitations, CCSD(T), [17] in combination with the ANO0 basis set [18] and in the frozen core (fc) approximation. A high-level equilibrium structure of cyclopentadiene was calculated at the CCSD(T)/cc-pwCVQZ level (cf. Ref. [19] and references therein) considering all electrons (ae) in the correlation treatment.

Assigning the spectrum of the main isotopologue was straightforward due to literature data covering frequencies up to  $390\text{ GHz}$  [4] and readily visible patterns. Literature data from frequency ranges not covered here [1,3,4] were incorporated into our analysis except data from Laurie [2] as their data shows a systematic offset (mean  $\nu_{\text{obs}} - \nu_{\text{calc}}$  value of  $136(114)\text{ kHz}$ ) and because most of their lines were remeasured in later works.

Substituting a single  $^{12}\text{C}$  with a  $^{13}\text{C}$  atom has considerable influence on the observed spectrum. When substituting the 1-C atom,<sup>3</sup> the  $a$ - and

<sup>3</sup> The labeling of carbon atoms is equivalent to the one in Scharpen et al. [1], where 1-C is the methylene carbon atom and the other carbons are numbered sequentially.

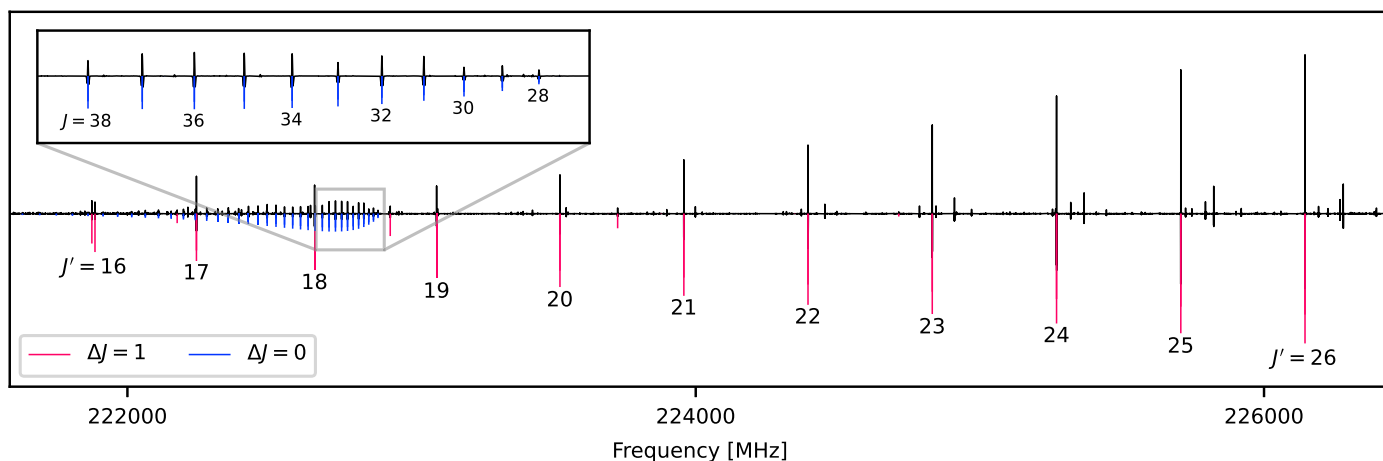


Fig. 2. Part of the experimental spectrum of cyclopentadiene in black. Typical  $\Delta J = 1$  and  $\Delta J = 0$  patterns of the  $b$ -type spectrum of cyclopentadiene are highlighted by the corresponding predictions in red and blue, respectively. The  $R$ -branch transitions are governed by  $\Delta J_{\Delta K_a, \Delta K_c} = 1_{\pm 1, 1}$  with  $K'_a = 26 - J'$  or  $27 - J'$  and  $J'$  as indicated. In the zoom-in,  $Q$ -branch transitions obey  $\Delta J_{\Delta K_a, \Delta K_c} = 0_{1, -1}$  and  $K'_a = J - 27$  or  $J - 26$ .

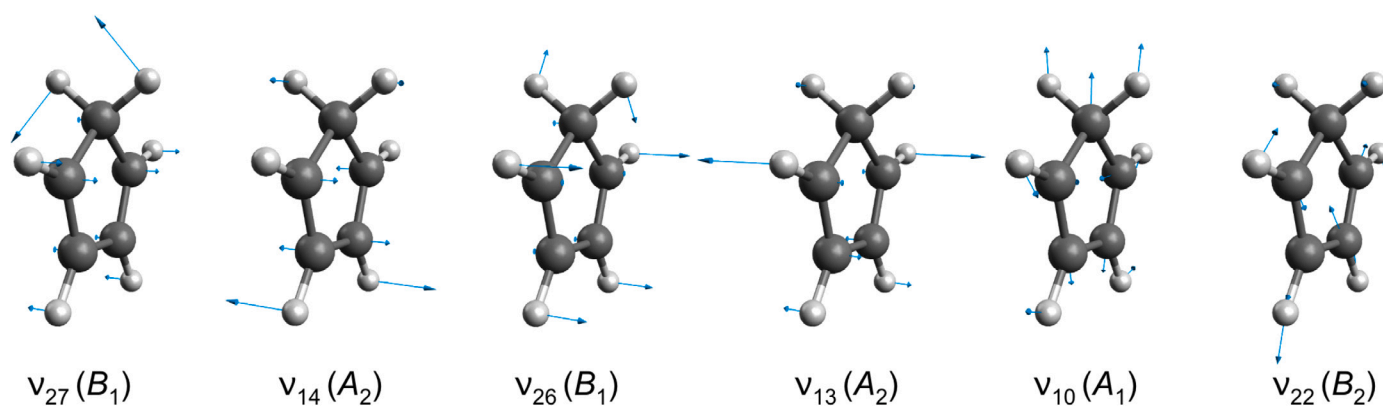


Fig. 3. The six energetically lowest vibrational fundamentals sorted to increasing energy from left to right.

$b$ -axes are swapped. Therefore, the  $A$  constant of the  $1\text{-}^{13}\text{C}$  isotopologue should be compared with the  $B$  constants of the other isotopologues and an  $a$ -type spectrum is observed. Substituting the 2-C or 3-C atom lifts the  $C_{2v}$  symmetry and rotates the principal axes in the  $a - b$  plane introducing an  $a$ -type dipole moment with a ratio  $\mu_a/\mu_b$  of 0.12 and 0.50, respectively [1]. Literature data covering lower frequencies were included in the analyses presented here [1]. Due to the low natural abundance, the analysis of the singly  $^{13}\text{C}$  substituted isotopologues was limited by their low SNR to frequencies below 250 GHz.

The resulting parameters for the ground vibrational states of the isotopologues (see Table 1) show good agreement with literature data (see Table B.2,<sup>4</sup>) although generally not within quoted uncertainties. As no literature data were available for the quartic centrifugal distortion constants of the singly substituted  $^{13}\text{C}$  isotopologues, these values were derived (for all analyzed isotopologues) from  $\text{fc-CCSD(T)/ANO0}$  force field calculations (see Table B.3). The good agreement between the calculated and experimental values confirms the physical meaningfulness of the experimental parameters with the exception of the  $d_2$  parameter of the parent isotopic species. This deviation might be a consequence of the very small magnitude of this parameter for the parent species combined with the influence of zero-point vibration.

<sup>4</sup> The CDMS results are used for the main isotopologue as they include more lines than Bogey et al. [4] and the  $\text{III}^1$  representation is used.

Trial fits of the parent isotopic species using the  $\text{I}^1$  representation reveal proper agreement between the experimental and calculated quartic centrifugal distortion constants at the cost of an overall degraded fit quality. The new global fits are extended significantly regarding the number of assigned transitions as well as the frequency and quantum number coverage. Compared to previous results, additional higher-order parameters were added and the accuracy of existing parameters was improved.

Vibrational motions of the six energetically lowest vibrational fundamentals are shown in Fig. 3. While the calculated vibrational wavenumbers show good agreement with literature values [7], there are substantial deviations of opposite sign for the  $\alpha_i^C$  values of the  $\nu_{10}$  and  $\nu_{22}$  fundamentals. The magnitude combined with the mirror-like appearance of the deviations suggests that they result from contributions of Coriolis coupling to the rotational constants [20–22]. As a result, the search for the vibrational states  $\nu_{10}$  and  $\nu_{22}$  did not rely on calculated predictions but on finding their spectroscopic patterns by visual means alone, a task challenged by the diminished intensity of the vibrational satellites due to their small Boltzmann factors of only 2%. To support the identification of low-intensity patterns, already assigned states were removed from the spectrum by deleting the experimental data points around their peak position. This was done in an iterative process for the strongest remaining pattern(s) as shown in Fig. 4. The effectiveness of Loomis-Wood plots was greatly improved by this

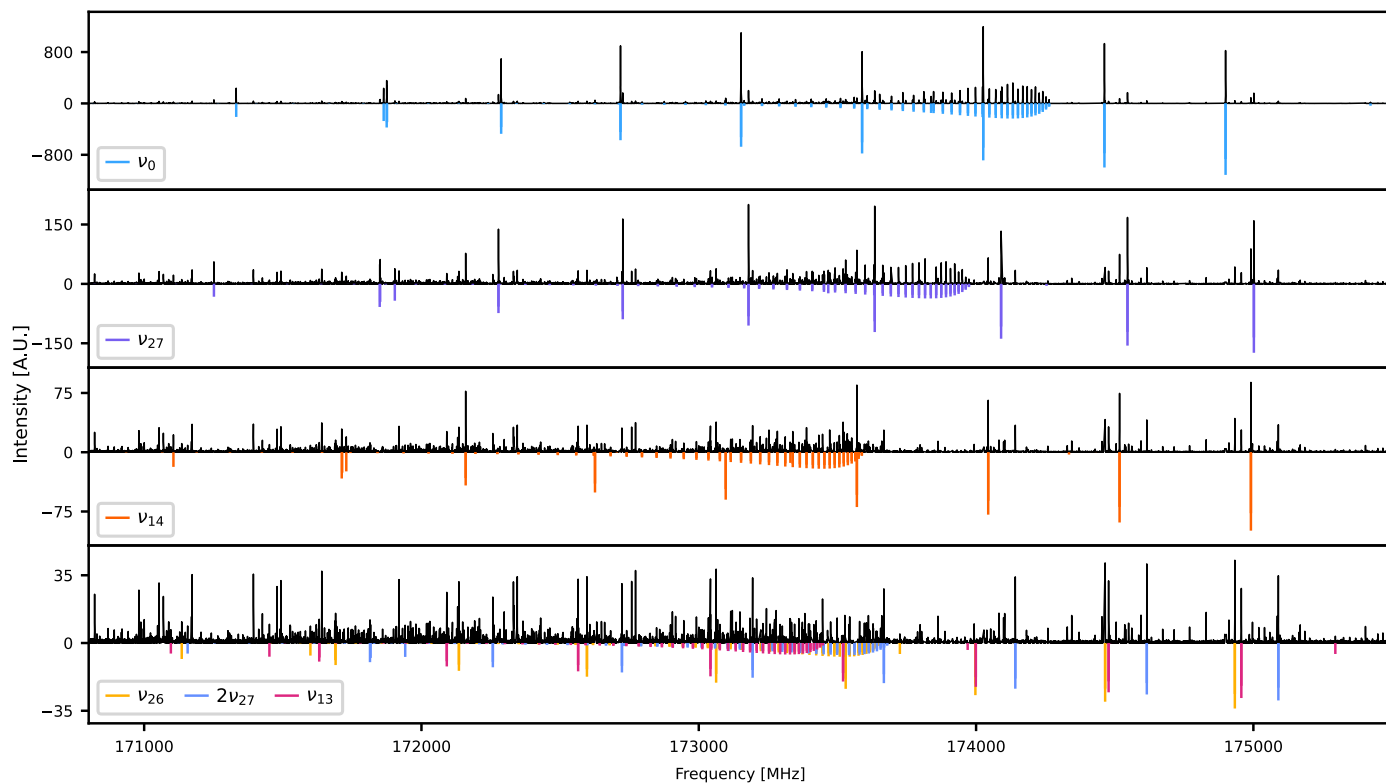


Fig. 4. The process of removing known vibrationally excited states from the experimental spectrum visualized. In the top row, the complete spectrum is shown together with the predicted stick spectrum for the vibrational ground state in blue. Removing all data points within 2.5 MHz of the assigned ground state positions yields the spectrum in the row below (with the y-axis being rescaled to match the reduced data). There the predicted stick spectrum of the energetically lowest vibrationally excited state  $\nu_{27}$  is shown in purple. Similarly, rows three and four show the spectrum after additionally removing lines belonging to  $\nu_{27}$  and  $\nu_{14}$ , respectively. This process greatly facilitates visual pattern recognition for vibrational states (and/or isotopologues) with lower intensities. The two lowest rows show that the method also has drawbacks, as some prominent lines from the predictions are missing in the experimental spectrum. This results from these lines being blended with transitions from already removed states. Combining this approach with Loomis-Wood plots increases the fault tolerance drastically.

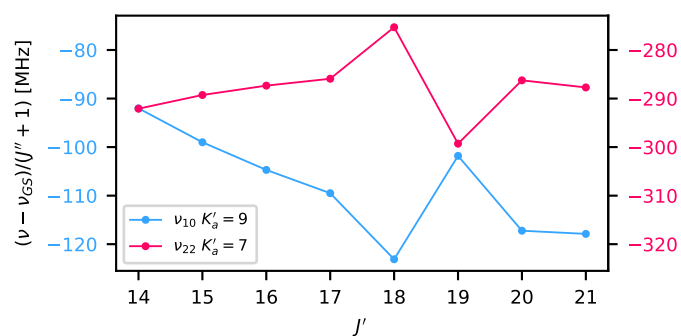


Fig. 5. Resonance plot of the  $K'_a = 9$  series of  $\nu_{10}$  and the  $K'_a = 7$  series of  $\nu_{22}$ . In all transitions  $\Delta J = \Delta K_a = \Delta K_c = 1$ . The mirror image-like deviations for  $J' = 18$  and 19 indicate an interaction that is centered around the respective energy levels with  $J' = 18$ .

procedure and allowed to assign the vibrational satellite spectra of  $\nu_{10}$  and  $\nu_{22}$  despite the large discrepancy between the calculated and experimental values of their  $C$  rotational constants. While molecular parameters of the eight energetically lowest vibrationally excited states of cyclopentadiene are presented here, satellites from states even higher in energy were easily visible and could be assigned readily. However, a tentative analysis hinted towards strong interactions between multiple of these states, putting their quantitative analysis beyond the scope of this work.

Within the eight energetically lowest vibrational states analyzed here, two interaction systems could be identified by mirror images in their residuals and resonance plots (see Fig. 5), the  $\nu_{10}/\nu_{22}$  dyad and the

$\nu_{26}/2\nu_{27}/\nu_{13}$  triad. The initial guess for the vibrational energy difference was approximated from the involved rotational energy levels. For the final model, 50 interstate transitions between  $\nu_{13}$  and  $2\nu_{27}$  as well as 20 interstate transitions between  $\nu_{10}$  and  $\nu_{22}$  were assigned. They result from wavefunction mixing due to the interactions and help determine the vibrational energy difference accurately. The interaction parameters were systematically tested with Pyckett.<sup>5</sup> From group theory it can be derived, that Coriolis interactions occur only between vibrational states of different symmetry and for each pair of states only a single symmetry (meaning  $a$ -,  $b$ -, or  $c$ - symmetry) of Coriolis interactions can occur [23–25].

The resulting rotational parameters of the vibrational states are given in Table 2 and the interaction parameters are given in Table 3. In general, the deviations of the rotational constants with respect to the vibrational ground state show good agreement with the rotation-vibration interaction constants from quantum chemical calculations, see Table A.1. Typically the obs-calc agreement is within 1 MHz but there are some slight deviations of about 2.5 MHz for  $\alpha^A$  of  $\nu_{10}$  and strong deviations for  $\alpha^C$  of  $\nu_{10}$  and  $\nu_{22}$  of about  $\pm 100$  MHz. However, the  $\alpha_{\nu_{10}}^C + \alpha_{\nu_{22}}^C$  values between the experiment and calculations agree well (15.765(71) MHz and 15.01 MHz, respectively) [20,27]. As mentioned, these systematic mirror image deviations result from Coriolis coupling contributions to the rotation-vibration interaction constant. Using equation 13 from Ref. [20] and the values obtained from the quantum chemical calculations, the Coriolis interaction term of the rotation-vibration interaction constants is calculated to be about  $\pm 103.42$  MHz.

<sup>5</sup> Pyckett is a Python wrapper around Pickett's SPFIT and SPCAT [12]. It can be installed via `pip install pyckett`.

**Table 2**

The resulting rotational parameters for the eight energetically lowest vibrationally excited states. The two interaction systems are indicated by blue and red colored table headers similar to Fig. 1.

Parameter	$\nu_{27}$	$\nu_{14}$	$\nu_{26}$	$2\nu_{27}$	$\nu_{13}$	$\nu_{27} + \nu_{14}$	$\nu_{10}$	$\nu_{22}$
<i>A</i>	/MHz	8429.339717(69)	8418.480575(89)	8408.25559(13)	8431.9322(70)	8395.70079(81)	8421.515(51)	8444.228(20)
<i>B</i>	/MHz	8214.788334(61)	8207.517052(80)	8217.21858(15)	8204.4205(78)	8220.5890(49)	8197.100(49)	8227.153(19)
<i>C</i>	/MHz	4274.157884(47)	4274.115571(50)	4272.629500(60)	4276.535426(89)	4273.326526(90)	4276.65964(11)	4264.049(50)
$-D_J$	/kHz	-2.696942(27)	-2.682148(34)	-2.646176(95)	-2.70645(22)	-2.58322(32)	-2.68418(41)	-2.9493(84)
$-D_{JK}$	/kHz	4.062326(43)	4.019933(63)	3.94434(31)	4.06999(22)	3.72832(65)	4.02211(92)	3.6197(86)
$-D_K$	/kHz	-1.682418(30)	-1.655183(41)	-1.61483(26)	a	-1.46181(34)	-1.65897(51)	-1.015(15)
$d_1$	/Hz	-34.402(29)	-38.531(38)	-58.791(54)	a	-98.7(1.7)	a	a
$d_2$	/mHz	40(13)	a	a	a	a	a	a
Transitions		2117	1736	1146	441	437	572	550
Lines		1223	996	618	224	231	286	277
RMS	/kHz	22.07	22.47	26.90 <sup>b</sup>	26.90 <sup>b</sup>	26.90 <sup>b</sup>	21.79	25.06 <sup>c</sup>
WRMS		0.85	0.74	0.86 <sup>b</sup>	0.86 <sup>b</sup>	0.86 <sup>b</sup>	0.60	0.74 <sup>c</sup>

Fits performed with SPFIT in the S-reduction and III<sup>1</sup> representation. Standard errors are given in parentheses. Parameters of the vibrational ground state are applied to all vibrationally excited states and difference values are fitted. Parameters not specified were fixed to the global values, see Table 1. Interstate transitions are counted towards the lower state for the transitions and lines statistics. <sup>a</sup>Parameter was fixed to the global value. <sup>b,c</sup>Reported values are values for the respective combined fits.

**Table 3**

The resulting energy differences (colored analog to Fig. 1 and Table 1) and interaction parameters for the interactions between  $\nu_{10}$  and  $\nu_{22}$  as well as  $\nu_{26}$ ,  $2\nu_{27}$ , and  $\nu_{13}$ .

$\nu_1$	$\nu_2$	ID <sup>a</sup>	Parameter	Value
$2\nu_{27}$	$\nu_{13}$	4000 $\nu_1\nu_2$	$\tilde{\nu}_{13} - \tilde{\nu}_{2\times 27}$	/cm <sup>-1</sup> 8.719589(3)
$2\nu_{27}$	$\nu_{13}$	4200 $\nu_1\nu_2$	$G_b$	/MHz 407.6(1.5)
$2\nu_{27}$	$\nu_{13}$	4100 $\nu_1\nu_2$	$G_{2b}$	/kHz -8.720(99)
$2\nu_{27}$	$\nu_{13}$	4101 $\nu_1\nu_2$	$F_{ac}$	/MHz 3.166(25)
$2\nu_{27}$	$\nu_{13}$	4101 $\nu_1\nu_2$	$F_{ac,J}$	/Hz -120.35(40)
$\nu_{26}$	$\nu_{13}$	6100 $\nu_1\nu_2$	$\tilde{\nu}_{13} - \tilde{\nu}_{26}$	/cm <sup>-1</sup> 36.5867(2)
$\nu_{26}$	$\nu_{13}$	6100 $\nu_1\nu_2$	$F_{ab}$	/MHz 6.4435(98)
$\nu_{26}$	$2\nu_{27}$	2100 $\nu_1\nu_2$	$\tilde{\nu}_{2\times 27} - \tilde{\nu}_{26}$	/cm <sup>-1</sup> 27.8671(2)
$\nu_{26}$	$2\nu_{27}$	2100 $\nu_1\nu_2$	$F_{bc}$	/MHz 2.521(16)
$\nu_{10}$	$\nu_{22}$	6000 $\nu_1\nu_2$	$\tilde{\nu}_{22} - \tilde{\nu}_{10}$	/cm <sup>-1</sup> 5.127415(4)
$\nu_{10}$	$\nu_{22}$	6200 $\nu_1\nu_2$	$G_c$	/MHz 4080.87(94)
$\nu_{10}$	$\nu_{22}$	6210 $\nu_1\nu_2$	$G_{2c}$	/kHz -136.5(7.3)
$\nu_{10}$	$\nu_{22}$	6100 $\nu_1\nu_2$	$G_{2c,K}$	/Hz 2.88(19)
$\nu_{10}$	$\nu_{22}$	6100 $\nu_1\nu_2$	$F_{ab}$	/MHz 7.35(17)
$\nu_{10}$	$\nu_{22}$	6110 $\nu_1\nu_2$	$F_{ab,K}$	/kHz 1.424(52)
$\nu_{10}$	$\nu_{22}$	6101 $\nu_1\nu_2$	$F_{ab,J}$	/Hz 241(15)

<sup>a</sup> The specified IDs are the respective parameter IDs used in the \*.par and \*.var files of SPFIT and SPCAT [12,26].

By subtracting this term, the corrected calculated values,  $\alpha_{\nu_{10},\text{corr}}^C = -111.18 \text{ MHz} + 103.42 \text{ MHz} = -7.76 \text{ MHz}$  and  $\alpha_{\nu_{22},\text{corr}}^C = 96.17 \text{ MHz} - 103.42 \text{ MHz} = -7.25 \text{ MHz}$ , agree with the experimental values within 1 MHz.

The two vibrational states closest in energy are the dyad as  $\nu_{22}$  is only 5.1 cm<sup>-1</sup> higher in energy than  $\nu_{10}$ . The strongest interactions are observed for even  $\Delta K_a$  values (see Fig. C.1) and the interstate transitions have even  $\Delta K_a$  and odd  $\Delta K_c$  values. For the triad,  $2\nu_{27}$  lies in the middle, 7.9 cm<sup>-1</sup> higher in energy than  $\nu_{26}$  and 36.6 cm<sup>-1</sup> lower than  $\nu_{13}$  with the interactions between  $2\nu_{27}$  and  $\nu_{13}$  being the strongest and appearing for odd  $\Delta K_a$  values (see Fig. C.2). The respective interstate transitions have even  $\Delta K_a$  and  $\Delta K_c$  values. The observed trends are similar for both interaction systems, with the center of the interaction increasing in  $K_a$  for increasing  $J$ . For the dyad, this pattern starts around  $J'' = 14$  and  $K_a'' = 3/5$  whereas for  $\nu_{13}$  and  $2\nu_{27}$  the pattern starts around  $J'' = 31$  and  $K_a'' = 0/1$ .

For the interaction between  $\nu_{10}$  and  $\nu_{22}$ , only the relative signs of the interaction parameters can be determined (inverting the signs of all interaction parameters results in the same fit/predictions). For the triad,  $\nu_{26}/2\nu_{27}/\nu_{13}$ , there are four equivalent sets of interaction parameter signs (see Appendix F). Additionally, due to high correlations between the interaction parameters, the presented parameter set should be seen as one of many possible solutions.

The Coriolis  $G_\alpha$  parameters between two fundamentals  $r$  and  $s$  were estimated from the results of the quantum chemical calculations as

follows

$$G_\alpha(r, s) = \zeta_{r,s}^\alpha * B_e^\alpha * \left( \sqrt{\frac{\omega_r}{\omega_s}} + \sqrt{\frac{\omega_s}{\omega_r}} \right) \quad (1)$$

Here,  $G_\alpha(r, s)$  are the Coriolis parameters of  $\alpha = a, b,$  or  $c$  symmetry,  $B_e^\alpha$  the respective equilibrium rotational constant,  $\omega$  the harmonic vibrations, and  $\zeta_{r,s}^\alpha$  the respective Coriolis coefficients. As an approximation, we used the experimental vibrational ground state rotational constants for the  $B_e^\alpha$  values (see Table 1) and the harmonic wavenumbers from the quantum chemical calculations (see Table A.1) for the  $\omega$ . For the dyad, this yields  $G_c(\nu_{22}, \nu_{10}) = 7854 \text{ MHz}$  which is of same magnitude as the experimental value of 4080.85(14) MHz. For the triad, only the interaction between the two fundamentals  $\nu_{13}$  and  $\nu_{26}$  was estimated to be  $G_c(\nu_{13}, \nu_{26}) = 875 \text{ MHz}$ . However, including  $G_c(\nu_{13}, \nu_{26})$  did not improve the fit which hints towards the interaction parameters (especially for the triad) being effective.

The resulting weighted root mean square (WRMS) values are around 0.8 indicating that our uncertainties are slightly conservative. The analyses of the singly <sup>13</sup>C substituted isotopologues have significantly lower root mean square (RMS) and WRMS values, which probably results from the lower number of assigned transitions and the limited frequency range (assignments were limited to frequencies below 250 GHz).

#### 4. Structure determination

Using the improved rotational constants obtained in this work and refitting the line positions of the deuterium substituted isotopologues (1- $d_1$ , 1- $d_2$ , 1- $d_3$ , 1,2,3,4,5- $d_5$ , and  $d_6$ ) from Damiani et al. [5], a semi-experimental equilibrium structure ( $r_e^{\text{SE}}$ ) has been derived. Refitting the deuterium isotopic data was essential due to a typo in the  $A$  constant of cyclopentadiene 1,2,3,4,5- $d_5$  in Damiani et al. (7707.857(5) MHz [5] vs. 7007.857(11) MHz obtained here). For the deuterated isotopologues, the  $A_0$ ,  $B_0$ , and  $C_0$  rotational parameters were floated while the quartic centrifugal distortion parameters were fixed to their calculated values (fc-CCSD(T)/ANO0 level). All experimental isotopic  $A_0$ ,  $B_0$ , and  $C_0$  rotational constants were then corrected for the effects of zero-point vibration calculated at the fc-CCSD(T)/ANO0 level (see Table D.4) and the  $r_e^{\text{SE}}$  structure was derived with the STRFIT software [28]. A comparison of the  $r_e^{\text{SE}}$  structure against *ab initio* values calculated at the fc-CCSD(T)/ANO0 and ae-CCSD(T)/cc-pwCVQZ levels is given in Appendix D. As can be seen, the agreement between the  $r_e^{\text{SE}}$  and the high-level ae-CCSD(T)/cc-pwCVQZ structural parameters is excellent, to (well) within 10<sup>-3</sup> Å and 0.1 ° for bond lengths and angles, respectively.

## 5. Conclusions

In the present study, the rotational spectrum coverage of cyclopentadiene was extended up to 510 GHz by measuring 250 GHz of high-resolution broadband spectra. This allowed to significantly increase the number of assigned lines for the main isotopologue from about 150 to 3510. As a result, the newly determined parameters produce much more reliable frequency predictions, especially for high frequencies and high quantum numbers (see Fig. E.3). Especially *R*-branch transitions above 330 GHz and *Q*-branch transitions are now in much better agreement. The presented data allows for astronomical searches at higher frequencies and over a much broader quantum number range. Similarly, the number of assigned lines for the three singly  $^{13}\text{C}$  substituted isotopologues was increased from about 10 each to well over 200 each. Their frequency coverage was much improved from only microwave data to up to 250 GHz.

Lastly, the dominant vibrational satellite spectra of cyclopentadiene were described for the first time, including their interactions. Especially the energetically lowest-lying vibrational states are analyzed over a broad quantum number range permitting reliable predictions.

Future work might be targeted at deuterated isotopologues or vibrationally excited states higher in energy. Whereas analyses of deuterated isotopologues would be simplified by the use of enriched samples, the energetically higher vibrationally excited states could benefit from double-resonance techniques [29]. Additionally, the analyzed vibrational satellite spectrum is a great aid for rovibrational studies in the infrared. Rovibrational transitions between already analyzed states will be accurately predicted except for the band center and even rovibrational transitions with only one known vibrational state will benefit from the possibility of using techniques like the Automated Spectral Assignment Procedure [30].

### CRediT authorship contribution statement

**Luis Bonah:** Writing – original draft, Visualization, Validation, Supervision, Software, Investigation, Formal analysis. **Benedikt Helmsstaedter:** Writing – review & editing, Validation, Investigation, Formal analysis. **Jean-Claude Guillemin:** Writing – review & editing, Project administration, Conceptualization. **Stephan Schlemmer:** Writing – review & editing, Supervision, Project administration, Funding acquisition, Conceptualization. **Sven Thorwirth:** Writing – review & editing, Visualization, Validation, Supervision, Project administration, Conceptualization.

### Declaration of competing interest

The authors declare that they have no known competing financial interests or personal relationships that could have appeared to influence the work reported in this paper.

### Acknowledgments

We wish to acknowledge an anonymous referee for their careful reading of the manuscript and providing useful suggestions. The authors from Cologne gratefully acknowledge the Collaborative Research Center 1601 (SFB 1601 sub-project A4) funded by the Deutsche Forschungsgemeinschaft (DFG, German Research Foundation) – 500700252.

J.-C.G. thanks the national program CNRS PCMI (Physics and Chemistry of the Interstellar Medium) and the CNES for a grant (CMISTEP).

### Appendix A. Vibrational wavenumbers and rotation-vibration interaction constants

See Table A.1.

**Table A.1**

Rotation-vibration interaction constants  $\alpha_i$ , harmonic and anharmonic wavenumbers  $\tilde{\nu}_i$  from quantum chemical calculations at the CCSD(T)/ANO0 level as well as the wavenumbers reported by Castellucci et al. [7]. Rotation-vibration interaction constants are in MHz and wavenumbers in  $\text{cm}^{-1}$ . Literature values are taken from liquid phase spectra if not specified otherwise.

Mode		$-\alpha_{\text{calc}}^A$	$-\alpha_{\text{calc}}^B$	$-\alpha_{\text{calc}}^C$	$\tilde{\nu}_{\text{calc}}^{\text{anh}}$	$\tilde{\nu}_{\text{calc}}^{\text{harm}}$	$\tilde{\nu}_{\text{lit}}$ [7]
$\nu_{27}$	$B_1$	3.77	-11.22	2.93	339	340	350
$\nu_{14}$	$A_2$	-6.86	-17.19	2.74	497	502	516 <sup>a</sup>
$\nu_{26}$	$B_1$	-16.56	-8.26	1.15	658	670	664 <sup>b</sup>
$\nu_{13}$	$A_2$	-30.06	-4.22	1.94	691	701	700
$\nu_{10}$	$A_1$	-6.44	2.62	-111.18	789	799	802
$\nu_{22}$	$B_2$	18.45	2.51	96.17	793	804	805
$\nu_{25}$	$B_1$	-830.70	-33.86	-0.80	896	920	891
$\nu_{12}$	$A_2$	-19.44	-55.71	-0.81	897	917	941 <sup>a</sup>
$\nu_9$	$A_1$	815.34	27.89	-20.22	903	920	915
$\nu_{24}$	$B_1$	2.38	-12.17	0.22	905	927	925
$\nu_{21}$	$B_2$	-11.03	23.84	5.81	953	972	959
$\nu_8$	$A_1$	2.39	-14.20	-4.82	1015	1006	994
$\nu_{20}$	$B_2$	17.40	7.20	-4.29	1085	1104	1090
$\nu_7$	$A_1$	14.67	-1.33	2.07	1102	1120	1106
$\nu_{11}$	$A_2$	-8.06	-0.53	2.43	1102	1131	1100 <sup>a</sup>
$\nu_{19}$	$B_2$	-0.34	1.60	-9.04	1236	1266	1239
$\nu_{18}$	$B_2$	-1.90	0.52	-8.39	1278	1310	1292
$\nu_6$	$A_1$	2.59	-3.70	-5.98	1360	1393	1365
$\nu_5$	$A_1$	-4.14	9.97	7.68	1389	1428	1378
$\nu_4$	$A_1$	-17.62	-4.69	-5.98	1503	1547	1500
$\nu_{17}$	$B_2$	-15.81	-3.48	-4.02	1572	1615	1580
$\nu_3$	$A_1$	-4.70	-4.77	-0.72	2905	3042	2886
$\nu_{23}$	$B_1$	-3.34	-3.42	-1.21	2929	3086	2900
$\nu_{16}$	$B_2$	-6.12	-7.20	-3.40	3084	3216	3043
$\nu_2$	$A_1$	-6.23	-7.71	-3.53	3090	3225	3075
$\nu_1$	$A_1$	-6.84	-7.91	-3.67	3113	3250	3091
$\nu_{15}$	$B_2$	-6.86	-7.52	-3.53	3115	3242	3105

<sup>a</sup> Solid-phase value (other literature energy values are taken from liquid phase spectra).

<sup>b</sup> Gas-phase high-resolution infrared spectroscopy yields a value of  $663.84800(5)\text{cm}^{-1}$  [6].

### Appendix B. Rotational constants from literature and quantum chemical calculations

See Tables B.2 and B.3.

### Appendix C. Interaction hotspots

See Figs. C.1 and C.2.

### Appendix D. Semi-experimental equilibrium structure

Equilibrium structural parameters of cyclopentadiene (bond lengths in Å, angles in degrees) calculated at the fc-CCSD(T)/ANO0 and ae-CCSD(T)/cc-pwCVQZ levels of theory and determined semi-experimentally. See text for details.

X						
X 1 rd						
C 2 rd 1 a90						
C 3 r1 2 a1 1 d90						
C 3 r1 2 a1 4 d180						
C 4 r2 3 a2 5 d0						
C 5 r2 3 a2 4 d0						
H 4 r3 3 a3 2 d180						
H 5 r3 3 a3 2 d180						
H 6 r4 4 a4 8 d0						
H 7 r4 5 a4 9 d0						
H 3 r5 2 a5 1 d0						
H 3 r5 2 a5 12 d180						
		ANO0	/	pwCVQZ	/	reSE
rd =		1.0	/	1.0	/	1.0
a90 =		90.0	/	90.0	/	90.0

**Table B.2**

Literature values of the rotational constants for the main isotopologue (from the CDMS [31,32]) and for the singly substituted  $^{13}\text{C}$  isotopologues (from Damiani et al. [5])

Param.		c-C <sub>5</sub> H <sub>6</sub> [31,32]	1- <sup>13</sup> C [5]	2- <sup>13</sup> C [5]	3- <sup>13</sup> C [5]
<i>A</i>	/MHz	8426.1111(11)	8226.028(9)	8419.949(6)	8345.097(10)
<i>B</i>	/MHz	8225.6387(11)	8219.434(7)	8040.358(6)	8108.662(7)
<i>C</i>	/MHz	4271.4377(11)	4217.760(6)	4219.419(4)	4219.067(7)
$-D_J$	/kHz	-2.6948(13)	-	-	-
$-D_{JK}$	/kHz	4.0626(29)	-	-	-
$-D_K$	/kHz	-1.6842(17)	-	-	-
$d_1$	/Hz	-39.7(18)	-	-	-
Transitions		157	-	-	-
Lines		92	-	-	-
RMS	/kHz	30.676	-	-	-
WRMS		1.02253	-	-	-

**Table B.3**

Quartic centrifugal distortion constants (III<sup>1</sup> representation) of the main isotopologue and the singly substituted  $^{13}\text{C}$  isotopologues as calculated at the fc-CCSD(T)/ANO0 level.

Param.		c-C <sub>5</sub> H <sub>6</sub>	1- <sup>13</sup> C	2- <sup>13</sup> C	3- <sup>13</sup> C
$-D_J$	/kHz	-2.58744	-2.54647	-2.52934	-2.5328
$-D_{JK}$	/kHz	3.89513	3.83687	3.80924	3.81731
$-D_K$	/kHz	-1.61171	-1.58884	-1.57739	-1.58123
$d_1$	/Hz	-44.0093	61.0209	-20.1082	-11.8137
$d_2$	/Hz	0.751250	-2.71914	-3.62988	1.22695

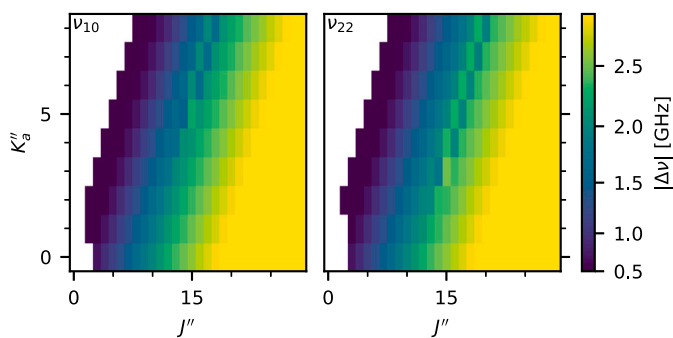


**Fig. C.1.** Absolute shifts in transition frequency between predictions with and without interactions for  $\Delta J_{\Delta K_a, \Delta K_c} = 1_{1,1}$  transitions. The heatmaps of the interacting vibrational states  $\nu_{10}$  (left) and  $\nu_{22}$  (right) show the same pattern when shifted by  $\Delta K_a = 2$ . The center of the interactions increases in  $K_a$  with increasing  $J$  value.

r1	=	1.515110	/	1.500253	/	1.49906(34)
a1	=	51.526426	/	51.537508	/	51.541(15)
d90	=	90.0	/	90.0	/	90.0
d180	=	180.0	/	180.0	/	180.0
r2	=	1.361296	/	1.346357	/	1.34635(35)
a2	=	109.368447	/	109.329183	/	109.330(24)
d0	=	0.0	/	0.0	/	0.0
r3	=	1.087290	/	1.078491	/	1.07865(24)
a3	=	124.008184	/	124.075312	/	124.01(11)
r4	=	1.087975	/	1.079202	/	1.07907(22)
a4	=	126.235302	/	126.127498	/	126.082(60)
r5	=	1.102197	/	1.093823	/	1.09441(17)
a5	=	126.576616	/	126.701234	/	126.710(12)

## Appendix E. Comparison of initial and final residuals

See Fig. E.3.

## Appendix F. Signs of Coriolis interaction parameters

It is common when treating Coriolis interactions that there are multiple equivalent parameter sets for the analysis which only differ in the signs of the Coriolis interaction parameters [33,34]. Even

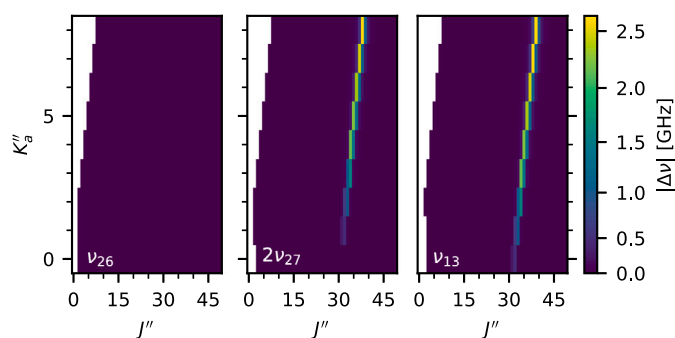


**Fig. C.2.** Absolute shifts in transition frequency between predictions with and without interactions for  $\Delta J_{\Delta K_a, \Delta K_c} = 1_{1,1}$  transitions. The heatmaps of the interacting vibrational states  $\nu_{26}$  (left),  $2\nu_{27}$  (middle) and  $\nu_{13}$  (right) highlight that the strongest interactions are between  $2\nu_{27}$  and  $\nu_{13}$  with  $\Delta K_a = 2$ . The center of the interactions increases in  $K_a$  with increasing  $J$  value. In contrast to Fig. C.1, the  $x$ -axis and the  $z$ -axis (being the heatmap color) are scaled differently to highlight the main interactions better.

though the calculated Coriolis interaction parameters have a defined sign, it typically cannot be determined experimentally. The equivalent interaction parameter sets of the  $\nu_{10}/\nu_{22}$  diad are

$$\{G_c, G_{2c}, G_{2c,K}, F_{ab}, F_{ab,K}, F_{ab,J}\} \quad (\text{F.1})$$

$$\{-G_c, -G_{2c}, -G_{2c,K}, -F_{ab}, -F_{ab,K}, -F_{ab,J}\}$$

This means inverting all parameter signs results in exactly the same fit/frequency predictions. The triad, being  $\nu_{26}$ ,  $2\nu_{27}$ , and  $\nu_{13}$ , has four equivalent interaction parameter sets, being

$$\{G_b^{12}, G_{2b}^{12}, F_{ac}^{12}, F_{ac,J}^{12}, F_{bc}^{01}, F_{ab}^{02}\}$$

$$\{G_b^{12}, G_{2b}^{12}, F_{ac}^{12}, F_{ac,J}^{12}, -F_{bc}^{01}, -F_{ab}^{02}\} \quad (\text{F.2})$$

$$\{-G_b^{12}, -G_{2b}^{12}, -F_{ac}^{12}, -F_{ac,J}^{12}, -F_{bc}^{01}, F_{ab}^{02}\}$$

$$\{-G_b^{12}, -G_{2b}^{12}, -F_{ac}^{12}, -F_{ac,J}^{12}, F_{bc}^{01}, -F_{ab}^{02}\}$$

where for brevity the superscript indices specifying the vibrational states are given as their respective vibrational identifiers used in the \*.par file of SPFIT: 0  $\equiv$   $\nu_{26}$ , 1  $\equiv$   $\nu_{13}$ , and 2  $\equiv$   $2\nu_{27}$ .

For both interacting systems, the relative signs within one Coriolis symmetry and two-state connection have to stay fixed. For the triad, the signs for the different Coriolis symmetries can be exchanged in pairs.

## Appendix G. Supplementary data

Supplementary material related to this article can be found online at <https://doi.org/10.1016/j.jms.2024.111967>.

## Data availability

The input and output files of SPFIT will be provided as supplementary material.

Table D.4

Rotational constants (MHz) and zero-point vibrational corrections (fc-CCSD(T)/ANO0, MHz) of cyclopentadiene isotopologues.

	c-C <sub>5</sub> H <sub>6</sub>	1- <sup>13</sup> C <sub>1</sub>	2- <sup>13</sup> C	3- <sup>13</sup> C	1-d <sub>1</sub>	1-d <sub>2</sub>	1-d <sub>3</sub>	1,2,3,4,5-d <sub>5</sub>	d <sub>6</sub>
A <sub>0</sub>	8426.109	8226.053	8420.043	8345.132	8129.952	8414.045	8307.036	7007.858	6608.398
B <sub>0</sub>	8225.640	8219.483	8040.425	8108.714	7859.534	7591.889	7678.126	6681.888	6607.340
C <sub>0</sub>	4271.437	4217.759	4219.411	4219.065	4145.090	4091.154	4090.254	3529.302	3444.129
ΔA	63.046	66.046	62.748	63.249	65.660	63.130	64.793	49.690	48.552
ΔB	66.461	60.796	64.627	63.844	58.864	58.628	56.982	48.475	46.425
ΔC	34.228	33.512	33.672	33.580	33.263	32.018	31.969	25.954	25.158
A <sub>e</sub> <sup>SE</sup>	8489.155	8292.100	8482.792	8408.381	8195.612	8477.175	8371.829	7057.549	6656.950
B <sub>e</sub> <sup>SE</sup>	8292.102	8280.279	8105.053	8172.558	7918.399	7650.517	7735.108	6730.363	6653.765
C <sub>e</sub> <sup>SE</sup>	4305.665	4251.271	4253.082	4252.645	4178.353	4123.172	4122.222	3555.255	3469.288

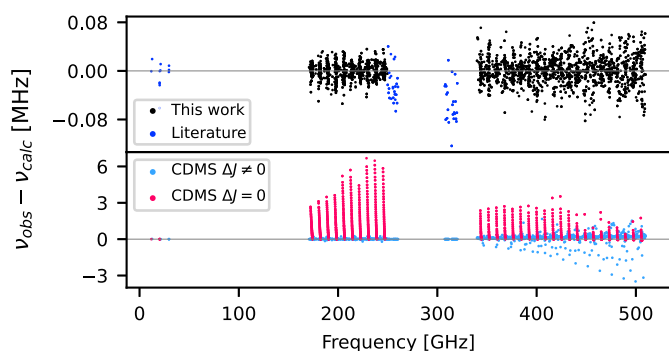


Fig. E.3. Residuals of the vibrational ground state of the main isotopologue for the predictions from this work (top) compared with the residuals for the predictions from the CDMS [31,32] (based on data of previous reports [1,4]). Colors distinguish between literature assignments and new assignments in the top row and between Q- and R-branch transitions in the bottom row. This work greatly improves predictions for R-branch transitions above 330 GHz and Q-branch transitions above 40 GHz.

## References

- [1] L.H. Scharpen, V.W. Laurie, Structure of cyclopentadiene, *J. Chem. Phys.* 43 (1965) 2765–2766, <http://dx.doi.org/10.1063/1.1697207>.
- [2] V.W. Laurie, Microwave spectrum and dipole moment of cyclopentadiene, *J. Chem. Phys.* 24 (1956) 635–636, <http://dx.doi.org/10.1063/1.1742585>.
- [3] R.C. Benson, W.H. Flygare, Molecular Zeeman effect of cyclopentadiene and isoprene and comparison of the magnetic susceptibility anisotropies, *J. Am. Chem. Soc.* 92 (1970) 7523–7529, <http://dx.doi.org/10.1021/ja00729a001>.
- [4] M. Bogey, C. Demuyne, J.L. Destombes, The millimeter wave spectrum of cyclopentadiene, *J. Mol. Spectrosc.* 132 (1988) 277–279, [http://dx.doi.org/10.1016/0022-2852\(88\)90074-4](http://dx.doi.org/10.1016/0022-2852(88)90074-4).
- [5] D. Damiani, L. Ferretti, E. Gallinella, Structure of cyclopentadiene from microwave spectra of several deuterated species, *Chem. Phys. Lett.* 37 (1976) 265–269, [http://dx.doi.org/10.1016/0009-2614\(76\)80212-6](http://dx.doi.org/10.1016/0009-2614(76)80212-6).
- [6] S.R. Boardman, S.A. Bone, P.B. Davies, N.A. Martin, High-resolution FTIR and diode laser jet spectroscopy of cyclopentadiene, *J. Mol. Spectrosc.* 143 (1990) 100–110, [http://dx.doi.org/10.1016/0022-2852\(90\)90264-q](http://dx.doi.org/10.1016/0022-2852(90)90264-q).
- [7] E. Castellucci, P. Manzelli, B. Fortunato, E. Gallinella, P. Mirone, Vibrational spectra and normal-coordinate treatment of cyclopentadiene and its deuterated derivatives, *Spectrochim. Acta A* 31 (1975) 451–461, [http://dx.doi.org/10.1016/0584-8539\(75\)80037-7](http://dx.doi.org/10.1016/0584-8539(75)80037-7).
- [8] J. Cernicharo, M. Agúndez, C. Cabezas, B. Tercero, N. Marcelino, J.R. Pardo, P. de Vicente, Pure hydrocarbon cycles in TMC-1: Discovery of ethynyl cyclopropenylidene, cyclopentadiene, and indene, *Astron. Astrophys.* 649 (2021) L15, <http://dx.doi.org/10.1051/0004-6361/202141156>.
- [9] M.A. Martin-Drumel, J. van Wijngaarden, O. Zingsheim, F. Lewen, M.E. Harding, S. Schlemmer, S. Thorwirth, Millimeter- and submillimeter-wave spectroscopy of disulfur dioxide, OSSO, *J. Mol. Spectrosc.* 307 (2015) 33–39, <http://dx.doi.org/10.1016/j.jms.2014.11.007>.
- [10] B. Helmstaedter, Sub-millimeter Rotational Spectroscopy of Cyclopentadiene – An Analysis of the Ground State and Vibrational Satellite Spectrum up to 250 GHz (Master's thesis), I. Physikalisches Institut, Universität zu Köln, 2024.
- [11] L. Bonah, O. Zingsheim, H.S.P. Müller, J.-C. Guillemin, F. Lewen, S. Schlemmer, LLWP—A new Loomis-Wood software at the example of acetone-<sup>13</sup>C<sub>1</sub>, *J. Mol. Spectrosc.* 388 (2022) 111674, <http://dx.doi.org/10.1016/j.jms.2022.111674>.
- [12] H.M. Pickett, The fitting and prediction of vibration-rotation spectra with spin interactions, *J. Mol. Spectrosc.* 148 (1991) 371–377, [http://dx.doi.org/10.1016/0022-2852\(91\)90393-o](http://dx.doi.org/10.1016/0022-2852(91)90393-o).
- [13] L. Bonah, S. Schlemmer, J.-C. Guillemin, M.E. Harding, S. Thorwirth, On the spectroscopy of phosphalkynes: Millimeter- and submillimeter wave study of C<sub>2</sub>H<sub>3</sub>CP, *J. Phys. Chem. A* 128 (2024) 4859–4866, <http://dx.doi.org/10.1021/acs.jpca.4c02566>.
- [14] D.A. Matthews, L. Cheng, M.E. Harding, F. Lipparini, S. Stopkowicz, T.-C. Jagau, P.G. Szalay, J. Gauss, J.F. Stanton, Coupled-cluster techniques for computational chemistry: The CFOUR program package, *J. Chem. Phys.* 152 (2020) <http://dx.doi.org/10.1063/5.0004837>.
- [15] M.E. Harding, T. Metzroth, J. Gauss, A.A. Auer, Parallel calculation of CCSD and CCSD(T) analytic first and second derivatives, *J. Chem. Theory Comput.* 4 (2008) 64–74, <http://dx.doi.org/10.1021/ct700152c>.
- [16] C. Puzzarini, J.F. Stanton, J. Gauss, Quantum-chemical calculation of spectroscopic parameters for rotational spectroscopy, *Int. Rev. Phys. Chem.* 29 (2010) 273–367, <http://dx.doi.org/10.1080/01442351003643401>.
- [17] K. Raghavachari, G.W. Trucks, J.A. Pople, M. Head-Gordon, A fifth-order perturbation comparison of electron correlation theories, *Chem. Phys. Lett.* 157 (1989) 479–483, [http://dx.doi.org/10.1016/s0009-2614\(89\)87395-6](http://dx.doi.org/10.1016/s0009-2614(89)87395-6).
- [18] J. Almlöf, P.R. Taylor, General contraction of Gaussian basis sets. I. Atomic natural orbitals for first- and second-row atoms, *J. Chem. Phys.* 86 (1987) 4070–4077, <http://dx.doi.org/10.1063/1.451917>.
- [19] S. Thorwirth, M.E. Harding, J.B. Dudek, M.C. McCarthy, Equilibrium molecular structures of vinyl carbon chains: Vinyl acetylene, vinyl diacetylene, and vinyl cyanide, *J. Mol. Spectrosc.* 350 (2018) 10–17, <http://dx.doi.org/10.1016/j.jms.2018.05.001>.
- [20] I.M. Mills, Vibration-rotation structure in asymmetric and symmetric top molecules, in: K.N. Rao (Ed.), *Molecular Spectroscopy: Modern Research*, Academic Press, 1972, pp. 115–140.
- [21] E. Törneng, C.J. Nielsen, P. Klaeboe, H. Hopf, H. Priebe, The i.r., Raman and microwave spectra of 1-butene-3-yne (vinylacetylene) and 1-butene-3-yne-4d, *Spectrochim. Acta A* 36 (1980) 975–987, [http://dx.doi.org/10.1016/0584-8539\(80\)80177-2](http://dx.doi.org/10.1016/0584-8539(80)80177-2).
- [22] C.P. Endres, G.C. Mellau, M.E. Harding, M.-A. Martin-Drumel, H. Lichau, S. Thorwirth, High-resolution infrared study of vinyl acetylene: The ν<sub>13</sub> (214 cm<sup>-1</sup>) and ν<sub>18</sub> (304 cm<sup>-1</sup>) fundamentals, *J. Mol. Spectrosc.* 379 (2021) 111469, <http://dx.doi.org/10.1016/j.jms.2021.111469>.
- [23] H.A. Jahn, Note on Coriolis coupling terms in polyatomic molecules, *Phys. Rev.* 56 (1939) 680–683, <http://dx.doi.org/10.1103/physrev.56.680>.
- [24] D.R.J. Boyd, H.C. Longuet-Higgins, Coriolis interaction between vibration and rotation in symmetric top molecules, *Proc. R. Soc. Lond. Ser. A* 213 (1952) 55–73, <http://dx.doi.org/10.1098/rspa.1952.0110>.
- [25] I.M. Mills, Coriolis interactions, intensity perturbations and potential functions in polyatomic molecules, *Pure Appl. Chem.* 11 (1965) 325–344, <http://dx.doi.org/10.1351/pac196511030325>.
- [26] B.J. Drouin, Practical uses of SPFIT, *J. Mol. Spectrosc.* 340 (2017) 1–15, <http://dx.doi.org/10.1016/j.jms.2017.07.009>.
- [27] J.M.L. Martin, J.P. Franco, R. Gijbels, The anharmonic force field of thioformaldehyde, H<sub>2</sub>CS, by ab initio methods, *J. Mol. Spectrosc.* 168 (1994) 363–373, <http://dx.doi.org/10.1006/jmsp.1994.1285>.
- [28] Z. Kisiel, Least-squares mass-dependence molecular structures for selected weakly bound intermolecular clusters, *J. Mol. Spectrosc.* 218 (2003) 58–67, [http://dx.doi.org/10.1016/s0022-2852\(02\)00036-x](http://dx.doi.org/10.1016/s0022-2852(02)00036-x).
- [29] O. Zingsheim, L. Bonah, F. Lewen, S. Thorwirth, H.S.P. Müller, S. Schlemmer, Millimeter-wave double-modulation double-resonance spectroscopy, *J. Mol. Spectrosc.* 381 (2021) 111519, <http://dx.doi.org/10.1016/j.jms.2021.111519>.
- [30] M.A. Martin-Drumel, C.P. Endres, O. Zingsheim, T. Salomon, J. van Wijngaarden, O. Piralí, S. Gruet, F. Lewen, S. Schlemmer, M.C. McCarthy, S. Thorwirth, The SOLEIL view on sulfur rich oxides: The S<sub>2</sub>O bending mode ν<sub>2</sub> at 380 cm<sup>-1</sup> and its analysis using an Automated Spectral Assignment Procedure (ASAP), *J. Mol. Spectrosc.* 315 (2015) 72–79, <http://dx.doi.org/10.1016/j.jms.2015.02.014>.

- [31] C.P. Endres, S. Schlemmer, P. Schilke, J. Stutzki, H.S.P. Müller, The Cologne Database for Molecular Spectroscopy, CDMS, in the Virtual Atomic and Molecular Data Centre, VAMDC, *J. Mol. Spectrosc.* 327 (2016) 95–104, <http://dx.doi.org/10.1016/j.jms.2016.03.005>.
- [32] H.S.P. Müller, S. Thorwirth, D.A. Roth, G. Winnewisser, The Cologne Database for Molecular Spectroscopy, CDMS, *Astron. Astrophys.* 370 (2001) L49–L52, <http://dx.doi.org/10.1051/0004-6361:20010367>.
- [33] K. Islami, B.P. Winnewisser, J. Preusser, M. Winnewisser,  $\text{H}^{13}\text{C}^{14}\text{NO}$ : Independent parameters describing the Coriolis resonance systems (00002)/(00010) and (00012)/(00020), *J. Mol. Spectrosc.* 176 (1996) 403–415, <http://dx.doi.org/10.1006/jmsp.1996.0102>.
- [34] H.S.P. Müller, A. Maeda, F. Lewen, S. Schlemmer, I.R. Medvedev, E. Herbst, Rotational spectroscopy of the thioformaldehyde isotopologues  $\text{H}_2\text{CS}$  and  $\text{H}_2\text{C}^{34}\text{S}$  in four interacting excited vibrational states and an account on the rotational spectrum of thioketene,  $\text{H}_2\text{CCS}$ , *Mol. Phys.* 122 (2023) <http://dx.doi.org/10.1080/00268976.2023.2262057>.

# 9. Double Resonance Spectroscopy of Glycidaldehyde

## Bibliographic Information

L. Bonah, J.-C. Guillemin, A. Belloche, S. Thorwirth, H. S. P. Müller, S. Schlemmer, Leveraging MMW-MMW Double Resonance Spectroscopy to Understand the Pure Rotational Spectrum of Glycidaldehyde and 17 of its Vibrationally Excited States, *ACS Earth Space Chem.* in press (2025). doi:10.1021/acsearthspacechem.4c00360

The supporting information is provided in Sec. A.8.

## Author's contribution

The author of this thesis performed the measurements and the analysis. Furthermore, he wrote the original draft and provided the visualization.

## Context

This study analyzes the rotational spectrum of glycidaldehyde ((C<sub>2</sub>H<sub>3</sub>O)CHO), a structural analog of the astronomically ubiquitous oxirane (*c*-C<sub>2</sub>H<sub>4</sub>O).<sup>45-49</sup> DR measurements facilitated the identification of 17 vibrationally excited states and greatly simplified the interaction analysis by unambiguously identifying interstate transitions. The study demonstrates the unique power of DR measurements to confidently identify subnetworks of the energy term diagram which can easily be extended with LWPs.

## Copyright Notice

Reprinted with permission from *ACS Earth Space Chem.* 2025, **XXX**, XXXX. © 2025 American Chemical Society.

# Leveraging MMW-MMW Double Resonance Spectroscopy to Understand the Pure Rotational Spectrum of Glycidaldehyde and 17 of its Vibrationally Excited States

Luis Bonah,<sup>\*,†</sup> Jean-Claude Guillemin,<sup>‡</sup> Arnaud Belloche,<sup>¶</sup> Sven Thorwirth,<sup>\*,†</sup>  
Holger S. P. Müller,<sup>†</sup> and Stephan Schlemmer<sup>†</sup>

<sup>†</sup>*I. Physikalisches Institut, Universität zu Köln, Zùlpicher Str. 77, 50937 Köln, Germany*

<sup>‡</sup>*Univ Rennes, Ecole Nationale Supérieure de Chimie de Rennes, CNRS, ISCR –  
UMR6226, 35000 Rennes, France*

<sup>¶</sup>*Max-Planck-Institut für Radioastronomie, Auf dem Hügel 69, 53121 Bonn, Germany*

E-mail: bonah@ph1.uni-koeln.de; sthorwirth@ph1.uni-koeln.de

## Abstract

Broadband measurements of glycidaldehyde in the frequency ranges 75–170 GHz and 500–750 GHz were recorded to extend previous analyses of its pure rotational spectrum in the microwave region. The rotational parameters of the ground vibrational states for the main isotopologue and the three singly <sup>13</sup>C substituted isotopologues were considerably improved and additional higher-order parameters were determined.

To identify new vibrationally excited states in the dense and convoluted spectrum, an updated version of the double-modulation double-resonance spectroscopy technique was used. Connecting transitions with a shared energy level into series and expanding these via Loomis-Wood plots proved to be a powerful method, which allowed the identification of 11 new vibrationally excited states in addition to the already known aldehyde torsions,  $v_{21} = 1$  to  $v_{21} = 6$ . Interactions between several vibrational states were observed and three interacting systems were treated successfully.

Rotational transitions of glycidaldehyde were searched for in the imaging spectral line survey ReMoCA obtained with the Atacama

Large Millimeter/submillimeter Array (ALMA) toward the high-mass star-forming region Sgr B2(N). The observed spectra were modeled under the assumption of local thermodynamic equilibrium (LTE). Glycidaldehyde, an oxirane derivative, was not detected toward Sgr B2(N2b). The upper limit on its column density implies that it is at least six times less abundant than oxirane in this source.

## Keywords

Absorption Spectroscopy, CCSD(T), Coriolis Interactions, Fermi Resonances, Double-Modulation Double-Resonance Spectroscopy, Vibrational Satellites

## 1 Introduction

To date, only a handful of ring molecules with heteroatoms in the ring have been detected in space. Beginning with the smallest possible ring molecules, the three triatomics  $c$ -SiC<sub>2</sub>,<sup>1</sup>  $c$ -MgC<sub>2</sub>,<sup>2</sup> and  $c$ -CaC<sub>2</sub><sup>3</sup> were first detected toward the carbon-rich asymptotic giant branch star CW Leo (IRC +10216) in

1984, 2022 and 2024, respectively. SiC<sub>2</sub> was found recently also toward the Galactic Center molecular cloud G+0.693–0.027.<sup>4</sup> Similarly, the four-atom molecule *c*-SiC<sub>3</sub> was detected in 1999 in the circumstellar envelope of CW Leo. The two somewhat more complex ring molecules oxirane (*c*-C<sub>2</sub>H<sub>4</sub>O) and propylene oxide (CH<sub>3</sub>CHCH<sub>2</sub>O) were first detected toward the high-mass star-forming region Sagittarius B2(N) in 1997<sup>5</sup> and 2016,<sup>6</sup> respectively. Oxirane was later also observed toward hot core regions,<sup>7</sup> Galactic center molecular clouds,<sup>8</sup> a low-mass protostar,<sup>9</sup> and pre-stellar cores.<sup>10</sup>

The presence of oxirane in the interstellar medium gives rise to the question whether or not oxirane derivatives are astronomically abundant. Glycidaldehyde ((C<sub>2</sub>H<sub>3</sub>O)CHO), also known as oxiranecarboxaldehyde or 2,3-epoxy-propanal, is such a derivative in which one of oxirane’s H atoms is substituted by a –CHO functional group. Its rotational spectrum is known from a previous study in the microwave range (8–40 GHz) by Creswell et al. from 1977.<sup>11</sup> There, the authors analyzed the ground vibrational states of the main isotopologue and the three singly substituted <sup>13</sup>C isotopologues in natural abundance. Additionally, the lowest vibrational fundamental, the aldehyde torsion at about 125 cm<sup>-1</sup>, was followed up to  $v_{21} = 7$ . However, even for the ground vibrational state only quartic centrifugal distortion parameters were determined, making frequency extrapolations to higher frequency ranges rapidly inaccurate.

In the present study, the frequency coverage was extended to the millimeter and sub-millimeter ranges reaching frequencies as high as 750 GHz. The dense and convoluted spectrum of glycidaldehyde makes it an ideal case study for double-modulation double-resonance (DM-DR) spectroscopy,<sup>12</sup> which allows to filter the spectrum for lines sharing an energy level. This simplified the analysis immensely, proved critical in identifying new vibrationally excited states, and understanding interactions between them. In total, 17 vibrationally excited states of the main isotopologue were analyzed along with the ground vibrational states of the main isotopologue and the three singly substituted

<sup>13</sup>C isotopologues.

## 2 Experimental Details

Broadband as well as double-resonance measurements were recorded at two experimental setups in Cologne with a sample synthesized on gram scale according to a previously reported procedure.<sup>13</sup> The broadband measurements cover the frequency ranges 75–170 GHz and 500–750 GHz. Double-resonance (DR) measurements in the frequency range 75–120 GHz were used to confirm relationships between lines, identify new series of transitions, and find pure rotational transitions between vibrationally excited states (so-called interstate transitions) that arise due to wavefunction mixing when vibrational states interact with each other. The DR measurements were performed with a modified version of the double-modulation double-resonance (DM-DR) method (see Sec. 2.2) described previously.<sup>12</sup>

### 2.1 Experimental Setups

Two absorption experiments were used to record the broadband spectra, each consisting of a source, an absorption cell, and a detector. The sources consist of synthesizers with subsequent amplifier-multiplier chains. The radiation is guided through the absorption cells and into the detector via lenses, mirrors, and horn antennas. For the higher frequency range of 500–750 GHz, the absorption cell consists of a single 5 m borosilicate glass cell in a double-pass setup for a total absorption path of 10 m. The lower frequency range setup (75–170 GHz) uses two 7 m borosilicate glass cells in a single-pass configuration for a total absorption path of 14 m. Double-pass configurations are foregone here as this lower-frequency experiment is also used for the DR measurements where the second polarization direction is used to align the pump and probe sources radiation co-spatially (see Sec. 2.2). Different Schottky detectors were used for frequencies below 500 GHz and a cryogenically cooled hot-electron bolometer (QMC QNbB/PTC(2+XBI)) was used for

measurements above 500 GHz. All experimental setups use frequency modulation with a  $2f$ -demodulation scheme to increase the signal-to-noise ratio (SNR). As a result, absorption features look similar to a second derivative of a Voigt profile. The lower frequency experimental setup is described in more detail elsewhere.<sup>12</sup>

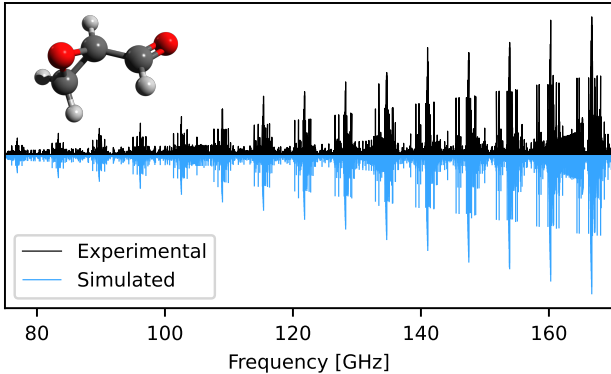


Figure 1: The intensity-calibrated broadband spectrum of glycidaldehyde (black) from 75 GHz to 170 GHz in comparison with the simulated stick spectrum (blue). The ground vibrational state analysis was used for the intensity calibration. For better visual comparability, only experimental data points with positive signals are shown here. The stick-and-ball representation of glycidaldehyde is shown in the top left.

All measurements were performed at room temperature with filling pressures around  $10\ \mu\text{bar}$ . Standing waves were removed from the measurements with a self-written Fourier filtering script<sup>1</sup>. Additionally, after completing the ground vibrational state analysis, the broadband measurements were intensity calibrated using the ground vibrational state predictions (see Fig. 1). All  $v = 0$  transitions predicted to have an intensity  $>10^{-5}\ \text{nm}^2\text{MHz}$  were fitted with a second derivative Voigt profile. Blends were considered by summing the intensities of all predictions within 200 kHz of the prediction of interest. The ratio of the predicted intensities and fitted intensities were then used to create a calibration curve with values in between the calibration points be-

<sup>1</sup>Available at <https://pypi.org/project/fftfilter/> or with pip via `pip install fftfilter`

ing interpolated. These post-processing steps greatly facilitated the visual detection of weak patterns in Loomis-Wood plots.

## 2.2 Improved DM-DR Setup

An improved version of the double-modulation double-resonance (DM-DR) setup originally described in Zingsheim et al.<sup>12</sup> was used for the DM-DR measurements. The great advantage of DM-DR measurements is their ability to filter the spectrum for lines (so-called probe transitions) sharing an energy level with an already known transition, the so-called pump transition. This greatly facilitates the assignment and analysis process as it allows to filter dense spectra for specific lines which is especially useful to unambiguously identify weak, blended and/or strongly perturbed transitions.

The DM-DR setup used here is based on the conventional 75–120 GHz absorption setup described in Sec. 2.1. A second, more powerful source, the pump source, is added covering the frequency range of 70–110 GHz and polarized orthogonally to the probe radiation allowing for co-spatial alignment of the probe and pump radiation via a polarizing grid. The probe frequency is tuned to record the spectrum whereas the radiation of the pump source is fixed to the frequency of a known pump transition and not measured by the detector. Instead, the pump radiation is used to split the energy levels of the pump transition via the Autler-Townes effect.<sup>14,15</sup> As a result, all transitions sharing an energy level with the pump transition split symmetrically into two transitions of half intensity. This is highlighted in the simulated 2D spectra in Fig. 2. The left half of the figure shows the case when the probe and pump transition share an energy level and the pump radiation is on. The heatmap shows the absorption of the probe radiation for the offsets of the probe and pump frequencies, i.e., that both sources are resonant with their respective transitions in the center of the heatmap. The plots to the left and the bottom show the 1D spectra along the dashed lines in the same colors. The right half shows the case when the probe and pump transition do not share an energy level or the pump radi-

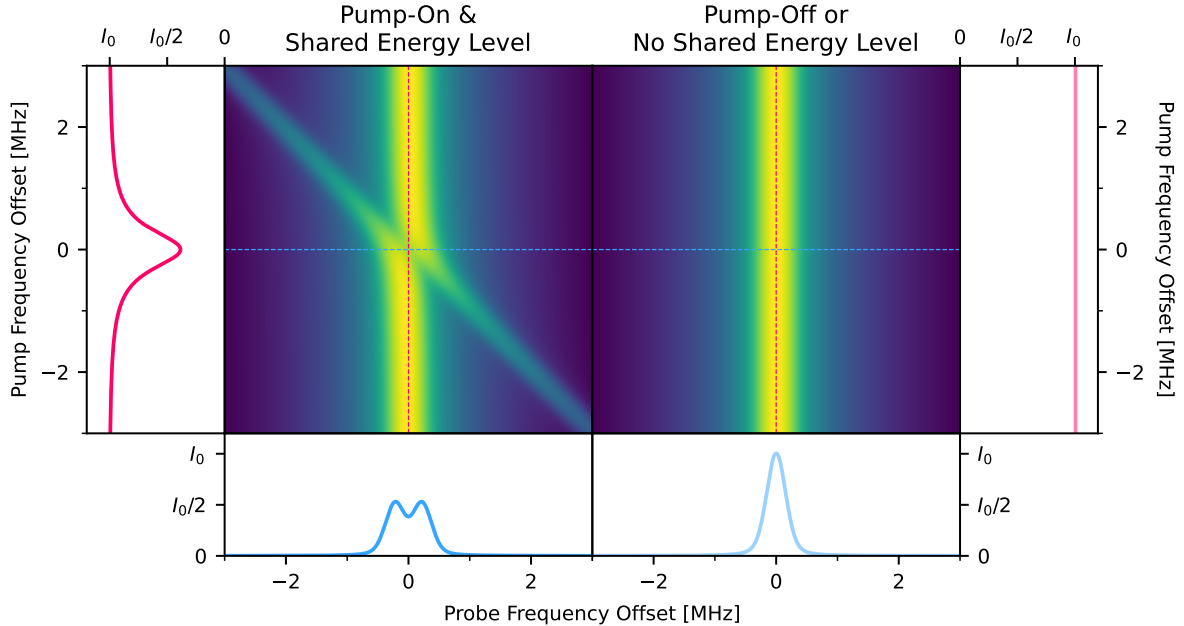


Figure 2: Simulated 2D spectra of the probe radiation absorption for the cases of a shared energy level (left half) and no pump radiation or no shared energy level between probe and pump transition (right half). The  $x$ - and  $y$ -axis depict the frequency offsets of the probe and pump source, respectively. The dashed lines in the heatmaps indicate the slices that are shown in the plots to the sides and on the bottom.

ation is turned off. It is apparent that in this case, the 2D spectrum does not depend on the pump frequency.

A straight-forward way to determine if the probe and pump transition share an energy level is to subtract the spectra measured with and without pump source - basically subtracting the left and right 1D slices in blue. The subtraction should be performed on a very short time scale to mitigate the influence of fluctuations in the experimental conditions which could otherwise lead to false positive signals (see Fig. 8 in Zingsheim et al.<sup>12</sup>). This was realized in the previous setup<sup>12</sup> by amplitude modulating the pump source and a corresponding  $1f$ -demodulation of the detector signal. Additionally, a frequency modulation of the probe source combined with a  $2f$ -demodulation of the detector signal was employed to increase the SNR.

The two consecutive demodulation steps are non-ideal for multiple reasons. Firstly, using a sine signal to realize a subtraction has an efficiency of only  $2/\pi \approx 64\%$ . Secondly, two lock-in amplifiers arranged in serial result in many

of their parameters influencing each other (e.g. the dependence of the signal on both time constants).

These shortcomings can be mitigated by using a digital DM-DR setup which performs the second demodulation in the measurement software. The intensity is measured with and without the pump source by digitally turning the pump source's radio frequency power on and off and subtracting the respective intensities on the computer. However, this procedure introduces additional overhead in the form of switching the radio frequency on and off<sup>2</sup>.

Another possibility, applied here, is to operate the probe source in continuous wave mode and apply an FM to the pump source requiring only a single lock-in amplifier for the demodulation. The single FM of the pump source simultaneously increases the SNR and removes all transitions from the DM-DR spectrum that do not share an energy level with the pump

<sup>2</sup>This overhead has greater efficiency than the  $2/\pi \approx 64\%$  efficiency of the previous DM-DR setup for integration times  $\geq 28$  ms. This integration time is well surpassed in our measurements.

transition. The working principle is explained by the red 1D slices along the pump frequency axis in Fig. 2. If the probe and pump transition share an energy level, the signal along the pump frequency axis has a strong dip at the center position whereas if no energy level is shared the signal is constant (left-most and right-most plots of Fig. 2, respectively). The two cases are distinguished via the FM of the pump source and subsequent  $2f$ -demodulation of the detector signal. For the pump-off case, this results in a zero signal after the lock-in amplifier but a strong signal for the pump-on case. Analogously to the conventional case, the FM also improves the SNR for the pump-on case. However, the FM amplitude has to be adjusted as the linewidth of the conventional case (bottom right plot of Fig. 2) depends on the different broadening effects but the linewidth along the pump frequency axis (left-most plot of Fig. 2) also strongly depends on the magnitude of the Autler-Townes splitting.

The simplicity of the new setup is highlighted by it differing from the conventional setup only in the lock-in amplifier being connected to the pump instead of the probe source synthesizer (and the obvious addition of a pump source). This makes switching between the two measurement techniques as simple as changing a single cable connection.

Additionally, the current pump-modulated setup showed greater sensitivity for the detuning of the pump source in our measurements and simulations. Therefore, false positive signals (due to transitions close to the pump transition being pumped off-resonantly) are more easily distinguished. However, simulations also show that this behavior is very dependent on the magnitude of the Autler-Townes splitting and the chosen FM amplitudes. In summary, for molecules with similar (transition) dipole moments as glycidaldehyde, the new setup is noticeably more sensitive to false positive signals arising from off-resonant pumping than the previous setup.<sup>12</sup>

### 3 Quantum chemical calculations

Complementary quantum chemical calculations of glycidaldehyde have been performed at the coupled-cluster singles and doubles (CCSD) level augmented by a perturbative treatment of triple excitations, CCSD(T),<sup>16</sup> together with correlation consistent polarized valence and polarized weighted core-valence basis sets, as well as atomic natural orbital basis sets, specifically, cc-pVTZ,<sup>17</sup> cc-pwCVTZ,<sup>18</sup> and ANO0.<sup>19</sup> Equilibrium geometries have been calculated using analytic gradient techniques,<sup>20</sup> while harmonic frequencies have been computed using analytic second-derivative techniques.<sup>21,22</sup> For anharmonic computations using the cc-pVTZ and ANO0 basis sets second-order vibrational perturbation theory (VPT2)<sup>23</sup> has been employed and additional numerical differentiation of analytic second derivatives has been applied to obtain the third and fourth derivatives required for the application of VPT2.<sup>22,24</sup>

All calculations have been carried out using the CFOUR program package;<sup>25,26</sup> for some of the calculations the parallel version of CFOUR<sup>27</sup> has been used. The resulting rotation-vibration interaction constants, harmonic and fundamental wavenumbers, fundamental intensities, energy-dependence on the aldehyde torsional angle, and optimized molecular structures are given in Sec. 1 of the Supporting Information.

### 4 Spectroscopic Fingerprint of Glycidaldehyde

Glycidaldehyde ((C<sub>2</sub>H<sub>3</sub>O)CHO) is an asymmetric rotor with Ray’s asymmetry parameter of  $\kappa = (2B - A - C)/(A - C) = -0.98$  which is very close to the prolate limit of  $-1$ . Creswell et al. determined its three dipole moment components to be  $\mu_a = 1.932(5)$  D,  $\mu_b = 1.511(17)$  D, and  $\mu_c = 0.277(156)$  D resulting in strong *a*- and *b*-type spectra accompanied by a considerably weaker *c*-type spectrum.<sup>11</sup> Additionally, four fundamental vibrational modes lie below



Table 1: Approximated energies from the Boltzmann analysis  $\tilde{\nu}_{\text{appr}}$  in  $\text{cm}^{-1}$ , rotational constant differences  $\Delta A$ ,  $\Delta B$ ,  $\Delta C$  with respect to the ground vibrational state of the main isotopologue in MHz, number of rejected lines, the number of transitions,  $RMS$  in kHz, and  $WRMS$  values for the analyzed states. Comparison with the calculated values (see Sec. 1 of the Supporting Information) yielded the state labels given in the first column. Interaction systems are indicated by mutual colors analog to Fig. 3.

Vib. State	$\tilde{\nu}_{\text{appr}}$	$\Delta A$	$\Delta B$	$\Delta C$	Rejected	Transitions	$RMS$	$WRMS$
(0, 0, 0, 0)	0	0.00	0.00	0.00	0	6921	28.52	0.86
(1, 0, 0, 0)	125(27)	-138.84	12.89	5.16	0	5218	29.77	0.88
(2, 0, 0, 0)	257(42)	-273.89	25.64	10.27	0	3091	18.83	0.58
(0, 1, 0, 0)	312(14)	125.26	-1.82	-0.54	0	2356	17.95	0.59
(0, 0, 1, 0)	361(17)	-17.71	-0.73	-4.72	1 <sup>a</sup>	2614 <sup>a</sup>	28.16 <sup>a</sup>	0.87 <sup>a</sup>
(3, 0, 0, 0)	390(41)	-406.36	38.33	15.34	1 <sup>a</sup>	2614 <sup>a</sup>	28.16 <sup>a</sup>	0.87 <sup>a</sup>
(1, 1, 0, 0)	437(22)	-23.99	11.48	4.46	0	793	18.18	0.56
(1, 0, 1, 0)	469(20)	-132.46	10.50	0.32	0 <sup>b</sup>	1930 <sup>b</sup>	33.88 <sup>b</sup>	0.94 <sup>b</sup>
(0, 0, 0, 1)	516(14)	-3.18	-1.84	-2.01	0 <sup>b</sup>	1930 <sup>b</sup>	33.88 <sup>b</sup>	0.94 <sup>b</sup>
(4, 0, 0, 0)	538(54)	-533.90	50.87	20.47	0 <sup>b</sup>	1930 <sup>b</sup>	33.88 <sup>b</sup>	0.94 <sup>b</sup>
(2, 1, 0, 0)	584(37)	-166.96	24.45	9.34	0	676	25.12	0.74
(2, 0, 1, 0)	595(40)	-253.18	23.29	6.11	0 <sup>c</sup>	1016 <sup>c</sup>	23.73 <sup>c</sup>	0.66 <sup>c</sup>
(0, 2, 0, 0)	612(33)	250.42	-3.61	-1.05	15	541	54.75	1.48
(1, 0, 0, 1)	637(21)	-148.11	11.91	3.28	27	564	82.51	2.14
(5, 0, 0, 0)	640(75)	-666.26	63.13	25.08	0 <sup>c</sup>	1016 <sup>c</sup>	23.73 <sup>c</sup>	0.66 <sup>c</sup>
(0, 1, 1, 0)	677(22)	89.93	-1.36	-4.75	5	223	87.91	2.32
(1, 2, 0, 0)	754(24)	90.18	10.10	3.77	0	359	23.94	0.62
(6, 0, 0, 0)	767(61)	-682.75	65.89	24.96	110	269	195.76	4.22
<sup>13</sup> C <sub>2</sub> $v_0$	0	-141.82	-5.77	-1.11	0	107	38.70	0.59
<sup>13</sup> C <sub>1</sub> $v_0$	0	-333.54	-42.43	-48.41	0	354	30.18	0.59
<sup>13</sup> C <sub>4</sub> $v_0$	0	-84.48	-22.40	-18.28	0	347	31.07	0.54

The rotational constant differences are defined as  $\Delta A = A_v - A_0 \approx -\alpha_v^A$  (analog for  $B$  and  $C$ ). The  $\alpha_v^{A/B/C}$  are the first-order rotation-vibration interaction constants.

<sup>a,b,c</sup> Reported values are values for the respective combined fits.

tions are typically around  $10 \text{ cm}^{-1}$  with a maximum deviation of  $56 \text{ cm}^{-1}$  ( $1.04 \sigma$ ) for (4, 0, 0, 0). The rejected lines and  $RMS$  values in Tab. 1 show that the vibrational states (0, 2, 0, 0), (1, 0, 0, 1), (0, 1, 1, 0), and (6, 0, 0, 0)<sup>5</sup> could not be fit to experimental accuracy, hinting toward so far unaccounted interactions between these states and/or states not found yet. Therefore, these vibrational states were only fit to (incomplete) sets of quartic parameters as higher-order

<sup>5</sup>The vibrational state (6, 0, 0, 0) is most likely interacting with the not yet found (3, 0, 1, 0) state, as  $(3 + n, 0, 0, 0)$  and  $(n, 0, 1, 0)$  are interaction partners for  $n = 0, 1, 2$ . Similarly, (1, 0, 0, 1) could be interacting with (5, 0, 0, 0) and (2, 0, 1, 0). However, no conclusive evidence was found in the present analysis.

parameters had physically unreasonable values. The obtained quartic distortion constants are probably highly effective and therefore should be viewed with caution. Lastly, we searched for the gauche rotamer which is calculated to lie about 2.4 kcal/mol above the trans rotamer which is studied here (see Sec. 1.4 of the Supporting Information). However, it could not be identified in the spectrum due to its low relative intensity of about 1%.

## 4.1 Interactions

Three interacting systems, two dyads and one triad (see Fig. 3), were identified via mirror images in their resonance plots (see Fig. 4 for an

Table 2: Rotational parameters for the vibrationally excited states showing no signs of interactions.

Parameter	(0, 0, 0, 0)	(1, 0, 0, 0)	(2, 0, 0, 0)	(0, 1, 0, 0)	(1, 1, 0, 0)	(2, 1, 0, 0)	(1, 2, 0, 0)
$A$	/MHz 18 241.103 87(19)	18 102.259 87(32)	17 967.217 08(41)	18 366.364 03(43)	18 217.1127(12)	18 074.1423(20)	18 331.280(12)
$B$	/MHz 3272.930 495(19)	3285.825 204(35)	3298.572 751(46)	3271.112 670(47)	3284.406 419(84)	3297.377 50(15)	3283.025 60(38)
$C$	/MHz 3137.715 975(19)	3142.876 056(34)	3147.986 355(43)	3137.177 298(46)	3142.173 601(83)	3147.053 19(13)	3141.482 00(35)
$-D_J$	/Hz -562.8157(35)	-584.9696(62)	-609.597(13)	-558.715(13)	-579.465(61)	-603.75(13)	-574.32(19)
$-D_{JK}$	/kHz -12.384 92(12)	-11.720 27(17)	-11.027 35(27)	-12.729 52(33)	-12.044 46(52)	-11.3350(14)	-12.3495(37)
$-D_K$	/kHz -17.025 86(82)	-13.8831(12)	-11.6549(19)	-21.0929(21)	-16.681(52)	-14.005(91)	a
$d_1$	/Hz -23.785 67(83)	-28.8834(16)	-35.1890(27)	-21.8173(33)	-25.6225(39)	-31.1609(83)	-22.28(20)
$d_2$	/Hz -3.807 94(52)	-4.652 23(67)	-5.655 47(99)	-4.107 49(61)	-4.8411(12)	-5.8701(48)	-4.95(13)
$H_J$	/μHz 135.13(19)	180.54(35)	225.2(12)	154.86(98)	a	a	a
$H_{JK}$	/mHz 74.152(29)	70.182(32)	65.758(48)	77.045(61)	a	60.76(60)	a
$H_{KJ}$	/Hz -1.119 31(26)	-1.027 23(44)	-0.9564(10)	-1.1710(15)	-1.0768(19)	-1.1680(33)	-1.444(22)
$H_K$	/Hz 0.9252(19)	0.6232(23)	0.4223(36)	1.0476(42)	a	a	a
$h_1$	/μHz 66.782(64)	86.99(13)	103.91(35)	80.28(41)	a	a	a
$h_2$	/μHz 65.84(16)	74.34(17)	81.01(26)	a	a	a	a
$h_3$	/μHz 3.147(18)	4.354(34)	5.792(53)	4.281(47)	a	a	a
$L_{JJK}$	/nHz -435.5(20)	a	a	a	a	a	a
$L_{JK}$	/μHz 15.181(61)	a	a	a	a	a	a
$L_{KKJ}$	/μHz -148.17(22)	-138.96(50)	-119.5(23)	-194.2(38)	a	a	a
$L_K$	/μHz 98.5(17)	a	a	a	a	a	a
$l_2$	/pHz -457(10)	a	a	a	a	a	a
$P_{JK}$	/pHz -170.2(49)	a	a	a	a	a	a

Fits performed with SPFIT in the S-reduction and I<sup>r</sup> representation. Standard errors are given in parentheses. Parameters of the ground vibrational state are applied to all vibrationally excited states and difference values are fitted. Here, the ground state values and the difference values are summed up to facilitate readability. <sup>a</sup> Parameter was fixed to the ground vibrational state value.

Table 3: Rotational parameters for perturbed vibrationally excited states. Interaction systems are indicated by mutual colors analog to Fig. 3.

Parameter	(3, 0, 0, 0)	(0, 0, 1, 0)	(4, 0, 0, 0)	(0, 0, 0, 1)	(1, 0, 1, 0)	(5, 0, 0, 0)	(2, 0, 1, 0)
$A$	/MHz 17 834.7414(11)	18 223.392 39(85)	17 707.206(32)	18 237.9200(18)	18 108.640(31)	17 574.843(90)	17 987.919(69)
$B$	/MHz 3311.259 35(52)	3272.204 50(53)	3323.7963(60)	3271.087 87(14)	3283.4265(59)	3336.0644(60)	3296.2155(61)
$C$	/MHz 3153.059 84(49)	3132.991 66(51)	3158.1879(37)	3135.706 95(14)	3138.0404(41)	3162.8010(64)	3143.8250(62)
$-D_J$	/Hz -635.609(31)	-567.666(39)	-683.43(48)	-551.24(13)	-582.06(46)	-687.08(56)	-632.22(47)
$-D_{JK}$	/kHz -10.331 13(87)	-12.197 06(68)	-9.2938(43)	-12.871 15(75)	-11.6039(30)	-8.817(13)	-10.778(14)
$-D_K$	/kHz -9.9554(30)	-18.3383(23)	-9.44(11)	-11.246(85)	-19.101(82)	-5.1(30)	-3.5(25)
$d_1$	/Hz -42.790(11)	-29.140(11)	-54.78(12)	-14.4775(93)	-39.04(11)	-56.93(33)	-51.52(30)
$d_2$	/Hz -6.7421(25)	-4.2187(22)	-9.753(33)	-1.848(13)	-5.788(29)	-9.18(17)	-7.25(14)
$H_J$	/μHz a	198.1(19)	a	a	a	a	a
$H_{JK}$	/mHz 62.33(24)	a	a	a	a	a	35.8(26)
$H_{KJ}$	/Hz -0.8813(13)	a	a	-0.8041(31)	-0.9355(47)	-0.6191(82)	a
$H_K$	/mHz 326.7(62)	a	a	a	a	a	a
$h_2$	/μHz 100.4(10)	a	a	a	a	a	a

Fits performed with SPFIT in the S-reduction and I<sup>r</sup> representation. Standard errors are given in parentheses. Parameters of the ground vibrational state (see Tab. 2) are applied to all vibrationally excited states and difference values are fitted. Here, the ground state values and the difference values are summed up to facilitate readability. <sup>a</sup> Parameter was fixed to the ground vibrational state value.

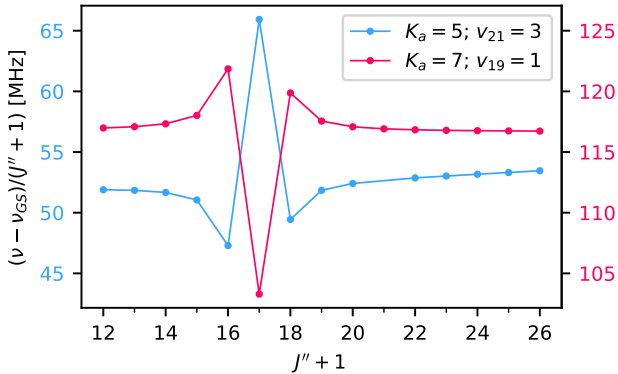


Figure 4: Resonance plot for the  $3\nu_{21}/\nu_{19}$  dyad. A  $\Delta K_a = 2$  interaction for the  $K_a = 5$  series of  $\nu_{21} = 3$  and the  $K_a = 7$  series of  $\nu_{19} = 1$  is highlighted by the mirrored patterns. Here, the  $J = K_a + K_c$  asymmetry components are shown but the figure is nearly identical for the other asymmetry component. The respective  $y$ -axes are shifted to highlight the mirror image nature of the two series which is a clear sign of an interaction between the two states centered around  $J = 17$ .

example case). For the  $(4, 0, 0, 0)$ ,  $(0, 0, 0, 1)$ , and  $(1, 0, 1, 0)$  triad as well as the  $(5, 0, 0, 0)$ , and  $(2, 0, 1, 0)$  dyad, the initial vibrational energy separations were approximated from the rotational energies of the strongest mirror images in the resonance plots<sup>6</sup>. The analysis of the  $(3, 0, 0, 0)$  and  $(0, 0, 1, 0)$  dyad was greatly simplified by finding interstate transitions between vibrationally excited states using the DM-DR method. This yielded their vibrational energy separation with rotational precision (see Fig. 5 for an example). Transitions between vibra-

<sup>6</sup>To approximate the initial vibrational energy separations, first, the energy levels at the center of the interaction are identified in resonance plots (e.g.  $17_{7,10}$  of  $\nu_{19} = 1$  and  $17_{5,12}$  of  $\nu_{21} = 3$  in Fig. 4). Their rovibrational energies, consisting of a calculated vibrational energy and the rotational energy from the best-fit rotational model, are retrieved from the \*.egy file produced by SPCAT.<sup>29</sup> Then, the rovibrational energies of the two states are equalized by adding an energy offset to one of the two vibrational states (in the example of  $\nu_{21} = 3$  and  $\nu_{19} = 1$  the calculated vibrational energies  $E_{\nu_{19}=1}^{\text{calc}}$  and  $E_{\nu_{21}=3}^{\text{calc}}$  are used together with the offset energy  $\Delta E_{\nu_{21}=3}$ ). Once first interaction parameters are included in the combined fit, the offset energy can be floated in the fit and will result in a highly accurate value for the vibrational energy separation.

Table 4: Rotational parameters for the ground vibrational states of the three singly substituted  $^{13}\text{C}$  isotopologues of glycidaldehyde.

Parameter	$^{13}\text{C}_2$	$^{13}\text{C}_1$	$^{13}\text{C}_4$
$A$	/MHz 18 099.286(46)	17 907.566(41)	18 156.623(21)
$B$	/MHz 3267.164 09(87)	3230.498 76(74)	3250.529 47(27)
$C$	/MHz 3136.601 01(66)	3089.309 08(70)	3119.439 19(27)
$-D_J$	/Hz -559.12(33)	-554.49(18)	-561.62(19)
$-D_{JK}$	/kHz -12.145(14)	-11.9148(14)	-11.9002(13)
$-D_K$	/kHz a	a	a
$d_1$	/Hz -22.16(37)	-26.93(33)	a
$d_2$	/Hz a	a	a

Fits performed with SPFIT in the S-reduction and I<sup>r</sup> representation. Standard errors are given in parentheses. Parameters of the main isotopologue (see Tab. 2) are applied to all isotopologues and difference values are fitted. Here, the main isotopologue values and the difference values are summed up to facilitate readability. <sup>a</sup> Parameter was fixed to the main isotopologue value.

tionally excited states become allowed due to the interactions which result in the rovibrational levels being linear combinations of the rovibrational levels of the interacting vibrational states. This means the rovibrational levels shown on the right-hand side of Fig. 5 are linear combinations with the labels corresponding to the largest contribution. For example, the rovibrational level labeled  $17_{7,10} \nu_{19} = 1$  is a linear combination of  $17_{7,10} \nu_{19} = 1$  and  $17_{5,12} \nu_{21} = 3$  (similarly  $16_{5,11} \nu_{21} = 3$  will also contain parts of  $16_{7,9} \nu_{19} = 1$ ). As a result, the transition between the states labeled  $16_{5,11} \nu_{21} = 3$  and  $17_{7,10} \nu_{19} = 1$  becomes allowed.

As glycidaldehyde has  $C_1$  symmetry,  $a$ -,  $b$ -, and  $c$ -type Coriolis interactions as well as Fermi resonances are allowed by symmetry considerations between any combination of vibrational modes. For each interaction system, the leading parameters for the different interaction types were tested with *Pyckett* and the influence on the *RMS*, *WRMS*, and rejected lines were monitored. When lower-order parameters were added, subsequently higher-order parameters of the same interaction type were tested. The final interaction parameter set includes Fermi,  $a$ -,  $b$ -, and  $c$ -type Coriolis terms as seen in Tab. 5. The absolute signs of the interaction parameters could not be determined from the fit, only their relative signs.<sup>33,34</sup>

To find the regions where the interactions have the strongest influence, the shifts in tran-

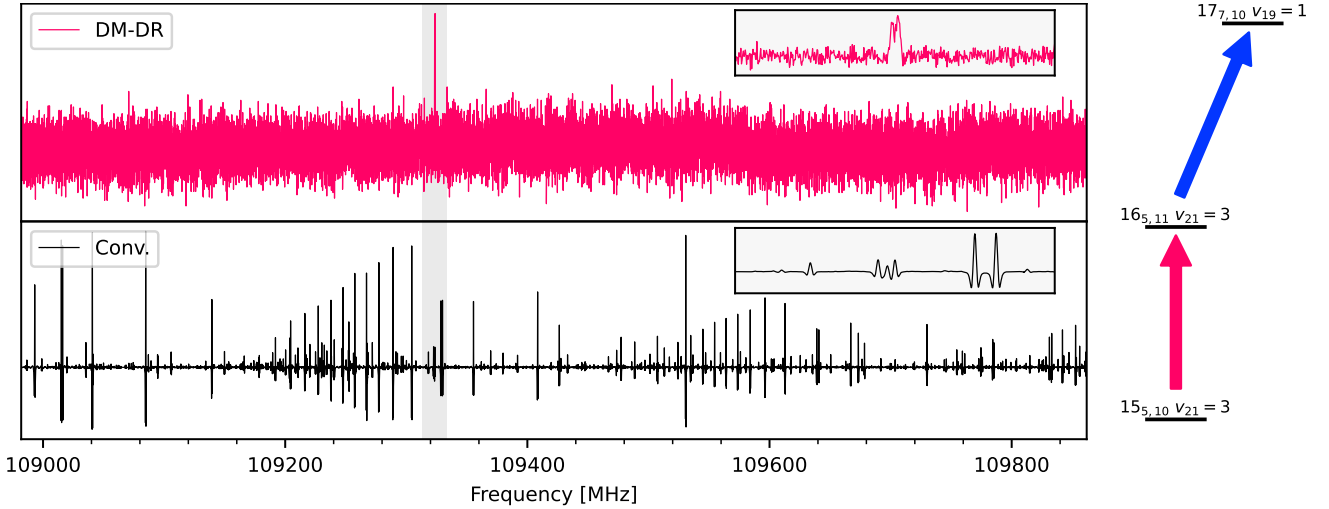


Figure 5: DM-DR (top) and conventional measurement (bottom) of the same frequency range. On the right, the transition of interest, an interstate transition, is indicated in blue and the pump transition is indicated in red. Due to the DM-DR scheme, only lines sharing an energy level with the pump transition have a signature in the top plot, unambiguously identifying the weak interstate transition. As can be seen from the zoom into the gray marked area, there are many candidate lines in the conventional spectrum but only a single line in the DM-DR spectrum.

sition frequency between predictions with and without interactions were calculated (see Sec. 3 of the Supporting Information). When comparing these plots for coupled vibrational states, mirror images highlight the rotational states that are interaction partners. For all three interacting systems the trends were very similar as  $\Delta K_a$  decreases with increasing  $K_a$  value. Exemplary for the energetically lowest dyad, there are clear mirror image patterns for  $K_a = 2$  of  $(3, 0, 0, 0)$  and  $K_a = 6$  of  $(0, 0, 1, 0)$  resulting in  $\Delta K_a = 4$  for these lower  $K_a$  values. For higher  $K_a$  values mirror image patterns can be seen e.g. for  $K_a = 11$  and  $K_a = 12$ , respectively, resulting in  $\Delta K_a = 1$  for these higher  $K_a$  values.

For low  $K_a$  values the interactions between  $(3, 0, 0, 0)$  and  $(0, 0, 1, 0)$  are most prominent around  $J = 16$  for  $K_a = 5$  and  $K_a = 7$ , respectively (see Fig. 4). Further strong interactions are found around  $J = 32$  between  $K_a = 11$  and  $K_a = 12$  in addition to  $\Delta K_a = 0$  interactions for the highest measured values of  $K_a$ , being 15 to 20.

For the  $(4, 0, 0, 0)$ ,  $(0, 0, 0, 1)$ , and  $(1, 0, 1, 0)$  triad, the dominant shifts are between  $(4, 0, 0, 0)$  and  $(1, 0, 1, 0)$ . At low  $K_a$  values, the prominent interactions are around  $J = 32$

between  $K_a = 7$  and  $K_a = 9$ . For higher  $K_a$  values  $\Delta K_a = 1$  interactions dominate with the biggest shifts around  $J = 37$  between  $K_a = 14$  and  $K_a = 15$ , respectively.

For the  $(5, 0, 0, 0)$ , and  $(2, 0, 1, 0)$  dyad the strongest interactions are around  $J \geq 50$  between  $K_a = 17$  and  $K_a = 18$ , respectively.

Due to the limitations in the frequency coverage,  $a$ -type transitions of the interacting systems are typically assigned up to  $J = 26$ . As a consequence, the centers of some perturbations lie outside our quantum number range and are determined via the predictions with and without interaction parameters.

The resulting rotational parameters (see Tab. 3) are deemed to be effective, particularly for the  $(4, 0, 0, 0)$ ,  $(0, 0, 0, 1)$ , and  $(1, 0, 1, 0)$  triad, as can be seen in the parameter progression for the quartic parameters (see Sec. 4 of the Supporting Information). This could result from so far unaccounted interactions with other states where the effects are too weak to be identified in the residuals or the corresponding quantum number ranges have not been observed yet.

Lastly, both  $(2, 1, 0, 0)$ , and  $(1, 2, 0, 0)$  show hints for perturbations at higher  $K_a$  values but

Table 5: Energy differences and interaction parameters for the three interacting systems. Interaction systems are ordered by increasing energy and are indicated by mutual colors analog to Fig. 3.

$v_1$	$v_2$	ID <sup>a</sup>	Parameter	Value
(3, 0, 0, 0)	(0, 0, 1, 0)	$\tilde{\nu}_{(3,0,0,0)} - \tilde{\nu}_{(0,0,1,0)}$	$/\text{cm}^{-1}$	11.244 876(41)
(3, 0, 0, 0)	(0, 0, 1, 0)	$0v_1v_2$	$W$	$/\text{GHz}$ -65.6194(16)
(3, 0, 0, 0)	(0, 0, 1, 0)	$1v_1v_2$	$W_J$	$/\text{kHz}$ 295.3(13)
(3, 0, 0, 0)	(0, 0, 1, 0)	$400v_1v_2$	$W_2$	$/\text{kHz}$ -28.454(68)
(3, 0, 0, 0)	(0, 0, 1, 0)	$401v_1v_2$	$W_{2,J}$	$/\text{Hz}$ -1.848(24)
(3, 0, 0, 0)	(0, 0, 1, 0)	$4000v_1v_2$	$G_b$	$/\text{MHz}$ -164.86(31)
(3, 0, 0, 0)	(0, 0, 1, 0)	$6000v_1v_2$	$G_c$	$/\text{MHz}$ 177.25(29)
(3, 0, 0, 0)	(0, 0, 1, 0)	$6001v_1v_2$	$G_{c,J}$	$/\text{kHz}$ -1.685(20)
(3, 0, 0, 0)	(0, 0, 1, 0)	$6100v_1v_2$	$F_{ab}$	$/\text{MHz}$ -2.583(16)
(4, 0, 0, 0)	(0, 0, 0, 1)	$\tilde{\nu}_{(0,0,0,1)} - \tilde{\nu}_{(4,0,0,0)}$	$/\text{cm}^{-1}$	25.8639(62)
(4, 0, 0, 0)	(0, 0, 0, 1)	$2100v_1v_2$	$F_{bc}$	$/\text{MHz}$ 1.958(11)
(4, 0, 0, 0)	(0, 0, 0, 1)	$2101v_1v_2$	$F_{bc,J}$	$/\text{Hz}$ -128.8(74)
(4, 0, 0, 0)	(1, 0, 1, 0)	$\tilde{\nu}_{(4,0,0,0)} - \tilde{\nu}_{(1,0,1,0)}$	$/\text{cm}^{-1}$	12.6794(48)
(4, 0, 0, 0)	(1, 0, 1, 0)	$0v_1v_2$	$W$	$/\text{GHz}$ 134.42(10)
(4, 0, 0, 0)	(1, 0, 1, 0)	$10v_1v_2$	$W_K$	$/\text{MHz}$ -9.71(14)
(4, 0, 0, 0)	(1, 0, 1, 0)	$4000v_1v_2$	$G_b$	$/\text{MHz}$ 422.7(11)
(4, 0, 0, 0)	(1, 0, 1, 0)	$4010v_1v_2$	$G_{b,K}$	$/\text{MHz}$ -1.250(17)
(4, 0, 0, 0)	(1, 0, 1, 0)	$4200v_1v_2$	$G_{2b}$	$/\text{kHz}$ -4.419(76)
(4, 0, 0, 0)	(1, 0, 1, 0)	$4210v_1v_2$	$G_{2b,K}$	$/\text{Hz}$ 53.6(17)
(4, 0, 0, 0)	(1, 0, 1, 0)	$4100v_1v_2$	$F_{ac}$	$/\text{MHz}$ -6.91(12)
(5, 0, 0, 0)	(2, 0, 1, 0)	$\tilde{\nu}_{(5,0,0,0)} - \tilde{\nu}_{(2,0,1,0)}$	$/\text{cm}^{-1}$	12.9327(51)
(5, 0, 0, 0)	(2, 0, 1, 0)	$0v_1v_2$	$W$	$/\text{GHz}$ -198.923(80)
(5, 0, 0, 0)	(2, 0, 1, 0)	$400v_1v_2$	$W_2$	$/\text{kHz}$ 26.3(13)
(5, 0, 0, 0)	(2, 0, 1, 0)	$4000v_1v_2$	$G_b$	$/\text{MHz}$ 432.455(55)
(5, 0, 0, 0)	(2, 0, 1, 0)	$4101v_1v_2$	$F_{ac,J}$	$/\text{Hz}$ 314.0(30)

<sup>a</sup> The specified IDs are the respective parameter IDs used in the \*.par and \*.var files of SPFIT and SPCAT.<sup>29,32</sup>

no interaction partners were identified as of yet.

## 4.2 Fit Results

Except for the aforementioned vibrationally excited states, (0, 2, 0, 0), (1, 0, 0, 1), (0, 1, 1, 0), and (6, 0, 0, 0), all analyses reproduce the spectrum with about experimental uncertainty and only a single line was rejected from the fit due to  $|\nu_{\text{obs}} - \nu_{\text{calc}}|/\Delta\nu > 10$  (see Tab. 1). The resulting rotational parameters are given in Tab. 2 for vibrational states showing no signs of interactions and in Tab. 3 for the interacting vibrational states.

In their previous study, Creswell et al. presented fits for  $v_{21} = 0, 1, 2$  with full sets of quartic rotational constants. The relative deviations for the rotational constants are all below  $10^{-5}$  even though not within their uncertainties. The quartic parameters differ by a few percent except  $d_2$  which differs by up to 45%. For  $v_{21} = 3, 4, 5, 6$  Creswell et al. fitted

only rigid rotor Hamiltonians without accounting for any interactions. Thus, even the rotational constants differ greatly (up to  $150\sigma^7$ ). However, their study was much more limited in frequency coverage, only 8–40 GHz, and quantum number coverage, with only 31 transitions with  $J_{\text{max}} = 31$  for  $v_{21} = 0, 1, 2$  and 10 transitions with  $J_{\text{max}} = 6$  for  $v_{21} = 3, 4, 5, 6$ . Furthermore, no interactions were accounted for at all by Creswell et al.<sup>11</sup>

The values for the ground vibrational state also show good agreement with values obtained from quantum chemical calculations (see Tab. S2 of the Supporting Information). The three parameters  $H_J$ ,  $h_1$ , and  $d_2$  show the highest relative deviations at 27%, 26%, and 21%, respectively.

## 4.3 Singly substituted <sup>13</sup>C Species

The singly substituted <sup>13</sup>C species were more difficult to analyze because of their low natural abundance resulting in a smaller number of assignable lines. This is especially apparent for the <sup>13</sup>C<sub>2</sub> species, for which only about 100 lines could be assigned due to its  $A$  and  $B$  values being close to the main isotopologue values (see Tab. 1). As a result, many of its  $a$ -type transitions are close to or blended with much stronger transitions. The resulting parameters are shown in Tab. 4 with the notation from Creswell et al.<sup>11</sup> being used to label the carbon atoms.

The rotational constants agree nicely with the values obtained by Creswell et al.<sup>11</sup> as the relative deviations are below  $10^{-5}$  and all deviations are within  $1.5\sigma$ . Higher order parameters were included by Creswell et al.<sup>11</sup> only as fixed values of the main isotopologue’s ground vibrational state.

## 4.4 Estimation of the $c$ -type Dipole Moment

Creswell et al. determined the  $c$ -type dipole moment to be 0.277(156) D. To derive a more ac-

<sup>7</sup>The values for  $v_{21} = 6$  agree the best as in this work the interaction partner of  $v_{21} = 6$  was not found meaning two highly effective fits were compared.

curate value, in the present study, the  $c$ -type dipole moment was determined via comparison of experimental line intensities. A selection of 28  $c$ -type transitions was compared with  $b$ -type transitions close in frequency by fitting a 2nd derivative Voigt profile to the experimental lineshapes. The resulting  $c$ -type dipole moment, calculated as the mean value and the standard deviation of the 28 transition pairs, is 0.334(39) D. Additionally, the calculated equilibrium  $c$ -type dipole moment (ae-CCSD(T)-cc-pwCVTZ level, 0.276 D) was corrected for effects of zero-point vibrations (fc-CCSD(T)/cc-pVTZ, 0.023 D) resulting in a vibrationally averaged dipole moment of  $\mu_c = 0.253$  D, which is about  $2\sigma$  smaller than the experimental value.

The new experimental value agrees with the previously determined value within their uncertainties but has a significantly smaller uncertainty. Systematic errors occur as (among other things) the power of the probe source is frequency dependent, and the pressure, which influences the lineshape and thereby center intensities, rises over time. These effects were not taken into account but their impact was minimized by comparing transitions nearby in frequency (and thereby also in time). Additionally, lines might be blended with other lines so far not assigned and therefore their amplitudes might be influenced. The systematic uncertainty might thus be slightly higher than the reported statistical uncertainty.

## 5 Search for Glycidaldehyde toward Sgr B2(N)

### 5.1 Observations

We used the imaging spectral line survey Re-exploring Molecular Complexity with ALMA (ReMoCA) that targeted the high-mass star-forming protocluster Sgr B2(N) with the Atacama Large Millimeter/submillimeter Array (ALMA) to search for glycidaldehyde in the interstellar medium. Details about the data reduction and the method of analysis of this survey can be found elsewhere.<sup>35,36</sup> The main features of the survey are the fol-

lowing. It covers the frequency range from 84.1 GHz to 114.4 GHz at a spectral resolution of 488 kHz (1.7 to 1.3 km s<sup>-1</sup>). This frequency coverage was obtained with five different tunings of the receivers. The phase center was located halfway between the two hot molecular cores Sgr B2(N1) and Sgr B2(N2), at the equatorial position  $(\alpha, \delta)_{J2000} = (17^{\text{h}}47^{\text{m}}19^{\text{s}}.87, -28^{\circ}22'16''.0)$ . The observations achieved a sensitivity per spectral channel ranging between 0.35 mJy beam<sup>-1</sup> and 1.1 mJy beam<sup>-1</sup> (rms) depending on the tuning, with a median value of 0.8 mJy beam<sup>-1</sup>. The angular resolution (HPBW) varies between  $\sim 0.3''$  and  $\sim 0.8''$  with a median value of  $0.6''$  that corresponds to  $\sim 4900$  au at the distance of Sgr B2 (8.2 kpc).<sup>37</sup>

For this work we analyzed the spectra toward the position called Sgr B2(N2b) by Belloche et al.<sup>36</sup> It is located in the secondary hot core Sgr B2(N2) at  $(\alpha, \delta)_{J2000} = (17^{\text{h}}47^{\text{m}}19^{\text{s}}.83, -28^{\circ}22'13''.6)$ . This position was chosen as a compromise between getting narrow line widths to reduce the level of spectral confusion and keeping a high enough H<sub>2</sub> column density to detect less abundant molecules.

Like in our previous ReMoCA studies,<sup>35,36</sup> we compared the observed spectra to synthetic spectra computed under the assumption of local thermodynamic equilibrium (LTE) with the astronomical software Weeds.<sup>38</sup> This assumption is justified by the high densities of the regions where hot-core emission is detected in Sgr B2(N)  $> 1 \times 10^7$  cm<sup>-3</sup>, see Bonfand et al.<sup>39</sup>. The calculations take into account the finite angular resolution of the observations and the optical depth of the rotational transitions. We derived by eye a best-fit synthetic spectrum for each molecule separately, and then added together the contributions of all identified molecules. Each species was modeled with a set of five parameters: size of the emitting region ( $\theta_s$ ), column density ( $N$ ), temperature ( $T_{\text{rot}}$ ), linewidth ( $\Delta V$ ), and velocity offset ( $V_{\text{off}}$ ) with respect to the assumed systemic velocity of the source,  $V_{\text{sys}} = 74.2$  km s<sup>-1</sup>. The linewidth and velocity offset were obtained directly from the well-detected and not contaminated lines. The size of the emission of a given molecule

was estimated from integrated intensity maps of transitions of this molecule that were found to be relatively free of contamination from other species.

## 5.2 Search for glycidaldehyde toward Sgr B2(N2b)

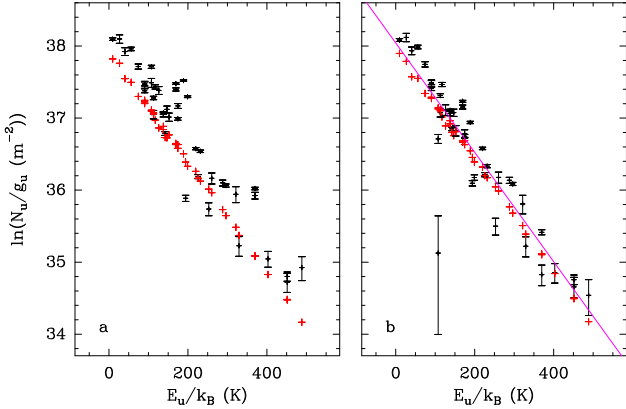


Figure 6: Population diagram of  $c\text{-C}_2\text{H}_4\text{O}$  toward Sgr B2(N2b). The observed data points are shown in black while the synthetic populations are shown in red. No correction is applied in panel **a**. In panel **b**, the optical depth correction has been applied to both the observed and synthetic populations and the contamination by all other species included in the full model has been subtracted from the observed data points. The purple line is a linear fit to the observed populations (in linear-logarithmic space). The fit yields a temperature of  $132 \pm 10$  K.

Before searching for glycidaldehyde toward Sgr B2(N2b), we modeled the rotational emission of the related cyclic molecule oxirane,  $c\text{-C}_2\text{H}_4\text{O}$ . We used the spectroscopic predictions available in the Cologne database for molecule spectroscopy (CDMS)<sup>40</sup> for the vibrational ground state (version 3 of entry 44504), which are mainly based on work by Müller et al.<sup>41</sup>. Oxirane is well detected toward Sgr B2(N2b), with two dozens of lines in its vibrational ground state easily identified (see Sec. 5 of the Supporting Information). Integrated intensity maps of lines of oxirane that are free of contamination suggest an emission size on the order of  $0.7''$ . Fig. 6 shows the population diagram of oxirane. A fit to this popula-

tion diagram yields a rotational temperature of  $132 \pm 10$  K. Assuming a temperature of 130 K, we adjusted a synthetic LTE spectrum to the observed spectrum and obtained the best-fit column density of oxirane reported in Tab. 6 that corresponds to the spectrum shown in red in Sec. 5 of the Supporting Information.

To search for glycidaldehyde toward Sgr B2(N2b) using the spectroscopic predictions obtained in Sec. 4, we computed a synthetic LTE spectrum assuming the same velocity offset, linewidth, emission size, and rotational temperature as those derived for oxirane (Tab. 6) and keeping the column density of glycidaldehyde as the only free parameter. We did not find any evidence for glycidaldehyde in this source. The synthetic spectrum used to estimate the upper limit to its column density is shown in red in Fig. 7. This upper limit is reported in Tab. 6. We conclude from this analysis that glycidaldehyde is at least 6 times less abundant than oxirane in Sgr B2(N2b).

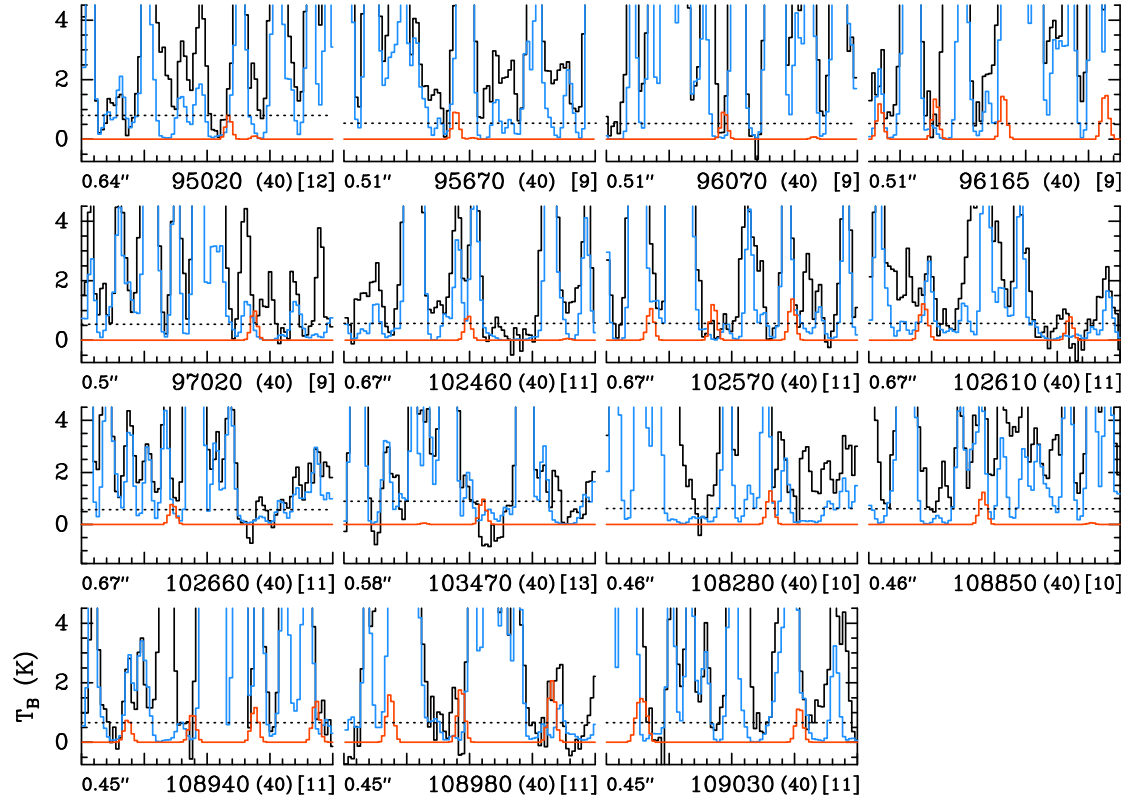


Figure 7: Selection of rotational transitions of glycidaldehyde,  $c-(\text{C}_2\text{H}_3\text{O})\text{CHO}$  covered by the ReMoCA survey. The LTE synthetic spectrum of  $c-(\text{C}_2\text{H}_3\text{O})\text{CHO}$  used to derive the upper limit on its column density toward Sgr B2(N2b) is displayed in red and overlaid on the observed spectrum shown in black. The blue synthetic spectrum contains the contributions of all molecules identified in our survey so far, but not the species shown in red. The values written below each panel correspond from left to right to the half-power beam width, the central frequency in MHz, the width in MHz of each panel in parentheses, and the continuum level in K of the baseline-subtracted spectra in brackets. The  $y$ -axis is labeled in brightness temperature units (K). The dotted line indicates the  $3\sigma$  noise level.

Table 6: Parameters of our best-fit LTE model of oxirane toward Sgr B2(N2b) and upper limit for glycidaldehyde.

Molecule	Status <sup>(a)</sup>	$N_{\text{det}}$ <sup>(b)</sup>	Size <sup>(c)</sup> ( $''$ )	$T_{\text{rot}}$ <sup>(d)</sup> (K)	$N$ <sup>(e)</sup> ( $\text{cm}^{-2}$ )	$F_{\text{vib}}$ <sup>(f)</sup>	$F_{\text{conf}}$ <sup>(g)</sup>	$\Delta V$ <sup>(h)</sup> ( $\text{km s}^{-1}$ )	$V_{\text{off}}$ <sup>(i)</sup> ( $\text{km s}^{-1}$ )	$\frac{N_{\text{ref}}}{N}$ <sup>(j)</sup>
$c\text{-C}_2\text{H}_4\text{O}, \nu = 0^*$	d	28	0.7	130	4.0 (16)	1.00	1.00	3.5	0.0	1
$c\text{-(C}_2\text{H}_3\text{O)CHO}, \nu = 0$	n	0	0.7	130	< 7.1 (15)	1.43	1.00	3.5	0.0	> 5.6

<sup>(a)</sup>d: detection, n: nondetection. <sup>(b)</sup>Number of detected lines conservative estimate, see Sect. 3 of<sup>42</sup>. One line of a given species may mean a group of transitions of that species that are blended together. <sup>(c)</sup>Source diameter ( $FWHM$ ). <sup>(d)</sup>Rotational temperature. <sup>(e)</sup>Total column density of the molecule.  $x$  ( $y$ ) means  $x \times 10^y$ . <sup>(f)</sup>Correction factor that was applied to the column density to account for the contribution of vibrationally excited states, in the cases where this contribution was not included in the partition function of the spectroscopic predictions. <sup>(g)</sup>Correction factor that was applied to the column density to account for the contribution of other conformers in the cases where this contribution could be estimated but was not included in the partition function of the spectroscopic predictions. <sup>(h)</sup>Linewidth ( $FWHM$ ). <sup>(i)</sup>Velocity offset with respect to the assumed systemic velocity of Sgr B2(N2b),  $V_{\text{sys}} = 74.2 \text{ km s}^{-1}$ . <sup>(j)</sup>Column density ratio, with  $N_{\text{ref}}$  the column density of the previous reference species marked with a  $\star$ .

## 6 Conclusions

In the present study, coverage of the experimental rotational spectrum of glycidaldehyde has been extended greatly by measuring 345 GHz of broadband spectra in frequency intervals reaching as high as 750 GHz. The ground vibrational state, 17 vibrationally excited states, and the three singly substituted  $^{13}\text{C}$  isotopologues were analyzed by combining the powers of LWPs and DM-DR measurements, which act as precise filters on the rather complicated spectrum. Additionally, DM-DR measurements facilitated measuring interstate transitions between vibrationally excited states, yielding their vibrational energy separation with rotational precision. In total, three interacting systems were examined and could be reproduced to about experimental accuracy. The presented data allow for radio astronomical searches over a wide range of frequencies and quantum numbers. Searches of glycidaldehyde’s ground vibrational state with ALMA toward Sgr B2(N2b) were not successful implying that glycidaldehyde is at least six times less abundant than oxirane in this source. For future laboratory studies and astronomical searches of vibrationally excited states toward warm regions, the explicit interaction description in combined fits will be essential.<sup>43</sup> In the present study, foregoing the explicit interaction treatment and using only single-state fits would have resulted in about 20% of the approximately 16 000 total lines being rejected (due to  $|\nu_{\text{obs}} - \nu_{\text{calc}}|/\Delta\nu > 10$ ) and considerably worse  $RMS$  and  $WRMS$  values.

Future studies might be targeted at filling the remaining frequency gaps and the analysis of so-far untreated interactions. Future steps for the DM-DR method include implementing a demodulation scheme with the sum (or difference) of the  $1f$ - and  $2f$ -demodulation frequencies or in the ideal case with a custom function being the product of a sine function with the  $2f$ -demodulation frequency and a  $\pm 1$  rectangle function for the subtraction.

Now that the rotational spectrum of glycidaldehyde is known very well, it might be worthwhile to check for the status of other substituted oxiranes,  $c\text{-C}_2\text{H}_3\text{O-X}$ . A current census of the spectroscopic knowledge of six selected species has been given recently.<sup>44</sup> While rotational spectroscopic data have been collected for four of those ( $X = \text{CH}_3, \text{C}_2\text{H}, \text{CN},$  and  $\text{CHO}$ ), at least two simple representatives ( $X = \text{OH}, \text{NH}_2$ ) still await their microwave spectroscopic characterization.

## Data availability

The input and output files of SPFIT will be provided as supplementary material. These files as well as auxiliary files will be deposited in the data section of the CDMS. Calculations of rotational spectra of the main isotopic species will be available in the catalog section of the CDMS.

## Supporting Information Available

The calculated structures, rotation-vibration interaction constants, vibrational energies, and intensities. Residuals histograms for assignments from this work and Creswell et al.<sup>11</sup> The transition shift due to interactions for one exemplary interaction system. Parameter progression plot for the  $v_{21} = n$  states. Additional figure of the ReMoCA survey illustrating the detection of oxirane.

**Acknowledgement** Glycidaldehyde studied in this work is an aldehyde derivative of glyceraldehyde, a sugar molecule, which according to the laboratory work of Prof. Dr. Harold Linartz is tentatively formed through recombination of reactive carbon bearing radicals along the well known CO to CH<sub>3</sub>OH hydrogenation route. Therefore, this work is dedicated to the memory of our colleague and friend Harold Linartz.

LB, ST, HSPM, and SS gratefully acknowledge the Collaborative Research Center 1601 (SFB 1601 sub-project A4) funded by the Deutsche Forschungsgemeinschaft (DFG, German Research Foundation) – 500700252. JCG thanks the national program CNRS PCMI (Physics and Chemistry of the Interstellar Medium) and the CNES for a grant (CMISTEP). This paper makes use of the following ALMA data: ADS/JAO.ALMA#2016.1.00074.S. ALMA is a partnership of ESO (representing its member states), NSF (USA), and NINS (Japan), together with NRC (Canada), NSC and ASIAA (Taiwan), and KASI (Republic of Korea), in cooperation with the Republic of Chile. The Joint ALMA Observatory is operated by ESO, AUI/NRAO, and NAOJ. The interferometric data are available in the ALMA archive at <https://almascience.eso.org/aq/>.

## References

(1) Thaddeus, P.; Cummins, S. E.; Linke, R. A. Identification of the SiCC radical toward IC +10216 - The first

molecular ring in an astronomical source. *Astrophys. J.* **1984**, *283*, L45.

- (2) Changala, P. B.; Gupta, H.; Cernicharo, J.; Pardo, J. R.; Agúndez, M.; Cabezas, C.; Tercero, B.; Guélin, M.; McCarthy, M. C. Laboratory and Astronomical Discovery of Magnesium Dicarbide, MgC<sub>2</sub>. *Astrophys. J. Lett.* **2022**, *940*, L42.
- (3) Gupta, H.; Changala, P. B.; Cernicharo, J.; Pardo, J. R.; Agúndez, M.; Cabezas, C.; Tercero, B.; Guélin, M.; McCarthy, M. C. Calcium Chemistry in Carbon-rich Circumstellar Environments: The Laboratory and Astronomical Discovery of Calcium Dicarbide, CaC<sub>2</sub>. *Astrophys. J. Lett.* **2024**, *966*, L28.
- (4) Massalkhi, S.; Jiménez-Serra, I.; Martín-Pintado, J.; Rivilla, V. M.; Colzi, L.; Zeng, S.; Martín, S.; Tercero, B.; de Vicente, P.; Requena-Torres, M. A. The first detection of SiC<sub>2</sub> in the interstellar medium. *Astron. Astrophys.* **2023**, *678*, A45.
- (5) Dickens, J. E.; Irvine, W. M.; Ohishi, M.; Ikeda, M.; Ishikawa, S.; Nummelin, A.; Hjalmarsen, A. Detection of Interstellar Ethylene Oxide (c-C<sub>2</sub>H<sub>4</sub>O). *Astrophys. J.* **1997**, *489*, 753–757.
- (6) McGuire, B. A.; Carroll, P. B.; Loomis, R. A.; Finneran, I. A.; Jewell, P. R.; Remijan, A. J.; Blake, G. A. Discovery of the interstellar chiral molecule propylene oxide (CH<sub>3</sub>CHCH<sub>2</sub>O). *Science* **2016**, *352*, 1449–1452.
- (7) Nummelin, A.; Dickens, J. E.; Bergman, P.; Hjalmarsen, A.; Irvine, W. M.; Ikeda, M.; Ohishi, M. Abundances of ethylene oxide and acetaldehyde in hot molecular cloud cores. *Astron. Astrophys.* **1998**, *337*, 275–286.
- (8) Requena-Torres, M. A.; Martín-Pintado, J.; Martín, S.; Morris, M. R. The Galactic Center: The Largest Oxygen-bearing Organic Molecule Repository. *Astrophys. J.* **2008**, *672*, 352–360.

- (9) Lykke, J. M. et al. The ALMA-PILS survey: First detections of ethylene oxide, acetone and propanal toward the low-mass protostar IRAS 16293-2422. *Astron. Astrophys.* **2016**, *597*, A53.
- (10) Bacmann, A.; Faure, A.; Berteaud, J. Cold and Yet Complex: Detection of Ethylene Oxide in a Prestellar Core. *ACS Earth Space Chem.* **2019**, *3*, 1000–1013.
- (11) Creswell, R. A.; Manor, P. J.; Assink, R. A.; Schwendeman, R. H. Microwave spectrum, torsional excitation energy, partial structure, and dipole moment of oxiranecarboxaldehyde. *J. Mol. Spectrosc.* **1977**, *64*, 365–375.
- (12) Zingsheim, O.; Bonah, L.; Lewen, F.; Thorwirth, S.; Müller, H. S. P.; Schlemmer, S. Millimeter-millimeter-wave double-modulation double-resonance spectroscopy. *J. Mol. Spectrosc.* **2021**, *381*, 111519.
- (13) Payne, G. B. A new epoxy aldehyde: Synthesis of glycidaldehyde from acrolein and hydrogen peroxide. *J. Am. Chem. Soc.* **1958**, *80*, 6461–6461.
- (14) Autler, S. H.; Townes, C. H. Stark Effect in Rapidly Varying Fields. *Phys. Rev.* **1955**, *100*, 703–722.
- (15) Cohen-Tannoudji, C.; Dupont-Roc, J.; Grynberg, G. *Atom—Photon Interactions*; John Wiley & Sons, Ltd, 2008; Chapter 6, pp 407–514.
- (16) Raghavachari, K.; Trucks, G. W.; Pople, J. A.; Head-Gordon, M. A 5th-order perturbation comparison of electron correlation theories. *Chem. Phys. Lett.* **1989**, *157*, 479–483.
- (17) Dunning, T. H. Gaussian basis sets for use in correlated molecular calculations .1. The atoms boron through neon and hydrogen. *J. Chem. Phys.* **1989**, *90*, 1007–1023.
- (18) Peterson, K. A.; Dunning, T. H. Accurate correlation consistent basis sets for molecular core-valence correlation effects: The second row atoms Al–Ar and the first row atoms B–Ne revisited. *J. Chem. Phys.* **2002**, *117*, 10548–10560.
- (19) Almlöf, J.; Taylor, P. R. General contraction of Gaussian basis sets .1. Atomic natural orbitals for 1st-row and 2nd-row atoms. *J. Chem. Phys.* **1987**, *86*, 4070–4077.
- (20) Watts, J. D.; Gauss, J.; Bartlett, R. J. Open-shell analytical energy gradients for triple excitation many-body, coupled-cluster methods - MBPT(4), CCSD+T(CCSD), CCSD(T), and QCISD(T). *Chem. Phys. Lett.* **1992**, *200*, 1–7.
- (21) Gauss, J.; Stanton, J. F. Analytic CCSD(T) second derivatives. *Chem. Phys. Lett.* **1997**, *276*, 70–77.
- (22) Stanton, J. F.; Gauss, J. Analytic second derivatives in high-order many-body perturbation and coupled-cluster theories: computational considerations and applications. *Int. Rev. Phys. Chem.* **2000**, *19*, 61–95.
- (23) Mills, I. M. In *Molecular Spectroscopy: Modern Research*; Rao, K. N., Mathews, C. W., Eds.; Academic Press: New York, 1972; pp 115–140.
- (24) Stanton, J. F.; Lopreore, C. L.; Gauss, J. The equilibrium structure and fundamental vibrational frequencies of dioxirane. *J. Chem. Phys.* **1998**, *108*, 7190–7196.
- (25) Stanton, J. F.; Gauss, J.; Cheng, L.; Harding, M. E.; Matthews, D. A.; Szalay, P. G. CFOUR, Coupled-Cluster techniques for Computational Chemistry, a quantum-chemical program package. With contributions from A. A. Auer, R. J. Bartlett, U. Benedikt, C. Berger, D. E. Bernholdt, Y. J. Bomble, O. Christiansen, F. Engel, R. Faber, M. Heckert, O. Heun, M. Hilgenberg, C. Huber, T.-C. Jagau, D. Jonsson, J. Jusélius, T. Kirsch, K.

- Klein, W. J. Lauderdale, F. Lipparini, T. Metzroth, L. A. Mück, D. P. O’Neill, D. R. Price, E. Prochnow, C. Puzzarini, K. Ruud, F. Schiffmann, W. Schwalbach, C. Simmons, S. Stopkowicz, A. Tajti, J. Vázquez, F. Wang, J. D. Watts and the integral packages MOLECULE (J. Almlöf and P. R. Taylor), PROPS (P. R. Taylor), ABACUS (T. Helgaker, H. J. Aa. Jensen, P. Jørgensen, and J. Olsen), and ECP routines by A. V. Mitin and C. van Wüllen. For the current version, see <http://www.cfour.de>.
- (26) Matthews, D. A.; Cheng, L.; Harding, M. E.; Lipparini, F.; Stopkowicz, S.; Jagau, T.-C.; Szalay, P. G.; Gauss, J.; Stanton, J. F. Coupled-cluster techniques for computational chemistry: The CFOUR program package. *J. Chem. Phys.* **2020**, *152*, 214108.
- (27) Harding, M. E.; Metzroth, T.; Gauss, J.; Auer, A. A. Parallel calculation of CCSD and CCSD(T) analytic first and second derivatives. *J. Chem. Theory Comput.* **2008**, *4*, 64–74.
- (28) Bonah, L.; Zingsheim, O.; Müller, H. S. P.; Guillemin, J.-C.; Lewen, F.; Schlemmer, S. LLWP—A new Loomis-Wood software at the example of Acetone- $^{13}\text{C}_1$ . *J. Mol. Spectrosc.* **2022**, *388*, 111674.
- (29) Pickett, H. M. The fitting and prediction of vibration-rotation spectra with spin interactions. *J. Mol. Spectrosc.* **1991**, *148*, 371–377.
- (30) Winnewisser, G. Millimeter Wave Rotational Spectrum of HSSH and DSSD. II. Anomalous K Doubling Caused by Centrifugal Distortion in DSSD. *J. Chem. Phys.* **1972**, *56*, 2944–2954.
- (31) Bonah, L.; Schlemmer, S.; Guillemin, J.-C.; Harding, M. E.; Thorwirth, S. On the spectroscopy of phosphalkynes: Millimeter- and submillimeter wave study of  $\text{C}_2\text{H}_5\text{CP}$ . *J. Phys. Chem. A* **2024**, *128*, 4859–4866.
- (32) Drouin, B. J. Practical uses of SPFIT. *J. Mol. Spectrosc.* **2017**, *340*, 1–15.
- (33) Bonah, L.; Helmstaedter, B.; Guillemin, J.-C.; Schlemmer, S.; Thorwirth, S. Extending the rotational spectrum of cyclopentadiene towards higher frequencies and vibrational states. *J. Mol. Spectrosc.* **2024**, 111967.
- (34) Islami, K.; Winnewisser, B. P.; Preusser, J.; Winnewisser, M.  $\text{H}^{13}\text{C}^{14}\text{NO}$ : Independent Parameters Describing the Coriolis Resonance Systems (00002)/(00010) and (00012)/(00020). *J. Mol. Spectrosc.* **1996**, *176*, 403–415.
- (35) Belloche, A.; Garrod, R. T.; Müller, H. S. P.; Menten, K. M.; Medvedev, I.; Thomas, J.; Kisiel, Z. Re-exploring Molecular Complexity with ALMA (ReMoCA): interstellar detection of urea. *Astron. Astrophys.* **2019**, *628*, A10.
- (36) Belloche, A.; Garrod, R. T.; Zingsheim, O.; Müller, H. S. P.; Menten, K. M. Interstellar detection and chemical modeling of iso-propanol and its normal isomer. *Astron. Astrophys.* **2022**, *662*, A110.
- (37) Reid, M. J. et al. Trigonometric Parallaxes of High-mass Star-forming Regions: Our View of the Milky Way. *Astrophys. J.* **2019**, *885*, 131.
- (38) Maret, S.; Hily-Blant, P.; Pety, J.; Bardeau, S.; Reynier, E. Weeds: a CLASS extension for the analysis of millimeter and sub-millimeter spectral surveys. *Astron. Astrophys.* **2011**, *526*, A47.
- (39) Bonfand, M.; Belloche, A.; Garrod, R. T.; Menten, K. M.; Willis, E.; Stéphane, G.; Müller, H. S. P. The complex chemistry of hot cores in Sgr B2(N): influence of cosmic-ray ionization and thermal history. *Astron. Astrophys.* **2019**, *628*, A27.
- (40) Müller, H. S. P.; Schlöder, F.; Stutzki, J.; Winnewisser, G. The Cologne Database for Molecular Spectroscopy, CDMS: a

useful tool for astronomers and spectroscopists. *Journal of Molecular Structure* **2005**, *742*, 215–227.

- (41) Müller, H. S. P.; Guillemin, J.-C.; Lewen, F.; Schlemmer, S. Rotational spectroscopy of isotopic oxirane,  $c\text{-C}_2\text{H}_4\text{O}$ . *J. Mol. Spectrosc.* **2022**, *384*, 111584.
- (42) Belloche, A.; Müller, H. S. P.; Garrod, R. T.; Menten, K. M. Exploring molecular complexity with ALMA (EMoCA): Deuterated complex organic molecules in Sagittarius B2(N2). *Astron. Astrophys.* **2016**, *587*, A91.
- (43) Endres, C. P.; Martin-Drumel, M.-A.; Zingsheim, O.; Bonah, L.; Pirali, O.; Zhang, T.; Sánchez-Monge, A.; Möller, T.; Wehres, N.; Schilke, P.; McCarthy, M. C.; Schlemmer, S.; Caselli, P.; Thorwirth, S. SOLEIL and ALMA views on prototypical organic nitriles:  $\text{C}_2\text{H}_5\text{CN}$ . *J. Mol. Spectrosc.* **2021**, *375*, 111392.
- (44) Ellinger, Y.; Pauzat, F.; Markovits, A.; Allaire, A.; Guillemin, J.-C. The quest of chirality in the interstellar medium: I. Lessons of propylene oxide detection. *Astron. Astrophys.* **2020**, *633*, A49.

## 10. Conclusions and Outlook

In the course of this thesis, the rotational spectra of the four astrophysically relevant COMs acetone- $^{13}\text{C}_1$ , ethyl phosphoethyne, cyclopentadiene, and glycidaldehyde were analyzed. For each molecule, high-resolution broadband spectra were recorded with three different absorption spectrometers in Cologne ranging from 37 GHz to 1102 GHz, resulting in a total of 2.2 THz of high-resolution spectra<sup>a</sup>. For ethyl phosphoethyne, this marked its first spectroscopic characterization in the gas phase while for the other molecules previous laboratory work was greatly extended.<sup>42,144–150</sup> All molecules are asymmetric tops and span almost the entire range of Ray’s asymmetry parameter.<sup>58</sup> Ethyl phosphoethyne ( $\kappa = -0.98$ ) and glycidaldehyde ( $\kappa = -0.98$ ) are nearly prolate symmetric tops, acetone- $^{13}\text{C}_1$  ( $\kappa = 0.32$ ) is quite asymmetric, and cyclopentadiene ( $\kappa = 0.90$ ) is rather close to the oblate limit of +1.

For the analysis, the spectroscopic toolbox was updated in certain areas and new tools were introduced in other areas. A newly developed measurement software was used together with various post-processing steps that allow to optimize the phase of the measurement in retrospect, to remove standing waves from the broadband scans, to intensity calibrate the spectrum with an initial model of the molecule, and to remove known lines from the spectrum. Combining this with Loomis-Wood plots in the LLWP software facilitated spectral identification, especially of weak series, which was particularly important for the analysis of isotopologues in natural abundance and vibrationally excited states high in energy. SPFIT/SPCAT<sup>59</sup> or ERHAM<sup>88,89</sup> were used to fit and predict the spectra. Wrapper programs were developed for both codes to seamlessly test the influence of adding parameters to or omitting parameters from the Hamiltonians. Together with the ability to easily check residual plots in the GUI of LLWP, this accelerated the process of building quantum mechanical models to experimental accuracy, especially for vibrational states showing signs of interactions. For the most challenging vibrational states of glycidaldehyde, DR spectroscopy was used to identify transitions sharing an energy level. This proved invaluable for following weak and perturbed series, and for unambiguously reconstructing small subnetworks of the energy term diagram.

The combination of this toolbox with the high sensitivity of the experimental setups

---

<sup>a</sup>For acetone- $^{13}\text{C}_1$  1024 GHz were covered, 550 GHz for ethyl phosphoethyne, 350 GHz for cyclopentadiene, and 345 GHz for glycidaldehyde.

facilitated the identification of singly  $^{13}\text{C}$  substituted isotopologues in natural abundance (1.1 %) and vibrationally excited states up to about  $850\text{ cm}^{-1}$  in energy, corresponding to a Boltzmann factor of only 1.5 %. Except for acetone, the singly  $^{13}\text{C}$  substituted isotopologues of all species were analyzed, while 8 and 17 vibrationally excited states were assigned for cyclopentadiene and glycidaldehyde, respectively. Five interaction systems, due to Coriolis and/or Fermi interactions between the vibrational states, were identified and described in combined fits. The isotopologue data, besides their relevance as tracers of the astronomical  $^{12}\text{C}/^{13}\text{C}$  ratio, are also useful for the determination of (partial) semi-experimental equilibrium structures. Empirical structures have been derived here for ethyl phosphoethyne and cyclopentadiene. The data on the vibrationally excited states can serve as astronomical thermometers. In addition, a large number of so-far unknown lines (u-lines) in astronomical surveys are thought to originate either from rare isotopologues or vibrationally excited states.<sup>15</sup>

The tools presented for the analysis process made the analysis both efficient and reliable, as is evident from the high numbers of spectroscopic assignments and the good agreement between experimental data and the quantum mechanical models. The resulting frequency predictions allow for radio astronomical searches over a wide range of frequencies and quantum numbers.

## Outlook

Obvious future steps are to fill gaps in the frequency coverage of the rotational analyses and to extend the analyses to more isotopologues or vibrationally excited states higher in energy. The analyses of additional isotopologues would most likely require enriched samples to counteract their low natural abundances, but would improve the determined structure for cyclopentadiene and allow to determine an unconstrained structure for ethyl phosphoethyne. Similarly, the analysis of vibrational states high in energy could benefit from measuring the spectra at higher temperatures to increase their population and thus the intensity of their vibrational satellite spectra. The identification of further vibrational states could allow to analyze the interactions of vibrational states for which the interaction partner has not yet been found. The interaction analysis could also benefit from a detour via the rovibrational spectrum with ASAP.

The DR method opens up many interesting possibilities for the future. Starting with a technical note, an additional modulation/demodulation scheme could be tested, which uses an FM for the probe source, an amplitude modulation (AM) for the pump source, and for the demodulation the product of a  $2f$ -sine function and a  $\pm 1$  rectangle function for the subtraction. This would yield the same efficiency as with the current setup but the FM amplitude would not depend on the transition dipole moment, which would be an advantage for unbiased searches. Second, extending the frequency range of the pump

source would increase the size of the subnetworks that can be fully reconstructed without requiring QM models. The optimal case, i.e. both probe and pump source cover the complete spectral range, would reveal the entire energy diagram in a single 2D scan. To speed up such 2D scans, DR measurements could be combined with chirped-pulse spectroscopy. Recording two free-induction decays shifted in phase by  $180^\circ$ , one with and one without the pump radiation, would immediately realize the subtraction as in the DM-DR case. Another possibility is to extend DR measurements to rovibrational measurements. If a laser is used to pump rovibrational transitions, even vibrational states high in energy might be accessible and their satellite spectra could be unambiguously distinguished from other vibrational state spectra.

Finally, also the tools for the analysis could be further improved. In ethyl phosphoethyne, internal rotation and interactions between vibrational states have to be treated simultaneously, requiring the development of new codes to fit and predict the spectra. The most time-consuming part of the analysis, the interaction analysis, could be accelerated by using DR techniques over wider frequency ranges or by updating QCC codes to routinely provide results for Coriolis parameters between combination modes and overtones. Furthermore, neural networks could be trained in pattern recognition of spectra (with and without interactions) to automatically identify them in the spectra.<sup>151</sup>

## Closing Words

This thesis presents the rotational analyses of four COMs of astrophysical interest. A wide variety of tools have been used, including QCC, LWPs, and DR techniques. The four analyses each highlight a different tool, making this thesis both a report of the analyses and a guide to the methods and tool usage. Similar to a real toolbox, each tool has its strengths and limitations. Hopefully, this thesis will help future spectroscopists to find the right tool for their specific spectroscopic problem and to keep up with the ever-increasing pace of astronomical studies.

# A. Appendix

## A.1 Higher-Order Centrifugal Distortion Constants

The centrifugal distortion constants up to tenth order are given in Watson's  $A$ -reduction<sup>54,55</sup> and in the  $S$ -reduction.<sup>56,57</sup> For the  $A$ -reduction, the centrifugal distortion constants are defined as

$$\begin{aligned}
\mathbf{H}_{\text{cd}}^{(4)} &= -\Delta_J \mathbf{J}^4 - \Delta_{JK} \mathbf{J}^2 \mathbf{J}_z^2 - \Delta_K \mathbf{J}_z^4 \\
&\quad - \frac{1}{2} \left\{ \delta_J \mathbf{J}^2 + \delta_K \mathbf{J}_z^2, \mathbf{J}_{\pm}^2 \right\} \\
\mathbf{H}_{\text{cd}}^{(6)} &= +\Phi_J \mathbf{J}^6 + \Phi_{JK} \mathbf{J}^4 \mathbf{J}_z^2 + \Phi_{KJ} \mathbf{J}^2 \mathbf{J}_z^4 + \Phi_K \mathbf{J}_z^6 \\
&\quad + \frac{1}{2} \left\{ \phi_J \mathbf{J}^4 + \phi_{JK} \mathbf{J}^2 \mathbf{J}_z^2 + \phi_K \mathbf{J}_z^4, \mathbf{J}_{\pm}^2 \right\} \\
\mathbf{H}_{\text{cd}}^{(8)} &= +L_J \mathbf{J}^8 + L_{JJK} \mathbf{J}^6 \mathbf{J}_z^2 + L_{JK} \mathbf{J}^4 \mathbf{J}_z^4 + L_{KKJ} \mathbf{J}^2 \mathbf{J}_z^6 + L_K \mathbf{J}_z^8 \\
&\quad + \frac{1}{2} \left\{ l_J \mathbf{J}^6 + l_{JK} \mathbf{J}^4 \mathbf{J}_z^2 + l_{KJ} \mathbf{J}^2 \mathbf{J}_z^4 + l_K \mathbf{J}_z^6, \mathbf{J}_{\pm}^2 \right\} \\
\mathbf{H}_{\text{cd}}^{(10)} &= +P_J \mathbf{J}^{10} + P_{JJK} \mathbf{J}^8 \mathbf{J}_z^2 + P_{JK} \mathbf{J}^6 \mathbf{J}_z^4 + P_{KJ} \mathbf{J}^4 \mathbf{J}_z^6 + P_{KKJ} \mathbf{J}^2 \mathbf{J}_z^8 + P_K \mathbf{J}_z^{10} \\
&\quad + \frac{1}{2} \left\{ p_J \mathbf{J}^8 + p_{JJK} \mathbf{J}^6 \mathbf{J}_z^2 + p_{JK} \mathbf{J}^4 \mathbf{J}_z^4 + p_{KKJ} \mathbf{J}^2 \mathbf{J}_z^6 + p_K \mathbf{J}_z^8, \mathbf{J}_{\pm}^2 \right\}
\end{aligned} \tag{A.1}$$

where  $\{a, b\} = ab + ba$  is the anticommutator and  $\mathbf{J}_{\pm}^n = \mathbf{J}_+^n + \mathbf{J}_-^n$ .

For the  $S$ -reduction, the centrifugal distortion constants are defined as

$$\begin{aligned}
\mathbf{H}_{\text{cd}}^{(4)} &= -D_J \mathbf{J}^4 - D_{JK} \mathbf{J}^2 \mathbf{J}_z^2 - D_K \mathbf{J}_z^4 \\
&\quad + d_1 \mathbf{J}^2 \mathbf{J}_{\pm}^2 + d_2 \mathbf{J}_{\pm}^4 \\
\mathbf{H}_{\text{cd}}^{(6)} &= H_J \mathbf{J}^6 + H_{JK} \mathbf{J}^4 \mathbf{J}_z^2 + H_{KJ} \mathbf{J}^2 \mathbf{J}_z^4 + H_K \mathbf{J}_z^6 \\
&\quad + d_1 \mathbf{J}^4 \mathbf{J}_{\pm}^2 + d_2 \mathbf{J}^2 \mathbf{J}_{\pm}^4 + d_3 \mathbf{J}_{\pm}^6 \\
\mathbf{H}_{\text{cd}}^{(8)} &= L_J \mathbf{J}^8 + L_{JJK} \mathbf{J}^6 \mathbf{J}_z^2 + L_{JK} \mathbf{J}^4 \mathbf{J}_z^4 + L_{KKJ} \mathbf{J}^2 \mathbf{J}_z^6 + L_K \mathbf{J}_z^8 \\
&\quad + l_1 \mathbf{J}^6 \mathbf{J}_{\pm}^2 + l_2 \mathbf{J}^4 \mathbf{J}_{\pm}^4 + l_3 \mathbf{J}^2 \mathbf{J}_{\pm}^6 + l_4 \mathbf{J}_{\pm}^8 \\
\mathbf{H}_{\text{cd}}^{(10)} &= P_J \mathbf{J}^{10} + P_{JJK} \mathbf{J}^8 \mathbf{J}_z^2 + P_{JK} \mathbf{J}^6 \mathbf{J}_z^4 + P_{KJ} \mathbf{J}^4 \mathbf{J}_z^6 + P_{KKJ} \mathbf{J}^2 \mathbf{J}_z^8 + P_K \mathbf{J}_z^{10} \\
&\quad + p_1 \mathbf{J}^8 \mathbf{J}_{\pm}^2 + p_2 \mathbf{J}^6 \mathbf{J}_{\pm}^4 + p_3 \mathbf{J}^4 \mathbf{J}_{\pm}^6 + p_4 \mathbf{J}^2 \mathbf{J}_{\pm}^8 + p_5 \mathbf{J}_{\pm}^{10}
\end{aligned} \tag{A.2}$$

## A.2 Reduced Energy Diagrams

The reduced energy diagrams are shown for glycidaldehyde (Fig. A.1) and cyclopentadiene (Fig. A.2).

For glycidaldehyde, a near prolate asymmetric top, the reduced energy is given by

$$E_{\text{red}} = E - \frac{B + C}{2} J(J + 1) \quad (\text{A.3})$$

while for cyclopentadiene, a near oblate asymmetric top, the reduced energy is given by

$$E_{\text{red}} = E - \frac{A + B}{2} J(J + 1) \quad (\text{A.4})$$

For energy levels with the same  $J$  value, the same energy offset is subtracted. As a result, series of energy levels (levels with the same values of  $K_a$  or  $K_c$ , and  $J - K_a - K_c$ ) are close to straight lines which makes comparing their qualitative behavior much easier.

For glycidaldehyde, similar to a prolate symmetric top, the energy levels increase for the same  $J$  value with  $K_a$ . However, while the levels with same  $J$  and  $K_a$  value are paired for low  $J$  values, they diverge with increasing  $J$ , and for high  $J$  values levels with same  $J$  and  $K_c$  value are paired in energy. Due to the origin of the quasi-good quantum numbers  $K_a$  and  $K_c$ , the case where levels with same  $K_a$  values are paired is called prolate pairing and the case where levels with same  $K_c$  values are paired is called oblate pairing.

For cyclopentadiene, similar to an oblate symmetric top, the energy levels decrease for the same  $J$  value with  $K_c$ . For low values of  $J$ , the energy levels are oblate paired whereas for high  $J$  values they are prolate paired.

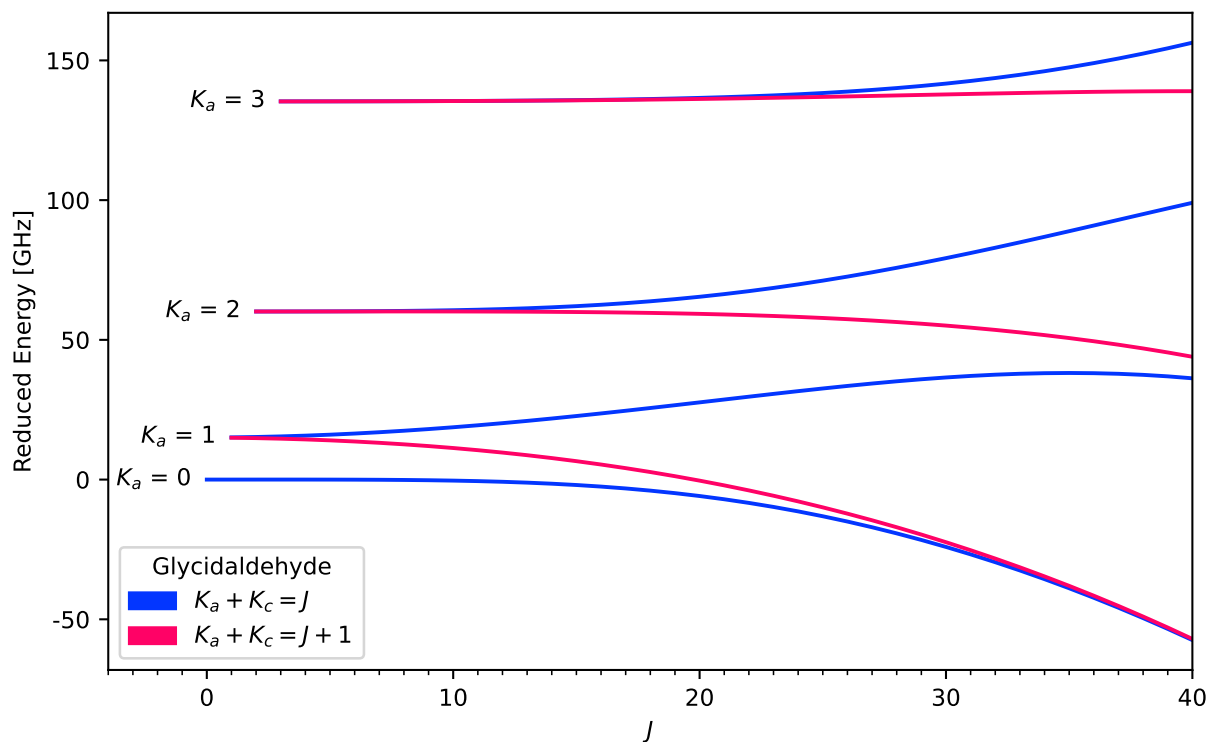


**Figure A.1:** Reduced energy diagram for glycidaldehyde. For low  $J$  values, energy levels with same  $J$  and  $K_a$  values are paired, while for high  $J$  values, levels with the same  $K_c$  value are paired.

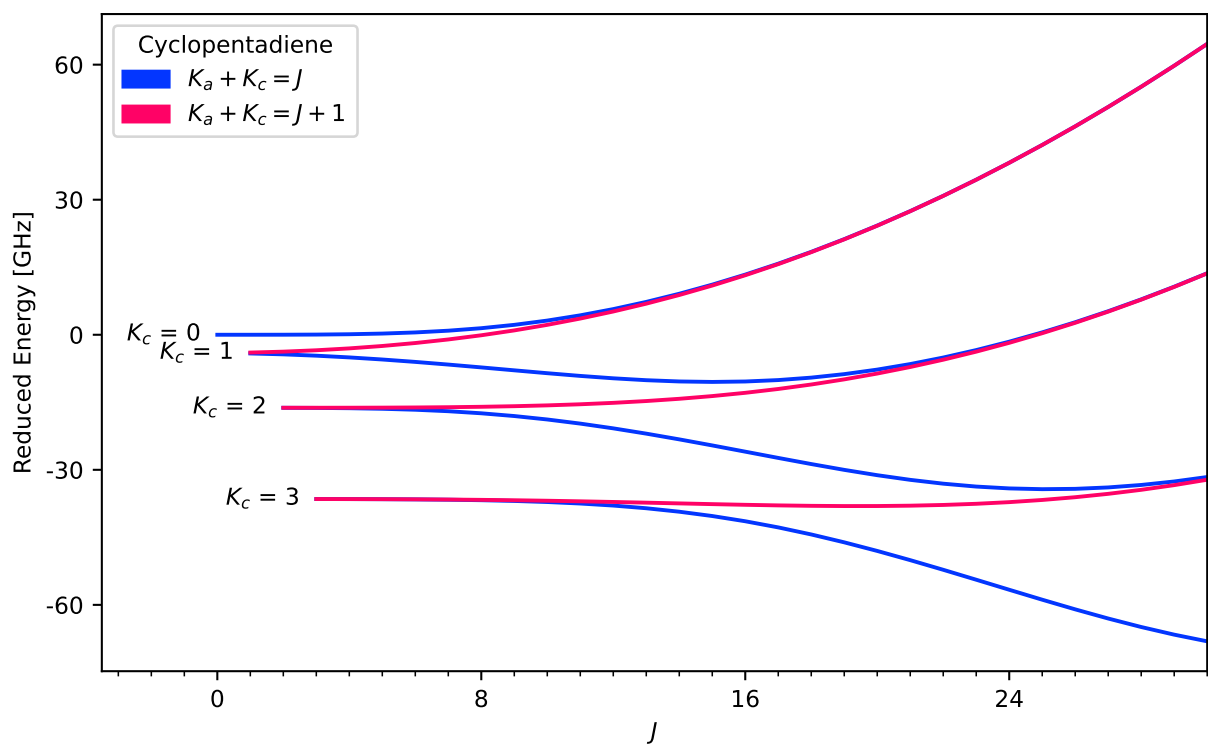


**Figure A.2:** Reduced energy diagram for cyclopentadiene. For low  $J$  values, energy levels with same  $J$  and  $K_c$  values are paired, while for high  $J$  values, levels with the same  $K_a$  value are paired.

### A.3 (Sub-)Millimeter Spectrometer

A schematic view of the experimental setup of the (Sub-)Millimeter spectrometer. By employing a double-pass setup, the absorption path of the 5 m absorption cell is doubled to 10 m. The ingoing vertically polarized radiation is reflected at the other end of the absorption cell by a rooftop mirror that simultaneously turns its polarization by 90°. The outgoing horizontally polarized radiation is outcoupled by a polarization filter into the detector.

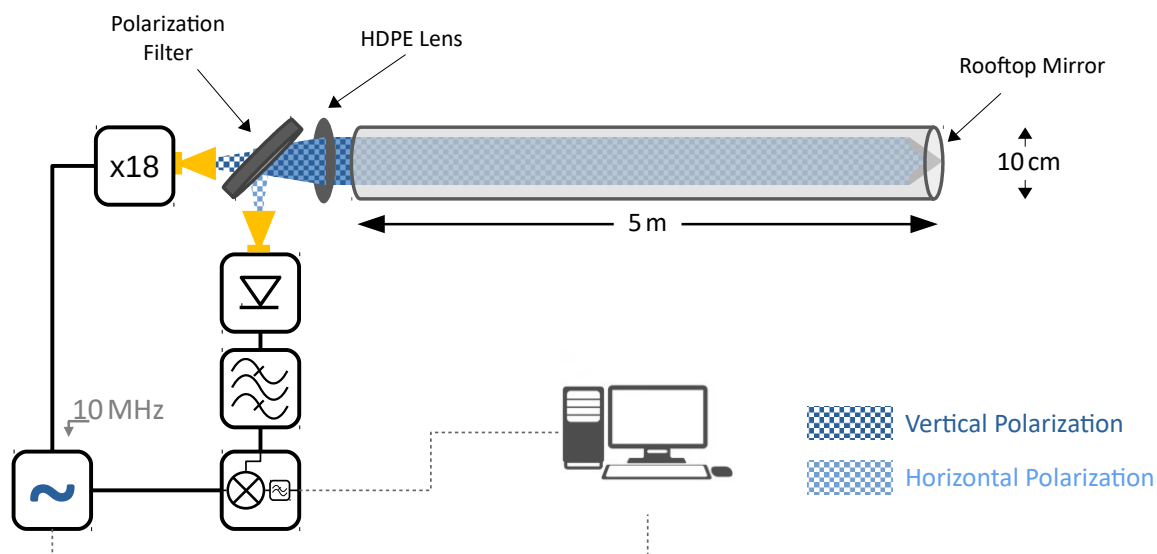


**Figure A.3:** Experimental setup of the (Sub-)Millimeter spectrometer. The setup is similar to the THz spectrometer, but a rooftop mirror and a polarization filter are used to double the absorption path (so-called double-pass setup).

## A.4 Examples of Residual Plots

Residual plots are an important quality criterion for each analysis. Here, the residuals for the analysis of the ground state of glycidaldehyde are used as an example to show what residuals of a good analysis look like (Fig. A.4), what residuals look like if a parameter is missing, or if there are other deficiencies of the model (Fig. A.5), and how misassignments are visible in the residuals (Fig. A.6). As these are just examples, the residual plots are limited to transitions between 75 GHz and 170 GHz. Points are plotted with a transparency of 80 % except for assignments with  $\frac{|\nu_{\text{obs}} - \nu_{\text{calc}}|}{\Delta\nu} > 5$  which are highlighted in solid red.

The residual plot of the actual analysis (see Sec. 9) is shown in Fig. A.4. The distribution in  $y$ -direction is fairly random and the overall spread is quite low as no assignment deviates by more than 80 kHz from its predicted position. Also, no trends are visible, making this an example of a very good residual distribution.

In contrast, for the residual plot in Fig. A.5 the parameters  $L_{JK}$  and  $P_{JK}$  were removed from the model. The shown residuals are the best-fit residuals for the modified model. Strong trends are visible in the residuals, resulting from transitions high in  $J$  (and  $K_a$ ). Their absolute deviations reach up to 2.5 MHz. When such trends are spotted in residual plots, they are a strong hint toward missing parameters and the addition of sensible parameters to the model should be tested. The output of *pyckett\_add* for this exemplary case is presented in Fig. A.8.

Two misassignments were introduced into the residuals shown in Fig. A.6. The residuals look similar to Fig. A.4, but the two misassignments are stark outliers at about 1.5 MHz

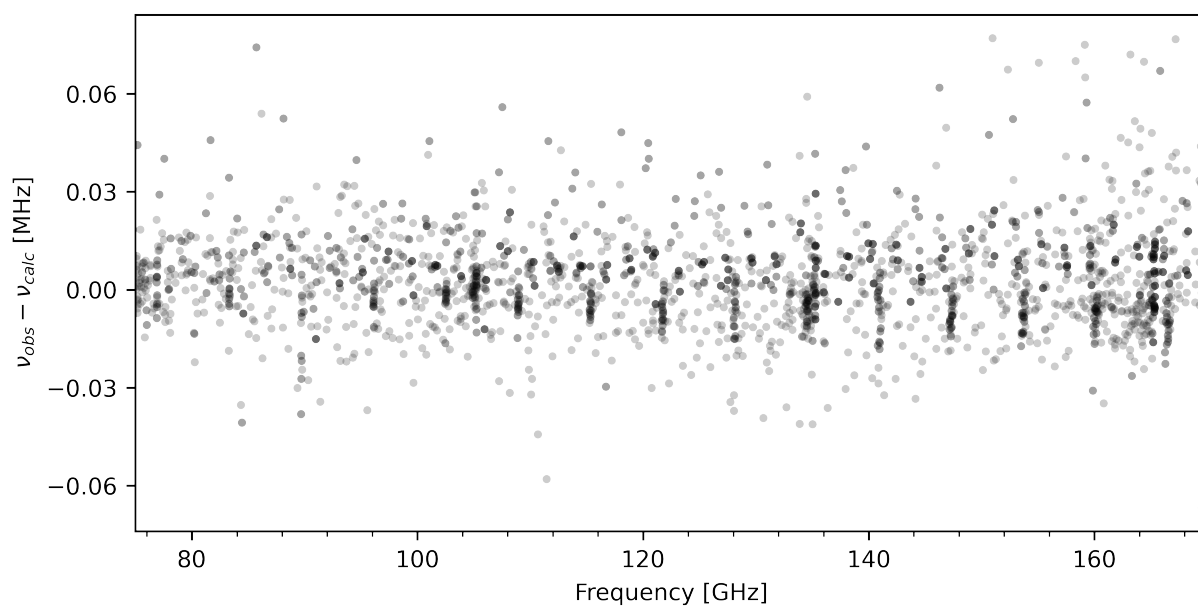


**Figure A.4:** Residual plot for the ground state analysis of glycidaldehyde. This is an example of a good residual distribution as it is fairly evenly distributed, the overall spread is quite small, and no trends are visible.

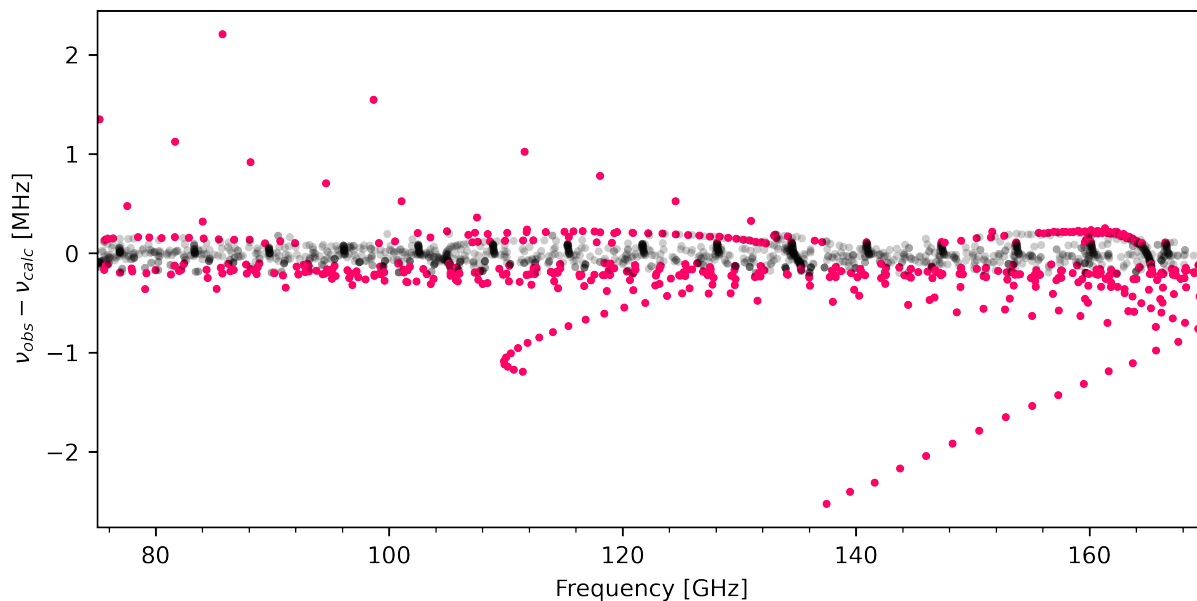


**Figure A.5:** Residual plot for the modified ground state analysis of glycidaldehyde. The two parameters  $L_{JK}$  and  $P_{JK}$  were omitted from the model leading to big deviations which are clearly forming trends.

and  $-1$  MHz. Examining them in LWPs would quickly identify them as wrong assignments. Correcting them is essential, as otherwise they are either rejected from the fit or, even worse, if the rejection threshold is set too high, they are included and heavily influence the parameters in the fit.

As is shown by these examples, residual plots are a great tool to identify problems with the assignments or model and are therefore vital for assigning spectra efficiently and reliably.

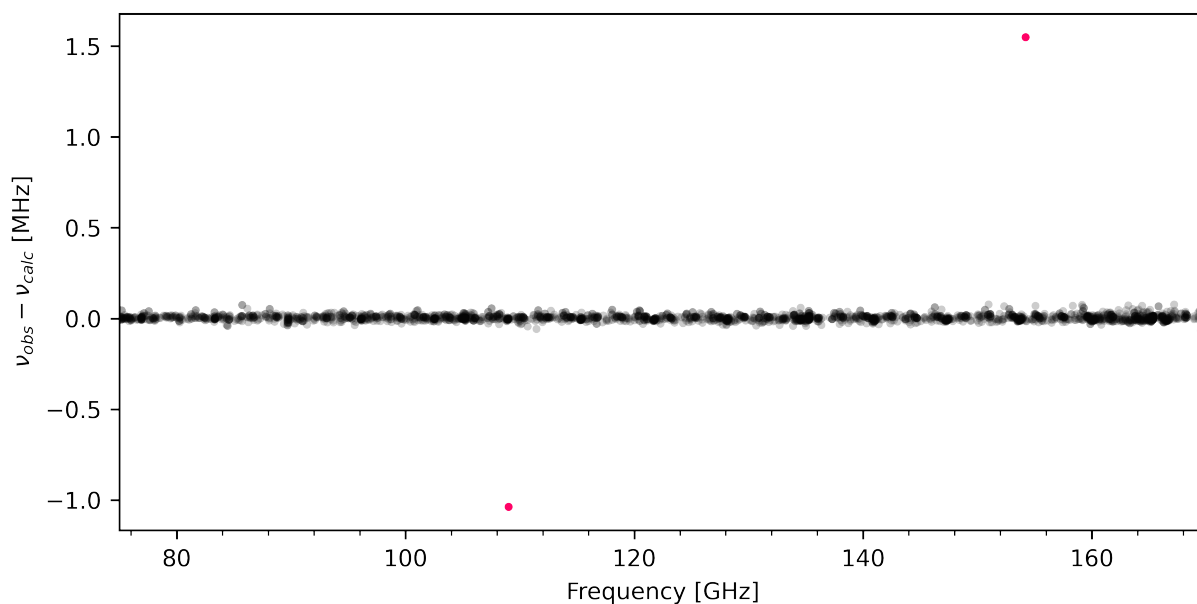


**Figure A.6:** Residual plot for the modified ground state analysis of glycidaldehyde. Two misassignments were added to the *\*.lin* file and are seen as the two red outliers. Removing or correcting them is essential for the analysis.

## A.5 Examples of *pyckett\_omit* and *pyckett\_add*

Example use cases of the *pyckett\_omit* and *pyckett\_add* commands are given in the following.

The example of *pyckett\_omit*, shown in Fig. A.7, is for the final combined fit of  $\nu_{10}$  and  $\nu_{22}$  of cyclopentadiene (see Sec. 8). The first line is how the command is invoked. *pyckett\_omit* is the command name, *Analysis\_v10v22* the path (excluding the file extension) of the *\*.par* and *\*.lin* files of the corresponding analysis, and *--skipfixed* specifies that fixed parameters (parameters that are not floated in the fit) should not be tested. The subsequent lines are the output generated by the program, representing a table. The first column specifies the parameter that was omitted, *INITIAL* being the case where no parameter was omitted, and the following columns provide the resulting RMS, number of rejected lines, and whether the fit was diverging.

Omitting any parameter either considerably increases the initial RMS of 27.38 kHz or leads to many lines being rejected from the fit. Given that there are no misassignments which could be responsible for lines being rejected, this means all the parameters are essential

```
>>> pyckett_omit Analysis_v10v22 --skipfixed
```

ID	RMS [kHz]	RejLines	Diverging
INITIAL	27.38	0	NEVER
610101	83.34	0	PREVIOUS
40100	81.72	3	PREVIOUS
211	100.84	13	PREVIOUS
610001	56.52	39	PREVIOUS
2011	87.80	350	PREVIOUS
10000	0.00	554	NEVER
20000	0.00	554	NEVER
30000	0.00	554	NEVER
200	0.00	554	LAST
1100	0.00	554	LAST
2000	0.00	554	LAST
10011	0.00	554	NEVER
20011	0.00	554	LAST
30011	0.00	554	NEVER
1111	0.00	554	LAST
11	0.00	554	NEVER
600001	0.00	554	NEVER
600101	0.00	554	LAST

**Figure A.7:** Example of the *pyckett\_omit* command. The first line is the command invocation and the subsequent lines are the generated output. The output provides in table form the influence of omitting each of the specified parameters on the RMS value, number of rejected lines, and whether the fit is diverging.

```
>>> pyckett_add Glycidaldehydev0 --sreduction
```

ID	RMS [kHz]	RejLines	Diverging	Init Value	Final Value
20000	409.61	0	NEVER	1.00e-37	7.61e-04
50399	409.70	0	NEVER	1.00e-37	-1.48e-20
3299	205.34	0	NEVER	1.00e-37	1.03e-14
60199	410.11	0	NEVER	1.00e-37	-1.38e-17
4199	410.09	0	NEVER	1.00e-37	5.75e-15
60299	410.09	0	NEVER	1.00e-37	-8.27e-22
5099	409.89	0	NEVER	1.00e-37	2.35e-14
40399	409.38	0	NEVER	1.00e-37	-1.97e-16
10000	406.93	0	NEVER	1.00e-37	1.93e-02
30000	409.25	0	NEVER	1.00e-37	9.40e-04
70099	408.82	0	NEVER	1.00e-37	-1.12e-16
499	406.72	0	NEVER	1.00e-37	8.05e-16
1499	405.46	0	NEVER	1.00e-37	-1.06e-17
2299	102.10	0	NEVER	1.00e-37	9.97e-12
2399	120.77	0	NEVER	1.00e-37	8.70e-16

Initial values were an RMS of 410.09 kHz, 0 rejected lines, and diverging NEVER.

Best run is parameter 2299 with a final parameter value of 9.97e-12, RMS of 102.10 kHz, 0 rejected lines, and diverging NEVER.

**Figure A.8:** Example of the *pyckett\_add* command. The first line is the command invocation and the subsequent lines are the generated output. The output shows in table form the influence that adding each parameter has on the RMS value, number of rejected lines, and whether the fit is diverging or not. Additionally, the initial and final parameter values are given.

for the model and should not be omitted. If a parameter results in a similar RMS value without increasing the number of rejected lines or the fit diverging, there is a high chance that it is not determined and can be omitted from the model.

Especially analyses of interactions between vibrationally excited states benefit from testing which parameters could be omitted as the high correlation between parameters makes it non straight-forward to evaluate this from intuition alone.

A first example of *pyckett\_add* is already given in Fig. 4.2. The example presented here uses the ground state analysis of glycidaldehyde where  $L_{JK}$  and  $P_{JK}$  were removed from the model, as introduced for Fig. A.5. The output of *pyckett\_add* shown in Fig. A.8 highlights that the two parameters with the SPFIT parameter IDs 2299 and 2399 improve the fit considerably. Both parameters decrease the RMS from about 400 kHz to about 100 kHz and result in neither rejected lines nor the fit diverging. In addition, their final parameter values are physically sensible. The two parameter IDs correspond to  $L_{JK}$  and  $P_{JK}$ , the two parameters which were removed for educational purposes.

## A.6 Graphical User Interfaces

In the following, the GUIs of different pieces of software will be shown and explained.

With the *retrophase* software, shown in Fig. A.9, the phase of the demodulation process can be changed retrospectively. Both the in-phase or  $X$  component (blue signal in the top plot) and the quadrature or  $Y$  component (red signal in the top plot) are saved in the measurement file by TRACE.  $X$  and  $Y$  can be seen as the two components of a

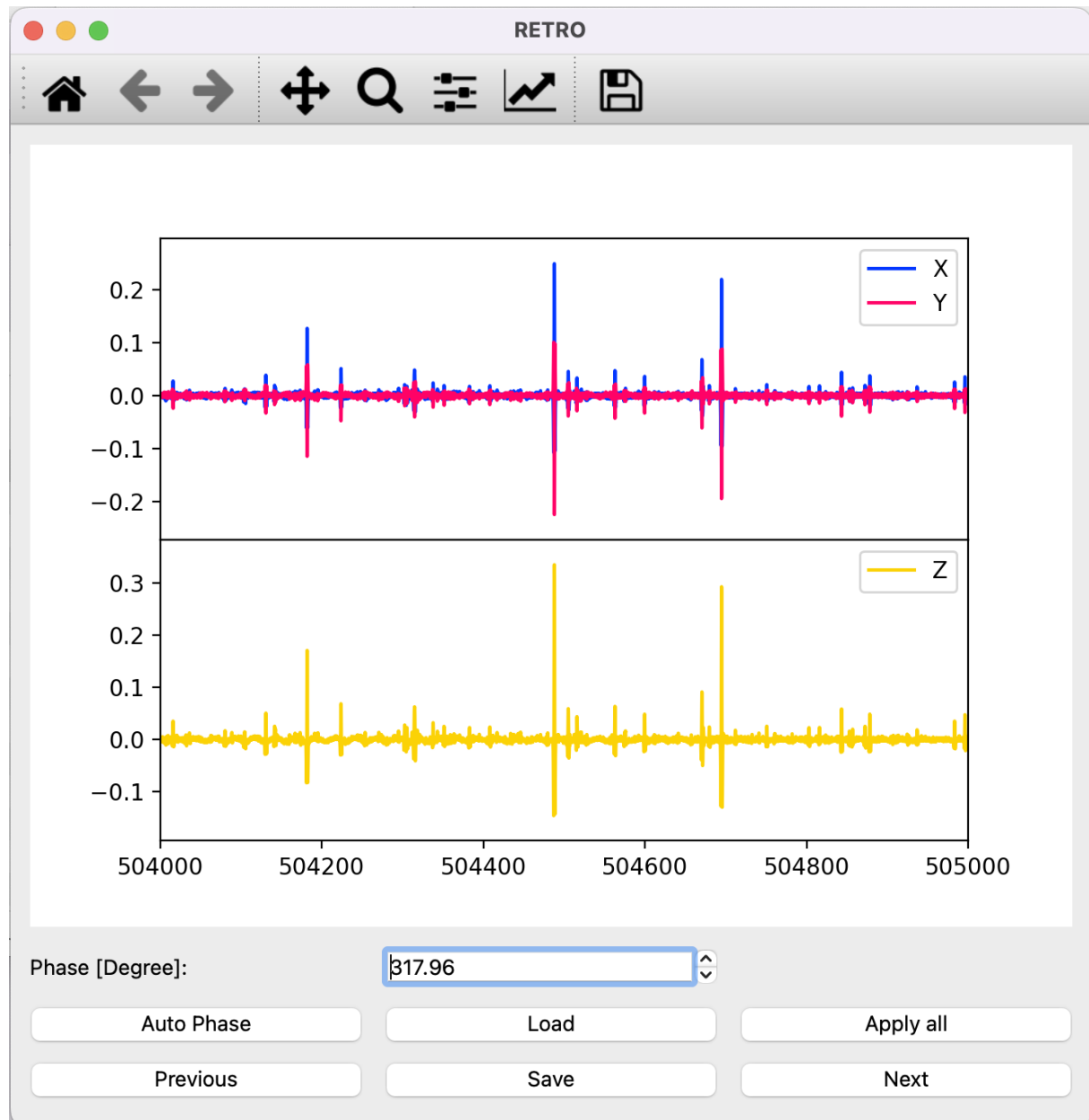


**Figure A.9:** The GUI of the *retrophase* software. The top plot shows the  $X$  (blue) and  $Y$  (red) components of the measurement, which can be understood as a vector. On the bottom, the  $Z$  component corresponds to the  $X$  component of the vector after rotation by the specified (or automatically optimized) angle. In this example, the phase is shifted by  $317.96^\circ$  which improves the maximum signal from about 0.25 mV to 0.35 mV.

vector. The  $Z$  signal (yellow signal in the bottom plot) is the  $X$  component of the vector after rotation by the specified angle. *retrophase* provides an *auto phase* functionality to automatically find the angle that maximizes the signal of the spectrum. The phase offset can also be applied to all loaded measurements (if all measurements were performed with the same non-optimal phase) or the program can be used without the GUI in a headless mode to automatically optimize the phase for all measurements in a folder.

The *fftfilter* software is used to remove standing waves from measurements and shown in Fig. A.10. The measurement files are loaded either via the menu or by drag-and-dropping the files onto the GUI. On top, the Fourier transformed spectrum is shown. The middle plot shows the original spectrum (light blue) and the baseline (red). On the bottom, the spectrum is shown after removal of the standing wave. A cut-off frequency, indicated by the red dashed line, is set interactively by clicking into the Fourier transformed spectrum or by moving the cut-off slider. All Fourier coefficients below the cut-off frequency are set to zero before performing the inverse Fourier transform to obtain the spectrum without

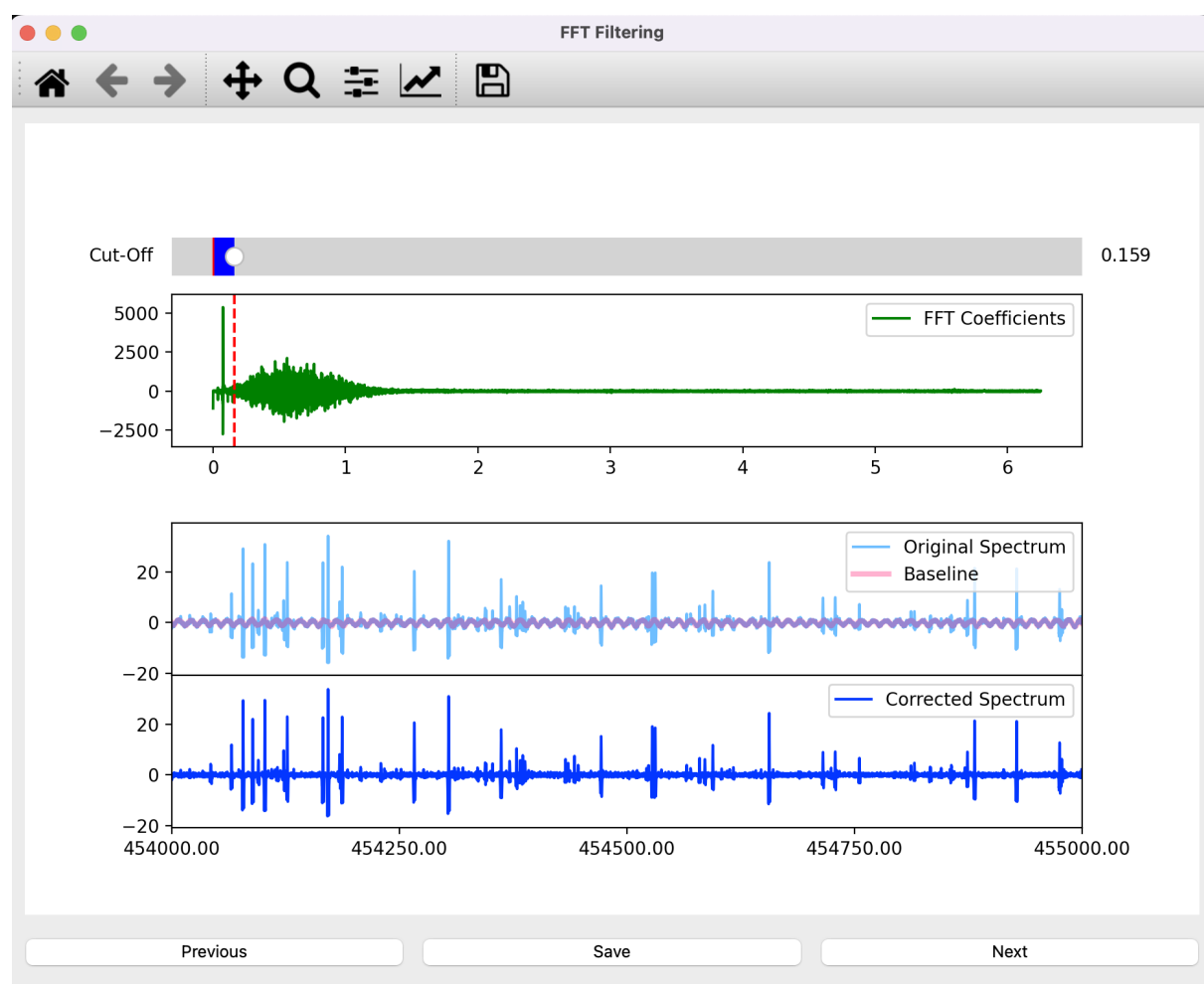


**Figure A.10:** The GUI of the *fftfilter* software. The Fourier transformed spectrum (top plot) of the original spectrum (middle plot in light blue), the calculated baseline (middle plot in red) and the corrected spectrum (bottom plot) are shown.

standing waves. The baseline is calculated as the inverse Fourier transform of only the coefficients below the cut-off frequency. The buttons on the bottom or keyboard shortcuts are used to save the corrected spectrum to a new file and to select the next or previous file. The measurement software TRACE is shown in Fig. A.11 and Fig. A.12. On the left hand side, the measurement queue lists the measurements to be performed next. In addition, the buttons to add a single measurement, a batch of measurements, or a user-specified list of measurements are found there. In both figures, a broadband scan is performed in 1 GHz batches interleaved with reproducibility measurements of a strong transition at 358 914 MHz. The log window on the bottom shows messages and errors. The current measurement is shown in Fig. A.11 in the plot window and the progress is indicated by the progress bar beneath the log window. For each spectrum, both the in-phase and quadrature components are saved for later phase optimization with *retrophase*. The quadrature component is not shown in the GUI, but the magnitude ( $X^2 + Y^2$ ) can be shown instead of the in-phase component  $X$  if the optimal phase is uncertain. In Fig. A.11, the right hand window provides the different settings for the measurements. Conventional and different DR modes are supported by the software. The ability to create custom measurement queues and the error reporting result a high level of automation.

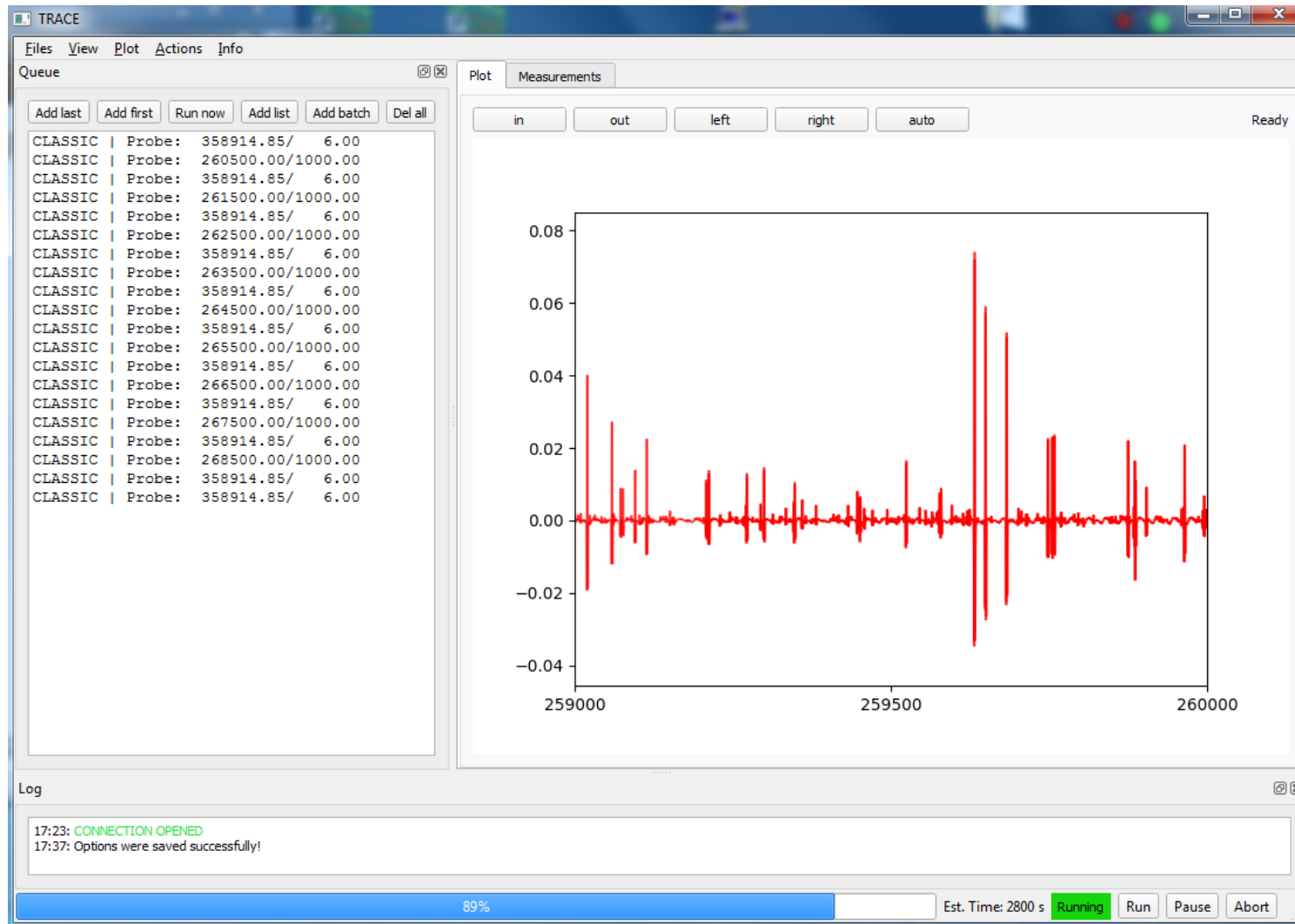
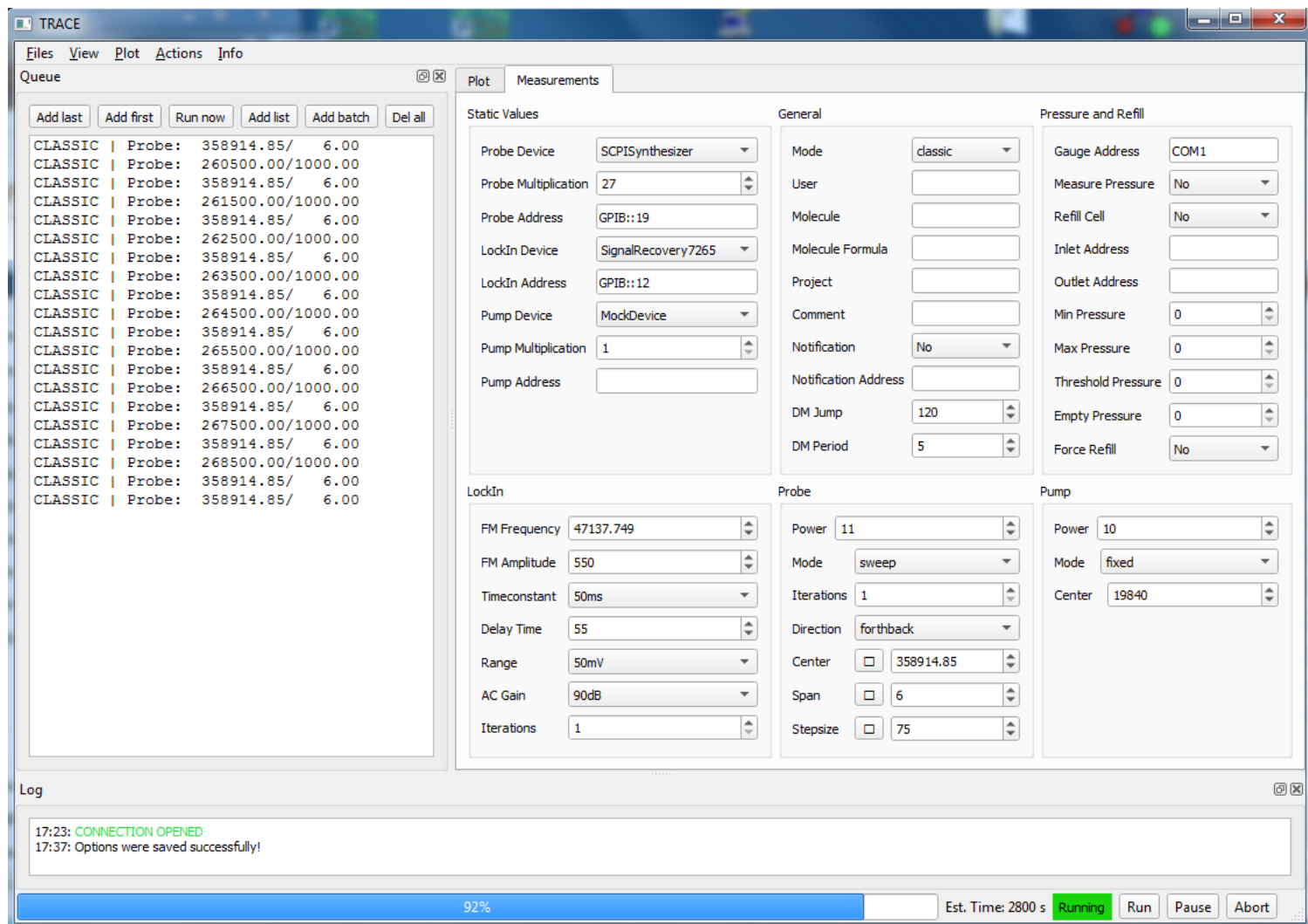


Figure A.11: The GUI of TRACE with the spectrum of the current measurement shown on the right hand side.



**Figure A.12:** The GUI of TRACE with the measurement settings shown on the right hand side.

## A.7 SI for MM- and Sub-MM-Wave Study of C<sub>2</sub>H<sub>5</sub>CP

This section provides the supporting information for the following manuscript:

L. Bonah, S. Schlemmer, J.-C. Guillemin, M. E. Harding, S. Thorwirth, On the Spectroscopy of Phosphaalkynes: Millimeter- and Submillimeter-Wave Study of C<sub>2</sub>H<sub>5</sub>CP, *J. Phys. Chem. A* 128 (2024) 4859–4866. doi:10.1021/acs.jpca.4c02566.

The main manuscript is presented in Sec. 7.

### Copyright Notice

Reprinted with permission from *J. Phys. Chem. A* 2024, **128**, 4859-4866. © 2024 American Chemical Society.

**Supporting Information:**

**On the Spectroscopy of Phosphaalkynes:**

**Millimeter- and Submillimeter-Wave Study of**

**$C_2H_5CP$**

Luis Bonah,<sup>†</sup> Stephan Schlemmer,<sup>†</sup> Jean-Claude Guillemin,<sup>‡</sup> Michael E.  
Harding,<sup>¶</sup> and Sven Thorwirth<sup>\*,†</sup>

<sup>†</sup>*I. Physikalisches Institut, Universität zu Köln, Zùlpicher Str. 77, 50937 Köln, Germany*

<sup>‡</sup>*Univ Rennes, Ecole Nationale Supérieure de Chimie de Rennes, CNRS, ISCR –  
UMR6226, 35000 Rennes, France*

<sup>¶</sup>*Institut für Nanotechnologie, Karlsruher Institut für Technologie (KIT), Kaiserstr. 12,  
76131 Karlsruhe, Germany*

E-mail: sthorwirth@ph1.uni-koeln.de

## Internal Coordinates

Structural parameters of C<sub>2</sub>H<sub>5</sub>CP (bond lengths in Å, angles in degrees) calculated at the CCSD(T) level of theory as described in the main paper.

### Minimum Structure

H  
C 1 r1  
C 2 r2 1 a1  
C 3 r3 2 a2 1 d180  
X 4 rd 3 a90 2 d180  
P 4 r4 5 a3 3 d180  
H 2 r5 3 a4 1 d1  
H 2 r5 3 a4 1 md1  
H 3 r6 2 a5 1 d2  
H 3 r6 2 a5 1 md2

	fc-CCSD(T)/cc-pV(T+d)Z	/	fc-CCSD(T)/ANO1	/	ae-CCSD(T)/cc-pwCVTZ	/	ae-CCSD(T)/cc-pwCVQZ	
r1	=	1.091399750169	/	1.091434483954	/	1.089551930794	/	1.088731298792
r2	=	1.535893586362	/	1.535360578458	/	1.531854602535	/	1.529842301511
a1	=	110.337773354289	/	110.302504422938	/	110.363156775280	/	110.340765620417
r3	=	1.472280447045	/	1.470831321532	/	1.467330176455	/	1.465419738716
a2	=	112.199721299815	/	112.224893473485	/	112.257644477134	/	112.232104051430
d180	=	180.000000000000	/	180.000000000000	/	180.000000000000	/	180.000000000000
rd	=	1.000001432603	/	1.000000818630	/	1.000001432603	/	1.000001637260
a90	=	90.000000000000	/	90.000000000000	/	90.000000000000	/	90.000000000000
r4	=	1.556049658377	/	1.558178012329	/	1.548920652423	/	1.546262193406
a3	=	91.445620350371	/	91.467689068037	/	91.442689015710	/	91.463218503903
r5	=	1.090804694054	/	1.090796322788	/	1.088983880406	/	1.088187677773
a4	=	110.518940323890	/	110.538672558521	/	110.545544106426	/	110.556757104238
d1	=	120.153481746979	/	120.125356986080	/	120.150663157516	/	120.144847704733
md1	=	-120.153481746979	/	-120.125356986080	/	-120.150663157516	/	-120.144847704733
r6	=	1.094111701086	/	1.094111644799	/	1.092432140325	/	1.091757498190
a5	=	110.092247589610	/	110.069629547391	/	110.077360418925	/	110.102634313991
d2	=	58.724630166166	/	58.687155093401	/	58.671326579535	/	58.688205066274
md2	=	-58.724630166166	/	-58.687155093401	/	-58.671326579535	/	-58.688205066274

## Transition State

H  
C 1 r1  
C 2 r2 1 a1  
C 3 r3 2 a2 1 d0  
X 4 rd 3 a90 2 d180  
P 4 r4 5 a3 3 d180  
H 2 r5 3 a4 1 d1  
H 2 r5 3 a4 1 md1  
H 3 r6 2 a5 1 d2  
H 3 r6 2 a5 1 md2

	fc-CCSD(T)/cc-pV(T+d)Z	/	fc-CCSD(T)/ANO1	/	ae-CCSD(T)/cc-pwCVTZ	/	ae-CCSD(T)/cc-pwCVQZ	
r1	=	1.089420190933	/	1.089516227711	/	1.087600995495	/	1.086942193969
r2	=	1.551031295925	/	1.550673757933	/	1.547016625446	/	1.544877613057
a1	=	110.898339941307	/	110.917592687697	/	110.913997081790	/	110.901128437096
r3	=	1.471871020191	/	1.470497864702	/	1.466901708628	/	1.465018275330
a2	=	113.078007661519	/	113.123615610578	/	113.135670768232	/	113.127660296892
d0	=	0.000000000000	/	0.000000000000	/	0.000000000000	/	0.000000000000
rd	=	0.709959883196	/	1.560982220614	/	0.788974584738	/	1.098541117781
a90	=	90.000000000000	/	90.000000000000	/	90.000000000000	/	90.000000000000
d180	=	180.000000000000	/	180.000000000000	/	180.000000000000	/	180.000000000000
r4	=	1.556401050100	/	1.558519015686	/	1.549250368663	/	1.546612778595
a3	=	90.973881395985	/	91.033683611625	/	90.972888723607	/	91.026811204542
r5	=	1.090129558880	/	1.090142903059	/	1.088283408122	/	1.087481836858
a4	=	110.927913335861	/	110.954441622600	/	110.956708399506	/	110.975302610556
d1	=	119.986074792146	/	119.968566459615	/	119.980720568682	/	119.965345563525
md1	=	-119.986074792146	/	-119.968566459615	/	-119.980720568682	/	-119.965345563525
r6	=	1.093275771687	/	1.093272960607	/	1.091584133566	/	1.090920112441
a5	=	110.416718047936	/	110.408565913496	/	110.401820466528	/	110.434832335139
d2	=	121.418041449990	/	121.463437016831	/	121.470458964463	/	121.461422641011
md2	=	-121.418041449990	/	-121.463437016831	/	-121.470458964463	/	-121.461422641011

# Vibrational Wavenumbers and Rotation-Vibration Interaction Constants

Harmonic and anharmonic vibrational wavenumbers of C<sub>2</sub>H<sub>5</sub>CP (in cm<sup>-1</sup>) calculated at the CCSD(T) level of theory as described in the main paper.

**Table S1: Vibrational wavenumbers of C<sub>2</sub>H<sub>5</sub>CP calculated at the CCSD(T) level of theory using the cc-pV(T+d)Z and ANO1 basis sets (in cm<sup>-1</sup>).**

Mode	Harmonic		Anharmonic	
	pV(T+d)Z	ANO1	pV(T+d)Z	ANO1
$\nu_1(a')$	3124	3128	2981	2984
$\nu_2(a')$	3045	3046	2916	2953
$\nu_3(a')$	3037	3039	2909	2909
$\nu_4(a')$	1577	1582	1548	1551
$\nu_5(a')$	1507	1504	1464	1463
$\nu_6(a')$	1473	1470	1437	1423
$\nu_7(a')$	1410	1408	1377	1376
$\nu_8(a')$	1327	1326	1294	1293
$\nu_9(a')$	1079	1079	1053	1053
$\nu_{10}(a')$	988	987	962	962
$\nu_{11}(a')$	713	712	713	711
$\nu_{12}(a')$	484	484	479	479
$\nu_{13}(a')$	166	166	166	165
$\nu_{14}(a'')$	3129	3133	2985	2987
$\nu_{15}(a'')$	3072	3077	2922	2926
$\nu_{16}(a'')$	1503	1499	1469	1469
$\nu_{17}(a'')$	1282	1281	1251	1252
$\nu_{18}(a'')$	1090	1090	1066	1065
$\nu_{19}(a'')$	780	779	773	773
$\nu_{20}(a'')$	333	334	327	326
$\nu_{21}(a'')$	211	212	204	205

## Rotational Constants for Isotopologues

Detection of the singly substituted <sup>13</sup>C isotopic species of C<sub>2</sub>H<sub>5</sub>CP was made possible based on scaled (best estimate) rotational parameters summarized in Table S2 (columns *Scaled*). To arrive at those, the purely calculated rotational parameters (from equilibrium rotational constants  $A_e$ ,  $B_e$ , and  $C_e$  calculated at the ae-CCSD(T)/cc-pwCVQZ level of theory and zero-point vibrational corrections and centrifugal distortion constants calculated at the fc-CCSD(T)/ANO1 level of theory; columns *Calculated* in Table S2) were scaled by the ratio  $X_{0,exp}/X_{calc}$  of the parent isotopic species (see values of the main paper) for any given parameter  $X$ . For the rotational constants  $A$ ,  $B$ , and  $C$ ,  $X_{calc} = X_{0,calc}$  whereas for the quartic centrifugal distortion parameters  $X_{calc} = X_{e,calc}$ .

**Table S2: Calculated and scaled parameters of the singly substituted  $^{13}\text{C}$  isotopologues of  $\text{C}_2\text{H}_5\text{CP}$ .**

Parameter	Calculated	$^{13}\text{CH}_3\text{CH}_2\text{CP}$			Calculated	$\text{CH}_3^{13}\text{CH}_2\text{CP}$			Calculated	$\text{CH}_3\text{CH}_2^{13}\text{CP}$	
		Scaled	Experimental			Scaled	Experimental			Scaled	Experimental
$A$	/ MHz	24 834.546	24 834.903	24 834.81(19)	24 694.970	24 695.326	24 696.03(15)	25 115.082	25 115.444	25 115.37(19)	
$B$	/ MHz	2639.016	2641.048	2641.072 28(69)	2683.955	2686.021	2686.014 05(83)	2706.883	2708.967	2708.970 88(95)	
$C$	/ MHz	2456.132	2457.864	2457.885 62(70)	2493.577	2495.335	2495.328 16(71)	2517.681	2519.456	2519.453 45(67)	
$-D_J$	/ Hz	-862.556	-883.912	-883.46(13)	-840.369	-861.176	-861.16(15)	-876.158	-897.851	-897.91(23)	
$-D_{JK}$	/ kHz	24.342	24.691	24.6990(22)	21.893	22.207	22.2244(20)	24.132	24.478	24.467(13)	
$-D_K$	/ kHz	-533.219	-544.088	-552(19)	-509.613	-520.000	-505(20)	-549.499	-560.699	-563(18)	
$d_1$	/ Hz	-144.144	-149.914	-149.84(20)	-143.726	-149.479	-149.67(24)	-149.281	-155.257	-155.40(23)	
$d_2$	/ Hz	-6.922	-7.554	-7.635(45)	-7.622	-8.318	-8.242(74)	-7.475	-8.157	-8.133(43)	

**Table S3: Zero-point vibrational corrections to the rotational constants calculated at the fc-CCSD(T)/ANO1 level of theory and derived semi-experimental equilibrium rotational constants used for structural refinement (in MHz).**

	$\text{CH}_3\text{CH}_2\text{CP}$	$^{13}\text{CH}_3\text{CH}_2\text{CP}$	$\text{CH}_3^{13}\text{CH}_2\text{CP}$	$\text{CH}_3\text{CH}_2^{13}\text{CP}$
$\Delta A_0$	158.770	151.386	152.917	156.832
$\Delta B_0$	12.603	12.407	12.185	12.498
$\Delta C_0$	14.132	13.823	13.739	14.044
$A_e^{\text{SE}}$	25374.893	24986.196	24848.947	25272.202
$B_e^{\text{SE}}$	2721.746	2653.479	2698.199	2721.469
$C_e^{\text{SE}}$	2534.771	2471.709	2509.067	2533.497

## Reproducibility Measurements

To ensure the reproducibility of the measurements and to quantify the frequency uncertainty, one dedicated transition was measured repeatedly in between the broadband measurements for each frequency range. A second derivative Voigt profile was fitted to each of the measured reproducibility lines and the resulting frequency deviation from the mean center frequency  $\Delta\nu$ , the amplitude, the Gaussian FWHM, and the Lorentzian FWHM were determined. The results are shown for broadband measurement of the 500–760 GHz range in Figure S1.

The amplitude and the Lorentzian FWHM show four distinct cycles corresponding to the filling cycles of the absorption cell. The Gaussian FWHM is almost constant as would be expected. The frequency deviations span over 12.6 kHz and have a standard deviation of 2.7 kHz.

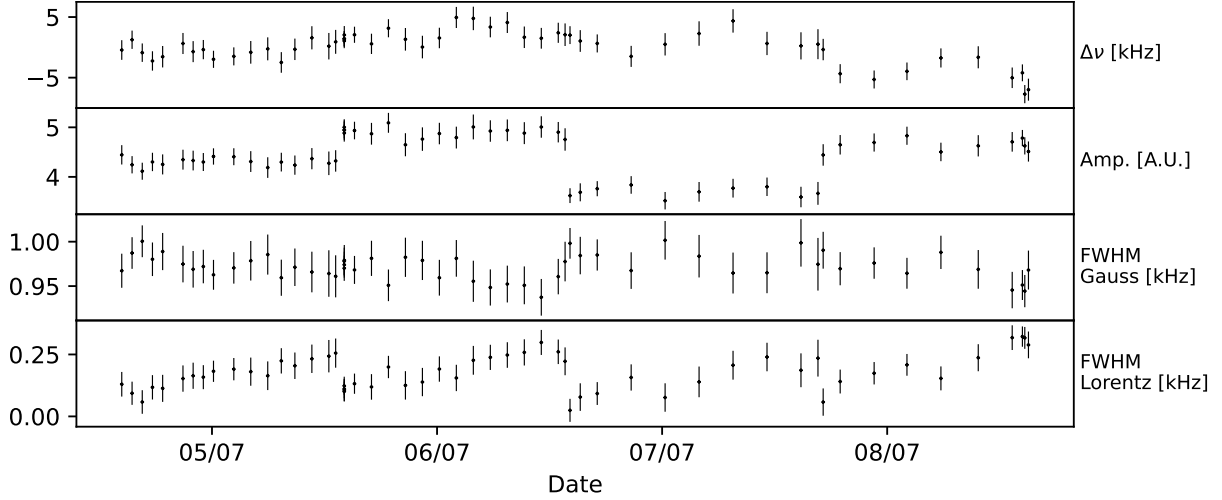


Figure S1: The key values and uncertainties of the reproducibility measurements plotted against the time of the measurement. Each measurement was fitted with a second derivative Voigt profile.

## Frequency Uncertainties

The uncertainties for the assignments were assigned semi-automatically. A Voigt profile fixed to the position of the assignment was fitted to the experimental data and the RMS between the fitfunction and the experimental spectrum was calculated and divided by the amplitude:

$$RMS/A = \frac{1}{A} \sqrt{\frac{\sum_i^N (I_{\text{exp},i} - I_{\text{fit},i})^2}{N}} \quad (1)$$

$I_{\text{exp},i}$  and  $I_{\text{fit},i}$  are the intensities at frequency  $i$  of the experimental data and fitfunction respectively,  $N$  is the number of datapoints in the fit range, and  $A$  is the amplitude (defined as the baseline to peak value) of the fitfunction.

This quantity possesses a few desirable features. It increases with decreasing  $SNR$  as well as with more asymmetric experimental lineshapes. Additionally, we performed simulations with artificial datasets of different noise and baseline levels that show a high correlation between the  $RMS/A$  value and the uncertainty of the center position from the fit.

The lines were divided into three groups based on their  $RMS/A$  values which were visually verified (see Figure S2).

The groups were assigned the uncertainties of 20 kHz for  $RMS/A < 0.05$ , 30 kHz for  $0.05 < RMS/A < 0.1$ , and 40 kHz for  $0.1 < RMS/A$ .

The minimum uncertainty is a result of the reproducibility measurements which show that the peak-to-peak variation of the center frequencies is below 20 kHz for all frequency ranges.

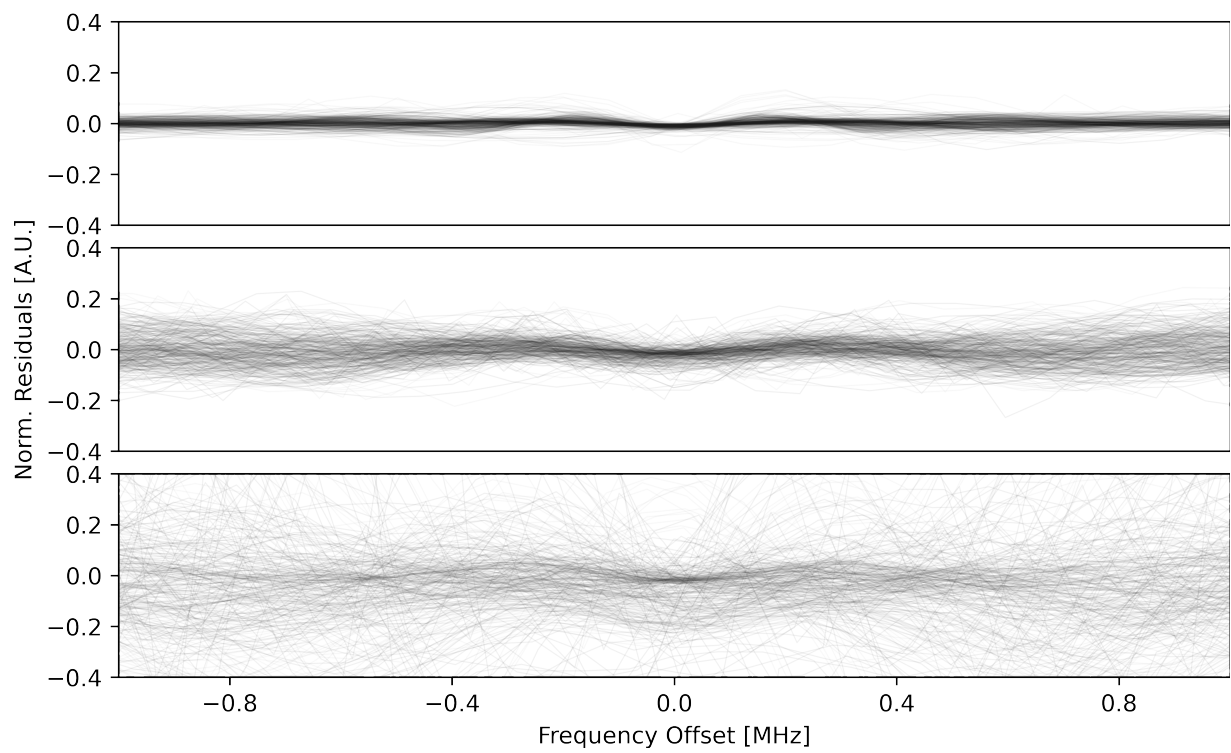


Figure S2: The normalized residuals, being the deviation between the fitted Voigt profile and the experimental data divided by the amplitude, for 500 random lines of the three groups of uncertainties (From top to bottom: 20 kHz, 30 kHz, and 40 kHz).

## A.8 SI for DR Spectroscopy of Glycidaldehyde

This section provides the supporting information for the following manuscript:

L. Bonah, J.-C. Guillemin, A. Belloche, S. Thorwirth, H. S. P. Müller, S. Schlemmer, Leveraging MMW-MMW Double Resonance Spectroscopy to Understand the Pure Rotational Spectrum of Glycidaldehyde and 17 of its Vibrationally Excited States, *ACS Earth Space Chem.* in press (2025). doi:10.1021/acsearthspacechem.4c00360

The main manuscript is presented in Sec. 9.

### Copyright Notice

Reprinted with permission from *ACS Earth Space Chem.* 2025, **XXX**, XXXX. © 2025 American Chemical Society.

# Leveraging MMW-MMW Double Resonance Spectroscopy to Understand the Pure Rotational Spectrum of Glycidaldehyde and 17 of its Vibrationally Excited States

Luis Bonah,<sup>\*,†</sup> Jean-Claude Guillemin,<sup>‡</sup> Arnaud Belloche,<sup>¶</sup> Sven Thorwirth,<sup>\*,†</sup>  
Holger S. P. Müller,<sup>†</sup> and Stephan Schlemmer<sup>†</sup>

<sup>†</sup>*I. Physikalisches Institut, Universität zu Köln, Zùlpicher Str. 77, 50937 Köln, Germany*

<sup>‡</sup>*Univ Rennes, Ecole Nationale Supérieure de Chimie de Rennes, CNRS, ISCR –  
UMR6226, 35000 Rennes, France*

<sup>¶</sup>*Max-Planck-Institut für Radioastronomie, Auf dem Hügel 69, 53121 Bonn, Germany*

E-mail: bonah@ph1.uni-koeln.de; sthorwirth@ph1.uni-koeln.de

# 1 Results from quantum-chemical Calculations

Quantum chemical calculations were performed with the CFOUR suite of programs<sup>1-3</sup> using the CCSD(T) method and selected basis sets, see the main manuscript for further details.

## 1.1 Results from structural optimization

Structures given in internal coordinates, bond lengths in Å and angles in degrees.

```
0
C 1 r1
C 2 r2 1 a1
C 3 r3 2 a2 1 d1
O 4 r4 3 a3 2 d2
H 4 r5 3 a4 5 d3
H 3 r6 4 a5 5 d4
H 2 r7 3 a6 4 d5
H 2 r8 3 a7 8 d6
```

CCSD(T)/ANO0	trans /	gauche
r1 =	1.43420 /	1.43235
r2 =	1.48361 /	1.48661
a1 =	59.34775 /	58.94422
r3 =	1.49877 /	1.50677
a2 =	117.98195 /	118.53886
d1 =	102.90610 /	105.49800
r4 =	1.21710 /	1.21656
a3 =	123.79074 /	123.93167
d2 =	140.19459 /	-42.78022
r5 =	1.11266 /	1.11208
a4 =	113.54339 /	114.34459
d3 =	-179.70399 /	178.48675
r6 =	1.09051 /	1.09238
a5 =	116.61499 /	116.05258
d4 =	-13.25035 /	165.66641
r7 =	1.09209 /	1.09114
a6 =	119.33438 /	117.93518
d5 =	-0.86220 /	1.62319
r8 =	1.09060 /	1.09098
a7 =	118.31371 /	118.84318
d6 =	-151.42552 /	-151.74063

CCSD(T)/cc-pVTZ	trans /	gauche
r1 =	1.42446 /	1.42234
r2 =	1.47605 /	1.47875
a1 =	59.27213 /	58.89010
r3 =	1.49299 /	1.50159
a2 =	117.81715 /	118.08989
d1 =	102.82853 /	105.07039
r4 =	1.21034 /	1.21017
a3 =	123.73519 /	123.32861
d2 =	140.09315 /	-40.94213
r5 =	1.10723 /	1.10595

a4	=	113.77282 /	115.21436
d3	=	-179.68757 /	178.64727
r6	=	1.08396 /	1.08563
a5	=	116.66463 /	116.49065
d4	=	-13.60498 /	166.89903
r7	=	1.08553 /	1.08455
a6	=	119.27469 /	117.70728
d5	=	-0.77269 /	1.36535
r8	=	1.08389 /	1.08437
a7	=	118.29029 /	118.87964
d6	=	-151.81966 /	-152.13362

CCSD(T)/cc-pwCVTZ		trans /	gauche
r1	=	1.42054 /	1.41842
r2	=	1.47170 /	1.47449
a1	=	59.27796 /	58.88819
r3	=	1.48904 /	1.49754
a2	=	117.84874 /	118.12269
d1	=	102.89003 /	105.16117
r4	=	1.20706 /	1.20685
a3	=	123.75754 /	123.37084
d2	=	139.92518 /	-41.47966
r5	=	1.10593 /	1.10465
a4	=	113.77666 /	115.18568
d3	=	-179.68728 /	178.63067
r6	=	1.08254 /	1.08420
a5	=	116.61333 /	116.42719
d4	=	-13.70496 /	166.48693
r7	=	1.08388 /	1.08294
a6	=	119.28744 /	117.73605
d5	=	-0.76120 /	1.42092
r8	=	1.08232 /	1.08279
a7	=	118.29670 /	118.88737
d6	=	-151.71214 /	-152.04099

## 1.2 Results from anharmonic force field

Negative rotation-vibration interaction constants, harmonic and fundamental vibrational wavenumbers, and the fundamental intensities calculated at the fc-CCSD(T)/cc-pVTZ level of theory are given in the following. Rotation-vibration interaction constants  $\alpha_v^{A/B/C}$  are reported as  $\Delta A = -\alpha_v^A \approx A_v - A_0$  (analogously for  $\Delta B$  and  $\Delta C$ ), as this allows for direct comparison with the difference parameters presented in the main manuscript.

Table S1: Calculated negative rotation-vibration interaction constants (in MHz), harmonic and fundamental vibrational wavenumbers (in  $\text{cm}^{-1}$ ), and fundamental band intensities (in  $\text{km/mol}$ ).

	$-\alpha_v^A$	$-\alpha_v^B$	$-\alpha_v^C$	$\tilde{\nu}_{\text{Harm}}$	$\tilde{\nu}_{\text{Fund}}$	$I_{\text{Fund}}$
$\nu_{21}$	-143.221	12.282	4.940	127	123	12
$\nu_{20}$	136.589	-1.794	-0.118	299	302	18
$\nu_{19}$	-14.513	-1.386	-4.971	354	347	8
$\nu_{18}$	19.024	-3.811	-2.195	505	504	2
$\nu_{17}$	-294.331	-7.761	-44.303	860	864	16
$\nu_{16}$	118.304	-3.742	17.223	868	851	23
$\nu_{15}$	24.459	1.453	11.821	904	877	28
$\nu_{14}$	-47.271	-0.621	-2.748	1017	995	13
$\nu_{13}$	-63.939	-0.280	-2.645	1096	1070	2
$\nu_{12}$	-121.403	31.873	-14.245	1155	1121	3
$\nu_{11}$	51.093	30.772	7.579	1160	1130	1
$\nu_{10}$	76.170	-6.621	-2.390	1183	1156	16
$\nu_9$	-9.596	1.019	3.521	1250	1222	6
$\nu_8$	-15.503	-1.662	0.520	1351	1315	3
$\nu_7$	-17.587	-3.056	-0.253	1432	1400	4
$\nu_6$	-10.028	-0.700	0.954	1531	1486	1
$\nu_5$	-9.113	-9.990	-8.943	1791	1759	148
$\nu_4$	-24.493	-0.282	0.434	2937	2788	65
$\nu_3$	-8.410	-2.020	-1.017	3112	3011	17
$\nu_2$	-27.639	-3.135	-2.964	3177	3036	5
$\nu_1$	1.509	-2.703	-1.868	3209	3058	13

### 1.3 Rotational constants

The calculated and experimental rotational constants and centrifugal distortion parameters are compared in Table S2. The equilibrium rotational constants  $B_e$  ( $A_e, C_e$ ) are calculated at the ae-CCSD(T)/cc-pwCVTZ level. Zero-point vibrational contributions  $\Delta B_0$  ( $\Delta A_0, \Delta C_0$ ) to the rotational constants and centrifugal distortion constants are calculated at the fc-CCSD(T)/cc-pVTZ level. Ground-state rotational constants are estimated as  $B_0 = B_e - \Delta B_0$  (similarly for  $A_0$  and  $C_0$ ).

Table S2: Rotational parameters of glycidaldehyde.

Parameter	Calculated	Experimental
$A_e$ /MHz	18 398.221	...
$B_e$ /MHz	3277.946	...
$C_e$ /MHz	3144.937	...
$\Delta A_0$ /MHz	195.930	...
$\Delta B_0$ /MHz	18.287	...
$\Delta C_0$ /MHz	21.205	...
$A_0$ /MHz	18 202.291	18 241.103 87(19)
$B_0$ /MHz	3259.659	3272.930 495(19)
$C_0$ /MHz	3123.732	3137.715 975(19)
$-D_J$ /Hz	-543.371	-562.8157(35)
$-D_{JK}$ /kHz	-11.966	-12.384 92(12)
$-D_K$ /kHz	-16.299	-17.025 86(82)
$d_1$ /Hz	-19.473	-23.785 67(83)
$d_2$ /Hz	-3.012	-3.807 94(52)
$H_J$ / $\mu$ Hz	98.4	135.13(19)
$H_{JK}$ /mHz	68.289	74.152(29)
$H_{KJ}$ /Hz	-1.017	-1.119 31(26)
$H_K$ /Hz	0.842	0.9252(19)
$h_1$ / $\mu$ Hz	49.7	66.782(64)
$h_2$ / $\mu$ Hz	55.0	65.84(16)
$h_3$ / $\mu$ Hz	2.5	3.147(18)
$L_{JJK}$ /nHz	...	-435.5(20)
$L_{JK}$ / $\mu$ Hz	...	15.181(61)
$L_{KKJ}$ / $\mu$ Hz	...	-148.17(22)
$L_K$ / $\mu$ Hz	...	98.5(17)
$l_2$ /pHz	...	-457(10)
$P_{JK}$ /pHz	...	-170.2(49)

## 1.4 Energy Dependence on Torsional Angle

The potential energy curve for the glycidaldehyde system as a function of the  $\text{CCCO}_{ald}$  dihedral angle corresponding to a rotation of the aldehyde group about the  $\text{C}-\text{CHO}_{ald}$  bond was calculated at the  $\text{fc-CCSD(T)/ANO0}$  level of theory. A step size of  $10^\circ$  was employed while varying all other structural parameters in the optimization. At this level of theory, in fully relaxed calculations, minima are finally calculated at torsional angles of  $140.19^\circ$  (trans) and  $317.22^\circ$  ( $-42.78^\circ$ , gauche), respectively.

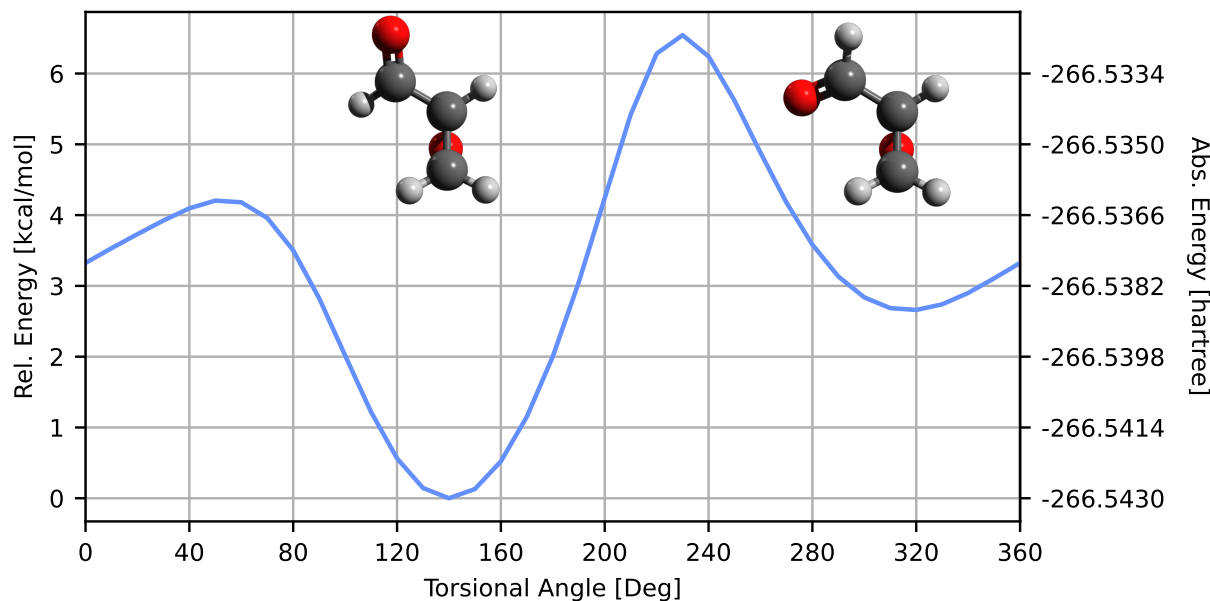


Figure S1: CCSD(T)/ANO0 relative potential energy curve for the glycidaldehyde system as a function of the  $\text{CCCO}_{ald}$  dihedral angle corresponding to a rotation of the aldehyde group about the  $\text{C}-\text{CHO}_{ald}$  bond. See text for more information.

Lastly, the energy difference between the trans- and gauche-forms of glycidaldehyde was calculated at a higher level of theory and including zero-point vibrational contributions. Structural calculations and anharmonic force fields were calculated at the  $\text{ae-CCSD(T)/cc-pwCVTZ}$  and  $\text{fc-CCSD(T)/ANO0}$  levels of theory, respectively.

	total_E /hartree	Delta_E /hartree	Delta_E /kcal/mol	ZPVE kcal /kcal/mol	Del_E w/ZPVE /kcal/mol
trans	-266.967272	0.000000	0.00	41.33	0.00
gauche	-266.963381	0.003892	2.44	41.27	2.38

## 2 Residuals Histograms

Residuals histograms of assignments performed in this work and performed by Creswell et al.<sup>4</sup> are given. The strong systematic offset in the assignments by Creswell et al. necessitated an increase of their transition frequency uncertainties.

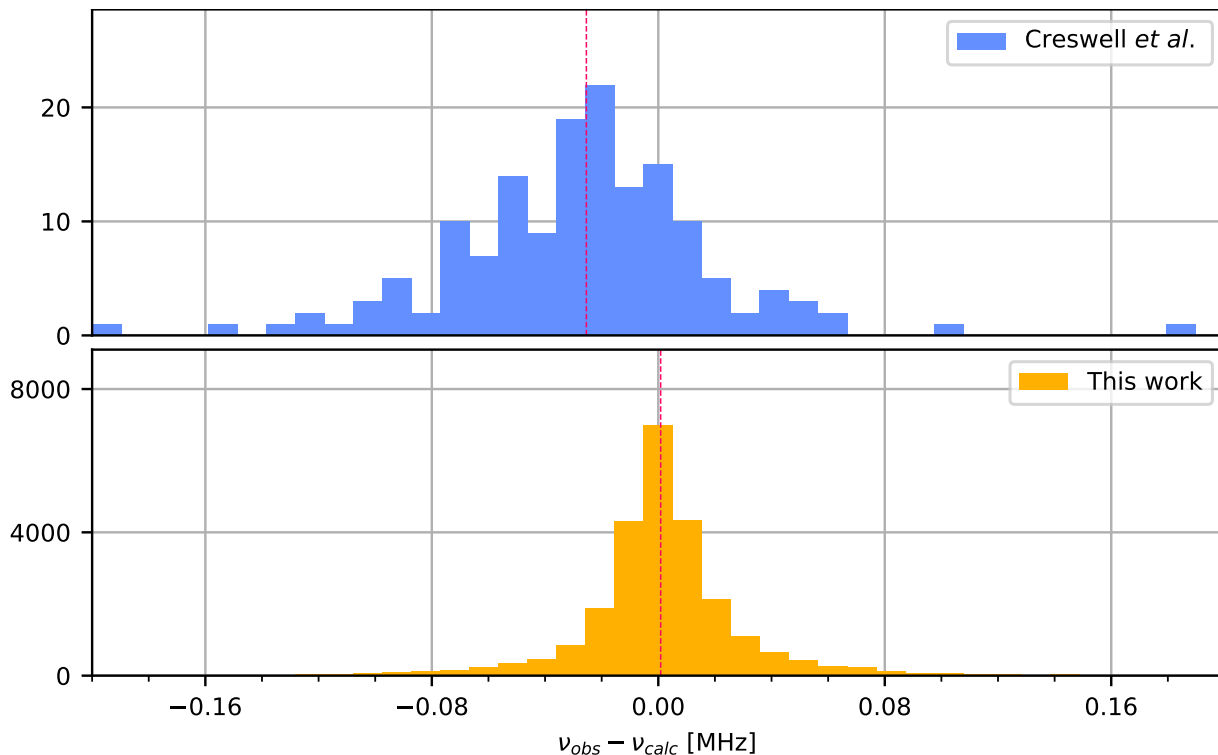


Figure S2: Histograms of the residuals for the assignments from Creswell et al.<sup>4</sup> and this work. The vibrationally excited states  $(0, 2, 0, 0)$ ,  $(1, 0, 0, 1)$ ,  $(0, 1, 1, 0)$ , and  $(6, 0, 0, 0)$  are excluded due to their untreated interactions. The histogram for assignments from this work has high symmetry and a mean value of less than 1 kHz (indicated by the red vertical line). In contrast, the assignments by Creswell et al. show a clear shift to the left with a mean value of  $-25$  kHz.

### 3 Influence of Interactions on Transitions

The influence of the interactions on the specified transitions is shown. Interacting energy levels can be identified by mirror-like patterns. This allows to determine the dominant  $\Delta K_a$  values of the interaction.

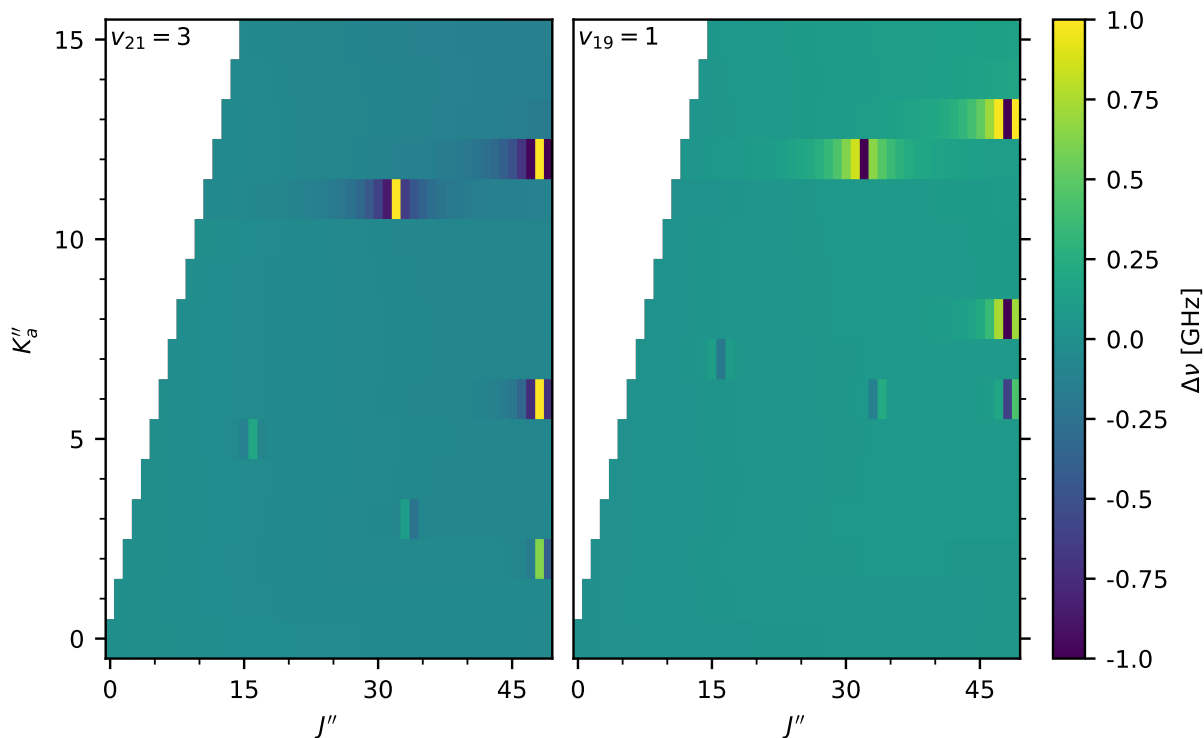


Figure S3: Shifts in transition frequency between predictions with and without interactions for transitions with  $\Delta J_{\Delta K_a, \Delta K_c} = 1_{0,1}$  and  $J = K_a + K_c$ . The heatmaps of the interacting vibrational states  $v_{21} = 3$  (right) and  $v_{19} = 1$  (left) show mirror image patterns with different  $\Delta K_a$  values. There are strong  $\Delta K_a = 1$  interactions between  $K_a = 11$  and  $K_a = 12$  as well as  $K_a = 12$  and  $K_a = 13$ . For lower  $K_a$  values, interactions up to  $\Delta K_a = 4$  are visible.  $\Delta K_a = 0$  interactions are more prominent in similar plots for  $b$ - and  $c$ -type transitions.

## 4 Parameter Progression $v_{21} = n$

The parameter progression for the  $v_{21} = n$  vibrational levels is shown for the quartic rotational parameters. The clear deviations of the  $v_{21} = 4$  parameters indicate a highly effective fit for this vibrational state.

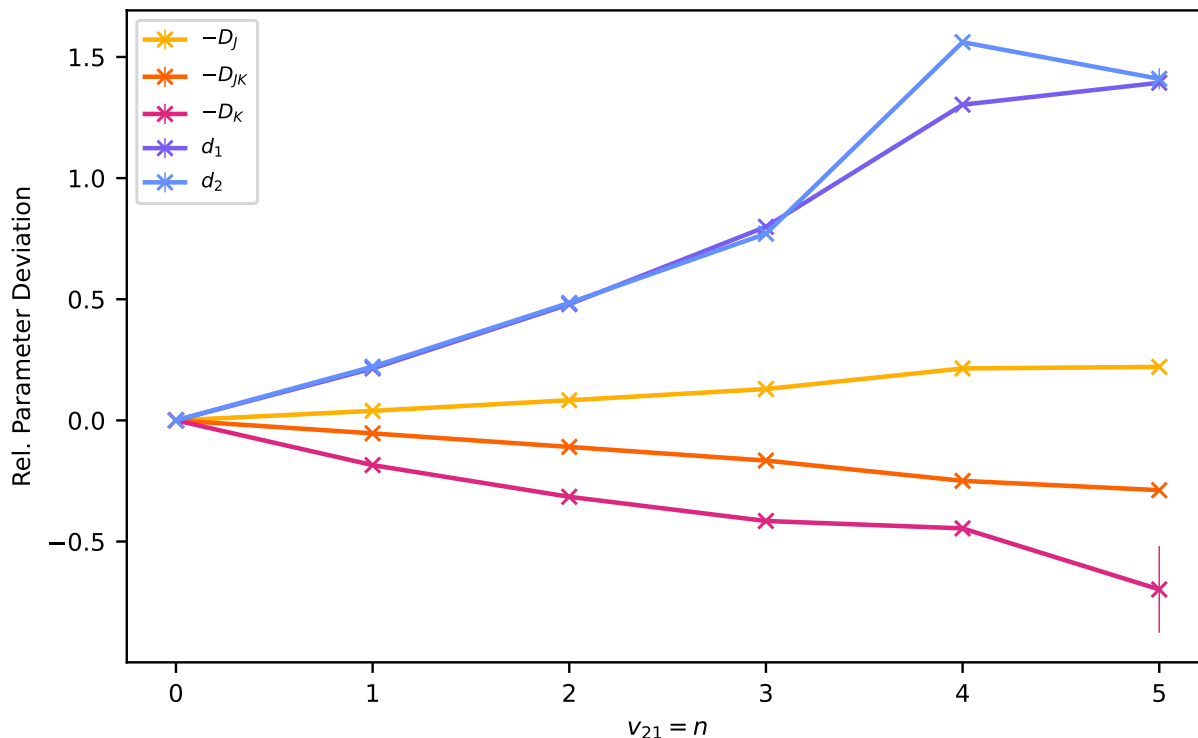


Figure S4: Parameter progression for the  $v_{21} = n$  vibrational states. Vertical lines indicate the associated uncertainties (which are extremely small except for some  $D_K$  values). Up to  $n = 3$ , all parameters progress smoothly but there are clear deviations for  $n = 4$ , especially in  $d_1$  and  $d_2$ . This indicates that the  $n = 4$  parameters are effective parameters. For  $v_{21} = 5$  the parameter  $D_K$  is poorly determined due to the limited quantum number coverage.  $v_{21} = 6$  is excluded as its analysis is significantly worse due to untreated interactions.

## 5 Additional figure from the ReMoCA survey

Figure S5 shows transitions of  $c\text{-C}_2\text{H}_4\text{O}$   $v = 0$  that are covered by the ReMoCA survey and significantly contribute to the signal detected toward Sgr B2(N2b). Transitions that are too heavily blended with much stronger emission from other molecules and therefore cannot contribute to the identification of  $c\text{-C}_2\text{H}_4\text{O}$  are not shown in this figure.

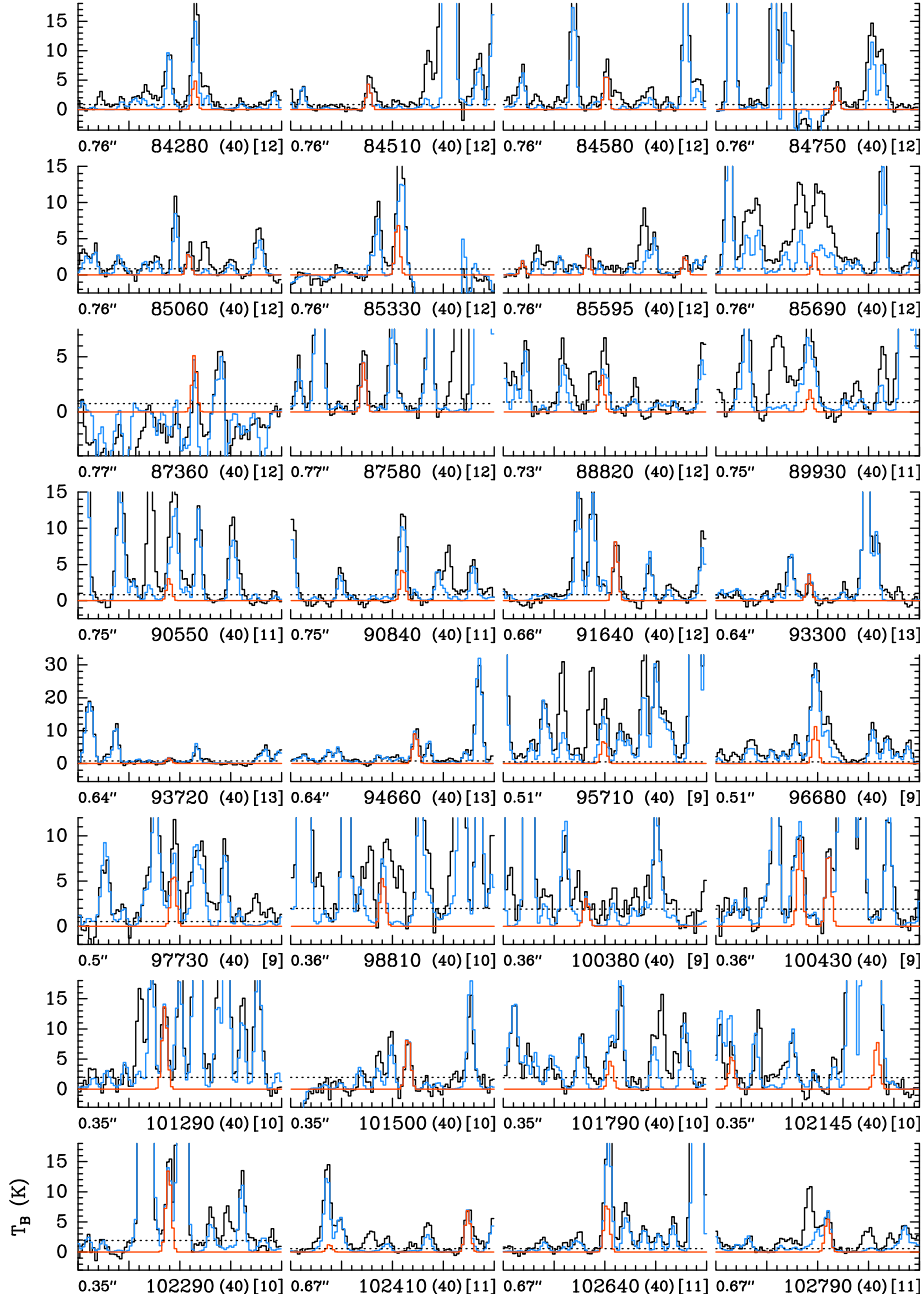


Figure S5: Selection of rotational transitions of oxirane  $c\text{-C}_2\text{H}_4\text{O}$  in its ground vibrational state covered by the ReMoCA survey. The LTE synthetic spectrum of  $c\text{-C}_2\text{H}_4\text{O}$ ,  $v = 0$  is displayed in red and overlaid on the observed spectrum of Sgr B2(N2b) shown in black. The blue synthetic spectrum contains the contributions of all molecules identified in our survey so far, including the contribution of the species shown in red. The values written below each panel correspond from left to right to the half-power beam width, the central frequency in MHz, the width in MHz of each panel in parentheses, and the continuum level in K of the baseline-subtracted spectra in brackets. The y-axis is labeled in brightness temperature units (K). The dotted line indicates the  $3\sigma$  noise level.

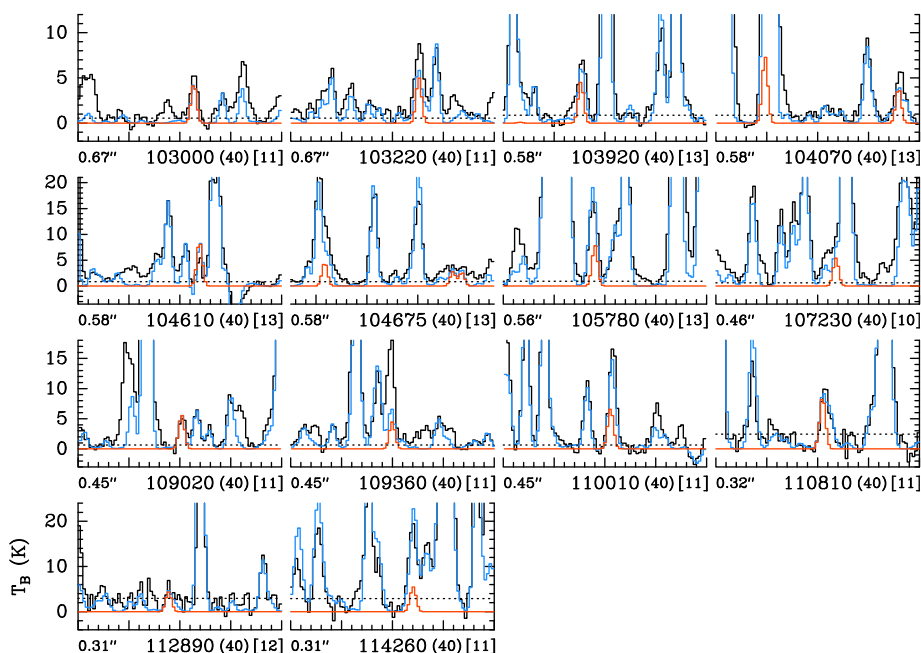


Figure S5: continued.

## References

- (1) Stanton, J. F.; Gauss, J.; Cheng, L.; Harding, M. E.; Matthews, D. A.; Szalay, P. G. CFOUR, Coupled-Cluster techniques for Computational Chemistry, a quantum-chemical program package. With contributions from A. A. Auer, R. J. Bartlett, U. Benedikt, C. Berger, D. E. Bernholdt, Y. J. Bomble, O. Christiansen, F. Engel, R. Faber, M. Heckert, O. Heun, M. Hilgenberg, C. Huber, T.-C. Jagau, D. Jonsson, J. Jusélius, T. Kirsch, K. Klein, W. J. Lauderdale, F. Lipparini, T. Metzroth, L. A. Mück, D. P. O'Neill, D. R. Price, E. Prochnow, C. Puzzarini, K. Ruud, F. Schiffmann, W. Schwalbach, C. Simmons, S. Stopkowicz, A. Tajti, J. Vázquez, F. Wang, J. D. Watts and the integral packages MOLECULE (J. Almlöf and P. R. Taylor), PROPS (P. R. Taylor), ABACUS (T. Helgaker, H. J. Aa. Jensen, P. Jørgensen, and J. Olsen), and ECP routines by A. V. Mitin and C. van Wüllen. For the current version, see <http://www.cfour.de>.
- (2) Matthews, D. A.; Cheng, L.; Harding, M. E.; Lipparini, F.; Stopkowicz, S.; Jagau, T.-C.; Szalay, P. G.; Gauss, J.; Stanton, J. F. Coupled-cluster techniques for computational chemistry: The CFOUR program package. *J. Chem. Phys.* **2020**, *152*, 214108.
- (3) Harding, M. E.; Metzroth, T.; Gauss, J.; Auer, A. A. Parallel calculation of CCSD and CCSD(T) analytic first and second derivatives. *J. Chem. Theory Comput.* **2008**, *4*, 64–74.
- (4) Creswell, R. A.; Manor, P. J.; Assink, R. A.; Schwendeman, R. H. Microwave spectrum, torsional excitation energy, partial structure, and dipole moment of oxiranecarboxaldehyde. *J. Mol. Spectrosc.* **1977**, *64*, 365–375.

# References

- [1] I. R. Medvedev, F. C. De Lucia, An Experimental Approach to the Prediction of Complete Millimeter and Submillimeter Spectra at Astrophysical Temperatures: Applications to Confusion-limited Astrophysical Observations, *Astrophys. J.* 656 (2007) 621–628. doi:10.1086/510379.
- [2] S. M. Fortman, I. R. Medvedev, C. F. Neese, F. C. De Lucia, A new approach to astrophysical spectra: The complete experimental spectrum of ethyl cyanide ( $\text{CH}_3\text{CH}_2\text{CN}$ ) between 570 and 645 GHz, *Astrophys. J.* 714 (2010) 476–486. doi:10.1088/0004-637x/714/1/476.
- [3] W. Ritz, On a New Law of Series Spectra, *Astrophys. J.* 28 (1908) 237. doi:10.1086/141591.
- [4] O. Asvany, K. M. T. Yamada, S. Brünken, A. Potapov, S. Schlemmer, Experimental ground-state combination differences of  $\text{CH}_5^+$ , *Science* 347 (2015) 1346–1349. doi:10.1126/science.aaa3304.
- [5] S. Brackertz, S. Schlemmer, O. Asvany, Searching for new symmetry species of  $\text{CH}_5^+$  – From lines to states without a model, *J. Mol. Spectrosc.* 342 (2017) 73–82. doi:10.1016/j.jms.2017.08.008.
- [6] O. Zingsheim, L. Bonah, F. Lewen, S. Thorwirth, H. S. P. Müller, S. Schlemmer, Millimeter-millimeter-wave double-modulation double-resonance spectroscopy, *J. Mol. Spectrosc.* 381 (2021) 111519. doi:10.1016/j.jms.2021.111519.
- [7] T. Dunham, Jr., Interstellar Neutral Potassium and Neutral Calcium, *Publ. Astron. Soc. Pac.* 49 (1937) 26. doi:10.1086/124759.
- [8] W. S. Adams, Some Results with the COUDÉ Spectrograph of the Mount Wilson Observatory, *Astrophys. J.* 93 (1941) 11. doi:10.1086/144237.
- [9] A. E. Douglas, G. Herzberg,  $\text{CH}^+$  in Interstellar Space and in the Laboratory, *Astrophys. J.* 94 (1941) 381. doi:10.1086/144342.
- [10] B. A. McGuire, 2021 Census of Interstellar, Circumstellar, Extragalactic, Protoplanetary Disk, and Exoplanetary Molecules, *Astrophys. J. Suppl. Ser.* 259 (2022) 30. doi:10.3847/1538-4365/ac2a48.
- [11] C. P. Endres, S. Schlemmer, P. Schilke, J. Stutzki, H. S. P. Müller, The Cologne Database for Molecular Spectroscopy, CDMS, in the Virtual Atomic and Molecular Data Centre, VAMDC, *J. Mol. Spectrosc.* 327 (2016) 95–104. doi:10.1016/j.jms.2016.03.005.

- 
- [12] H. S. P. Müller, S. Thorwirth, D. A. Roth, G. Winnewisser, The Cologne Database for Molecular Spectroscopy, CDMS, *Astron. Astrophys.* 370 (2001) L49–L52. doi:10.1051/0004-6361:20010367.
- [13] F. Tercero, J. A. López-Pérez, J. D. Gallego, F. Beltrán, O. García, M. Patino-Esteban, I. López-Fernández, G. Gómez-Molina, M. Diez, P. García-Carreño, I. Malo, R. Amils, J. M. Serna, C. Albo, J. M. Hernández, B. Vaquero, J. González-García, L. Barbas, J. A. López-Fernández, V. Bujarrabal, M. Gómez-Garrido, J. R. Pardo, M. Santander-García, B. Tercero, J. Cernicharo, P. de Vicente, Yebes 40 m radio telescope and the broad band Nanocosmos receivers at 7 mm and 3 mm for line surveys, *Astron. Astrophys.* 645 (2021) A37. doi:10.1051/0004-6361/202038701.
- [14] S. M. Fortman, I. R. Medvedev, C. F. Neese, F. C. De Lucia, How complete are astrophysical catalogs for the millimeter and submillimeter spectral region?, *Astrophys. J.* 725 (2010) L11–L14. doi:10.1088/2041-8205/725/1/L11.
- [15] E. Herbst, E. F. van Dishoeck, Complex Organic Interstellar Molecules, *Annu. Rev. Astron. Astrophys.* 47 (2009) 427–480. doi:10.1146/annurev-astro-082708-101654.
- [16] O. Fehér, L. V. Tóth, D. Ward-Thompson, J. Kirk, A. Kraus, V.-M. Pelkonen, S. Pintér, S. Zahorecz, Structure and stability in TMC-1: Analysis of NH<sub>3</sub> molecular line and Herschel continuum data, *Astron. Astrophys.* 590 (2016) A75. doi:10.1051/0004-6361/201424385. URL <http://dx.doi.org/10.1051/0004-6361/201424385>
- [17] E. Herbst, Chemistry of Star-Forming Regions, *J. Phys. Chem. A* 109 (18) (2005) 4017–4029. doi:10.1021/jp050461c. URL <http://dx.doi.org/10.1021/jp050461c>
- [18] K. M. Chick, P. Cassen, Thermal Processing of Interstellar Dust Grains in the Primitive Solar Environment, *Astrophys. J.* 477 (1) (1997) 398–409. doi:10.1086/303700. URL <http://dx.doi.org/10.1086/303700>
- [19] G. Wenzel, I. R. Cooke, P. B. Changala, E. A. Bergin, S. Zhang, A. M. Burkhardt, A. N. Byrne, S. B. Charnley, M. A. Cordiner, M. Duffy, Z. T. P. Fried, H. Gupta, M. S. Holdren, A. Lipnicky, R. A. Loomis, H. T. Shay, C. N. Shingledecker, M. A. Siebert, D. A. Stewart, R. H. J. Willis, C. Xue, A. J. Remijan, A. E. Wendlandt, M. C. McCarthy, B. A. McGuire, Detection of interstellar 1-cyanopyrene: A four-ring polycyclic aromatic hydrocarbon, *Science* 386 (2024) 810–813. doi:10.1126/science.adq6391.
- [20] G. Wenzel, T. H. Speak, P. B. Changala, R. H. J. Willis, A. M. Burkhardt, S. Zhang, E. A. Bergin, A. N. Byrne, S. B. Charnley, Z. T. P. Fried, H. Gupta, E. Herbst, M. S. Holdren, A. Lipnicky, R. A. Loomis, C. N. Shingledecker, C. Xue, A. J. Remijan, A. E. Wendlandt, M. C. McCarthy, I. R. Cooke, B. A. McGuire, Detections of interstellar aromatic nitriles 2-cyanopyrene and 4-cyanopyrene in TMC-1, *Nat. Astron.* (2024). doi:10.1038/s41550-024-02410-9.
-

- 
- [21] J. Cernicharo, C. Cabezas, R. Fuentetaja, M. Agúndez, B. Tercero, J. Janeiro, M. Juanes, R. I. Kaiser, Y. Endo, A. L. Steber, D. Pérez, C. Pérez, A. Lesarri, N. Marcelino, P. de Vicente, Discovery of two cyano derivatives of acenaphthylene ( $C_{12}H_8$ ) in TMC-1 with the QUIJOTE line survey, *Astron. Astrophys.* 690 (2024) L13. doi:10.1051/0004-6361/202452196.
- [22] D. Loru, C. Cabezas, J. Cernicharo, M. Schnell, A. L. Steber, Detection of ethynylbenzene in TMC-1 and the interstellar search for 1,2-diethynylbenzene, *Astron. Astrophys.* 677 (2023) A166. doi:10.1051/0004-6361/202347023.
- [23] M. L. Sita, P. B. Changala, C. Xue, A. M. Burkhardt, C. N. Shingledecker, K. L. Kelvin Lee, R. A. Loomis, E. Momjian, M. A. Siebert, D. Gupta, E. Herbst, A. J. Remijan, M. C. McCarthy, I. R. Cooke, B. A. McGuire, Discovery of Interstellar 2-Cyanoindene ( $2-C_9H_7CN$ ) in GOTHAM Observations of TMC-1, *Astrophys. J. Lett.* 938 (2022) L12. doi:10.3847/2041-8213/ac92f4.
- [24] J. Cernicharo, R. Fuentetaja, M. Agúndez, R. I. Kaiser, C. Cabezas, N. Marcelino, B. Tercero, J. R. Pardo, P. de Vicente, Discovery of fulvenallene in TMC-1 with the QUIJOTE line survey, *Astron. Astrophys.* 663 (2022) L9. doi:10.1051/0004-6361/202244399.
- [25] J. Cernicharo, M. Agúndez, R. I. Kaiser, C. Cabezas, B. Tercero, N. Marcelino, J. R. Pardo, P. de Vicente, Discovery of two isomers of ethynyl cyclopentadiene in TMC-1: Abundances of CCH and CN derivatives of hydrocarbon cycles, *Astron. Astrophys.* 655 (2021) L1. doi:10.1051/0004-6361/202142226.
- [26] J. Cernicharo, M. Agúndez, C. Cabezas, B. Tercero, N. Marcelino, J. R. Pardo, P. de Vicente, Pure hydrocarbon cycles in TMC-1: Discovery of ethynyl cyclopropenylidene, cyclopentadiene, and indene, *Astron. Astrophys.* 649 (2021) L15. doi:10.1051/0004-6361/202141156.
- [27] A. M. Burkhardt, K. Long Kelvin Lee, P. Bryan Changala, C. N. Shingledecker, I. R. Cooke, R. A. Loomis, H. Wei, S. B. Charnley, E. Herbst, M. C. McCarthy, B. A. McGuire, Discovery of the Pure Polycyclic Aromatic Hydrocarbon Indene ( $c-C_9H_8$ ) with GOTHAM Observations of TMC-1, *Astrophys. J. Lett.* 913 (2021) L18. doi:10.3847/2041-8213/abfd3a.
- [28] B. A. McGuire, R. A. Loomis, A. M. Burkhardt, K. L. K. Lee, C. N. Shingledecker, S. B. Charnley, I. R. Cooke, M. A. Cordiner, E. Herbst, S. Kalenskii, M. A. Siebert, E. R. Willis, C. Xue, A. J. Remijan, M. C. McCarthy, Detection of two interstellar polycyclic aromatic hydrocarbons via spectral matched filtering, *Science* 371 (2021) 1265–1269. doi:10.1126/science.abb7535.
- [29] B. A. McGuire, A. M. Burkhardt, S. Kalenskii, C. N. Shingledecker, A. J. Remijan, E. Herbst, M. C. McCarthy, Detection of the aromatic molecule benzonitrile ( $c-C_6H_5CN$ ) in the interstellar medium, *Science* 359 (2018) 202–205. doi:10.1126/science.aao4890.
-

- 
- [30] R. A. Loomis, A. M. Burkhardt, C. N. Shingledecker, S. B. Charnley, M. A. Cordiner, E. Herbst, S. Kalenskii, K. L. K. Lee, E. R. Willis, C. Xue, A. J. Remijan, M. C. McCarthy, B. A. McGuire, An investigation of spectral line stacking techniques and application to the detection of HC<sub>11</sub>N, *Nat. Astron.* 5 (2021) 188–196. doi:10.1038/s41550-020-01261-4.
- [31] Z. T. P. Fried, S. J. El-Abd, B. M. Hays, G. Wenzel, A. N. Byrne, L. Margulès, R. A. Motiyenko, S. T. Shipman, M. P. Horne, J. K. Jørgensen, C. L. Brogan, T. R. Hunter, A. J. Remijan, A. Lipnicky, R. A. Loomis, B. A. McGuire, Rotational Spectrum and First Interstellar Detection of 2-methoxyethanol Using ALMA Observations of NGC 6334I, *Astrophys. J. Lett.* 965 (2024) L23. doi:10.3847/2041-8213/ad37ff.
- [32] J. Cami, J. Bernard-Salas, E. Peeters, S. E. Malek, Detection of C<sub>60</sub> and C<sub>70</sub> in a Young Planetary Nebula, *Science* 329 (2010) 1180–1182. doi:10.1126/science.1192035.
- [33] B. H. Foing, P. Ehrenfreund, Detection of two interstellar absorption bands coincident with spectral features of C<sub>60</sub><sup>+</sup>, *Nature* 369 (1994) 296–298. doi:10.1038/369296a0.
- [34] G. A. H. Walker, D. A. Bohlender, J. P. Maier, E. K. Campbell, Identification of more interstellar C<sub>60</sub><sup>+</sup> bands, *Astrophys. J.* 812 (2015) L8. doi:10.1088/2041-8205/812/1/18.
- [35] S. Iglesias-Groth, M. Esposito, A search for near infrared bands of the fullerene cation C<sub>60</sub><sup>+</sup> in the protoplanetary nebula IRAS 01005+7910, *Astrophys. J.* 776 (2013) L2. doi:10.1088/2041-8205/776/1/12.
- [36] O. Berné, G. Mulas, C. Joblin, Interstellar C<sub>60</sub><sup>+</sup>, *Astron. Astrophys.* 550 (2013) L4. doi:10.1051/0004-6361/201220730.
- [37] M. T. Murphy, V. V. Flambaum, S. Muller, C. Henkel, Strong Limit on a Variable Proton-to-Electron Mass Ratio from Molecules in the Distant Universe, *Science* 320 (2008) 1611–1613. doi:10.1126/science.1156352.
- [38] A. Owens, S. N. Yurchenko, W. Thiel, V. Špirko, Enhanced sensitivity to a possible variation of the proton-to-electron mass ratio in ammonia, *Phys. Rev. A* 93 (2016). doi:10.1103/physreva.93.052506.
- [39] V. V. Ilyushin, Sensitivity to a possible variation of the proton-to-electron mass ratio of torsion–rotation transitions in acetone (CH<sub>3</sub>)<sub>2</sub>CO, *J. Mol. Spectrosc.* 300 (2014) 86–93. doi:10.1016/j.jms.2014.03.004.
- [40] M. D. Hanwell, D. E. Curtis, D. C. Lonie, T. Vandermeersch, E. Zurek, G. R. Hutchison, Avogadro: An advanced semantic chemical editor, visualization, and analysis platform, *J. Cheminform.* 4 (2012). doi:10.1186/1758-2946-4-17.
- [41] POV-Ray Community, Persistence of Vision Raytracer, Persistence of Vision Pty. Ltd. (2004), Persistence of Vision Pty. Ltd., Williamstown, Victoria, Australia.  
URL <http://www.povray.org>
-

- [42] M. H. Ordu, O. Zingsheim, A. Belloche, F. Lewen, R. T. Garrod, K. M. Menten, S. Schlemmer, H. S. P. Müller, Laboratory rotational spectroscopy of isotopic acetone,  $\text{CH}_3^{13}\text{C}(\text{O})\text{CH}_3$  and  $^{13}\text{CH}_3\text{C}(\text{O})\text{CH}_3$ , and astronomical search in Sagittarius B2(N2), *Astron. Astrophys.* 629 (2019) A72. doi:10.1051/0004-6361/201935887.
- [43] D. R. Johnson, F. J. Lovas, C. A. Gottlieb, E. W. Gottlieb, M. M. Litvak, P. Thaddeus, M. Guelin, Detection of interstellar ethyl cyanide, *Astrophys. J.* 218 (1977) 370. doi:10.1086/155691.
- [44] S. Cazaux, A. G. G. M. Tielens, C. Ceccarelli, A. Castets, V. Wakelam, E. Caux, B. Parise, D. Teyssier, The Hot Core around the Low-Mass Protostar IRAS 16293-2422: Scoundrels Rule!, *Astrophys. J.* 593 (2003) L51–L55. doi:10.1086/378038.
- [45] J. E. Dickens, W. M. Irvine, M. Ohishi, M. Ikeda, S. Ishikawa, A. Nummelin, A. Hjalmarsen, Detection of Interstellar Ethylene Oxide ( $c\text{-C}_2\text{H}_4\text{O}$ ), *Astrophys. J.* 489 (1997) 753–757. doi:10.1086/304821.
- [46] A. Nummelin, J. E. Dickens, P. Bergman, A. Hjalmarsen, W. M. Irvine, M. Ikeda, M. Ohishi, Abundances of ethylene oxide and acetaldehyde in hot molecular cloud cores, *Astron. Astrophys.* 337 (1998) 275–286.
- [47] M. A. Requena-Torres, J. Martin-Pintado, S. Martin, M. R. Morris, The Galactic Center: The Largest Oxygen-bearing Organic Molecule Repository, *Astrophys. J.* 672 (2008) 352–360. doi:10.1086/523627.
- [48] J. M. Lykke, A. Coutens, J. K. Jørgensen, M. H. D. van der Wiel, R. T. Garrod, H. S. P. Müller, P. Bjerkeli, T. L. Bourke, H. Calcutt, M. N. Drozdovskaya, C. Favre, E. C. Fayolle, S. K. Jacobsen, K. I. Öberg, M. V. Persson, E. F. van Dishoeck, S. F. Wampfler, The ALMA-PILS survey: First detections of ethylene oxide, acetone and propanal toward the low-mass protostar IRAS 16293-2422, *Astron. Astrophys.* 597 (2016) A53. doi:10.1051/0004-6361/201629180.
- [49] A. Bacmann, A. Faure, J. Berteaud, Cold and Yet Complex: Detection of Ethylene Oxide in a Prestellar Core, *ACS Earth Space Chem.* 3 (2019) 1000–1013. doi:10.1021/acsearthspacechem.9b00072.
- [50] S. M. Fortman, J. P. McMillan, C. F. Neese, S. K. Randall, A. J. Remijan, T. L. Wilson, F. C. De Lucia, An analysis of a preliminary ALMA Orion KL spectrum via the use of complete experimental spectra from the laboratory, *J. Mol. Spectrosc.* 280 (2012) 11–20. doi:10.1016/j.jms.2012.08.002.
- [51] F. C. De Lucia, S. M. Fortman, I. R. Medvedev, C. F. Neese, How Can We Use Complete Experimental Catalogs in the Complex Spectra Limit?, *Proc. Int. Astron. Union.* 7 (2011) 431–439. doi:10.1017/s1743921311025178.
- [52] W. Gordy, R. L. Cook, Microwave molecular spectra, Wiley, New York, NY, 1984.

- [53] D. Kivelson, E. B. Wilson, Approximate Treatment of the Effect of Centrifugal Distortion on the Rotational Energy Levels of Asymmetric-Rotor Molecules, *J. Chem. Phys.* 20 (1952) 1575–1579. doi:10.1063/1.1700219.
- [54] J. K. G. Watson, Centrifugal Corrections for Asymmetric-Top Molecules, *J. Chem. Phys.* 45 (1966) 1360–1361. doi:10.1063/1.1727763.
- [55] J. K. G. Watson, Determination of Centrifugal Distortion Coefficients of Asymmetric-Top Molecules, *J. Chem. Phys.* 46 (1967) 1935–1949. doi:10.1063/1.1840957.
- [56] G. Winnewisser, Millimeter Wave Rotational Spectrum of HSSH and DSSD. II. Anomalous  $K$  Doubling Caused by Centrifugal Distortion in DSSD, *J. Chem. Phys.* 56 (1972) 2944–2954. doi:10.1063/1.1677629.
- [57] B. P. van Eijck, Reformulation of quartic centrifugal distortion Hamiltonian, *J. Mol. Spectrosc.* 53 (1974) 246–249. doi:10.1016/0022-2852(74)90129-5.
- [58] B. S. Ray, Über die Eigenwerte des asymmetrischen Kreisels, *Z. Phys.* 78 (1932) 74–91. doi:10.1007/bf01342264.
- [59] H. M. Pickett, The fitting and prediction of vibration-rotation spectra with spin interactions, *J. Mol. Spectrosc.* 148 (1991) 371–377. doi:10.1016/0022-2852(91)90393-o.
- [60] H. M. Pickett, R. L. Poynter, E. A. Cohen, M. L. Delitsky, J. C. Pearson, H. S. P. Müller, Submillimeter, millimeter, and microwave spectral line catalog, *J. Quant. Spectrosc. Radiat. Transf.* 60 (1998) 883–890. doi:10.1016/s0022-4073(98)00091-0.
- [61] J. D. Kemp, K. S. Pitzer, Hindered Rotation of the Methyl Groups in Ethane, *J. Chem. Phys.* 4 (1936) 749–749. doi:10.1063/1.1749784.
- [62] J. D. Swalen, J. A. Ibers, Potential Function for the Inversion of Ammonia, *J. Chem. Phys.* 36 (1962) 1914–1918. doi:10.1063/1.1701290.
- [63] J. E. Kilpatrick, K. S. Pitzer, R. Spitzer, The Thermodynamics and Molecular Structure of Cyclopentane, *J. Am. Chem. Soc.* 69 (1947) 2483–2488. doi:10.1021/ja01202a069.
- [64] J. Laane, Far-Infrared Spectra and the Ring-Puckering Potential Function of Silacyclopent-3-ene and Silacyclopent-3-ene-1,1-d<sub>2</sub>, *J. Chem. Phys.* 50 (1969) 776–782. doi:10.1063/1.1671129.
- [65] J. Laane, Far-Infrared Spectrum and Ring-Puckering Potential of Silacyclopent-2-ene, *J. Chem. Phys.* 52 (1970) 358–360. doi:10.1063/1.1672691.
- [66] D. Cremer, J. A. Pople, General definition of ring puckering coordinates, *J. Am. Chem. Soc.* 97 (1975) 1354–1358. doi:10.1021/ja00839a011.
- [67] W. J. Orville-Thomas, M. Redshaw, *Internal Rotation in Molecules*, Wiley, 1974.

- 
- [68] C. C. Lin, J. D. Swalen, Internal Rotation and Microwave Spectroscopy, *Rev. Mod. Phys.* 31 (1959) 841–892. doi:10.1103/revmodphys.31.841.
- [69] I. Kleiner, Asymmetric-top molecules containing one methyl-like internal rotor: Methods and codes for fitting and predicting spectra, *J. Mol. Spectrosc.* 260 (2010) 1–18. doi:10.1016/j.jms.2009.12.011.
- [70] D. R. Herschbach, Calculation of Energy Levels for Internal Torsion and Over-All Rotation. III, *J. Chem. Phys.* 31 (1959) 91–108. doi:10.1063/1.1730343.
- [71] R. W. Kilb, C. C. Lin, E. B. Wilson, Calculation of Energy Levels for Internal Torsion and Over-All Rotation. II. CH<sub>3</sub>CHO Type Molecules; Acetaldehyde Spectra, *J. Chem. Phys.* 26 (1957) 1695–1703. doi:10.1063/1.1743607.
- [72] E. B. Wilson, C. C. Lin, D. R. Lide, Calculation of Energy Levels for Internal Torsion and Over-All Rotation. I. CH<sub>3</sub>BF<sub>2</sub> Type Molecules, *J. Chem. Phys.* 23 (1955) 136–142. doi:10.1063/1.1740512.
- [73] I. Kleiner, Spectroscopy of Interstellar Internal Rotors: An Important Tool for Investigating Interstellar Chemistry, *ACS Earth Space Chem.* 3 (2019) 1812–1842. doi:10.1021/acsearthspacechem.9b00079.
- [74] D. R. Herschbach, J. D. Swalen, Internal Barrier of Propylene Oxide from the Microwave Spectrum. II, *J. Chem. Phys.* 29 (1958) 761–776. doi:10.1063/1.1744588.
- [75] L. Pierce, Microwave Spectrum, Internal Barrier, Structure, Equilibrium Configuration, and Dipole Moment of Methyl Monofluorosilane, *J. Chem. Phys.* 29 (1958) 383–388. doi:10.1063/1.1744489.
- [76] L. Pierce, J. M. O’Reilly, Microwave spectrum, dipole moment, and internal barrier of 2-fluoropropene, *J. Mol. Spectrosc.* 3 (1959) 536–547. doi:10.1016/0022-2852(59)90046-3.
- [77] W. G. Fateley, F. A. Miller, Torsional frequencies in the far infrared – III: The form of the potential curve for hindered internal rotation of a methyl group, *Spectrochim. Acta* 19 (1963) 611–628. doi:10.1016/0371-1951(63)80125-3.
- [78] H. Dreizler, Rotational Spectra of Molecules with Two Internal Degrees of Freedom, in: K. N. Rao, C. W. Mathews (Eds.), *Molecular Spectroscopy: Modern Research*, Academic Press, 1972, Ch. 2.4, p. 59–72.
- [79] W. A. Majewski, J. F. Pfanstiel, D. F. Plusquellic, D. W. Pratt, *High resolution optical spectroscopy in the ultraviolet*, Wiley, 1995.
- [80] D. F. Plusquellic, R. D. Suenram, B. Maté, J. O. Jensen, A. C. Samuels, The conformational structures and dipole moments of ethyl sulfide in the gas phase, *J. Chem. Phys.* 115 (2001) 3057–3067. doi:10.1063/1.1385527.
-

- 
- [81] H. M. Pickett, Theoretical studies of internal rotation for an asymmetric top, *J. Chem. Phys.* 107 (1997) 6732–6735. doi:10.1063/1.474916.
- [82] H. Hartwig, H. Dreizler, The Microwave Spectrum of trans-2,3-Dimethyloxirane in Torsional Excited States, *Z. Naturforsch. Teil A* 51 (1996) 923–932. doi:10.1515/zna-1996-0807.
- [83] J. T. Hougen, I. Kleiner, M. Godefroid, Selection Rules and Intensity Calculations for a  $C_s$  Asymmetric Top Molecule Containing a Methyl Group Internal Rotor, *J. Mol. Spectrosc.* 163 (1994) 559–586. doi:10.1006/jmsp.1994.1047.
- [84] I. Kleiner, J. T. Hougen, Rho-axis-method Hamiltonian for molecules having one methyl rotor and  $C_1$  point-group symmetry at equilibrium, *J. Chem. Phys.* 119 (2003) 5505–5509. doi:10.1063/1.1599354.
- [85] V. V. Ilyushin, Z. Kisiel, L. Pszczólkowski, H. Mäder, J. T. Hougen, A new torsion–rotation fitting program for molecules with a sixfold barrier: Application to the microwave spectrum of toluene, *J. Mol. Spectrosc.* 259 (2010) 26–38. doi:10.1016/j.jms.2009.10.005.
- [86] V. Ilyushin, Millimeter wave spectrum of nitromethane, *J. Mol. Spectrosc.* 345 (2018) 64–69. doi:10.1016/j.jms.2017.12.005.
- [87] A. Belloche, A. A. Meshcheryakov, R. T. Garrod, V. V. Ilyushin, E. A. Alekseev, R. A. Motiyenko, L. Margulès, H. S. P. Müller, K. M. Menten, Rotational spectroscopy, tentative interstellar detection, and chemical modeling of N-methylformamide, *Astron. Astrophys.* 601 (2017) A49. doi:10.1051/0004-6361/201629724.
- [88] P. Groner, Effective rotational Hamiltonian for molecules with two periodic large-amplitude motions, *J. Chem. Phys.* 107 (1997) 4483–4498. doi:10.1063/1.474810.
- [89] P. Groner, Effective rotational Hamiltonian for molecules with internal rotors: Principles, theory, applications and experiences, *J. Mol. Spectrosc.* 278 (2012) 52–67. doi:10.1016/j.jms.2012.06.006.
- [90] J. H. Westerfield, S. E. Worthington-Kirsch, westerfit: A new program for spin–torsion–rotation spectra, *J. Mol. Spectrosc.* 404 (2024) 111928. doi:10.1016/j.jms.2024.111928.
- [91] H. Dreizler, H. D. Rudolph, Torsionsfeinstruktur im Rotationsspektrum des Dimethylsulfids und internes Hinderungspotential, *Z. Naturforsch. Teil A* 17 (1962) 712–732. doi:10.1515/zna-1962-0902.
- [92] J. D. Swalen, C. C. Costain, Internal Rotation in Molecules with Two Internal Rotors: Microwave Spectrum of Acetone, *J. Chem. Phys.* 31 (1959) 1562–1574. doi:10.1063/1.1730653.
- [93] R. J. Myers, E. B. Wilson, Application of Symmetry Principles to the Rotation-Internal Torsion Levels of Molecules with Two Equivalent Methyl Groups, *J. Chem. Phys.* 33 (1960) 186–191. doi:10.1063/1.1731075.
-

- 
- [94] L. Pierce, Internal Rotation in Double Internal Rotor Molecules: The Microwave Spectrum of Dimethyl Silane, *J. Chem. Phys.* 31 (1959) 547–548. doi:10.1063/1.1730396.
- [95] L. Pierce, Energy Levels for Internal and Over-All Rotation of Two-Top Molecules. I. Microwave Spectrum of Dimethyl Silane, *J. Chem. Phys.* 34 (1961) 498–506. doi:10.1063/1.1700973.
- [96] H. Rudolph, H. Dreizler, W. Maier, Mikrowellenspektrum, Struktur und Hinderungspotential des Dimethylsulfids, *Z. Naturforsch. Teil A* 15 (1960) 742.
- [97] H. V. L. Nguyen, W. Stahl, The microwave spectrum of isopropenyl acetate – An asymmetric molecule with two internal rotors, *J. Mol. Spectrosc.* 264 (2010) 120–124. doi:10.1016/j.jms.2010.10.002.
- [98] P. Groner, M. Winnewisser, I. R. Medvedev, F. C. De Lucia, E. Herbst, K. V. L. N. Sastry, The Millimeter- and Submillimeter-Wave Spectrum of Methyl Carbamate [CH<sub>3</sub>OC(:O)NH<sub>2</sub>], *Astrophys. J. Suppl. Ser.* 169 (2007) 28–36. doi:10.1086/511133.
- [99] A. Maeda, F. C. De Lucia, E. Herbst, Submillimeter-wave spectra of H<sub>12</sub>COOCH<sub>3</sub> and H<sub>13</sub>COOCH<sub>3</sub> in excited CH<sub>3</sub> torsional states, *J. Mol. Spectrosc.* 251 (2008) 293–300. doi:10.1016/j.jms.2008.03.014.
- [100] A. Maeda, I. R. Medvedev, F. C. De Lucia, E. Herbst, P. Groner, The Millimeter- and Submillimeter-Wave Spectrum of <sup>13</sup>C<sub>1</sub>-Methyl Formate (H<sub>13</sub>COOCH<sub>3</sub>) in the Ground State, *Astrophys. J. Suppl. Ser.* 175 (2008) 138–146. doi:10.1086/523303.
- [101] Z. Kisiel, L. Pszczółkowski, E. Białkowska-Jaworska, S. B. Charnley, The millimeter wave rotational spectrum of pyruvic acid, *J. Mol. Spectrosc.* 241 (2007) 220–229. doi:10.1016/j.jms.2006.12.011.
- [102] P. Groner, S. Albert, E. Herbst, F. C. De Lucia, Dimethyl Ether: Laboratory Assignments and Predictions through 600 GHz, *Astrophys. J.* 500 (1998) 1059–1063. doi:10.1086/305757.
- [103] P. Groner, S. Albert, E. Herbst, F. C. De Lucia, F. J. Lovas, B. J. Drouin, J. C. Pearson, Acetone: Laboratory Assignments and Predictions through 620 GHz for the Vibrational-Torsional Ground State, *Astrophys. J. Suppl. Ser.* 142 (2002) 145–151. doi:10.1086/341221.
- [104] U. Fuchs, G. Winnewisser, P. Groner, F. C. De Lucia, E. Herbst, trans-Ethyl Methyl Ether: Assignments and Predictions up to 400 GHz for the Vibrational-Torsional Ground State, *Astrophys. J. Suppl. Ser.* 144 (2003) 277–286. doi:10.1086/345100.
- [105] S. Herbers, O. Zingsheim, H. V. L. Nguyen, L. Bonah, B. Heyne, N. Wehres, S. Schlemmer, Internal rotation arena: Program performances on the low barrier problem of 4-methylacetophenone, *J. Chem. Phys.* 155 (2021) 224302. doi:10.1063/5.0070298.
-

- 
- [106] N. Ohashi, J. T. Hougen, The torsional-wagging tunneling problem and the torsional-wagging-rotational problem in hydrazine, *J. Mol. Spectrosc.* 112 (1985) 384–400. doi:10.1016/0022-2852(85)90170-5.
- [107] L. H. Coudert, J. T. Hougen, Analysis of the microwave and far infrared spectrum of the water dimer, *J. Mol. Spectrosc.* 139 (1990) 259–277. doi:10.1016/0022-2852(90)90064-w.
- [108] M. Oda, N. Ohashi, J. T. Hougen, A group-theoretical formalism for the large-amplitude vibration-rotation problem in methylamine-d<sub>1</sub>, *J. Mol. Spectrosc.* 142 (1990) 57–84. doi:10.1016/0022-2852(90)90292-x.
- [109] K. Kobayashi, T. Matsui, N. Mori, S. Tsunekawa, N. Ohashi, The microwave spectroscopy of trans-ethyl methyl ether in the first skeletal torsionally excited state, *J. Mol. Spectrosc.* 251 (2008) 301–304. doi:10.1016/j.jms.2008.03.007.
- [110] N. Ohashi, J. T. Hougen, The torsional-wagging tunneling problem and the torsional-wagging-rotational problem in methylamine, *J. Mol. Spectrosc.* 121 (1987) 474–501. doi:10.1016/0022-2852(87)90064-6.
- [111] N. Ohashi, S. Tsunekawa, K. Takagi, J. T. Hougen, Microwave spectrum of methyl amine: Assignment and analysis of the first torsional state, *J. Mol. Spectrosc.* 137 (1989) 33–46. doi:10.1016/0022-2852(89)90266-x.
- [112] P. Groner, Large-amplitude motion tunneling parameters in effective rotational Hamiltonians from rotation-internal rotation theory, *J. Mol. Spectrosc.* 156 (1992) 164–189. doi:10.1016/0022-2852(92)90101-s.
- [113] L. Bonah, Rotational Spectroscopy of Ethyl Cyanide – Establishing spectroscopic Linkages using DM-DR Spectroscopy, Master’s thesis, I. Physikalisches Institut, Universität zu Köln (2020).
- [114] M. A. Martin-Drumel, J. van Wijngaarden, O. Zingsheim, F. Lewen, M. E. Harding, S. Schlemmer, S. Thorwirth, Millimeter- and submillimeter-wave spectroscopy of disulfur dioxide, OSSO, *J. Mol. Spectrosc.* 307 (2015) 33–39. doi:10.1016/j.jms.2014.11.007.
- [115] L. Bonah, J.-C. Guillemin, A. Belloche, S. Thorwirth, H. S. P. Müller, S. Schlemmer, Leveraging MMW-MMW Double Resonance Spectroscopy to Understand the Pure Rotational Spectrum of Glycidaldehyde and 17 of its Vibrationally Excited States, *ACS Earth Space Chem.* in press (2025).
- [116] D. A. Matthews, L. Cheng, M. E. Harding, F. Lipparini, S. Stopkowicz, T.-C. Jagau, P. G. Szalay, J. Gauss, J. F. Stanton, Coupled-cluster techniques for computational chemistry: The CFOUR program package, *J. Chem. Phys.* 152 (2020). doi:10.1063/5.0004837.
- [117] M. E. Harding, T. Metzroth, J. Gauss, A. A. Auer, Parallel Calculation of CCSD and CCSD(T) Analytic First and Second Derivatives, *J. Chem. Theory Comput* 4 (2008) 64–74. doi:10.1021/ct700152c.
-

- 
- [118] J. F. Stanton, J. Gauss, L. Cheng, M. E. Harding, D. A. Matthews, P. G. Szalay, CFOUR, Coupled-Cluster techniques for Computational Chemistry, a quantum-chemical program package, With contributions from A. Asthana, A.A. Auer, R.J. Bartlett, U. Benedikt, C. Berger, D.E. Bernholdt, S. Blaschke, Y. J. Bomble, S. Burger, O. Christiansen, D. Datta, F. Engel, R. Faber, J. Greiner, M. Heckert, O. Heun, M. Hilgenberg, C. Huber, T.-C. Jagau, D. Jonsson, J. Jusélius, T. Kirsch, M.-P. Kitsaras, K. Klein, G.M. Kopper, W.J. Lauderdale, F. Lipparini, J. Liu, T. Metzroth, L. Monzel, L.A. Mück, D.P. O’Neill, T. Nottoli, J. Oswald, D.R. Price, E. Prochnow, C. Puzzarini, K. Ruud, F. Schiffmann, W. Schwalbach, C. Simmons, S. Stopkowicz, A. Tajti, T. Uhlřřová, J. Vázquez, F. Wang, J.D. Watts, P. Yergün. C. Zhang, X. Zheng, and the integral packages MOLECULE (J. Almlöf and P.R. Taylor), PROPS (P.R. Taylor), ABACUS (T. Helgaker, H.J. Aa. Jensen, P. Jørgensen, and J. Olsen), and ECP routines by A. V. Mitin and C. van Wüllen. For the current version, see <http://www.cfour.de>.
- [119] K. Raghavachari, G. W. Trucks, J. A. Pople, M. Head-Gordon, A fifth-order perturbation comparison of electron correlation theories, *Chem. Phys. Lett.* 157 (1989) 479–483. doi:10.1016/s0009-2614(89)87395-6.
- [120] J. Almlöf, P. R. Taylor, General contraction of Gaussian basis sets. I. Atomic natural orbitals for first- and second-row atoms, *J. Chem. Phys.* 86 (1987) 4070–4077. doi:10.1063/1.451917.
- [121] T. H. Dunning, Gaussian basis sets for use in correlated molecular calculations. I. The atoms boron through neon and hydrogen, *J. Chem. Phys.* 90 (1989) 1007–1023. doi:10.1063/1.456153.
- [122] K. A. Peterson, T. H. Dunning, Accurate correlation consistent basis sets for molecular core–valence correlation effects: The second row atoms Al–Ar, and the first row atoms B–Ne revisited, *J. Chem. Phys.* 117 (2002) 10548–10560. doi:10.1063/1.1520138.
- [123] T. H. Dunning, K. A. Peterson, A. K. Wilson, Gaussian basis sets for use in correlated molecular calculations. X. The atoms aluminum through argon revisited, *J. Chem. Phys.* 114 (2001) 9244–9253. doi:10.1063/1.1367373.
- [124] J. D. Watts, J. Gauss, R. J. Bartlett, Open-shell analytical energy gradients for triple excitation many-body, coupled-cluster methods: MBPT(4), CCSD+T(CCSD), CCSD(T), and QCISD(T), *Chem. Phys. Lett.* 200 (1992) 1–7. doi:10.1016/0009-2614(92)87036-o.
- [125] J. Gauss, J. F. Stanton, Analytic CCSD(T) second derivatives, *Chem. Phys. Lett.* 276 (1997) 70–77. doi:10.1016/s0009-2614(97)88036-0.
- [126] J. F. Stanton, J. Gauss, Analytic second derivatives in high-order many-body perturbation and coupled-cluster theories: Computational considerations and applications, *Int. Rev. Phys. Chem.* 19 (2000) 61–95. doi:10.1080/014423500229864.
-

- 
- [127] J. F. Stanton, C. L. Lopreore, J. Gauss, The equilibrium structure and fundamental vibrational frequencies of dioxirane, *J. Chem. Phys.* 108 (1998) 7190–7196. doi:10.1063/1.476136.
- [128] I. M. Mills, Vibration-Rotation Structure in Asymmetric- and Symmetric-Top Molecules, in: K. N. Rao, C. W. Mathews (Eds.), *Molecular Spectroscopy: Modern Research*, Academic Press, 1972, Ch. 3.2, pp. 115–140.
- [129] S. Thorwirth, M. E. Harding, O. Asvany, S. Brünken, P. Jusko, K. L. K. Lee, T. Salomon, M. C. McCarthy, S. Schlemmer, Descendant of the X-ogen carrier and a ‘mass of 69’: infrared action spectroscopic detection of  $\text{HC}_3\text{O}^+$  and  $\text{HC}_3\text{S}^+$ , *Mol. Phys.* 118 (2020). doi:10.1080/00268976.2020.1776409.
- [130] M. Bast, J. Böing, E. Plaar, T. Salomon, M. Schäfer, I. Savić, O. Asvany, S. Schlemmer, S. Thorwirth, Spectroscopic detection and characterization of cyanooxomethylum,  $\text{NCCO}^+$ , *in prep.*
- [131] C. Cabezas, Y. Endo, E. Roueff, N. Marcelino, M. Agúndez, B. Tercero, J. Cernicharo, Space and laboratory observation of the deuterated cyanomethyl radical HDCCN, *Astron. Astrophys.* 646 (2021) L1. doi:10.1051/0004-6361/202040210.
- [132] C. Cabezas, M. Agúndez, N. Marcelino, B. Tercero, S. Cuadrado, J. Cernicharo, Interstellar detection of the simplest aminocarbyne  $\text{H}_2\text{NC}$ : an ignored but abundant molecule, *Astron. Astrophys.* 654 (2021) A45. doi:10.1051/0004-6361/202141491.
- [133] N. Marcelino, M. Agúndez, B. Tercero, C. Cabezas, C. Bermúdez, J. D. Gallego, P. deVicente, J. Cernicharo, Tentative detection of  $\text{HC}_5\text{NH}^+$  in TMC-1, *Astron. Astrophys.* 643 (2020) L6. doi:10.1051/0004-6361/202039251.
- [134] C. Cabezas, M. Agúndez, N. Marcelino, B. Tercero, R. Fuentetaja, P. de Vicente, J. Cernicharo, Discovery of a new molecular ion,  $\text{HC}_7\text{NH}^+$ , in TMC-1, *Astron. Astrophys.* 659 (2022) L8. doi:10.1051/0004-6361/202142972.
- [135] J. Cernicharo, M. Agúndez, C. Cabezas, R. Fuentetaja, B. Tercero, N. Marcelino, Y. Endo, J. R. Pardo, P. de Vicente, Discovery of  $\text{C}_5\text{H}^+$  and detection of  $\text{C}_3\text{H}^+$  in TMC-1 with the QUIJOTE line survey, *Astron. Astrophys.* 657 (2022) L16. doi:10.1051/0004-6361/202142992.
- [136] F. W. Loomis, R. W. Wood, The Rotational Structure of the Blue-Green Bands of  $\text{Na}_2$ , *Phys. Rev.* 32 (1928) 223–236. doi:10.1103/physrev.32.223.
- [137] M. A. Martin-Drumel, C. P. Endres, O. Zingsheim, T. Salomon, J. van Wijngaarden, O. Pirali, S. Gruet, F. Lewen, S. Schlemmer, M. C. McCarthy, S. Thorwirth, The SOLEIL view on sulfur rich oxides: The  $\text{S}_2\text{O}$  bending mode  $\nu_2$  at  $380\text{ cm}^{-1}$  and its analysis using an Automated Spectral Assignment Procedure (ASAP), *J. Mol. Spectrosc.* 315 (2015) 72–79. doi:10.1016/j.jms.2015.02.014.
-

- 
- [138] B. J. Drouin, Practical uses of SPFIT, *J. Mol. Spectrosc.* 340 (2017) 1–15. doi:10.1016/j.jms.2017.07.009.
- [139] L. Bonah, S. Schlemmer, S. Thorwirth, Spectroscopy of Vibrationally Excited Complex Organic Molecules for Radio Astronomy, *in prep.*
- [140] L. Bonah, O. Zingsheim, H. S. P. Müller, J.-C. Guillemin, F. Lewen, S. Schlemmer, LLWP—A new Loomis-Wood software at the example of Acetone- $^{13}\text{C}_1$ , *J. Mol. Spectrosc.* 388 (2022) 111674. doi:10.1016/j.jms.2022.111674.
- [141] L. Bonah, S. Schlemmer, J.-C. Guillemin, M. E. Harding, S. Thorwirth, On the Spectroscopy of Phosphaalkynes: Millimeter- and Submillimeter-Wave Study of  $\text{C}_2\text{H}_5\text{CP}$ , *J. Phys. Chem. A* 128 (2024) 4859–4866. doi:10.1021/acs.jpca.4c02566.
- [142] E. Gibb, A. Nummelin, W. M. Irvine, D. C. B. Whittet, P. Bergman, Chemistry of the Organic-rich Hot Core G327.3-0.6, *Astrophys. J.* 545 (2000) 309–326. doi:10.1086/317805.
- [143] L. Bonah, B. Helmstaedter, J.-C. Guillemin, S. Schlemmer, S. Thorwirth, Extending the rotational spectrum of cyclopentadiene towards higher frequencies and vibrational states, *J. Mol. Spectrosc.* 408 (2025) 111967. doi:10.1016/j.jms.2024.111967.
- [144] F. J. Lovas, P. Groner, Microwave spectra of mono- $^{13}\text{C}$  substituted acetone,  $(\text{CH}_3)_2\text{CO}$ , *J. Mol. Spectrosc.* 236 (2006) 173–177. doi:10.1016/j.jms.2006.01.009.
- [145] V. W. Laurie, Microwave Spectrum and Dipole Moment of Cyclopentadiene, *J. Chem. Phys.* 24 (1956) 635–636. doi:10.1063/1.1742585.
- [146] L. H. Scharpen, V. W. Laurie, Structure of Cyclopentadiene, *J. Chem. Phys.* 43 (1965) 2765–2766. doi:10.1063/1.1697207.
- [147] R. C. Benson, W. H. Flygare, Molecular Zeeman Effect of Cyclopentadiene and Isoprene and Comparison of the Magnetic Susceptibility Anisotropies, *J. Am. Chem. Soc.* 92 (1970) 7523–7529. doi:10.1021/ja00729a001.
- [148] M. Bogey, C. Demuynek, J. L. Destombes, The millimeter wave spectrum of cyclopentadiene, *J. Mol. Spectrosc.* 132 (1988) 277–279. doi:10.1016/0022-2852(88)90074-4.
- [149] D. Damiani, L. Ferretti, E. Gallinella, Structure of cyclopentadiene from microwave spectra of several deuterated species, *Chem. Phys. Lett.* 37 (1976) 265–269. doi:10.1016/0009-2614(76)80212-6.
- [150] R. A. Creswell, P. J. Manor, R. A. Assink, R. H. Schwendeman, Microwave spectrum, torsional excitation energy, partial structure, and dipole moment of oxiranecarboxaldehyde, *J. Mol. Spectrosc.* 64 (1977) 365–375. doi:10.1016/0022-2852(77)90222-3.
- [151] D. P. Zaleski, K. Prozument, Automated assignment of rotational spectra using artificial neural networks, *J. Chem. Phys.* 149 (2018). doi:10.1063/1.5037715.
-

- [152] Blender Online Community, Blender - a 3D modelling and rendering package, Blender Foundation, Stichting Blender Foundation, Amsterdam.  
URL <http://www.blender.org>
- [153] G. Van Rossum, F. L. Drake, Jr., Python reference manual, Centrum voor Wiskunde en Informatica Amsterdam, 1995.

# List of Abbreviations

<b>ALMA</b>	Atacama Large Millimeter/submillimeter Array
<b>AM</b>	amplitude modulation
<b>AMC</b>	amplifier-multiplier chain
<b>ASAP</b>	Automated Spectral Assignment Procedure
<b>CDMS</b>	Cologne Database for Molecular Spectroscopy
<b>CFOUR</b>	Coupled-Cluster techniques for Computational Chemistry
<b>CLI</b>	command line interface
<b>COM</b>	complex organic molecule
<b>DM-DR</b>	double-modulation double-resonance
<b>DR</b>	double resonance
<b>EM</b>	electromagnetic
<b>ERHAM</b>	Effective Rotational HAMiltonian
<b>FIR</b>	far-infrared
<b>FM</b>	frequency modulation
<b>FWHM</b>	Full Width at Half Maximum
<b>GBT</b>	Green Bank Telescope
<b>GUI</b>	graphical user interface
<b>HDPE</b>	high-density polyethylene
<b>IR</b>	infrared
<b>IRAM</b>	Institut de Radioastronomie Millimétrique
<b>JWST</b>	James Webb Space Telescope
<b>LAM</b>	large amplitude motion
<b>LWP</b>	Loomis-Wood plot
<b>MMW</b>	millimeter-wavelength
<b>MW</b>	microwave
<b>PAS</b>	principal axis system
<b>QCC</b>	quantum chemical calculations
<b>QM</b>	quantum mechanical
<b>RF</b>	radio frequency
<b>RMS</b>	root mean square
<b>SOFIA</b>	Stratospheric Observatory For Infrared Astronomy
<b>SNR</b>	signal-to-noise ratio
<b>sub-MMW</b>	sub-millimeter-wavelength
<b>TRACE</b>	Tool for Remotely Accessing and Controlling Experiments
<b>UV</b>	ultraviolet
<b>WRMS</b>	weighted root mean square

# List of Figures

1.1	Opacity of Earth’s atmosphere . . . . .	2
1.2	The four COMs analyzed in this thesis . . . . .	4
2.1	Energy term diagram and spectrum of a linear molecule . . . . .	10
2.2	Energy term diagrams of a linear molecule, prolate and oblate symmetric top	12
2.3	Correlation diagram for asymmetric top energy levels . . . . .	14
2.4	Energy term diagrams for different $\kappa$ ’s . . . . .	15
2.5	Different transition types of an asymmetric top . . . . .	17
2.6	Population and Boltzmann factor of linear molecule . . . . .	19
2.7	Simulated spectrum of glycidaldehyde . . . . .	21
2.8	Potential function for threefold internal rotor . . . . .	22
2.9	Correlation diagram for internal rotation energy levels . . . . .	24
2.10	Internal rotation sublevels for zero, one, or two internal rotors . . . . .	26
3.1	Frequency coverage of experimental setups . . . . .	28
3.2	Experimental setup of the THz spectrometer setup . . . . .	30
3.3	DR setup at MIDAS-COINS . . . . .	31
4.1	Flowchart of the analysis process . . . . .	33
4.2	Example of the <i>pyckett_add</i> command . . . . .	38
A.1	Reduced energy plot for glycidaldehyde . . . . .	117
A.2	Reduced energy plot for cyclopentadiene . . . . .	117
A.3	Experimental setup of the (Sub-)Millimeter spectrometer . . . . .	118
A.4	Residual plot of glycidaldehyde . . . . .	119
A.5	Residual plot of glycidaldehyde for missing parameters . . . . .	120
A.6	Residual plot of glycidaldehyde with misassignments . . . . .	120
A.7	Example of <i>pyckett_omit</i> command . . . . .	121
A.8	Example of the <i>pyckett_add</i> command for two missing parameters . . . . .	122
A.9	GUI of the <i>retrophase</i> software . . . . .	123
A.10	GUI of the <i>fftfiltering</i> software . . . . .	124
A.11	GUI of the <i>TRACE</i> measurement software (1) . . . . .	126
A.12	GUI of the <i>TRACE</i> measurement software (2) . . . . .	127

# Acknowledgments

In the introduction, I explained how the fingerprint of a molecule depends on its surroundings. In the same way, this thesis hopefully gives a good insight into my environment over the last four years, into how much I have learned, and also into how much I have laughed and enjoyed this process. For that, I am deeply grateful to everyone who has accompanied me on this adventure! First and foremost, I would like to thank Prof. Dr. Stephan Schlemmer for being my supervisor and the first reviewer of this thesis, but especially for all the enriching discussions, the trust placed in me, and the freedom that came with it. Furthermore, I would like to thank Prof. Dr. Zbigniew Kisiel, and Prof. Dr. Laurent Margulès for being the additional reviewers, Prof. Dr. Mathias Schäfer for being the chair of the thesis defense committee, and Dr. Sven Thorwirth for taking the minutes.

I would like to thank Dr. Oliver Zingsheim for starting out as my co-supervisor and becoming a great friend. Thank you for all the fundamental discussions, all the answers to small and big questions – this was the foundation this thesis is built on! I would also like to thank Dr. Sven Thorwirth for solving all my chemical questions, calming me down when required, and being another great mentor!

I would like to thank Dr. Holger S. P. Müller for all the insights into fitting spectra and all the little quirks of SPFIT and SPCAT, Dr. Christian Endres for diving into every single little detail with me, Dr. Marie-Aline Martin-Drumel and Dr. Olivier Pirali for being such great hosts at SOLEIL and for all the late-night discussions, Dr. Jean-Claude Guillemin for his tireless work in the lab, providing samples without which this thesis would not have been possible, Dr. Arnaud Belloche for explaining to me the astronomers' side of the puzzle and his astronomical searches, PD Dr. Michael E. Harding for sharing his knowledge of QCC and helping me with the same, Dr. Frank Lewen for his magic touch with the experimental setups, and Benedikt Helmstaedter for all his work on cyclopentadiene.

I would like to thank Dr. Sven Thorwirth, Dr. Holger S. P. Müller, Dr. Sam J. P. Marlton, and Lise von Rötel for proofreading and constructive criticism of the manuscript.

I would like to thank all of the Molspekies for the great atmosphere – especially Lise for resurrecting my office plants several times, and Divita, Sam, and Wesley for all the work and non-work related discussions!

Finally, I would like to thank my parents and brothers for always supporting me and believing in me. If life was a highway, you were its guardrails, giving me a sense of safety most of the time, but never afraid to take a hit to keep me on the right track.

Furthermore, I thank the Collaborative Research Centres 956 and 1601 for their financial support, both funded by the Deutsche Forschungsgemeinschaft (DFG), and the teams behind the open source projects Avogadro,<sup>40</sup> POV-Ray,<sup>41</sup> Blender,<sup>152</sup> and Python3.<sup>153</sup>

# Eigenständigkeitserklärung

Hiermit versichere ich an Eides statt, dass ich die vorliegende Dissertation selbstständig und ohne die Benutzung anderer als der angegebenen Hilfsmittel und Literatur angefertigt habe. Alle Stellen, die wörtlich oder sinngemäß aus veröffentlichten und nicht veröffentlichten Werken dem Wortlaut oder dem Sinn nach entnommen wurden, sind als solche kenntlich gemacht. Ich versichere an Eides statt, dass diese Dissertation noch keiner anderen Fakultät oder Universität zur Prüfung vorgelegen hat; dass sie - abgesehen von unten angegebenen Teilpublikationen und eingebundenen Artikeln und Manuskripten - noch nicht veröffentlicht worden ist sowie, dass ich eine Veröffentlichung der Dissertation vor Abschluss der Promotion nicht ohne Genehmigung des Promotionsausschusses vornehmen werde. Die Bestimmungen dieser Ordnung sind mir bekannt. Darüber hinaus erkläre ich hiermit, dass ich die Ordnung zur Sicherung guter wissenschaftlicher Praxis und zum Umgang mit wissenschaftlichem Fehlverhalten der Universität zu Köln gelesen und sie bei der Durchführung der Dissertation zugrundeliegenden Arbeiten und der schriftlich verfassten Dissertation beachtet habe und verpflichte mich hiermit, die dort genannten Vorgaben bei allen wissenschaftlichen Tätigkeiten zu beachten und umzusetzen. Ich versichere, dass die eingereichte elektronische Fassung der eingereichten Druckfassung vollständig entspricht.

Teilpublikationen:

Endres *et al.*, *J. Mol. Spectrosc.* **375** (2021) 111391  
Zingsheim *et al.*, *J. Mol. Spectrosc.* **381** (2021) 111519  
Herbers *et al.*, *J. Chem. Phys.* **155** (2021) 224302  
Zingsheim *et al.*, *J. Mol. Spectrosc.* **384** (2022) 111565  
Zingsheim *et al.*, *Astron. Astrophys.* **662** (2022) A111  
Bonah *et al.*, *J. Mol. Spectrosc.* **388** (2022) 111674  
Changala *et al.*, *Astron. Astrophys.* **680** (2023) A19  
Thorwirth *et al.*, *Molecules* **29** (2024) 665  
Silva *et al.*, *J. Chem. Phys.* **160** (2024) 071101  
Bonah *et al.*, *J. Phys. Chem. A* **128** (2024) 4859  
Bonah *et al.*, *J. Mol. Spectrosc.* **408** (2025) 111967  
Bonah *et al.*, *ACS Earth Space Chem.* **in press** (2025)

---

Köln, den 13.01.2025